

**FINAL SCIENTIFIC/TECHNICAL REPORT**

**U.S. Department of Energy National Energy Technology Laboratory**

**Cooperative Agreement: DE-FE0026083**

**Project Title: Offshore CO<sub>2</sub> Storage Resource Assessment of the Northern Gulf of Mexico (Texas-Louisiana)**

**Principal Investigator: Dr. Tip Meckel**

**PH: 512-471-4306**

**[tip.meckel@beg.utexas.edu](mailto:tip.meckel@beg.utexas.edu)**

**Co-Principal Investigator: Mr. Ramon Trevino**

**PH: 512-471-3362**

**[ramon.trevino@beg.utexas.edu](mailto:ramon.trevino@beg.utexas.edu)**

**PRINCIPAL AUTHORS**

**Ramon Trevino**

**Tip Meckel**

**Submission Date: November 26, 2019**

**DUNS Number: 170230239**

**The University of Texas at Austin**

**Jackson School of Geosciences**

**Bureau of Economic Geology**

**University Station, Box X**

**Austin, Texas, 78713**

**Project Period: September 1, 2015 – August 31, 2019**

**Signature Submitting Official:** \_\_\_\_\_

## **DISCLAIMER**

This report was prepared as an account of work sponsored by an agency of the United States Government. Neither the United States Government nor any agency thereof, nor any of their employees, makes any warranty, express or implied, or assumes any legal liability or responsibility for the accuracy, completeness, or usefulness of any information, apparatus, product, or process disclosed, or represents that its use would not infringe privately owned rights. Reference herein to any specific commercial product, process, or service by trade name, trademark, manufacturer, or otherwise does not necessarily constitute or imply its endorsement, recommendation, or favoring by the United States Government or any agency thereof. The views and opinions of authors expressed herein do not necessarily state or reflect those of the United States Government or any agency thereof.

## Table of Contents

EXECUTIVE SUMMARY .....	12
1 Task 1.0 – Project Management, Planning, and Reporting.....	16
2 Task 2.0 – Conduct Regional Geologic Assessment .....	16
2.1 Subtask 2.1 – Database Development .....	16
2.2 Subtask 2.2 – Develop Comprehensive Data Set for Reservoir Properties .....	35
2.3 Subtask 2.3 – Develop Structural Closure Mapping for Reservoirs.....	39
2.4 Subtask 2.4 – Assess Seal Interval Characteristics .....	54
2.5 Subtask 2.5 – Analyze CO <sub>2</sub> Prospect Categories .....	87
3 Task 3.0 – Static Capacity Estimates .....	91
3.1 Subtask 3.1 – Regional Capacity Assessment.....	91
3.2 Subtask 3.2 – Local Prospect Resource Assessment .....	101
3.3 Subtask 3.3 – Data Management .....	107
4 Task 4.0 - Dynamic Capacity Assessments .....	111
4.1 Subtask 4.1 – Statistical Analysis of Production Data.....	111
4.2 Subtask 4.2 – EASiTool (Enhanced Analytical Simulation Tool) Application.....	118
5 Task 5.0 - Outreach and Stakeholder Engagement .....	131
5.1 Subtask 5.1 – Local Public and Stakeholder Outreach.....	132
5.2 Subtask 5.2 – Regional Outreach .....	134
6 PRODUCTS.....	136
7 PARTICIPANTS & OTHER COLLABORATING ORGANIZATIONS.....	140
8 IMPACT .....	141
9 REFERENCES CITED.....	150

## **List of Figures**

Figure 2.1.1 – Map of the study area (purple polygon) showing the status of the Petra well database early in the project (as of September 15, 2015). Wells with black dots had raster logs only. Green dots indicate wells with LAS digital SP curves, and red rhombs indicate wells with LAS that include gamma ray curves. ....	17
Figure 2.1.2 – Color coded map of the project’s study area showing the status of the well data in the Petra project. Wells with digital (LAS) SP curves are shown as green dots; wells with digital (LAS) gamma ray curves are shown as red rhombs; wells with rasters (no LAS) are showing with black dots, and cyan colored wells indicate wells without any current raster or LAS (digital) data.....	18
Figure 2.1.3 – Map of the study area showing wells and primary 3D seismic dataset (“TxLa Merge” highlighted in orange). The state - federal waters boundary is demarcated by the blue line subparallel to the coast. (Note that Texas state waters are wider than those of Louisiana.) The wells with digital logs in the study area, which have SP curves are shown with green dots; wells with gamma ray logs are shown with red rhombs; blue circles indicate wells with sonic and/or density logs, and wells with whole core for various intervals in the Miocene geologic section are indicated with red squares; orange squares represent cores for the interval of interest. Dip and strike cross-sections are indicated by red lines. ....	19
Figure 2.1.4 – Dip-oriented structural cross-section in Texas (AA’ in Figure 2.1.3).....	20
Figure 2.1.5 – Map showing the major seismic datasets included in the current Landmark OpenWorks project, “TexLa CO2.” Note that the dataset specifically pertinent to the current study resides between the yellow arrows “Trinity” and “Sabine.” .....	21
Figure 2.1.6 – Regional basemap with outlines of 2D and 3D seismic data loaded into the TexLa_CO2 seismic database “project.” “TexLa-Merge 3D” was acquired from SEI in September, 2015 and loaded in September/early October. “USGS 3Ds” were integrated with existing BEG local available 3Ds. BOEM 2D datasets were loaded and merged with regional 2D horizons data. ....	22
Figure 2.1.7 – Basemap of 3D seismic datasets from NAMSS that were uploaded to the project database including the two newly integrated datasets, West Cameron (blue) and Vermillion Phs 1-3 (Red).....	23
Figure 2.1.8 – Outlines of conventional 3D seismic datasets added to the project seismic database. The vertical maroon rectangle is the outline for the “Shell_High_Def” survey (350 Km <sup>2</sup> ) survey, and horizontal blue-green rectangle outlines the West Cameron_FairfieldNodel (800 Km <sup>2</sup> ) survey.....	23
Figure 2.1.9 – Screen capture of a neural network learning set being saved after successfully picking and flattening the first arrival in the GOM2012 dataset. Statistics in the center window show the various iterations level of success. The lower panel shows flattened first arrival with the proposed solution. After learning occurs on a training set, the software picks the entire dataset. ....	25
Figure 2.1.10 – Refractor flattening method handles large shot timing issues. Left panel shows 8 shots in the GOM2012 dataset flattened using a constant velocity for the water bottom. The right side shows large and small shifts in the shots to be flattened to T = 0 ms (milliseconds). The bulk shift of the shots is an issue similar to re-datuming and can be handled with a shift based on the left panel’s flattened intercept time with averaging to remove the large shifts. ....	25
Figure 2.1.11– Example of a banded shift (within yellow oval) seen on time slice (in the GOM2012 dataset) due to shot timing issues. This is possibly occurring along a sail line (series of shots in row) and may be in the original GPS data or simply a constant time delay. ....	26
Figure 2.1.12 – Panels of the GOM2012 dataset showing the effect of adding statics correction; left panel shows new statics; right is without statics correction. Since the reflections line up better after the statics	

correction, they stack together more strongly and appear to have greater coherency with increasing time.  
..... 27

Figure 2.1.13 – Panel showing effects of positional uncertainty corrections. Resolution around faults is greater on the left than on the right. Green arrows outline the fault edge which is not as defined in uncorrected data. .... 27

Figure 2.1.14 – Time slice showing “C” shaped artifacts (aka catenaries), which are due to the shot layout and must be removed by improved processing. These “footprints” may be a shot static issue or a slight phase shift. .... 28

Figure 2.1.15 – Geometry diagram of GOM2012 showing missing data; shots are the black dots and the receivers are pink. .... 29

Figure 2.1.16 – Geometry diagram showing the shots with bad data values, shots are the black dots and the receivers are pink. .... 30

Figure 2.1.17 – Geometry fold diagram (a.k.a. fold map) of GOM2012 showing the missing data in the lower left-hand corner of the survey as a blank straight line. .... 30

Figure 2.1.18 – Noise in shots shown by displaying channel 1 with each trace being a shot..... 31

Figure 2.1.19 - GOM2012 Inline 5722 before positional corrections or phase shifting filters (i.e., using only notch filters and shot signature derived from the whole shot). Other processing is the same as for the data in Figure 2.1.20. .... 32

Figure 2.1.20 - Gom2012 Inline 5722 showing increased resolution with depth, sharpened faults and salt sediment boundaries. Depth of interpretable reflections is about 1.25 seconds ..... 33

Figure 2.1.21 - Spectrum of data in figure 2.1.19. High frequency noise and signal to noise ratio of 1 or less. .... 34

Figure 2.1.22 Spectrum of data in Figure 2.1.20. Nearly 40Db cut on the low side and 50Db on all high frequencies contribute visually to better resolution. .... 34

Figure 2.1.23 Gom2012 Time slice at 145ms. Note the complete lack of resolution versus the results of new techniques (Figure 2.1.24)..... 34

Figure 2.1.24 – GOM2012 survey timeslice at 145 ms. Enhanced resolution of geologic features and amplitude balancing versus Figure 2.1.23. Banding along inlines is still evident but improved, it may be mitigated after migration..... 35

Figure 2.2.1 – Map of Galveston (TX6) and High Island (TX7) federal lease areas..... 36

Figure 2.2.2 – Comparison of reservoir porosity in Miocene pools in the Galveston and High Island lease areas. N=191; porosity standard deviation = 0.02529. .... 37

Figure 2.2.3 – Cross-plot of reservoir porosity vs. pool depth in the Galveston and High Island lease areas with p-value 2.5e-07.  $R^2 = 0.13$ ; n=191; porosity standard deviation = 0.02529..... 37

Figure 2.2.4 – Cross-plot of reservoir porosity vs. temperature in the Galveston and High Island lease areas with p-value 3.2 e-08.  $R^2 = 0.15$ ; n=191; porosity standard deviation = 0.02529..... 38

Figure 2.2.5 – Cross-plot of reservoir temperature vs. depth in the Galveston and High Island lease areas with p-value 2.2e-16.  $R^2 = 0.77$ ..... 38

Figure 2.3.1 – Vertical transect of the TexLa Merge 3D seismic cross-section showing interpreted horizons MFS04 – MFS12..... 40

Figure 2.3.2 – Two-way time interpolated structure of the TexLa Merge 3D Maximum Flooding Surface MFS10 horizon. A total of 214 fault planes (black polygons) penetrate the surface.....	41
Figure 2.3.3 – Two-way time interpolated structure of the TexLa Merge 3D Maximum Flooding Surface MFS12 horizon. A total of 204 fault planes (black polygons) penetrate the surface.....	41
Figure 2.3.4 – Extent of the regional 2D/3D seismic interpretation of MFS05. A total of 282 faults planes (black polygons) penetrate the surface.....	42
Figure 2.3.5 - MFS04 depth montage depicting a) TDQ method results, b) RMS method results, and c) the difference (TDQ minus RMS) between the two methods.....	44
Figure 2.3.6 - MFS05 depth montage depicting a) TDQ method results, b) RMS method results, and c) the difference (TDQ minus RMS) between the two methods.....	45
Figure 2.3.7 - MFS07 depth montage depicting a) TDQ method results, b) RMS method results, and c) the difference (TDQ minus RMS) between the two methods.....	46
Figure 2.3.8 - SB_M08 depth montage depicting a) TDQ method results, b) RMS method results, and c) the difference (TDQ minus RMS) between the two methods.....	47
Figure 2.3.9 - MFS09 depth montage depicting a) TDQ method results, b) RMS method results, and c) the difference (TDQ minus RMS) between the two methods.....	48
Figure 2.3.10 - SB_M09 depth montage depicting a) TDQ method results, b) RMS method results, and c) the difference (TDQ minus RMS) between the two methods.....	49
Figure 2.3.11 - MFS10 depth montage depicting a) TDQ method results, b) RMS method results, and c) the difference (TDQ minus RMS) between the two methods.....	50
Figure 2.3.12 - MFS12 depth montage depicting a) TDQ method results, b) RMS method results, and c) the difference (TDQ minus RMS) between the two methods.....	51
Figure 2.3.13 – Depth structure map of the MFS09 horizon (i.e., the base of regional seal) and the top of stacked reservoir layers within TexLa Merge area. Transparent yellow polygons are structural closures with maximum column height of 50 meters. White lines are the fetch area boundaries for their corresponding closures. Brown polygon are existing oil and gas fields in the state waters as defined by Seni et al. (1997). .....	52
Figure 2.3.14 - Map of faults’ maximum vertical displacements. The average displacement is approximately 20 meters; however, some major faults are much more than 50 meters. The scale is set to maximum 50-meter displacement (red) to better show the distribution.....	53
Figure 2.3.15 – Mapped closures (grey) based on 3D seismic; existing field outlines (brown) as defined by Seni et al, (1997) without the benefit of 3D seismic data, and faults’ maximum vertical displacements around the 24-L and 10-L sites. ....	53
Figure 2.4.1 – Left: Location map of available cores close to project study area. Right: Photograph of the slabbed core of Miocene mudstone of Well OCS-G-3496 A-3. ....	54
Figure 2.4.2a. Photograph of shaly mudstone, 12963 ft, OCS-G-3496 A-3.....	55
Figure 2.4.3 - Core description of OCS-G-3496 A-3, West Cameron Block 205, offshore Louisiana. ....	58
Figure 2.4.4a) EDS map with false color for elements showing silt particles of quartz (Q), K-feldspar (K-f), calcite (Ca), albite (Al) floating in clay matrix. Sample 1 .....	59
Figure 2.4.5a) EDS map with false color for elements showing silt particles of quartz (Q), K-feldspar (K-f), calcite (Ca), albite (Al) floating in clay matrix. Sample 1 .....	61

Figure 2.4.6a) SEM image showing secondary pores (arrow) partially filled with chlorite. Sample 1 ...	63
Figure 2.4.7 - SEM images and EDS elemental maps of siltstone (sample 8).....	66
Figure 2.4.8 – Location map of the core from well OCS-G-3492 C-4 (star). The well is slightly south of the other analyzed core OCS-G-3496 A-3 (Figure 2.4.1).....	67
Figure 2.4.9 - Core description of ARCO well OCS-G-3492 C-4, West Cameron Block 205, Louisiana offshore. ....	68
Figure 2.4.10 – SEM images and EDS elemental maps of the samples. ....	71
Figure 2.4.11 – SEM images of organic matter. ....	72
Figure 2.4.12 – SEM images showing occurrence of pores.....	73
Figure 2.4.13 – Cuttings from OCS-G-4435 #1 contain small, fragile shale flakes not suitable for ion milling and SEM study.....	74
Figure 2.4.14 – SEM images and EDS elemental maps of cutting samples from well COS-G-2305 #1. ...	77
Figure 2.4.15 – Graph of porosity vs. permeability of mudstone samples measured in mercury intrusion capillary pressure tests. ....	80
Figure 2.4.16 – Pore-throat-size distribution (incremental pore volume vs. pore aperture diameter) of the mudstone samples from mercury intrusion capillary pressure tests.....	81
Figure 2.4.17 – Time slices through the diffraction energy attribute volume. Note that the interval corresponding to a time of 200 ms displays areas of high diffraction energy alternating with low diffraction energy zones. This high contrast may indicate fluid saturation in the high-diffractivity areas. ....	83
Figure 2.4.18 – Diffraction energy attribute section (top) and time-migrated conventional section (bottom). The red dots outline an area which has high diffractivity. This may be associated with fluid saturation. Note that the strong-diffractivity area is not evident in the conventional seismic image (bottom). ....	84
Figure 2.4.19 – Depth domain transect of an inline showing the diffraction energy attribute (top) and the conventional seismic image (bottom). The sections are overlaid by borehole logs (near crossline 1600): spontaneous potential log (left, dark colors indicate more shale content) and electrical resistivity log (right, mostly red color). White arrows in the diffraction energy section indicate two high-diffractivity intervals, which correlate with resistivity decrease in the well log. Green arrows show faults connecting those two intervals. The shadow area at crossline 1800 is a data gap that was caused by the need for the HR3D survey acquisition ship to avoid an oil production platform. ....	85
Figure 2.4.20 – Depth slices from 165 m for the diffraction energy attribute (top) and similarity (a.k.a. continuity) attribute (bottom). White dashed lines indicate the boundary between the high-diffractivity and low diffractivity zones. Yellow arrows indicate faults on which two attributes correlate well. Red dot locates a well in which the wireline logs were recorded. Note the data gap area in the upper center-right portion of the survey next to the well. ....	86
Figure 2.4.21 – Time slice for input stack volume. The data appear with many gaps.....	87
Figure 2.4.22 – Seismic attributes (top) compared with diffraction energy (bottom). The gas chimney system area (red outline rectangle) appears as a strong source of diffraction waves.....	87
Figure 2.5.1 – Map of the study area showing wells and the primary 3D seismic dataset, “TexLa Merge” (highlighted in orange) The state - federal waters boundary is demarcated by the blue line subparallel to the coast (note that Texas state waters are wider than those of Louisiana). ....	88
Figure 2.5.2 – Dip-oriented structural well log cross-section (AA’ in Figure 5.1) including two wells with	

cores from the Miocene section. Multiple normal faults offset the stratigraphy (purple lines in Figure 5.1). Cored intervals from the Atlantic Richfield OCS G10266 and Vastar Resources SL 59455 (Figure 2.5.5) wells in High Island are highlighted in red. .... 89

Figure 2.5.3 – Core photographs from the Atlantic Richfield OCS G10266 well — High Island — a sandstone dominated interval (each core sleeve is about 60 cm long and 7 cm wide; the stratigraphic top is the upper left corner). .... 89

Figure 2.5.4 – Close-up photo of Atlantic Richfield OCS G10266 (API 427084032600) well’s core; each core photograph is 7 cm wide. (A) Very fine-grained structureless sandstone passing upward into slightly parallel laminated sandstone. (B) Low angle parallel to undulatory laminations in very fine-grained sandstone; laminae accentuated by mud drapes (note micro-fault at the top of the photo). (C) Deformed sandstone showing nearly vertical dip to the original laminae. (D) Thinly interbedded sandstone and mudstone with micro-faults; laminae accentuated by finely comminuted organic detritus (some double mud drapes are present). .... 90

Figure 2.5.5 – Core photographs from Vastar Resources SL 59455 (API 42708303160000) well — High Island — showing a mudstone dominated interval (each core sleeve is about 60 cm long and 9 cm wide; the stratigraphic top is the upper left corner). The poor condition of the core and unconsolidated nature of the sediment made it unsuitable for sedimentologic interpretation. .... 90

Figure 3.1.1 – Dip-oriented structural cross-section extending along the border between Texas and Louisiana. The top of the overpressure coincides roughly with MFS12 updip, but due to section displacement and expansion seaward it corresponds to MFS10 and even MFS9 farther downdip. The seal interval associated with MFS9 (*Amphistegina B*) can, in some instances, reach a thickness of about 250m. .... 91

Figure 3.1.2 – Initial net sandstone map of the stratigraphic interval from *Amphistegina B* (MFS9) to *Robulus B* (MFS10). Note that capacity was not estimated for the easternmost portion of the AOI (i.e., within the purple polygon) due to lack of useful well data. .... 92

Figure 3.1.3 – Map of the study area showing wells with digital logs in the study area offshore Texas and Louisiana. Out of the 725 digital logs with SP curves, 20 wells also have sonic or density logs (blue circles) and two wells are cored (olive squares). Normal faults (purple lines) and dip cross-section (dark blue line; see Figure 3.1.4) are also indicated. .... 93

Figure 3.1.4 – Dip-oriented structural cross-section including the most prospective reservoir interval (between *Amphistegina B* - MFS9 and *Robulus L* - MFS10) highlighted in light green. Multiple normal faults offset the stratigraphy. The top of the overpressure (dashed brown line) coincides roughly with MFS12 updip, but due to section displacement and expansion seaward it corresponds to MFS10 and even MFS9 farther downdip (toward the right side of the cross section). The seal interval is associated with MFS9 (*Amphistegina B*), a shale with a maximum thickness of about 250m. Sandstone is shown in yellow in all well logs; non-sandstone facies (mudstone) is denoted by gray. .... 93

Figure 3.1.5 – Net sandstone thickness ( $h_{net}$ ) map for the prospective interval (total area = 5575 km<sup>2</sup>; total volume = 1476 km<sup>3</sup>). The sandstone has a strike-elongated trend and reaches a maximum thickness of about 1500 ft (minimum 50 ft) and an average of about 900 ft. .... 93

Figure 3.1.6 – Porosity map of the Miocene interval in the study area Higher porosity values (>30%) result in larger pore volumes for CO<sub>2</sub> storage. .... 94

Figure 3.1.7 – Temperature, pressure, and CO<sub>2</sub> fluid density vs. depth. Note that the upper depth limit at which CO<sub>2</sub> remains in a supercritical state is marked by the red line (i.e., ~1 km = ~3,300ft). .... 95

Figure 3.1.8 – Mapped grid of CO<sub>2</sub> density at midpoint depth of the prospective interval. Note that CO<sub>2</sub>



density reaches a steady range between 600 and 700 kg/m <sup>3</sup> below supercritical depth with slightly higher values observed downdip.....	95
Figure 3.1.9 – Map of static CO <sub>2</sub> storage capacity ( $G_{CO2net}$ ) using the method of Wallace et al. (2014)....	96
Figure 3.1.10 – Workflow for 3D porosity prediction from well log and seismic data.....	97
Figure 3.1.11 – Seismic profile showing porosity derived from the (A) linear regression and (B) PNN...	98
Figure 3.1.12 – Sequence stratigraphic interpretation of Gamma ray log around the MFS09-MFS10 interval. The SS01 is interpreted to coincide with the sequence boundary between MFS09 and MFS10. This supports the development of channelized fluvio-deltaic systems between non-channelized inner shelf deposits below-and-above the SS01 level.....	100
Figure 3.1.13 – A) Linear multi-attribute derived porosity map of horizon SS01; B) Non-linear PNN derived porosity of horizon SS01; C) RMS amplitude map of horizon SS01 showing seismic geomorphic depositional features (channel belts). D) Interpretation of depositional features and faults based on RMS amplitude map of horizon SS01.....	101
Figure 3.2.1 – Map of coastal Texas districts, Railroad Commission of Texas. HI (High Island) 24L is labeled.....	102
Figure 3.2.2 – Stratigraphic chart and type log for HI 24L.....	103
Figure 3.2.3 – Structure map of the HC Sand reservoir. Footprint of historic hydrocarbon footprint is shown in pink striped polygon. Green wells have only a spontaneous potential (SP) curve, magenta wells have both SP and porosity curves. Lease blocks are labeled. Note that most of the hydrocarbon footprint occurs in Block 24.....	105
Figure 3.2.4 – Well log cross section oriented along depositional strike and highlighting the informal stratigraphic units mentioned in the text. Note the storage interval of interest (SIOI). Cross section line of section shown on Figure 3.2.3. ....	106
Figure 3.3.1 – Map of the study area (purple polygon) showing the status of the Petra well database as of September 15, 2015. Wells with black dots had raster logs only. Green dots indicate wells with LAS digital SP curves, and red rhombs indicate wells with LAS that include gamma ray.....	108
Figure 3.3.2 – Color coded map of the project’s study area showing the status of the well data in the Petra project. Wells with digital (LAS) SP curves are shown as green dots; wells with digital (LAS) gamma ray curves are shown as red rhombs; wells with rasters (no LAS) are showing with black dots, and cyan colored wells indicate wells without any current raster or LAS (digital) data.....	109
Figure 3.3.3 – Upload of 150 in-house digitized LAS SP well logs from the project database to the NETL EDX site.....	110
Figure 3.3.4 – Screen shot of the submission summary screen verifying submission of Klokov et al. (2017) to the NETL EDX site.....	111
Figure 4.1.1 – The geological location of 21 fields (highlighted) used for decline curve analysis (DCA). ....	112
Figure 4.1.2 – Plot of decline rate distribution for wells from the 21 analyzed gas fields.....	113
Figure 4.1.3 – Plot of decline coefficient distribution for wells in the 21 analyzed gas fields. ....	114
Figure 4.1.4 – Cumulative distribution plot for CBP rate per well in terms of reservoir age.....	116
Figure 4.1.5 – Cumulative distribution plot for CBP rate per well in terms of drive mechanism. ....	116

Figure 4.1.6 – Cumulative distribution plot for CBP rate per well in terms of structural trap type. ....	116
Figure 4.1.7 – Cumulative distribution plot for CBP rate per well in terms of reservoir porosity variation. ....	117
Figure 4.1.8 – Cumulative distribution plot for CBP rate per well in terms of reservoir permeability variation. ....	117
Figure 4.1.9 – Cumulative distribution plot for CBP rate per well in terms of reservoir thickness variation. ....	118
Figure 4.2.1 – Geographical location of the 91 offshore TXLA reservoirs in the study area (purple polygon) where EASiTool CO <sub>2</sub> storage capacity was estimated. Red shapes indicate gas fields, green shapes indicate oil fields. ....	119
Figure 4.2.2 – West Cameron 71 Field (reservoir 46) Input Parameters .....	123
Figure 4.2.3 – Storage capacity results for West Cameron 71 (46). Open boundary scenario. ....	124
Figure 4.2.4 – Storage capacity results for West Cameron 71 (46), closed boundary scenario.....	124
Figure 4.2.5 – Sensitivity Analysis for West Cameron 71 (46).....	125
Figure 4.2.6 – High Island 179 (NSD) Input Parameters.....	126
Figure 4.2.7 – Storage capacity results for High Island 179 (NSD). Open boundary scenario. ....	127
Figure 4.2.8 – Storage capacity results for High Island 179 (NSD), open boundary scenario. ....	127
Figure 4.2.9 – Storage capacity results for High Island 179 (NSD). Open boundary scenario. ....	128
Figure 4.2.10 – Cumulative Distribution Function of storage capacities of oil and gas reservoirs in the TXLA study area.....	131
Figure 5.1.1 – Photo of Vanessa Nunez-Lopez (standing) at the Austin Women in Oil & Gas seminar luncheon.....	133
Figure 5.1.2 – Flyer for the outreach meeting held by the Port Arthur, Texas Chamber of Commerce with leadership of project PI, Dr. Tip Meckel. ....	134
Figure 5.2.1 – Photo of attendees of the ASBPA field trip, April 15, 2019, on the last stop of the field trip, Mustang Island, Texas. ....	135
Figure 5.2.2 – Ramón Treviño presenting a CCS talk including results from the project at the 50 <sup>th</sup> annual Offshore Technology Conference (OTC) in Houston.....	136

## **List of Tables**

Table 2.2.1 – Definitions of some terms (Seni et al., 1997). .....	35
Table 2.2.2 – Mean, minimum and maximum porosity, pool depth and temperature values, respectively, for Galveston and High Island lease areas and for the two areas combined. N=191; porosity standard deviation = 0.02529. ....	39
Table 2.4.1 – Two examined cores (red) from West Cameron area among the potentially available cores near the study area. ....	54
Table 2.4.2 – Core samples taken for petrographic and other analyses. Samples in yellow analyzed with SEM. ....	56
Table 2.4.3 – The second examined core (red) from OCS-G-4392 C-4 from West Cameron Block, Louisiana offshore. ....	66
Table 2.4.4 – XRD mineral composition of mudstone core samples from well OCS-G-4392 C-4, West Cameron Block, offshore Louisiana. ....	68
Table 2.4.5 – Four wells examined for suitability of their well cuttings to be used for SEM analyses. ....	74
Table 2.4.6 – XRD mineral composition of mudstone core samples from two well in West Cameron Block, Louisiana. ....	78
Table 2.4.7 – Mercury intrusion capillary (MICP) tests’ porosity and permeability for mudstone samples from OCS-G-3496 #A-3 well. ....	79
Table 3.1.1 – Summary of static capacity parameters .....	96
Table 3.2.1 – Cumulative natural gas and oil production from Offshore Texas State Waters, RRC District 3, the HI 24L field, and the field’s HC sand reservoir. ....	102
Table 3.2.2 – P10, P50, and P90 values for utilized efficiency factors and storage capacity estimates using two workflows, 1) the NETL CO <sub>2</sub> Screen and 2) the 3D Effective Porosity model. $E_{\text{saline}} = E_v E_d$ was used for capacity estimations. ....	107
Table 4.1.1 – Texas and Louisiana fields used for DCA analysis states. ....	112
Table 4.2.1 – CO <sub>2</sub> storage capacity of oil and gas reservoirs in the TXLA region. ....	119
Table 4.2.2 – CO <sub>2</sub> storage capacity of oil and gas reservoirs in the TXLA region. ....	120
Table 4.2.3 – Performance of oil and gas reservoirs in the TXLA region. ....	129

---

## **EXECUTIVE SUMMARY**

The Offshore CO<sub>2</sub> Storage Resource Assessment of the Northern Gulf of Mexico (Texas-Louisiana) project (a.k.a., “TXLA” study) supports Goals 3 & 4 of the DOE NETL Carbon Storage Program Plan by supporting industry’s ability to predict CO<sub>2</sub> storage capacity in geologic formations to within +/- 30% by assessing potential regional storage formations in the State and federally regulated portions of the Gulf of Mexico.

The objective of project was to conduct an offshore carbon storage resource assessment of the Gulf of Mexico, Texas – Louisiana study area. This was accomplished by 1) assessing the carbon dioxide (CO<sub>2</sub>) storage capacity of depleted oil and natural gas reservoirs utilizing existing data (well logs, records and sample descriptions from existing or plugged/abandoned wells, available seismic surveys, existing core samples, and other available geologic and laboratory data) from historical hydrocarbon industry activities in the heavily explored portions of the inner continental shelf portions of the Texas and Louisiana Gulf of Mexico coastal areas; and 2) assessing the ability and capacity of saline formations in the region to safely and permanently store nationally-significant amounts of anthropogenic CO<sub>2</sub> using existing data. Additionally, the study identified at least one specific site with potential to store at least 30 million tonnes of CO<sub>2</sub> which may be considered in the future for commercial or integrated demonstration projects. The study also engaged the public and other stakeholders in the region through outreach activities to apprise them of the study objectives and results.

### **Task 1**

In consultation with NETL project managers, Karen Kluger, PhD and Jerry Carr, PhD, the PIs maintained the Project Management Plan (PMP) and revised it as needed. After receiving a one-year no-cost extension, which was required because of the temporary unavailability of staff to fulfill “Subtask 4.2 – EASiTool (Enhanced Analytical Simulation Tool) Application,” the project concluded under budget. As of project completion, the scope was fulfilled.

### **Task 2**

At the start of the project, examination of a pre-existing IHS Petra© database identified many dozens of wells in the database with wireline well log data (i.e., raster and/or LAS - log ASCII standard) (Figure 2.1.1), which could be utilized to achieve the project’s scope. Subsequently an additional 4337 rasters were purchased from vendor, MJ Systems. The rasters were from wells in Vermilion and Cameron Parishes, Louisiana and Chambers and Jefferson Counties, Texas. The MJ systems rasters were loaded into the Petra database and are shown in Figure 2.1.2. In addition to wireline well log data, a collection of micro-paleontological reports donated by Dr. Rashel Rosen was made available to the project. Where appropriate, the paleontological data were added to the Petra project for, respective, wells.

The “TexLa Merge” regional 3D seismic dataset was received and loaded into a new Landmark OpenWorks project. A geologic project named, “TexLa\_CO2,” which utilizes the Landmark Graphic OpenWorks (OW) platform and interpretation software was created and utilized throughout the study. As establishing regional geologic relationships is always important for subsurface geologic characterization, previously obtained 3D seismic datasets in the region were transferred into the OW project along with cultural data from the Texas and Louisiana coasts (Figure 2.1.3). USGS and BOEM 2D and 3D seismic data over areas of the Texas and Louisiana submerged continental shelf were also downloaded from the BOEM NAMSS site (National Archive of Marine Seismic Surveys) and loaded into the project database.

The project also had access to one HR3D (high-resolution 3D) survey dataset within its area of interest. Internally and informally, the dataset was labeled GOM2014 because the dataset was acquired in 2014. Research progress on a 2017 HR3D dataset from project DE-FE 0028193 “DOE-Field Validation of MVA Technology for Offshore CCS: Novel Ultra-High-Resolution 3D Marine Seismic Technology” (aka “Tomakomai”) suggested that the quality of GOM2014 could be improved by re-processing the dataset. The re-processing efforts on GOM2014 followed some of the methods developed for the Tomakomai survey.

Extensive reservoir data from Seni et al. (1997) for fields in and near the project’s study area were compiled, evaluated and upgraded (i.e., corrupt or inaccurate records identified and corrected or removed) in order to determine whether or not there were apparent geologic and/or geographic trends for reservoir parameters. Analysis of porosity suggested that there is low correlation between reservoir porosity and pool depth ( $R^2 = 0.13$ ) or reservoir porosity and temperature ( $R^2 = 0.15$ ). Not surprisingly, there is good correlation ( $R^2 = 0.77$ ) between reservoir temperature and reservoir depth. Miocene age reservoirs in High Island and Galveston federal lease blocks exhibit good porosity with relatively low variability throughout the area. The current hypothesis is that, at least with respect to reservoir porosity, the High Island and Galveston lease areas are analogs for the entire study area.

The process of identifying and interpreting key horizons in the seismic data began by interpreting shallow horizons in the TexLa Merge 3D seismic dataset and then systematically mapping deeper horizons. The two deepest horizons, MFS10 and MFS12 were mapped throughout the TexLa Merge 3D seismic volume. A total of seven horizons and associated fault plane polygons (MFS04, MFS05, SB-M08, MFS09, SB-M09, MFS10, and MFS12) were interpreted throughout the TexLa Merge 3D seismic volume. We used interpreted horizons from the TexLa Merge 3D seismic volume as starting points, then utilized 2D lines to extend interpretations into more distal areas lacking 3D data coverage (Figure 2.3.4). The 2D lines also served as means to integrate newly obtained, publicly available 3D seismic volumes.

Integrated analysis was performed on structural closures, fetch areas, existing fields, and fault maximum vertical displacement within the TexLa Merge 3D seismic area. The analysis was based on the MFS09 depth structure map as the structure that represents the bottom of a regional seal and the top of stacked potential reservoir strata. Structural closures are mostly faulted anticlines and 3-way dip fault dependent closures. The integrity of the faults, or the closures in general, may be related to the column height of existing gas fields within the TXLA area. The 24-L and 10-L hydrocarbon fields provide ideal information for the relationship between fault integrity, juxtaposition, closures, and column height.

A thorough search through the digital and written records of the BEG core archives at two of the BEG’s core repositories (i.e., Austin and Houston) yielded seven available cores close to the study area, four of which are offshore and three onshore. Two of the cores from West Cameron, Louisiana offshore, were studied in detail. The petrographic and petrophysical results from the core materials suggest consistently good sealing quality of the Miocene mudstone intervals in the West Cameron wells. Porosity is approximately 10%, and more importantly, permeability is low, (~ 0.001 md). Pore throat size distribution of MICP tests shows modal pore throat size sufficiently small for providing high sealing ability. As a result, the mudstone samples are able to retain a CO<sub>2</sub> column height of 52-309 m. Overall, the mudstone unit of the South Marsh Island well are siltier and more porous than the West Cameron counterpart and will have lower sealing ability. However, the mudstone seals in this area are still sufficiently tight as suggested by the presence of the large gas fields, such as Starfak and Tiger Shoal. The results show that the mudstone intervals of the Lower Miocene in the West Cameron area are consistent in terms of petrographic and petrophysical properties through the depth of investigation. The sealing performance should be excellent for the studied intervals.

In addition to analyzing core samples from seal intervals, the availability the GoM2014 HR3D dataset in the project study area provided the opportunity to investigate the macro-scale properties of the geologic

overburden including potential seal and non-seal facies, shallow structure and potential natural fluid flow (migration) pathways. In order to analyze potential fluid pathways in the HR3D dataset, a technique known as diffraction imaging was tested. Diffraction imaging is a seismic imaging technique that operates with waves scattered by geologic heterogeneities such as faults and fractures. This method is often presented as a high-resolution approach. Analysis of diffraction energy associated with a gas chimney identified on other HR3D datasets (i.e., in the San Luis Pass, TX area) improved confidence in the interpretation of active fluid migration in the GoM2014 dataset and thus provided higher confidence for using diffraction seismic techniques as a tool where fluid migration is not as easily identifiable using standard seismic attributes.

### Task 3

Regional static capacity was estimated using the methodology of Wallace et al. (2014), which was, in turn, a modification and refinement of the methodology of Goodman et al. (2011). The static capacity for the analyzed High Island 24L Field area was estimated to be 7.15 gigatonnes (Gt). Maximum and minimum computed storage values were 4.66 and 0.75 Mt/km<sup>2</sup> (megatonnes per square kilometer), respectively. Average and standard deviation were 2.55 Mt/km<sup>2</sup> and 0.75 Mt/km<sup>2</sup>, respectively. For the Miocene section of the prospective interval,  $\phi_{\text{tot}}$  (total porosity) varies from 30% to 33%, and CO<sub>2</sub> density ranges from 640 to 700 kg/m<sup>3</sup>.

The calculated P50 storage volume for the High Island 24L Field using the 3-D porosity model is approximately 190 million metric tonnes (Mt). A similar analysis using NETL's CO<sub>2</sub>-SCREEN tool results in an estimate of 170 Mt. CO<sub>2</sub>-SCREEN (CO<sub>2</sub> Storage Prospective Resource Estimation Excel Analysis) is an Excel-based tool and workflow that was developed by the US-DOE-NETL to screen geological formations for storage. The CO<sub>2</sub>-SCREEN result is 20 Mt less than the Goodman et al. (2011) calculated capacity because the former works in a 2-D space as the hydrocarbon footprint area had to be split into 15 equal square grid blocks, and it was not able to capture the entire area. Also, the effective porosities in CO<sub>2</sub>-SCREEN were much lower because a porosity map (convert 3-D to 2-D) was generated for the entire 3-D grid, including all three intervals (*Amphistegina B* unit, SIOI, and subjacent shale). Nonetheless, these values are relatively close, and they are significant in that they equal much more than the current project's 30 Mt minimum objective.

Throughout the study, an IHS Petra™ project was used as the primary database for well-based data management and interpretation. In addition to the Petra™ database, the project also established and maintained a database for the extensive 2D and 3D seismic datasets that were leased by or were publicly available to the study. The seismic database resided in the Haliburton Landmark™ geologic interpretation platform (i.e., "OpenWorks"). Initially, 7542 wells, 1141 LAS files, and 1087 geologic markers (picks) were loaded into OpenWorks database. As well logs were added to the Petra™ database, they were periodically uploaded to OpenWorks. Of the total, 41 wells had sonic and density curves needed for time to depth velocity modeling.

### Task 4

The production history and geological data for offshore GOM (Gulf of Mexico) oil and gas fields was obtained from Seni et al. (1997). The data for 100 fields in the GOM includes monthly production history data (oil, gas, and water) as well as reservoir petrophysical properties, drive mechanisms, trap type, and reservoir age. The volumes are reported in surface standard conditions, and we used calculated oil formation volume factor, water formation volume factor, and gas expansion factor to infer, respective, volumes at reservoir conditions.

Decline Curve Analysis (DCA) methodology is usually used for forecasting gas/oil production using historical production data. In the context of geo-sequestration (GS), DCA can be used as a proxy predictor

for how historically productive oil and gas reservoirs will function as CO<sub>2</sub> injection reservoirs.

The objective of the PNE (probability of non-exceedance) analysis was to present a statistical investigation concerning production rates in the studied offshore oil and gas reservoirs with a view to gaining further insight concerning forecasting of likely injection rates for similarly located future CO<sub>2</sub> storage projects. The PNE sensitivity analysis showed that reservoir age, drive mechanism, reservoir trap, and reservoir porosity are the key controlling parameters for productivity and consequently optimum CO<sub>2</sub> storage capacity. Another key finding was the negligible correlation between CBP with reservoir transmissivity and porosity.

The EASiTool (Enhanced Analytical Simulation Tool) capacity calculator, a GCCC-developed Windows application funded under DOE DE-FE0009301, is a closed-form analytical solution that was envisioned to provide fast, yet reliable estimates of CO<sub>2</sub> storage capacities of any geologic formation. It is used as a first screening of study areas containing many storage options, such as the offshore TXLA region.

Results from the EASiTool screening indicate that the total CO<sub>2</sub> storage capacity of the reservoirs of the analyzed fields is up to ~197 million metric tonnes. We consider this to be a conservative estimate, as the reservoir area required as input for EASiTool was derived from known cumulative production from the studied reservoirs, which constrains the available volume for CO<sub>2</sub> storage. In subtask 4.2, we used the EASiTool capacity calculator to assess the dynamic CO<sub>2</sub> storage capacities of the same oil and gas fields that were selected and analyzed in subtask 4.1.

A cumulative distribution function of estimated CO<sub>2</sub> storage capacities in the offshore TXLA study area shows that storage capacities across the region are not normally distributed. Fifty percent of the reservoirs have storage capacities of 1.5 million tonnes or less, meaning that the 50% probability is significantly lower than the average storage capacity (2.8285 million tonnes), with a standard deviation of 3.2881 million tonnes. Ninety percent of the reservoirs have capacities of 7.5 million tonnes or less.

## **Task 5**

Staff members on the project conducted sustained outreach to the public and stakeholders throughout the duration of the project. The efforts continued until near the end of the project's period of performance and commenced in the project's first quarter (2015) as reported by project subrecipient, Southern States Energy Board (SSEB). The examples of outreach and stakeholder engagement included in the current report are not an exhaustive list. Rather, they represent a sample of the efforts throughout the project's four years. Outreach efforts and results were reported on a quarterly basis and may be accessed, therein.

## **1 Task 1.0 – Project Management, Planning, and Reporting**

In consultation with NETL project managers, Karen Kluger, PhD and Jerry Carr, PhD, the PIs maintained the Project Management Plan (PMP) and revised it as needed. At completion of the project the scope had been fulfilled. After receiving a one-year no-cost extension that was needed because of the temporary unavailability of staff to fulfill “Subtask 4.2 – EASiTool (Enhanced Analytical Simulation Tool) Application,” the project concluded under budget.

As part of his project duties the PI (principal investigator), Dr. Meckel, supervised the research of graduate research assistants, Reinaldo Sabbagh, Emily Beckham, Izaak Ruiz and Omar Ramirez Garcia who contributed to the project scope.

Early in the project, the PIs coordinated establishment of a “supplemental agreement” with Seismic Exchange, Inc. (SEI), the owner of a regional 3D seismic dataset (TexLa Transition Zone Merge; aka, TexLa Merge) that became a data cornerstone of the project’s available datasets.

Key staff members of the project included nine scientists and two engineers, four graduate research assistants (GRAs) and six undergraduate research assistants. The undergraduate research assistants (URA’s) supervised by staff geologist, Dr. Olariu, were of great help in populating and maintaining the geologic database (i.e., wells, well logs, micro-paleontological data, etc.). (See PARTICIPANTS & OTHER COLLABORATING ORGANIZATIONS.)

Eight peer-reviewed articles were published based on research from the study. (See IMPACT section.)

Detailed research performance progress reports and cost plan status reports were generated and submitted on a quarterly basis. Milestone reports (e.g., “Quick-looks” reports) were submitted on a timely basis.

## **2 Task 2.0 – Conduct Regional Geologic Assessment**

### **2.1 Subtask 2.1 – Database Development**

#### **Well Database**

At the start of the project, examination of a pre-existing IHS Petra© database identified many dozens of wells within the database with wireline log (i.e., raster and/or LAS - log ASCII standard) well log data (Figure 2.1.1) that could be utilized to achieve the project’s scope. Subsequently and in addition, 4337 rasters were purchased from vendor, MJ Systems. The rasters were from wells in Vermilion and Cameron Parishes, Louisiana and Chambers and Jefferson Counties, Texas. The MJ systems rasters were loaded into the Petra database and are shown in Figure 2.1.2.



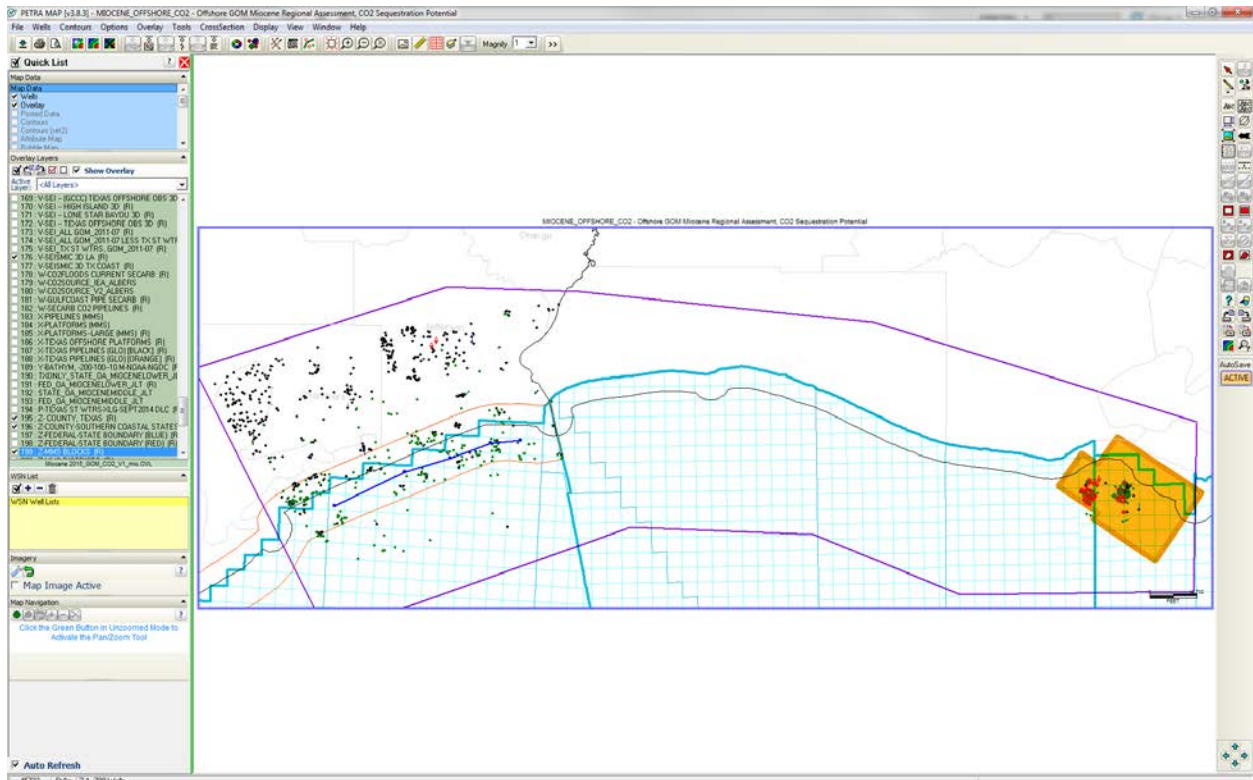


Figure 2.1.1 – Map of the study area (purple polygon) showing the status of the Petra well database early in the project (as of September 15, 2015). Wells with black dots had raster logs only. Green dots indicate wells with LAS digital SP curves, and red rhombs indicate wells with LAS that include gamma ray curves.

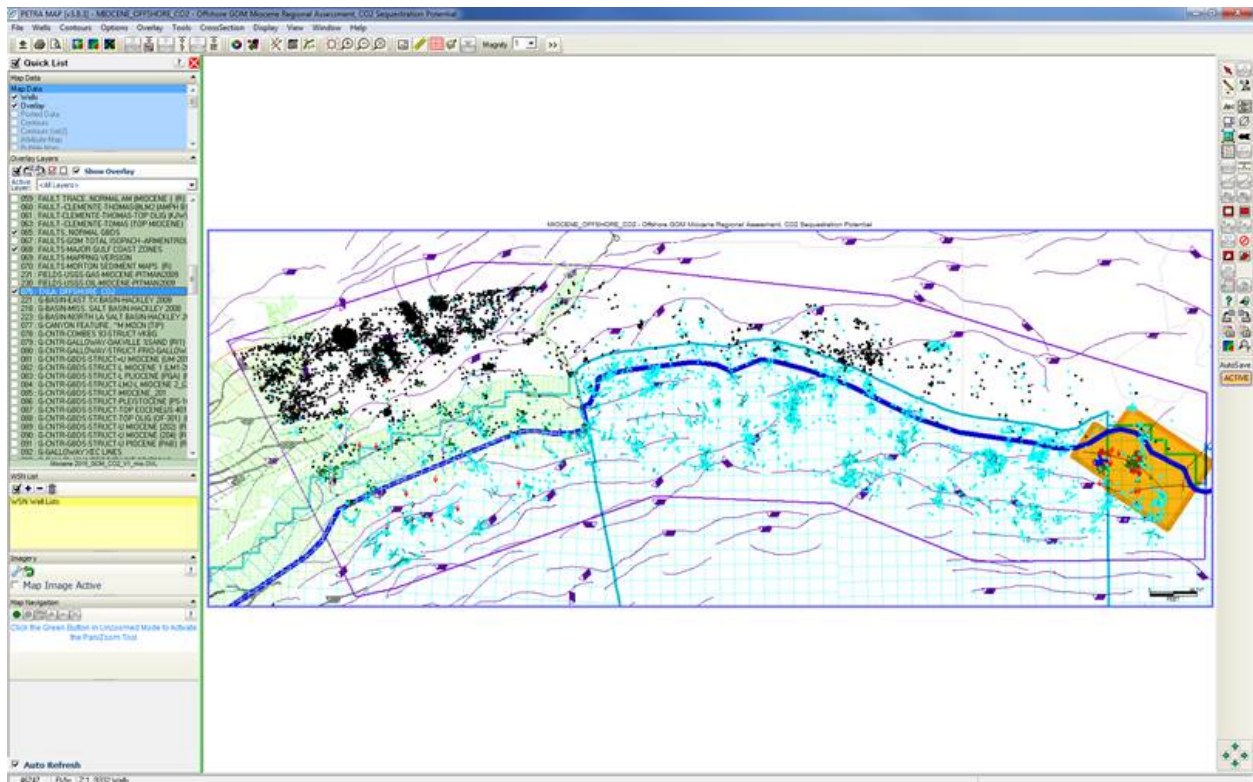


Figure 2.1.2 – Color coded map of the project’s study area showing the status of the well data in the Petra project. Wells with digital (LAS) SP curves are shown as green dots; wells with digital (LAS) gamma ray curves are shown as red rhombs; wells with rasters (no LAS) are showing with black dots, and cyan colored wells indicate wells without any current raster or LAS (digital) data.

In addition to wireline well log data, a collection of micro-paleontological reports donated by Dr. Rashel Rosen was made available to the project. Dr. Rosen, now retired, donated her collection to the University of Texas, Bureau of Economic Geology (BEG) in early 2014. The collection was in the form of PDF scans, and was reviewed to determine how much of it was pertinent to the project. Where appropriate, the paleontological data was added to the Petra project for, respective, wells.

As of the end of the project, there are 2016 wells with digital logs in the study area (Figure 2.1.3), 1887 of which have SP curves; 133 have gamma ray, 37 have either sonic or density logs and 15 wells have whole core. In the offshore sector there are 1254 digital logs with 1140 SP, 58 GR (gamma ray), 20 sonic or density logs and 3 wells have whole core.

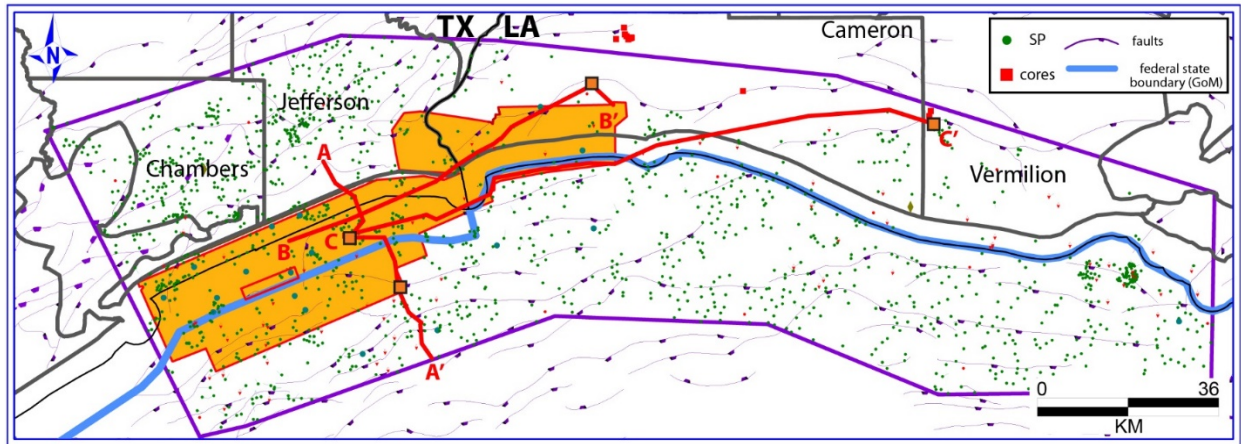


Figure 2.1.3 – Map of the study area showing wells and primary 3D seismic dataset (“TxLa Merge” highlighted in orange). The state - federal waters boundary is demarcated by the blue line subparallel to the coast. (Note that Texas state waters are wider than those of Louisiana.) The wells with digital logs in the study area, which have SP curves are shown with green dots; wells with gamma ray logs are shown with red rhombs; blue circles indicate wells with sonic and/or density logs, and wells with whole core for various intervals in the Miocene geologic section are indicated with red squares; orange squares represent cores for the interval of interest. Dip and strike cross-sections are indicated by red lines.

Multiple normal faults offset the stratigraphy (purple lines in Figure 2.1.4). The upper depth limit for CO<sub>2</sub> injection (SUPERCRITICAL – dashed purple line) is determined by the minimum temperature and pressure conditions at which CO<sub>2</sub> is supercritical (about 3300 ft). The lower depth limit for CO<sub>2</sub> injection (OVERPRESSURE - dashed brown line) is determined by the depth at which the hydrostatic pressure in the subsurface is significantly exceeded. The top of overpressure is obtained from a U.S. Geological Survey geopressure-gradient model of the regional pressure system spanning the onshore and offshore portions of Texas and Louisiana (Burke et al., 2012; Pitman, 2011). The top of the overpressure coincides roughly with MFS12 updip, but due to section displacement and expansion seaward it corresponds to MFS 10 and even MFS 9 farther downdip. The primary reservoir target intervals are the fluvio-deltaic sandstones between MFS 9 and MFS 10 and the primary sealing interval is the regional transgressive shale associated with *Amphistegina B* which in places can reach a thickness of about 250 m (~820 ft). The interval between MFS 9 and MFS 10 has been further subdivided in five 4<sup>th</sup> order cycles by flooding surfaces MFS 9\_1 to MFS9\_4.

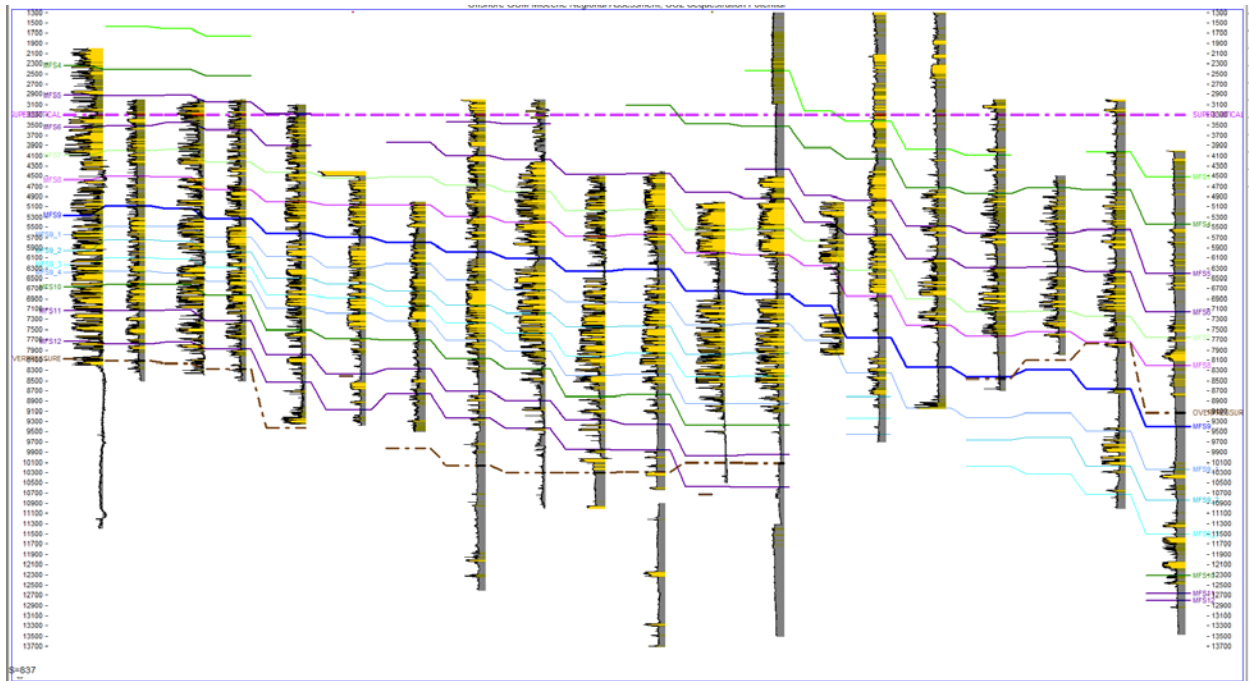


Figure 2.1.4 – Dip-oriented structural cross-section in Texas (AA' in Figure 2.1.3)

## Seismic Database

### *Conventional Seismic*

The “TexLa Merge” regional 3D seismic dataset was received and loaded into a new Landmark OpenWorks project. The data load included the following:

### Basic Products

- AVO PSTM Far Stack
- AVO PSTM Gathers
- AVO PSTM Mid Stack
- AVO PSTM MidFar Stack
- AVO PSTM Near Stack
- AVO PSTM Stack
- AVO PSTM Stack (2)
- AVO PSTM Velocity Cube
- Enhanced PSTM Stack
- PSTM Velocity Grid
- Raw Brute Stack
- Raw PSTM Gathers
- Raw PSTM Stack
- Stacking Velocity Grid

A geologic project database was created, called TexLa\_CO2, which utilizes the Landmark Graphic OpenWorks (OW) platform and interpretation software. As establishing regional geologic relationships is

always important to ascertain early in a geological study, previously obtained 3D seismic datasets in the region were transferred into the OW project along with cultural data from the Texas and Louisiana coast (Figure 2.1.3). This included the download of publicly available USGS and BOEM 2D seismic data over areas of the Texas and Louisiana Shelf. The coordinate system was set to UTM 15 WGS 84 to make it the most universal for Gulf of Mexico datasets. The TexLa Merge 3D dataset was delivered to the BEG in late September and all data were transferred to a secure disk server and replicated (for security). The Enhanced PTSM seismic volumes were loaded into the database and appropriately scaled for interpretation.

### Map of 3D data for the Tx-La OpenWorks project

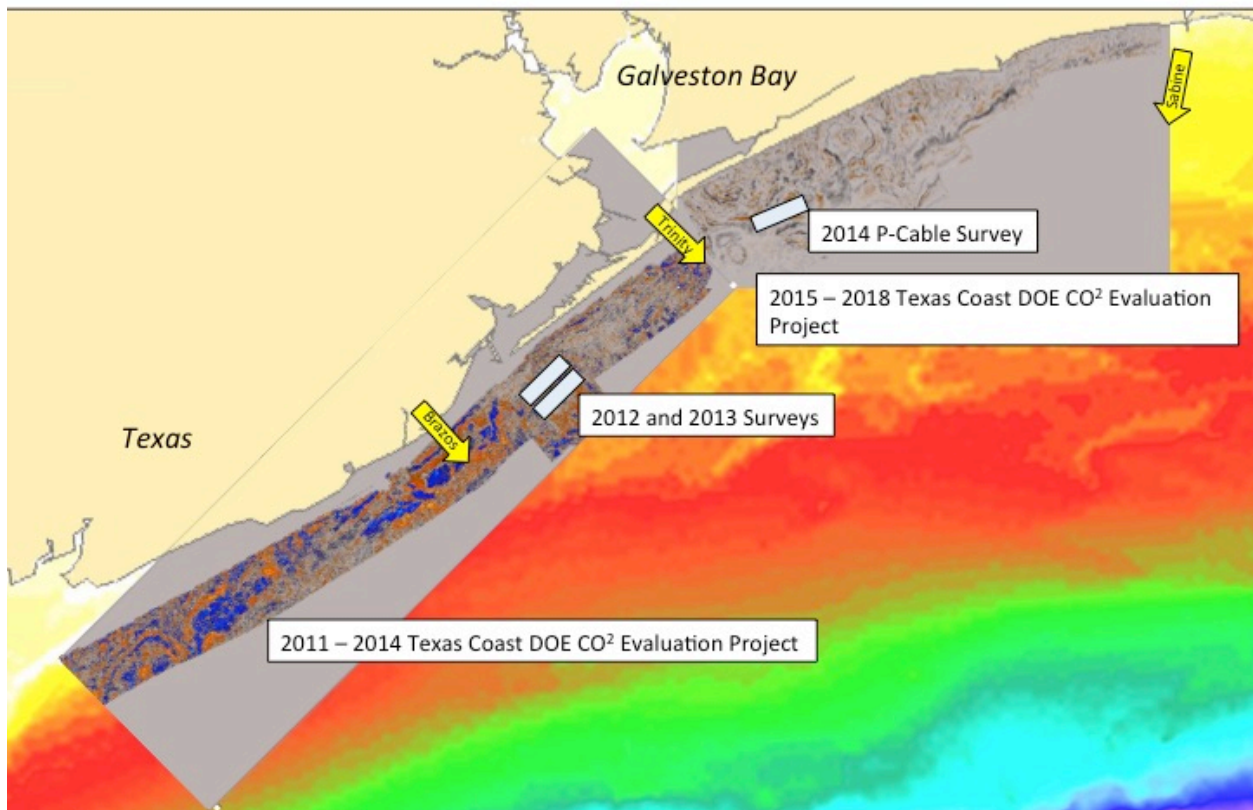


Figure 2.1.5 – Map showing the major seismic datasets included in the current Landmark OpenWorks project, “TexLa CO2.” Note that the dataset specifically pertinent to the current study resides between the yellow arrows “Trinity” and “Sabine.”

USGS and BOEM 2D and 3D seismic data were downloaded from the BOEM NAMSS site (National Archive of Marine Seismic Surveys) and loaded in to the project database (Figure 2.1.6). 2D lines were downloaded and categorized by locality, vintage, and quality. Three 3D datasets were also loaded and evaluated. Although the datasets were relatively small, they were located in areas outside the principle TexLa-Merge 3D and helpful for regional interpretation.

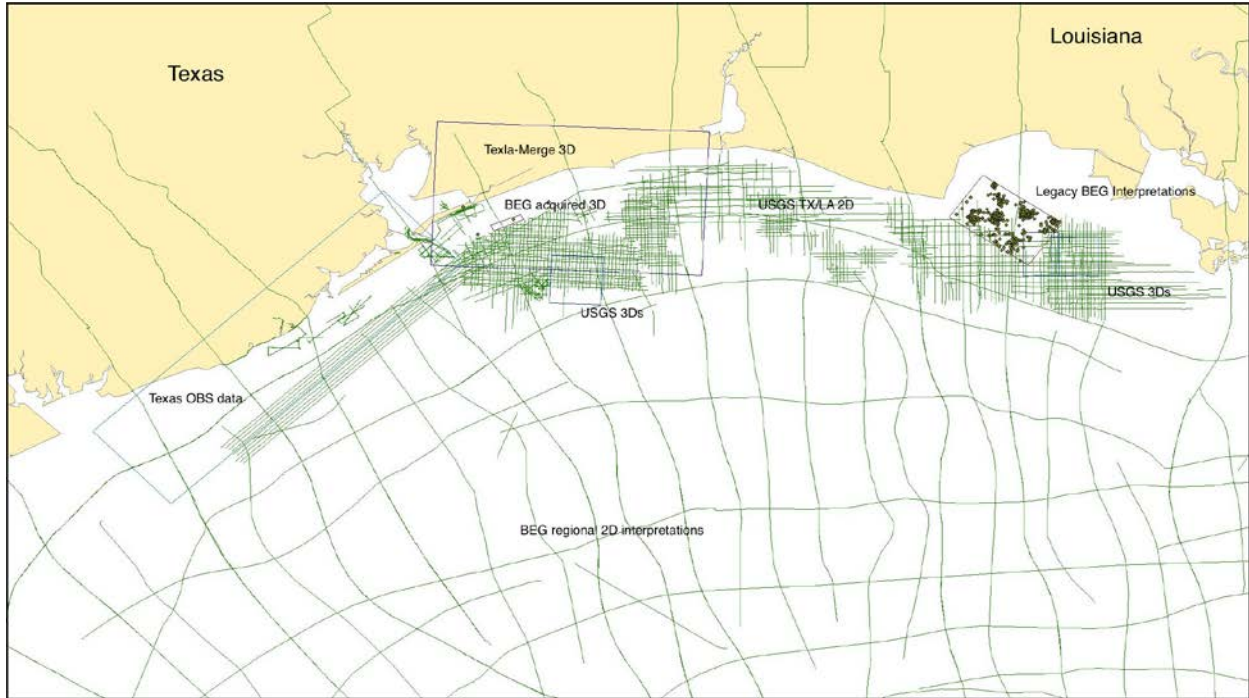


Figure 2.1.6 – Regional basemap with outlines of 2D and 3D seismic data loaded into the TexLa\_CO2 seismic database “project.” “TexLa-Merge 3D” was acquired from SEI in September, 2015 and loaded in September/early October. “USGS 3Ds” were integrated with existing BEG local available 3Ds. BOEM 2D datasets were loaded and merged with regional 2D horizons data.

3D seismic datasets acquired in Federal waters (OCS – offshore continental shelf) are held proprietary for 25 years. After 25 years, federal regulations required that the datasets be made available to the public. As the project’s time of performance coincided with the 25-year anniversaries of a significant amount of 3D seismic acquisition in the Gulf of Mexico, the NAMSS was monitored for newly publicly available 3D datasets within the project’s area of interest (AOI). Figure 2.1.7 shows publicly available 3D datasets added to the project’s seismic database as of March 31, 2017. Similarly, Figure 2.1.8 indicates two additional 3D datasets, “Shell\_High\_Def” and “West Cameron\_FairfieldNodal” that had been added to the project’s seismic database as of March 31, 2018. No other 3D datasets pertinent to the project were added subsequently.

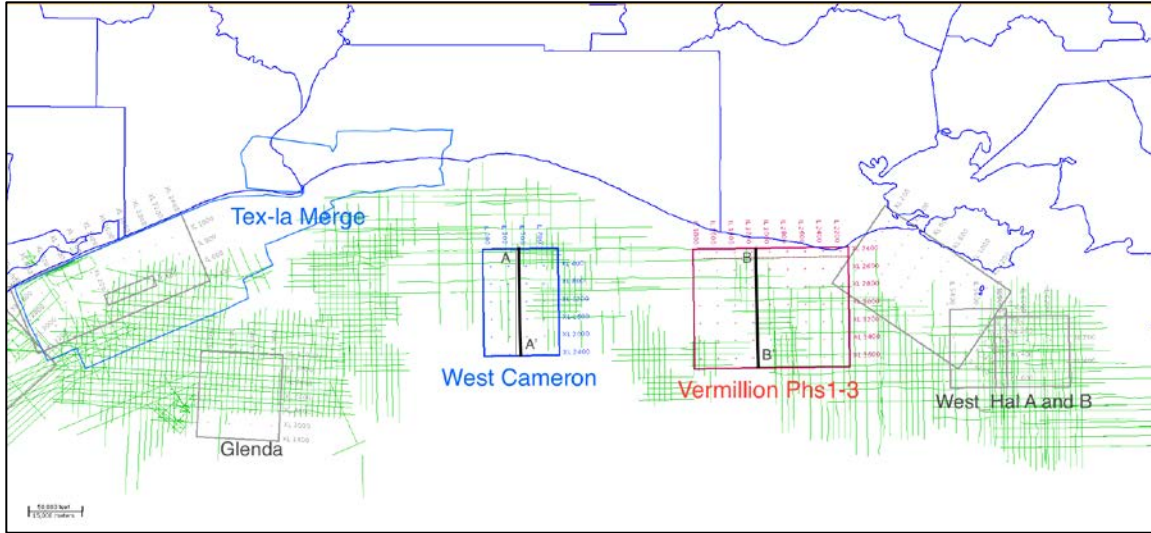


Figure 2.1.7 – Basemap of 3D seismic datasets from NAMSS that were uploaded to the project database including the two newly integrated datasets, West Cameron (blue) and Vermillion Phs 1-3 (Red).

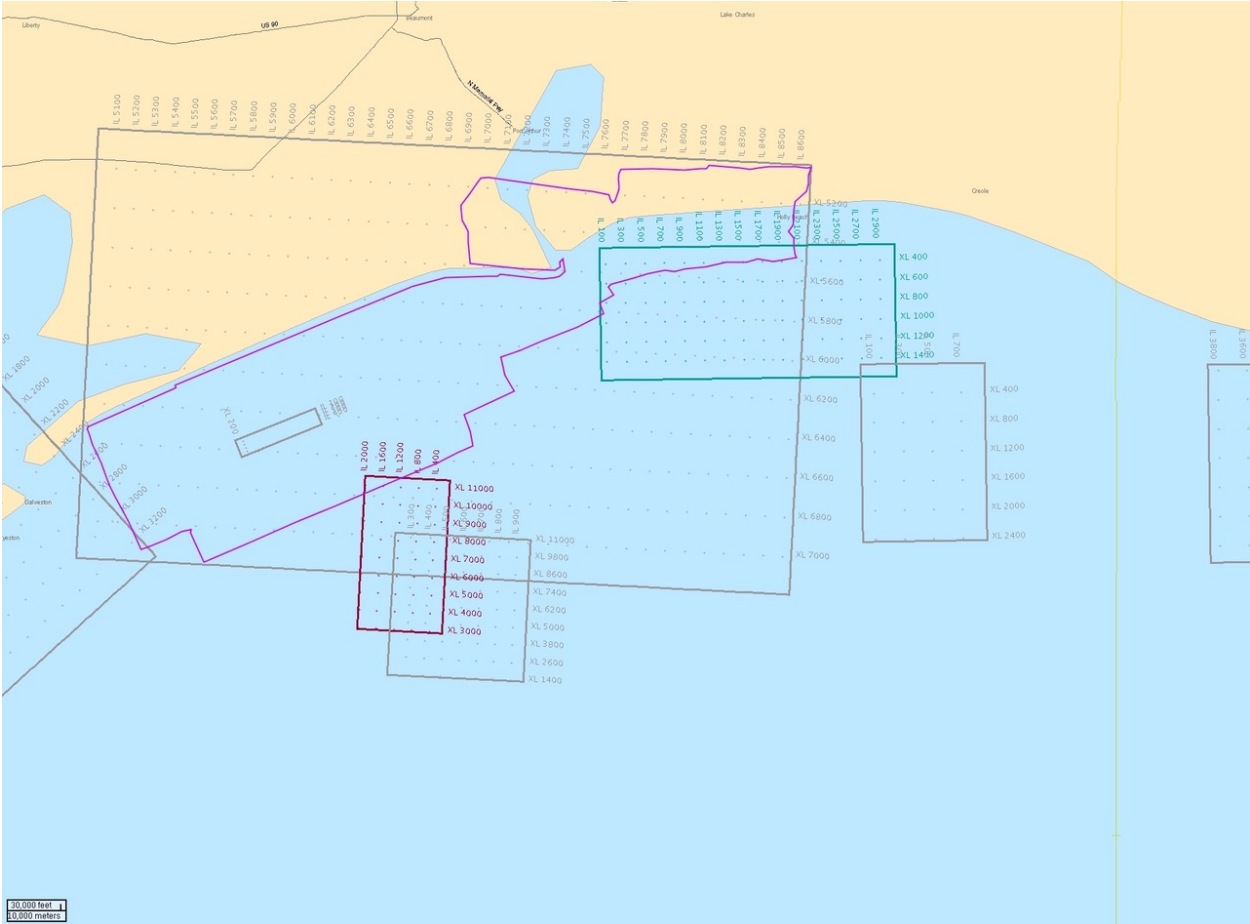


Figure 2.1.8 – Outlines of conventional 3D seismic datasets added to the project seismic database. The vertical maroon rectangle is the outline for the “Shell\_High\_Def” survey (350 Km<sup>2</sup>) survey, and horizontal blue-green rectangle outlines the West Cameron\_FairfieldNodel (800 Km<sup>2</sup>) survey.

### ***High Resolution 3D Seismic (HR3D)***

The project had access to one HR3D (high-resolution 3D) survey dataset within its area of interest. Internally, the dataset was labeled GOM2014 because the dataset was acquired in 2014. Datasets internally labeled GOM2012, GOM2013, and GOM2014 comprised the HR3D surveys available in the project's database. GOM2012 and GOM2013 are located off San Luis Pass (offshore western Galveston Is.); the GOM2014 survey is within of the TXLA area of study. Research progress on a 2017 HR3D dataset from project DE-FE 0028193 "DOE-Field Validation of MVA Technology for Offshore CCS: Novel Ultra-High-Resolution 3D Marine Seismic Technology" (aka "Tomakomai") suggested that the quality of GOM2014 could be improved by re-processing the dataset. The methods were first tested on GOM2012 and 2013 because their processing issues were less subtle than those of GOM2014 and thus any improvements were more verifiable.

The re-processing efforts on GOM2014 followed some of the methods developed for the Tomakomai survey. In fact, the major problem with increasing resolution in each survey was an uncertainty problem related to the position of the hydrophones within each shot. These errors are post GPS processing and account for small errors due to the hydrophone either being out of line (feathering) or diving and resurfacing motions (i.e., in the water column) caused by the tow line geometry.

In addition, signal-processing methods were developed to remove electrical noise using Weiner filters as opposed to using conventional notch filters. Surprisingly, Weiner filtering produces much better spatial resolution. Most of the work in this subject area is well understood and was eventually integrated into the processing flow.

#### **Positional uncertainty**

All HR3D surveys had some issues related to the calculation of receiver positions. As experience with the HR3D wide array layout progressed over the course of three Gulf of Mexico (GoM) HR3D surveys (i.e., 2012, 2013 and 2014), the coordinate problems were recognized and successively minimized. However, remaining positional uncertainty relates to actual XY positions versus calculations, thereof. Usually the GPS coordinates are measured on key areas of the spread and each individual hydrophone's XY coordinates are interpolated. What was found in Tomakomai and confirmed in the GoM HR3D datasets was that minor variations in XY position occurred frequently throughout all surveys.

The minor positional errors are most likely due to the currents, tow speed and wave levels. We believe that the hydrophones may also have developed a diving and rising harmonic pattern despite the use of stabilizers.

Feathering is the error of position when a cable of hydrophones does not properly align due to the above factors. It is a term usually reserved for long arrays with high currents and turns during acquisition. Nonetheless, in the HR3D surveys with shorter cables, the problem does exist, and since the survey is so high resolution in time and space, the small errors matter more.

#### **Machine Learning and Refractor Flattening**

Picking events in noisy data is a common problem in geophysics, and we pursued two solutions. The older neural net method of picking arrivals and shifting their positions to account for an isotropic velocity arrival distorted by positional uncertainty (Figure 2.1.9) is somewhat successful in these datasets. This method requires modifying refraction statics techniques for the problem. Large time shifts (shot delays) need to be handled separately.



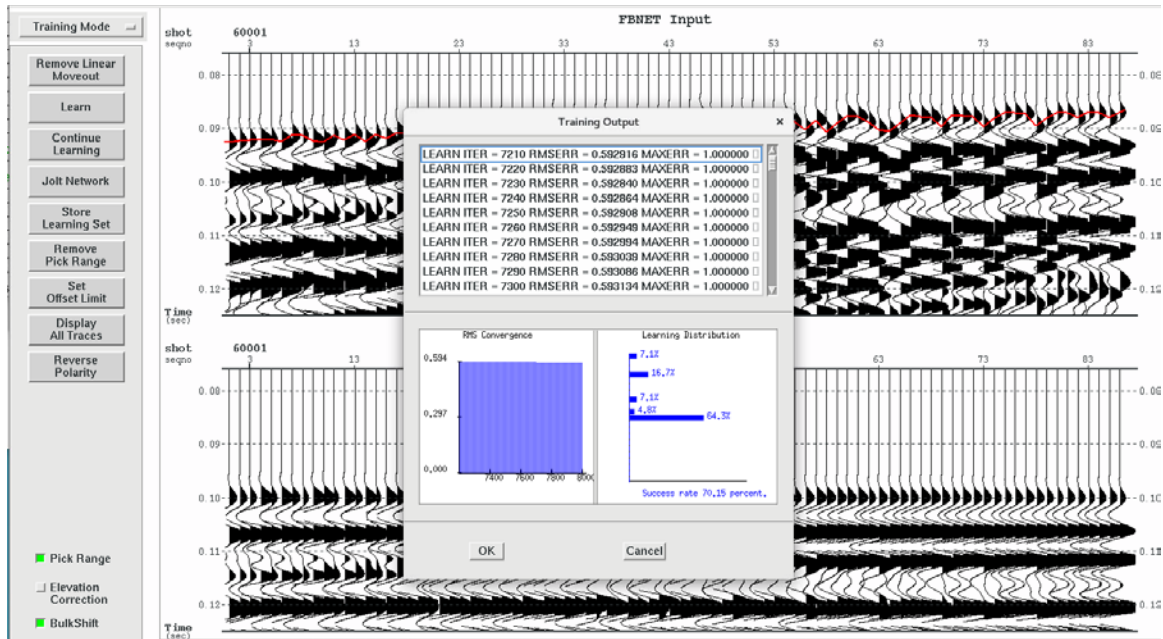


Figure 2.1.9 – Screen capture of a neural network learning set being saved after successfully picking and flattening the first arrival in the GOM2012 dataset. Statistics in the center window show the various iterations level of success. The lower panel shows flattened first arrival with the proposed solution. After learning occurs on a training set, the software picks the entire dataset.

Unique to the HR3D datasets is sampling of refraction energy due to the relatively long, for HR3D, (50m+) acquisition style. Using any first arrival method, we use a simple flattening and shifting the traces by the velocity of the water bottom back to a more reasonable position (offset) This method also has some drawbacks, but it does handle large shot variations. Figure 2.1.10 shows some flattened and shifted shots using the method. The uncertainty in the refract intercept time was solved.

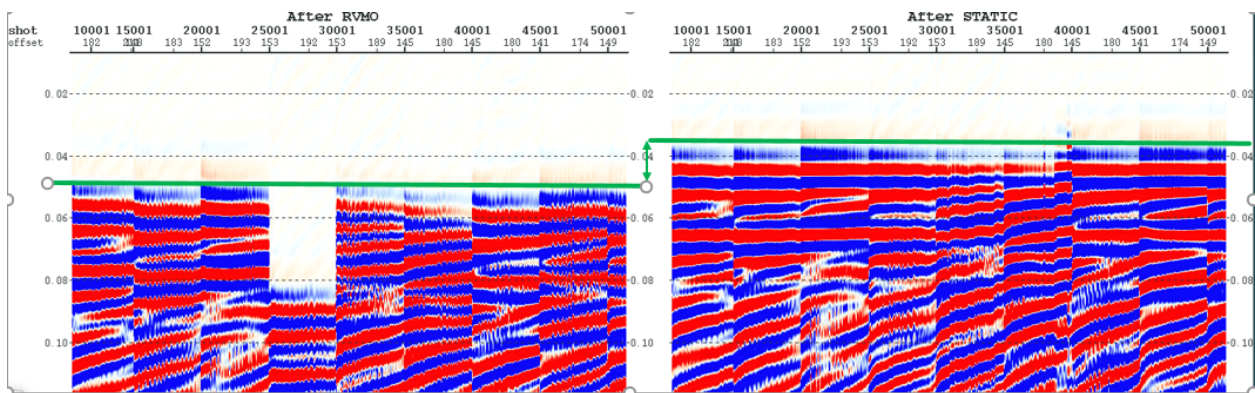


Figure 2.1.10 – Refractor flattening method handles large shot timing issues. Left panel shows 8 shots in the GOM2012 dataset flattened using a constant velocity for the water bottom. The right side shows large and small shifts in the shots to be flattened to T = 0 ms (milliseconds). The bulk shift of the shots is an issue similar to re-datuming and can be handled with a shift based on the left panel’s flattened intercept time with averaging to remove the large shifts.

## Shot Timing Issues

Shot timing issues are large (40ms +) and affect entire shots. The errors result in a “rectangular band” occurring on time slices of the data volume (Figure 2.1.11). Work to automate solutions to these issues continued.

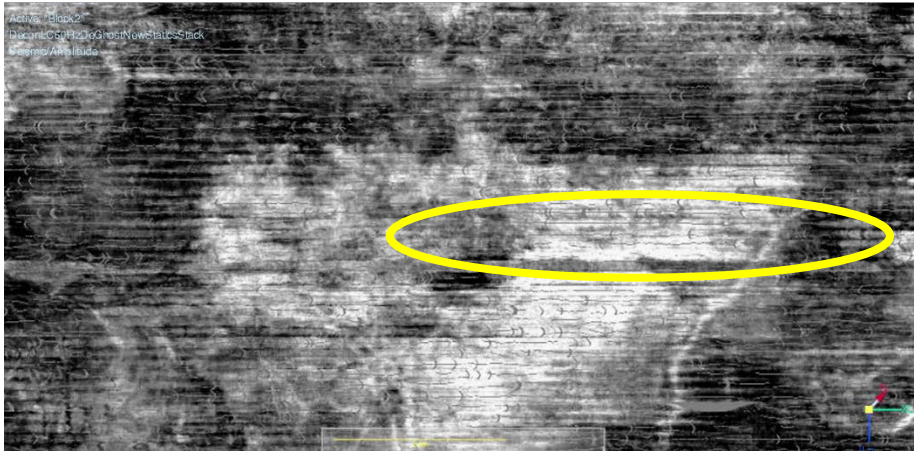


Figure 2.1.11– Example of a banded shift (within yellow oval) seen on time slice (in the GOM2012 dataset) due to shot timing issues. This is possibly occurring along a sail line (series of shots in row) and may be in the original GPS data or simply a constant time delay.

### **Overall Quality**

The quality of the data improved greatly with static shifts accounting for positional problems. The issue with implementing such a correction was getting a robust picking method. We are beginning to see geological features much earlier in time slice views, and in 2D sections fault resolution is enhanced.

### **Depth of Resolution**

Both the machine learning and refractor shift methods enhance coherency enough to increase the resolution with depth. Note: in Figure 2.1.12 there is a time shift in the sections due to the refractor flattening. The left side shows increased reflection coherency; the right side is without the statics shifts (positional uncertainty).

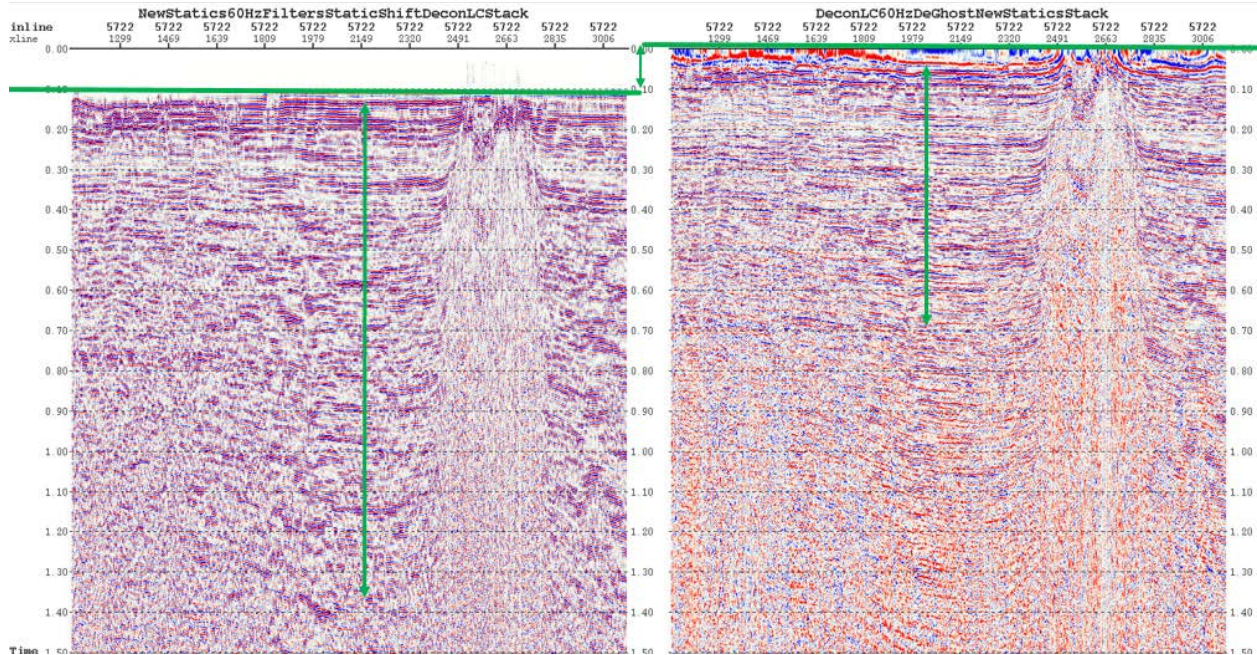


Figure 2.1.12 – Panels of the GOM2012 dataset showing the effect of adding statics correction; left panel shows new statics; right is without statics correction. Since the reflections line up better after the statics correction, they stack together more strongly and appear to have greater coherency with increasing time.

Positional uncertainty corrections also enhance fault resolution. In Figure 2.1.13 the fault enhancement is seen following the green arrows. In the previous work (bulk shift as before) on the right, the fault edges are not as well defined.

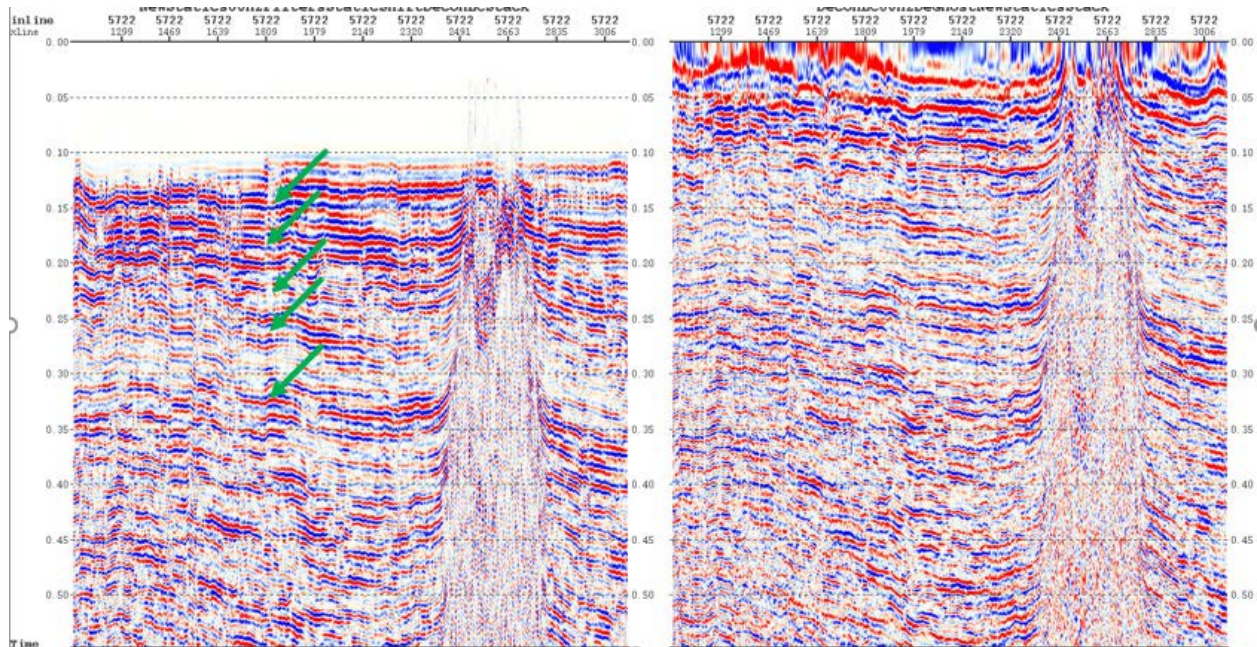


Figure 2.1.13 – Panel showing effects of positional uncertainty corrections. Resolution around faults is greater on the left than on the right. Green arrows outline the fault edge which is not as defined in uncorrected data.

Challenges included fixing the shot timing issues and fixing “footprint” like static shifts, which appear throughout the data. In Figure 2.1.14, “C” shaped artifacts (catenaries) are visible. They are possibly due to shot layout.

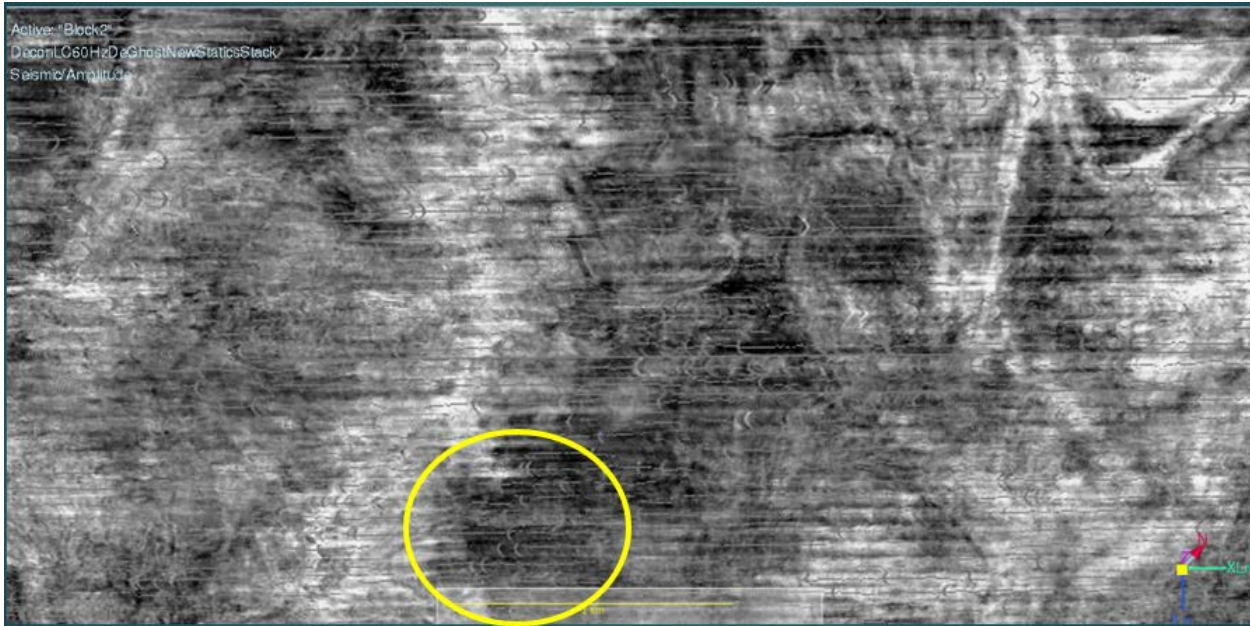


Figure 2.1.14 – Time slice showing “C” shaped artifacts (aka catenaries), which are due to the shot layout and must be removed by improved processing. These “footprints” may be a shot static issue or a slight phase shift.

As corrections to the positional errors were pursued, previously unknown errors were recognized; the errors seem to cause data loss and data quality problems. The errors are post GPS processing, and small errors due to the hydrophone positions were further examined. In addition, several new issues were discovered.

### **New Problems Discovered**

#### *Missing data*

Initially, the footprint of the survey and the banded phase shifts were considered to be positional problems. It was discovered, however, that 5-8% of the shots were being dropped from the processing due to a geometry problem. These shots were never binned correctly, which resulted in them being omitted during the data stacking processing step (Figure 2.1.15). This may have contributed to the foot print problems as well as data gaps. The problem came from a property called “Shot-Receiver Relationship” which was missing for the affected shots. Rebuilding the database brought this information to light as the missing shots were never assigned a cdp (common depth point) location.

#### *Data Values*

Shots were found containing all zeros and -inf (negative infinity?) values (Figure 2.1.16). When these data were combined with regular data the amplitude variations were distorted. The resulting fold map (Figure 2.1.17) gained from the missing shots and a small gap was created where the bad data shots were removed. It is suspected that some process may have caused this problem, perhaps during a crash of a program. Reviewing the SEG-D raw data again might be the only way to be sure this was wasn't an acquisition problem.

### Noise patterns

A pattern of noise, which occurred every 11<sup>th</sup> shot as a series for spikes was discovered in the GOM2013 dataset (Figure 2.1.18). This may have been an acquisition system problem, possibly cable related.

After these database/noise/geometry issues were examined, corrected and removed, work resumed to finish positional uncertainty particularly using 3D information.

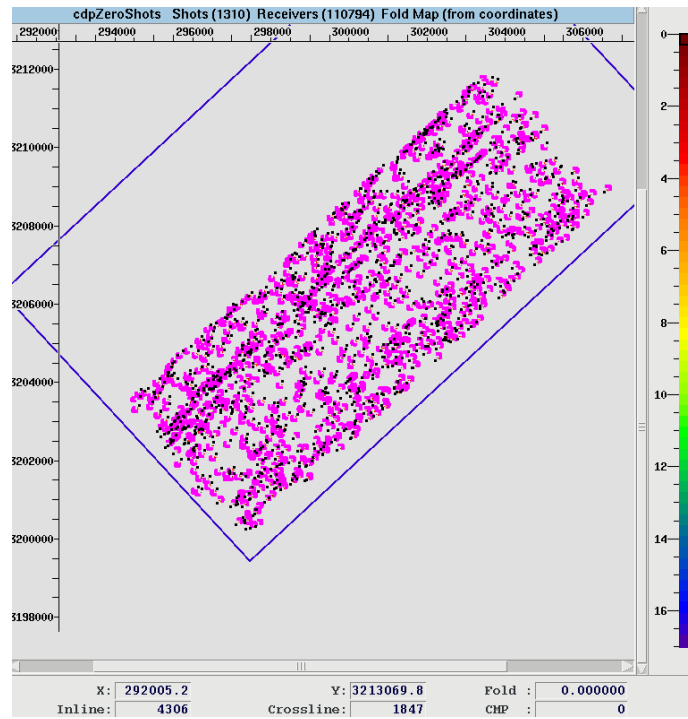


Figure 2.1.15 – Geometry diagram of GOM2012 showing missing data; shots are the black dots and the receivers are pink.

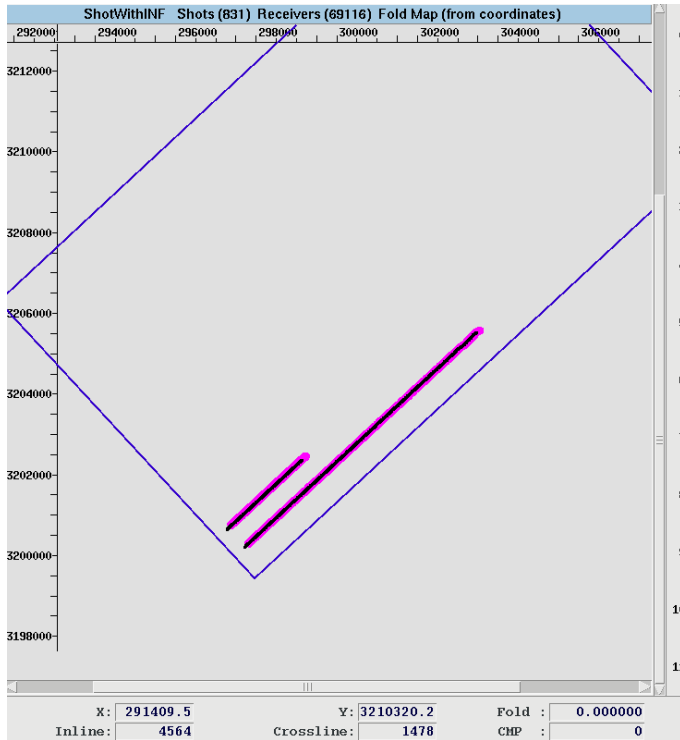


Figure 2.1.16 – Geometry diagram showing the shots with bad data values, shots are the black dots and the receivers are pink.

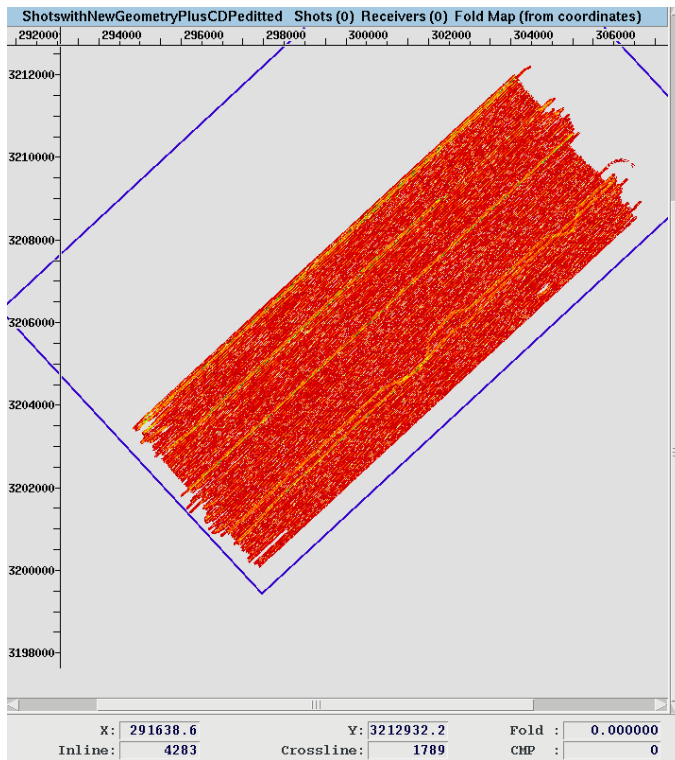


Figure 2.1.17 – Geometry fold diagram (a.k.a. fold map) of GOM2012 showing the missing data in the lower left-hand corner of the survey as a blank straight line.

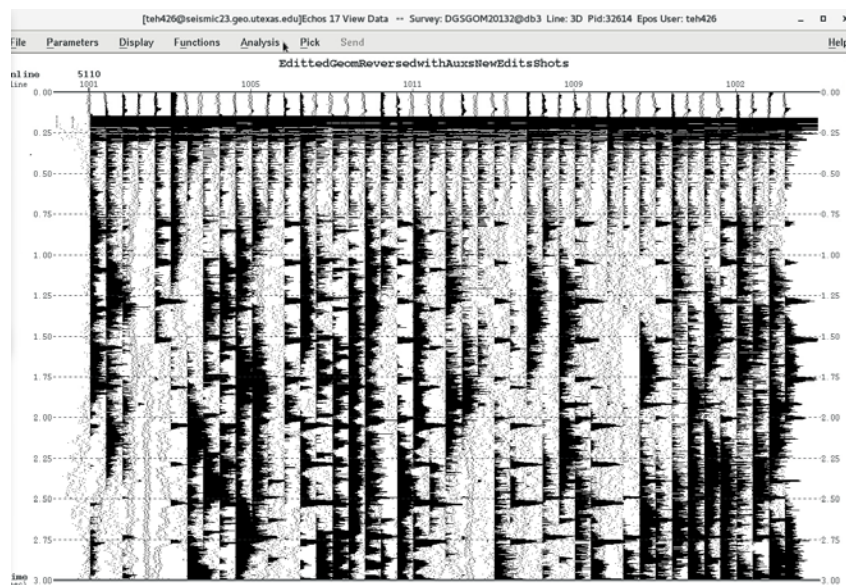


Figure 2.1.18 – Noise in shots shown by displaying channel 1 with each trace being a shot

### ***Problems Resolved***

Errors in geometry which caused missing values were fixed by changing some header values that were incorrect and re-applying the geometry. The “Shot-Receiver Relationship” was corrected using this method. Shots containing all zeros and -inf (negative infinity) values, were edited or replaced with the correct data. Some processes may have caused the data values to be distorted.

Reviewed the SEG-D raw data for all three surveys; also checked for missing values.

### ***Noise patterns***

A pattern of noise, which occurred every 11<sup>th</sup> shot as a series for spikes was discovered in the GOM2013 dataset.

### ***New Techniques***

There are four major innovations which produced improved results for GOM2012; some of the same techniques may be helpful for GOM2013 and GOM2104, but the latter two surveys did not have the heavy 60Hz noise (and harmonics) as GOM2012. These innovations applied to GOM2012 in steps:

1. Wiener type 60, 120 and 180Hz notch filters
2. Phase shifting filters for noise reduction
3. Positional corrections based on linear refractor and offset corrections
4. Stationary noise and minimum phase equivalent transfer function from precursor noise

Applying Wiener notch filters (Step 1) was a new idea developed for this dataset. Ordinary notch filters function like a band pass filter except that they filter a very small range of frequencies (e.g., 60 HZ) such as was in the power systems during survey acquisition. Improperly grounded generators on an iron boat will generate a great deal of 60 Hz noise in the data. Figure 2.1.19 (before) and Figure 2.1.20 (after) and Figure 2.1.21 (before) and Figure 2.1.22 (after) demonstrate some of the improvements in data quality.

Wiener notch filters not only remove specific noise frequencies but also improve the “shape” of the signal.

Mathematically the results should be similar for both Weiner notch and regular notch filters, but they are not; this can be seen in time slices of the data (Figure 2.1.23 & Figure 2.1.24).

A unique noise suppression filter was also applied (Step 2, phase shifting). This new technique involves applying the Peacock filter<sup>1</sup> a numerical implementation of the integral followed by a numerical derivative, which, theoretically, restores the data to their original state. However, immediate benefits included phase changes, spectrum enhancement and random noise reductions. This is under study in a separate project but was useful in improving the GOM2012 data.

Trace positional uncertainties (Step 3) were further reduced using alignment of offsets with known water velocity and the survey's bottom refractor. Steps 1 and 2 were applied first to enhance the first arrivals' amplitudes for automatic picking. This is a new application of static corrections making several simple assumptions about the offset error.

After the automatic picking was successfully applied to correct the positional uncertainty, the stationary noise removal and minimum phasing (step 4) was completed. Typically, this method uses the signal recorded as input data to the algorithm for creating a minimum phase equivalent<sup>2</sup>. We use the precursor noise recorded prior to the air gun firing. The Weiner filtering transforms the noise (60Hz etc.) to a spike near  $T = 0$ , which is not used in this technique.

Methods 1, 2 and 4 produce a better shaped spectrum, which is preferable for visually improving the data because without strong lows (near 0 Hz) the stacking, statics and velocities are much more accurate. Without the high frequency noise everything looks clearer; compare Figure 2.1.21 and Figure 2.1.22.

3D balancing and statics were applied to GOM2012; although, further work could yield more improvement. 3D FXY deconvolution greatly improved the quality of the data. Figure 2.1.24 is an example of the improved time slice; compare with Figure 2.1.23 which also lacks the four methods described here.

### GOM2012 Images

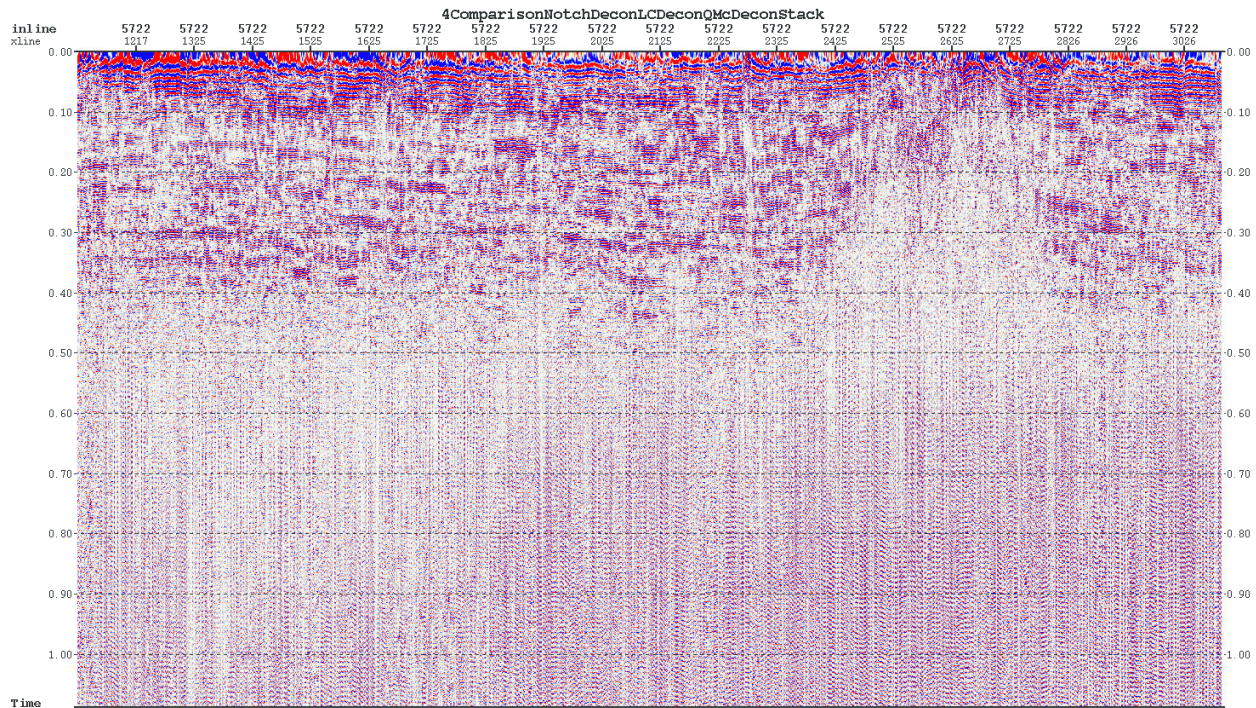


Figure 2.1.19 - GOM2012 Inline 5722 before positional corrections or phase shifting filters (i.e., using only notch filters and shot signature derived from the whole shot). Other processing is the same as for the data



in Figure 2.1.20.

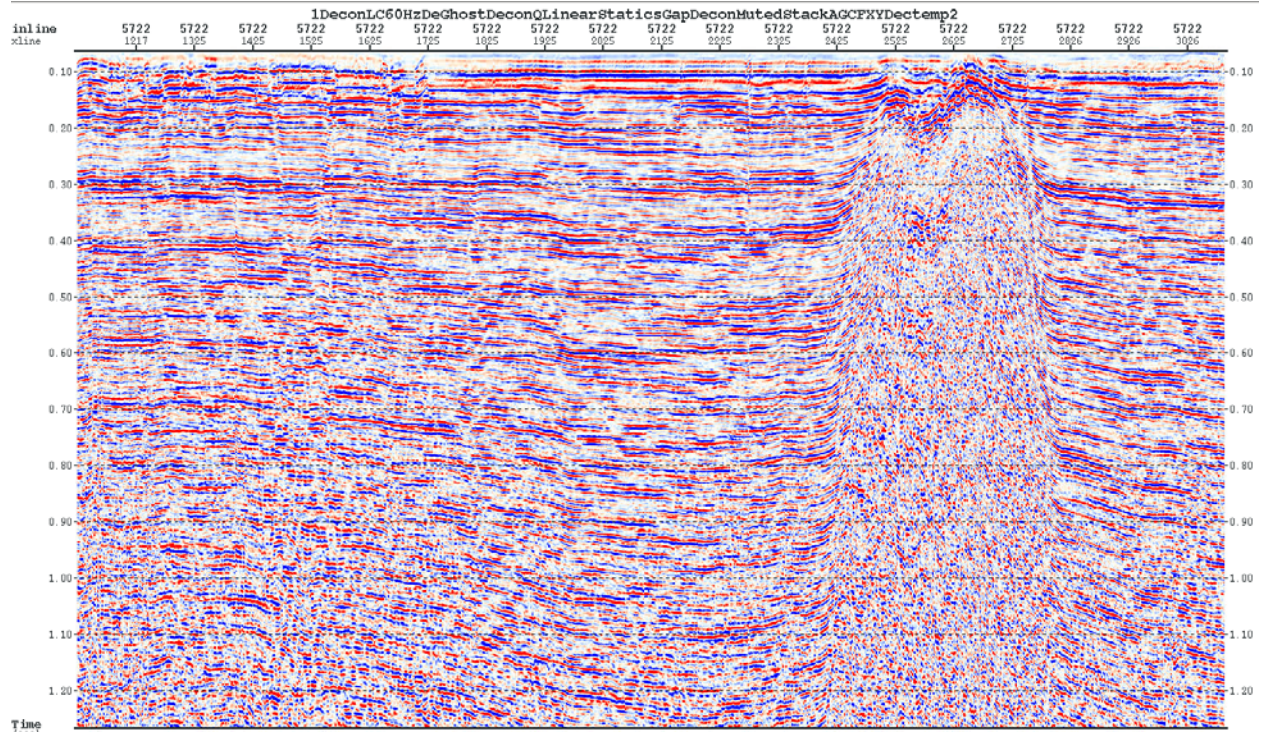


Figure 2.1.20 - Gom2012 Inline 5722 showing increased resolution with depth, sharpened faults and salt sediment boundaries. Depth of interpretable reflections is about 1.25 seconds

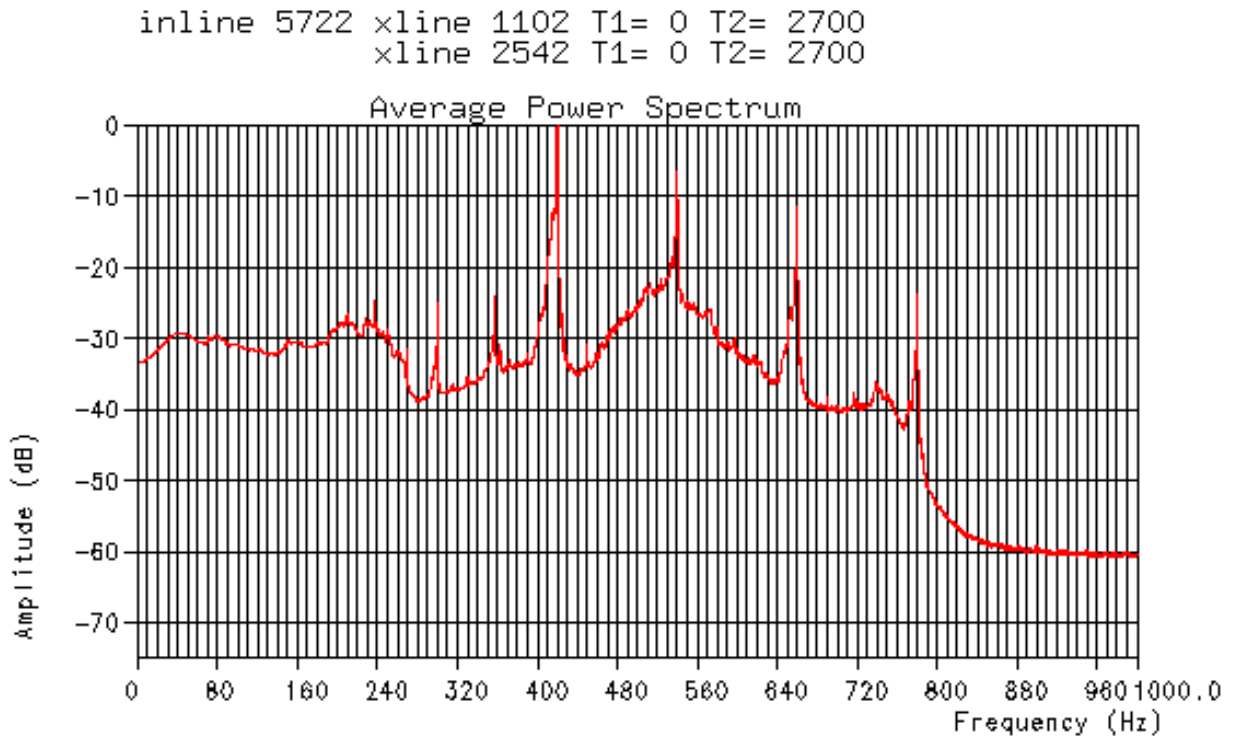


Figure 2.1.21 - Spectrum of data in figure 2.1.19. High frequency noise and signal to noise ratio of 1 or less.

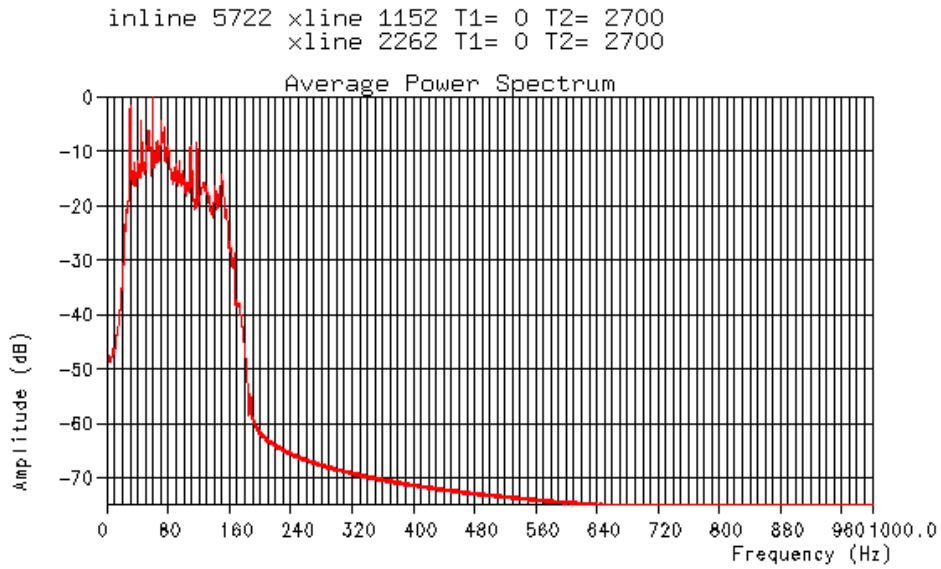


Figure 2.1.22 Spectrum of data in Figure 2.1.20. Nearly 40Db cut on the low side and 50Db on all high frequencies contribute visually to better resolution.

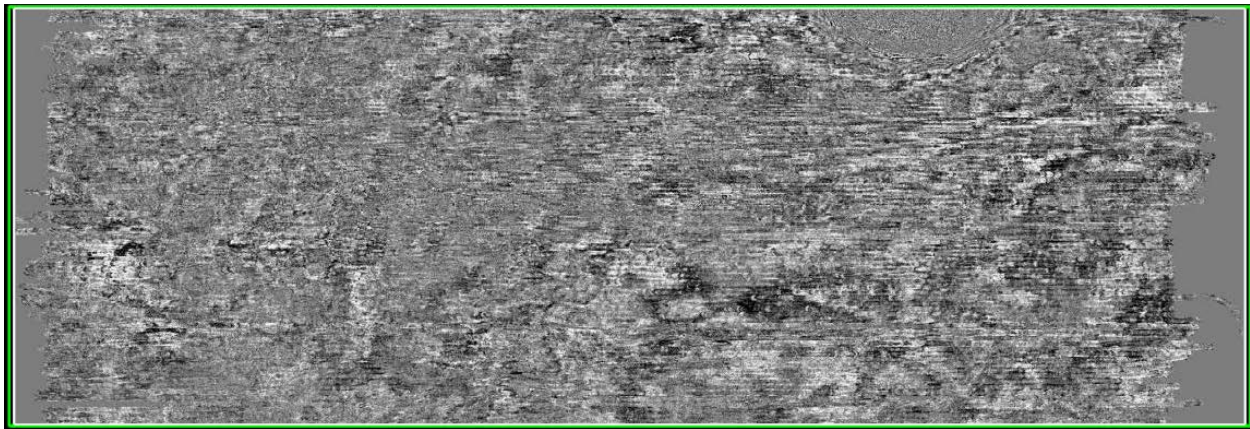


Figure 2.1.23 Gom2012 Time slice at 145ms. Note the complete lack of resolution versus the results of new techniques (Figure 2.1.24).

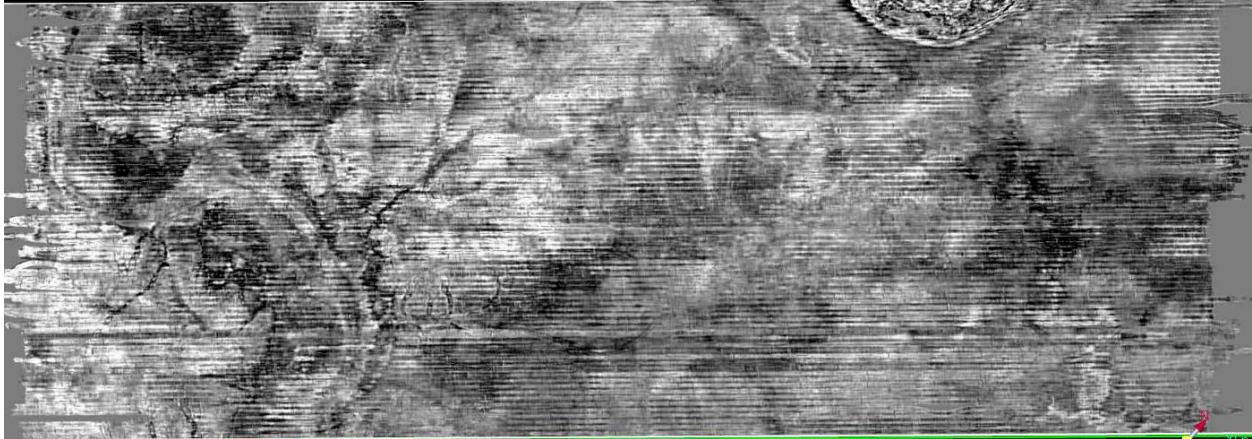


Figure 2.1.24 – GOM2012 survey timeslice at 145 ms. Enhanced resolution of geologic features and amplitude balancing versus Figure 2.1.23. Banding along inlines is still evident but improved, it may be mitigated after migration.

## References

- 1 Kenneth L. Peacock, (1979), "An optimum filter design for discrete integration," *GEOPHYSICS* 44: 722-729. <https://doi.org/10.1190/1.1440972>
- 2 The Wilson-Burg method of spectral factorization with application to helical Filtering Geophysical Prospecting, 51, 409-420 (2003) Sergey Fomel, Paul Savay, James Rickettz, and Jon F. Claerbout  
[https://www.google.com/url?sa=t&rct=j&q=&esrc=s&source=web&cd=1&ved=2ahUKEwiw0dfKnrfjAhVDVc0KHXznBDMQFjAAegQIAhAC&url=https%3A%2F%2Fpdfs.semanticscholar.org%2F9566%2Fe933da4ffe2fd19ca2e2c47a83c7ac25c1b0.pdf&usg=AOvVaw1doDWks\\_bofL1TfyNqlziA](https://www.google.com/url?sa=t&rct=j&q=&esrc=s&source=web&cd=1&ved=2ahUKEwiw0dfKnrfjAhVDVc0KHXznBDMQFjAAegQIAhAC&url=https%3A%2F%2Fpdfs.semanticscholar.org%2F9566%2Fe933da4ffe2fd19ca2e2c47a83c7ac25c1b0.pdf&usg=AOvVaw1doDWks_bofL1TfyNqlziA)

## 2.2 Subtask 2.2 – Develop Comprehensive Data Set for Reservoir Properties

Extensive reservoir data from (Seni et al., 1997) for fields in and near the project’s study area were compiled, evaluated and upgraded (i.e., corrupt or inaccurate records identified and corrected or removed) in order to determine whether or not there are apparent geologic and/or geographic trends for reservoir parameters. Much of the data in Seni et al. (1997) came from records of the Federal Bureau of Ocean Energy Management (BOEM) and are categorized using various terms. As those terms can be confusing, they are defined in Table 2.2.1. Initial statistical analyses of two Federal lease areas (Figure 2.2.1) in the westernmost extent of the project’s study area are presented in Figure 2.2.2- Figure 2.2.5. Figure 2.2.2 indicates low porosity variability of Miocene age pools across the two Federal lease blocks (Galveston and High Island). Further analysis of porosity suggests that there is low correlation between reservoir porosity and pool depth ( $R^2 = 0.13$ ; Figure 2.2.3) or reservoir porosity and temperature ( $R^2 = 0.15$ ; Figure 2.2.4);  $n = 191$ ; porosity standard deviation = 0.02529. Not surprisingly, there is good correlation ( $R^2 = 0.77$ ) between reservoir temperature and reservoir depth (Figure 2.2.5). In summary (Table 2.2.2), Miocene age reservoirs in High Island and Galveston federal lease blocks exhibit good porosity with relatively low variability throughout the area. The current hypothesis is that, at least with respect to reservoir porosity, the High Island and Galveston lease areas are analogs for the entire study area.

Table 2.2.1 – Definitions of some terms (Seni et al., 1997).

Term	Definition
------	------------

field	An accumulation, pool, or group of pools of hydrocarbons in the subsurface. A hydrocarbon field consists of a reservoir in a shape that will trap hydrocarbons and is covered by an impermeable, sealing rock.
reservoir	A subsurface body of rocks having sufficient porosity and permeability to store and transmit fluids. It is characterized by interpreting depositional style, structural style, lithology, trapping mechanism, and other features
pool	A subsurface oil accumulation. An oil field can consist of one or more oil pools or distinct reservoirs within a single trap.
play	Group of reservoirs genetically related by depositional origin, structural style or trap type, and nature of source rocks or seals. An area in which hydrocarbon accumulation or prospects of a given type occur.

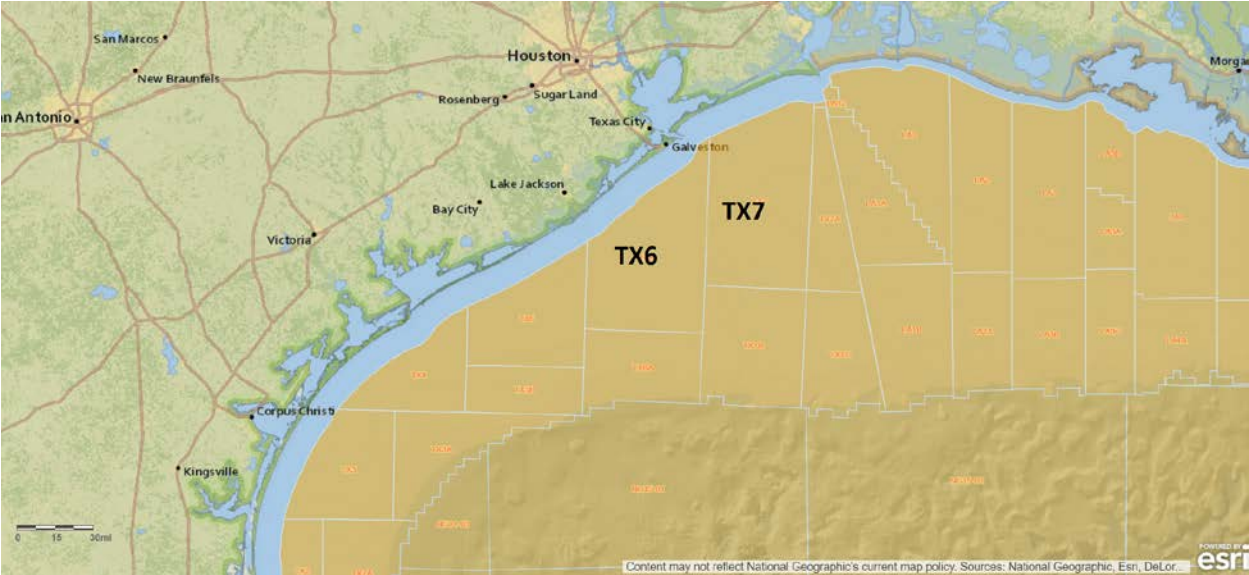


Figure 2.2.1 – Map of Galveston (TX6) and High Island (TX7) federal lease areas.

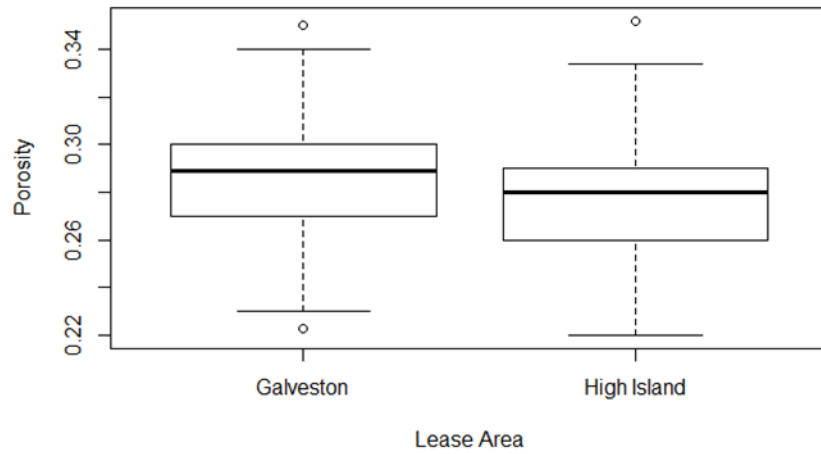


Figure 2.2.2 – Comparison of reservoir porosity in Miocene pools in the Galveston and High Island lease areas. N=191; porosity standard deviation = 0.02529.

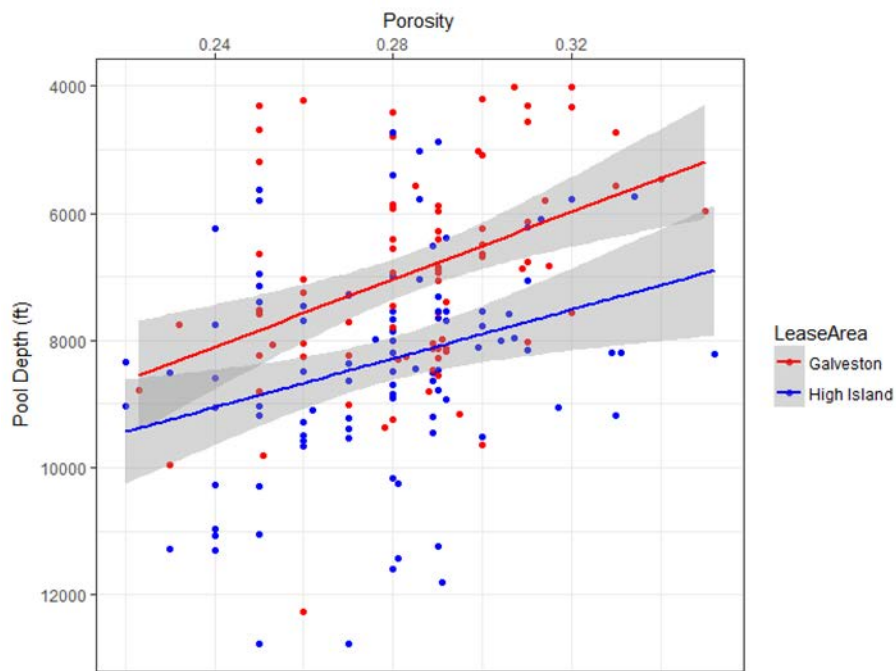


Figure 2.2.3 – Cross-plot of reservoir porosity vs. pool depth in the Galveston and High Island lease areas with p-value 2.5e-07.  $R^2 = 0.13$ ; n=191; porosity standard deviation = 0.02529.

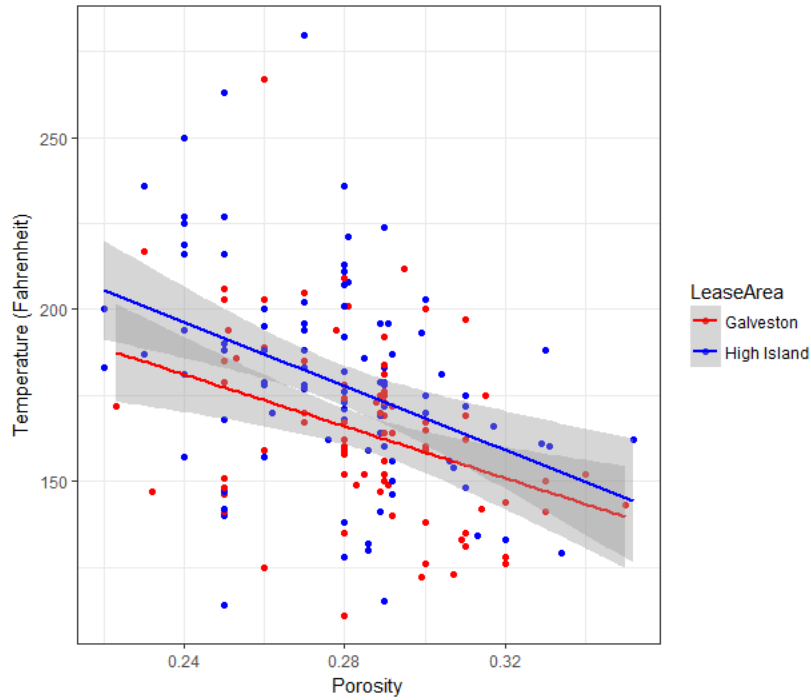


Figure 2.2.4 – Cross-plot of reservoir porosity vs. temperature in the Galveston and High Island lease areas with p-value  $3.2 \times 10^{-8}$ .  $R^2 = 0.15$ ;  $n=191$ ; porosity standard deviation = 0.02529.

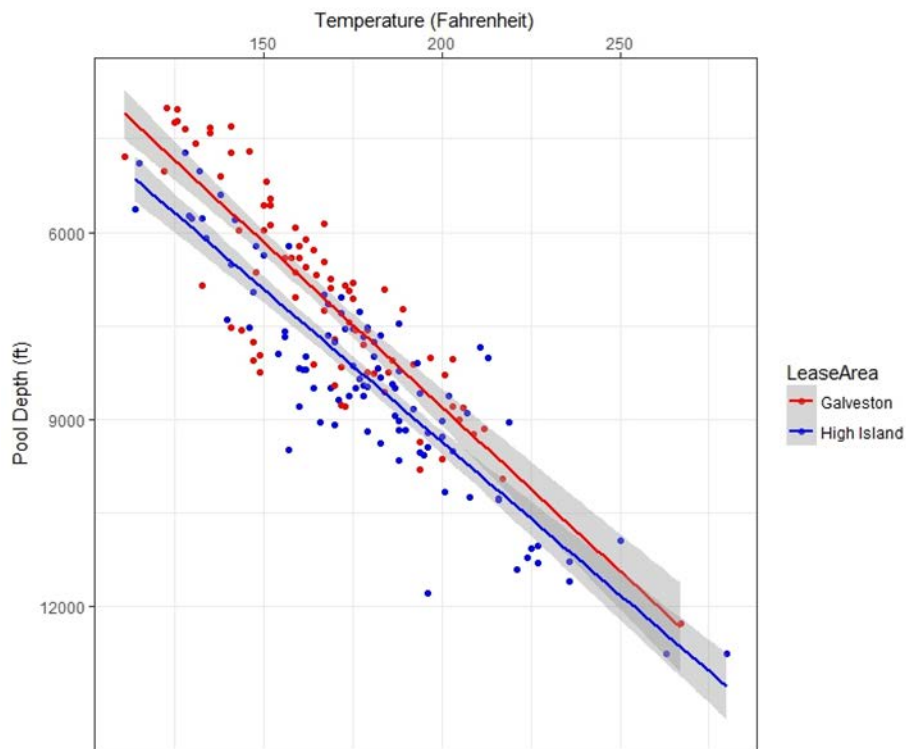


Figure 2.2.5 – Cross-plot of reservoir temperature vs. depth in the Galveston and High Island lease areas with p-value  $2.2 \times 10^{-16}$ .  $R^2 = 0.77$

Table 2.2.2 – Mean, minimum and maximum porosity, pool depth and temperature values, respectively, for Galveston and High Island lease areas and for the two areas combined. N=191; porosity standard deviation = 0.02529.

Mean Values	Galveston	High Island	Both	Minimum	Maximum
Porosity	0.29	0.28	0.28	0.22	0.35
Pool Depth (ft.)	6900	8348	7635	4005	12775
Temperature (°F)	164	178	172	68	280

### **2.3 Subtask 2.3 – Develop Structural Closure Mapping for Reservoirs TexLa Merge 3D Horizon Interpretations**

The process of identifying and interpreting key horizons in the seismic data began by interpreting shallow horizons (Figure 2.3.1) in the TexLa Merge 3D seismic volume, then systematically mapping deeper horizons. The two deepest horizons, MFS10 and MFS12 (Figure 2.3.1, Figure 2.3.2 and Figure 2.3.3) were mapped throughout the TexLa Merge 3D seismic volume. A total of seven horizons (Figure 2.3.1) and associated fault plane polygons (MFS04, MFS05, SB-M08, MFS09, SB-M09, MFS10, and MFS12) were interpreted throughout the TexLa Merge 3D seismic volume. We used interpreted horizons from the TexLa Merge 3D seismic volume as the starting point, then utilized 2D lines to extend interpretations into more distal areas lacking 3D data coverage (Figure 2.3.4).

The 2D lines also served as means to integrate newly obtained, publicly available 3D seismic volumes, Glenda 3D, West Cameron 3D, and Vermillion 3D, respectively, into the overall regional structural analysis (Figure 2.3.4). Time horizon MFS05 was extended into the majority of 2D/3D seismic coverage. In addition, as we extended seismic interpretations into more distal zones, these interpretations became less constrained, since each horizon was progressively deeper and consequently had poorer seismic resolution, making tracking the chronostratigraphic horizons more challenging. As expected, fault plane interpretations were more robust in the 3D seismic volumes relative to the sparsely spaced 2D seismic lines.

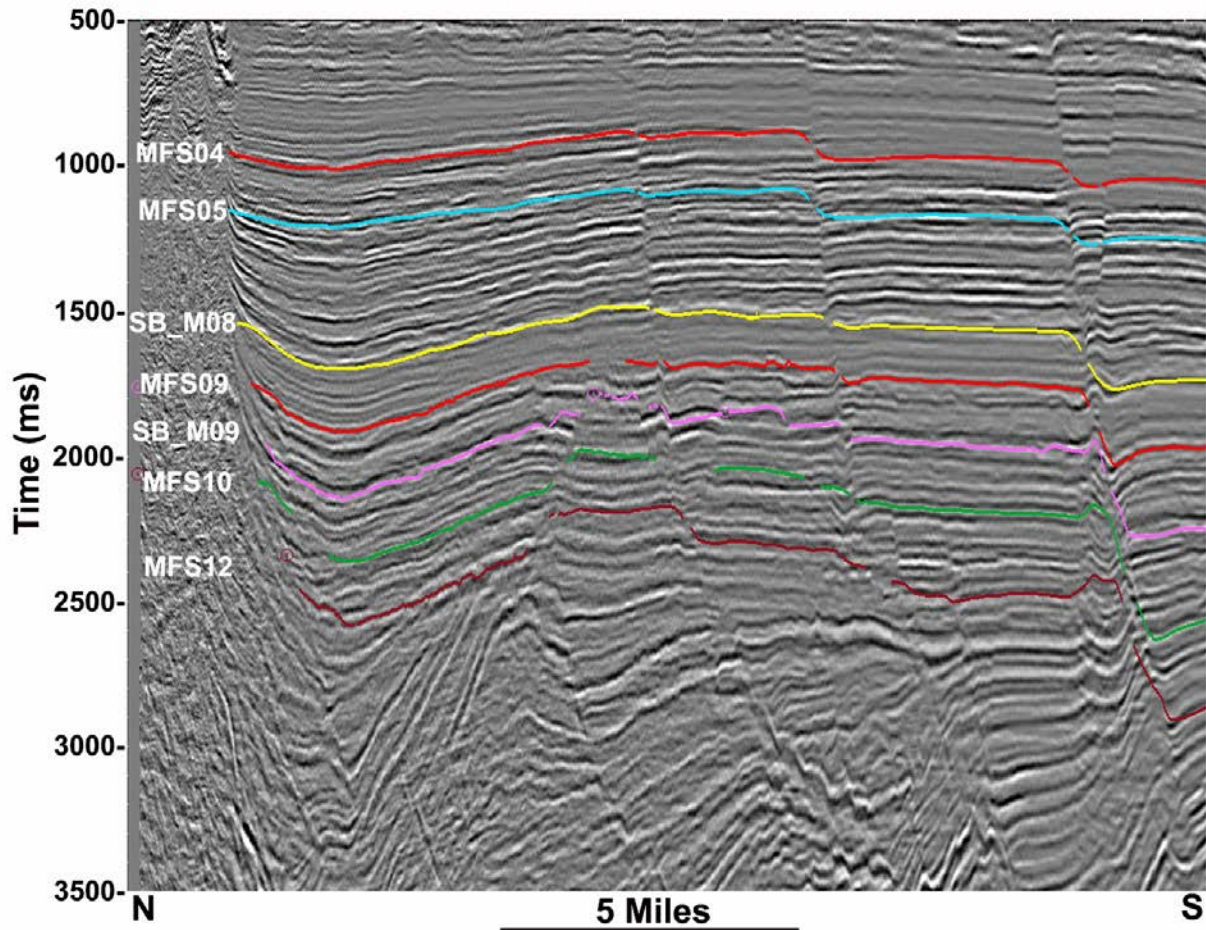


Figure 2.3.1 – Vertical transect of the TexLa Merge 3D seismic cross-section showing interpreted horizons MFS04 – MFS12.



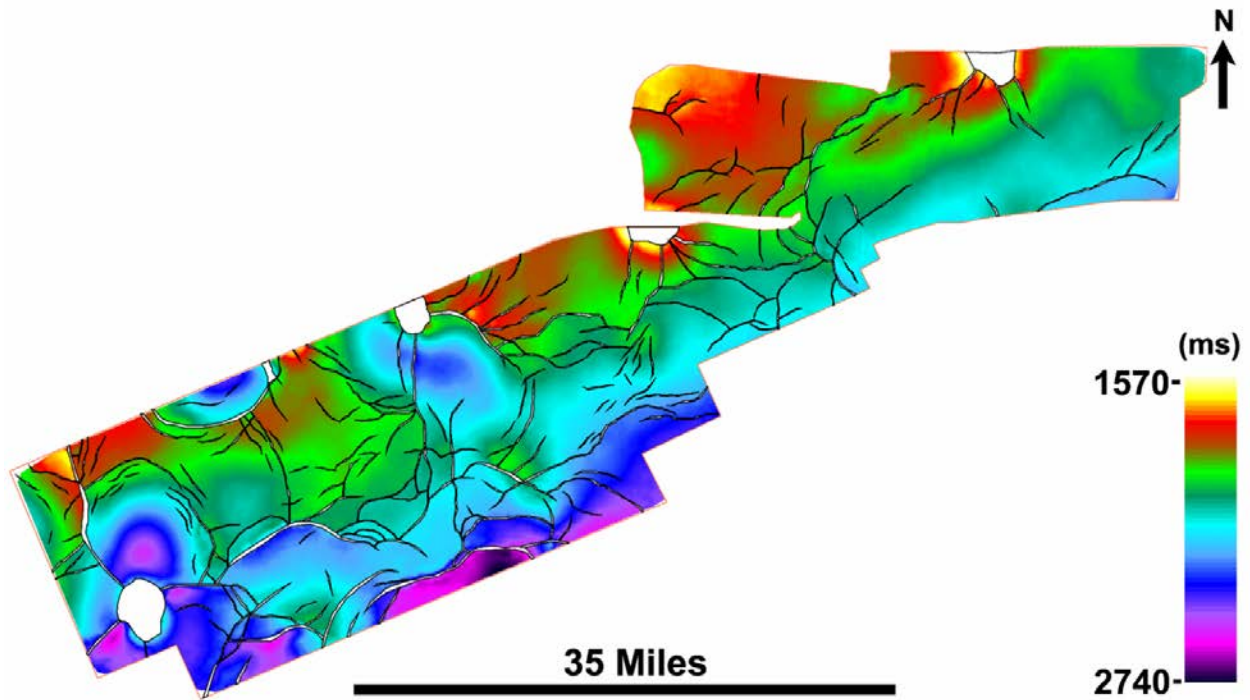


Figure 2.3.2 – Two-way time interpolated structure of the TexLa Merge 3D Maximum Flooding Surface MFS10 horizon. A total of 214 fault planes (black polygons) penetrate the surface.

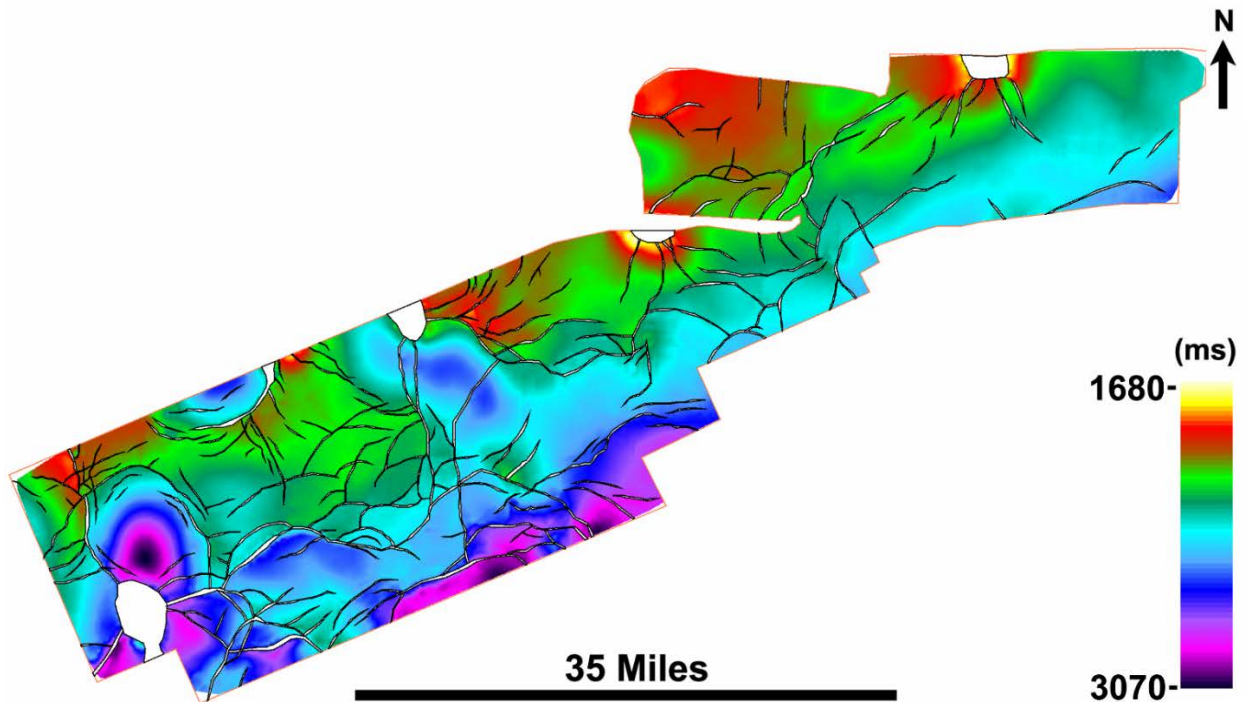


Figure 2.3.3 – Two-way time interpolated structure of the TexLa Merge 3D Maximum Flooding Surface MFS12 horizon. A total of 204 fault planes (black polygons) penetrate the surface.

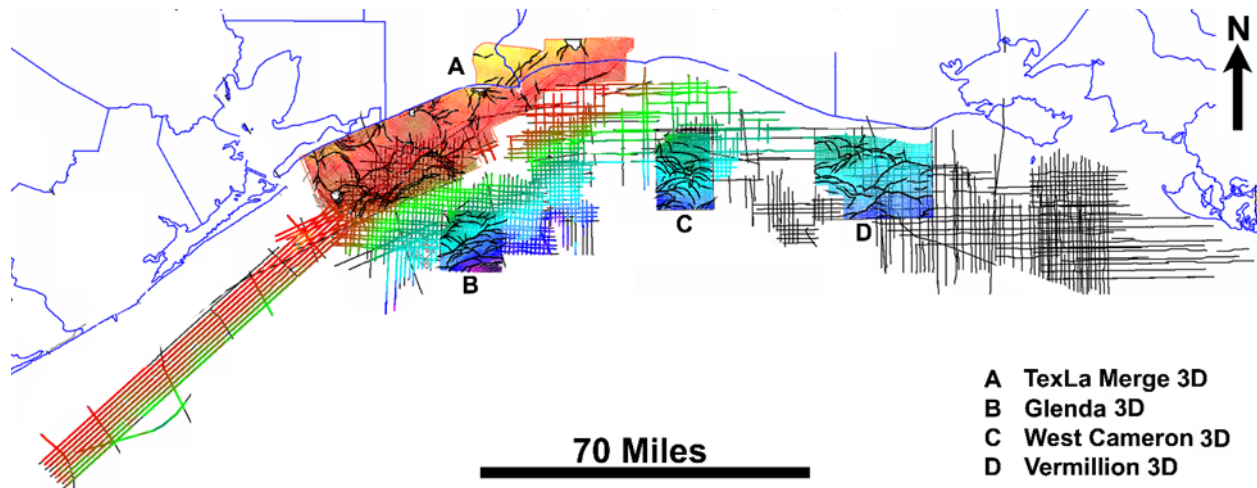


Figure 2.3.4 – Extent of the regional 2D/3D seismic interpretation of MFS05. A total of 282 faults planes (black polygons) penetrate the surface.

In-filling fault plane interpretations (polygons) in the 2D seismic coverage zones focused on key Maximum Flooding Surfaces and Sequence Boundaries. Subsequent interpretations of surfaces MFS04, MFS05, SB-M08, MFS09, SB-M09, MFS10, and MFS12 created a robust regional structural framework. In addition, a series of seismic attribute maps generated from the 3D seismic volumes were incorporated to identify reservoirs that may contain sufficient porosity to accommodate large volumes of CO<sub>2</sub>. By combining these elements, we were able to rank areas/reservoirs that would be ideal for future CO<sub>2</sub> sequestration projects of scale.

### Time-to-depth Conversion

Key horizons within the TexLa Merge 3D seismic survey (MFS04, MFS05, MFS07, SB\_M08, MFS09, SB\_M09, MFS10, and MFS12) were converted to measured depth (ft).

Three methods were tested for this conversion:

1. The first method was to apply (multiply) a conversion factor for each horizon that takes two-way time and converts it for each horizon. For example, the two-way time conversion factors (ft/ms) are MF05:3.19, SB-M08:3.53, and SB-M09:3.71, respectively. These factors were determined from sonic logs of Well #427084001600. This method relied on only one control point, and subsequently was abandoned.
2. A second method (TDQ) (Figure 2.3.5a) was to build an interval velocity model from wells where synthetic seismograms had been generated and matched to adjacent seismic traces that were subsequently depth registered with high confidence. The two-way time horizons were then pushed through the forward model resulting in converted depth horizons. The resulting values are in measured depth (ft) from the kelly bushing (KB) level. This method is the most robust and could be extended into the areas with only 2D seismic surveys.
3. A third method (Figure 2.3.5b) used a time-based average (RMS – root mean square) velocity cube provided by the data processing contractor. Each horizon was then domain-converted to depth within the TexLa3D seismic survey. All seismic bins contained velocity values ranging from between 4430 - 14500 ft/s. Regions of relatively higher and lower velocities can correspond to geologic features such as shallow salt diapirs (sub-vertical salt bodies) or high porosity zones, respectively, and other variations in density and elastic properties of the geologic section (e.g., fluid content, confining pressure vs. pore pressure, etc.). The values are in measured depth (ft) from

mean sea level (MSL). This conversion method can only be used within the 3D seismic coverage area. We then compared the two (TDQ vs RMS) methods and then quantified the difference in the results, keeping in mind the difference between kelly bushing and mean sea level, typically around 50 ft for offshore platforms.

The difference was calculated by subtracting the RMS depth converted horizons from the TDQ depth converted horizons (Figure 2.3.5 c). In the areas where there was little or no difference the result was low values (white to lighter colors). Areas where there is larger variations in the calculated depths are highlighted by much brighter colors. High reds indicate areas where the RMS depth converted horizon is deeper in measured depth relative to the corresponding TDQ depth converted horizons. Conversely, high blues indicated that the RMS depth converted horizon is shallower than the TDQ depth converted horizons.

When comparing the TDQ vs RMS depth structure maps (Figure 2.3.6 through Figure 2.3.12, there are few significant visual variations. However, there is a North to South linear inline anomaly evident in the RMS horizons. It is located in the middle of the TexLa3d emanating from a salt dome on the norther border (Figure 2.3.5). Any linear features that correspond with the inline/crossline direction are most likely artifacts introduced in acquisition and/or data processing that were not addressed properly. Regardless, when comparing the TDQ and RMS methods, areas near the salt dome flanks, hanging wall of large listric faults, and within the deepest portion of the mini basins, there are depth variations of as much as 900 ft. Most of the other areas are consistent, with variations of less than zero to 10 percent. Ultimately, the TDQ method was favored over the RMS method due to the linear (artificial) anomalies evident in the latter, and TDQ's ability to depth register horizons mapped from the 2D seismic data.

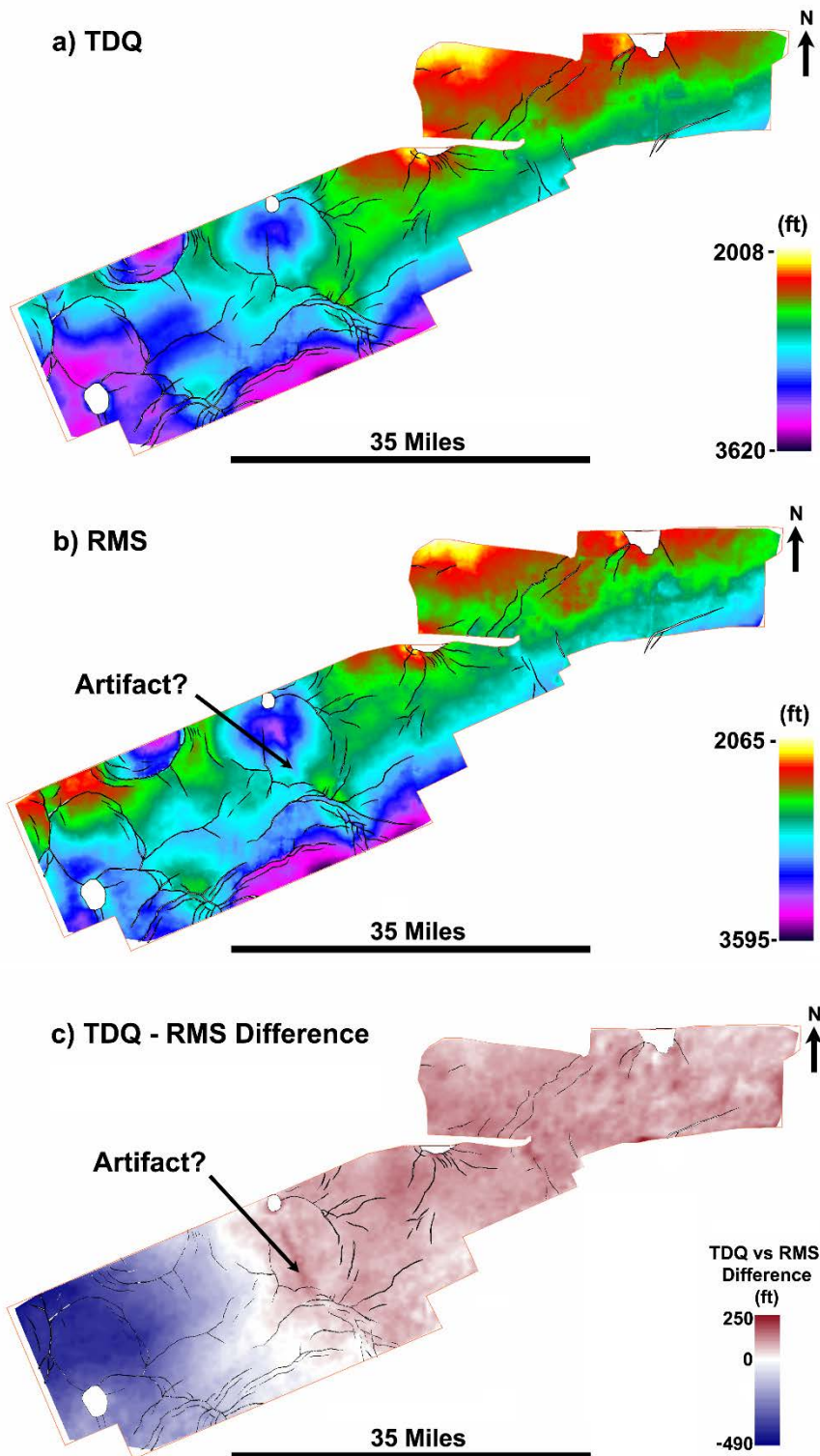


Figure 2.3.5 - MFS04 depth montage depicting a) TDQ method results, b) RMS method results, and c) the difference (TDQ minus RMS) between the two methods.

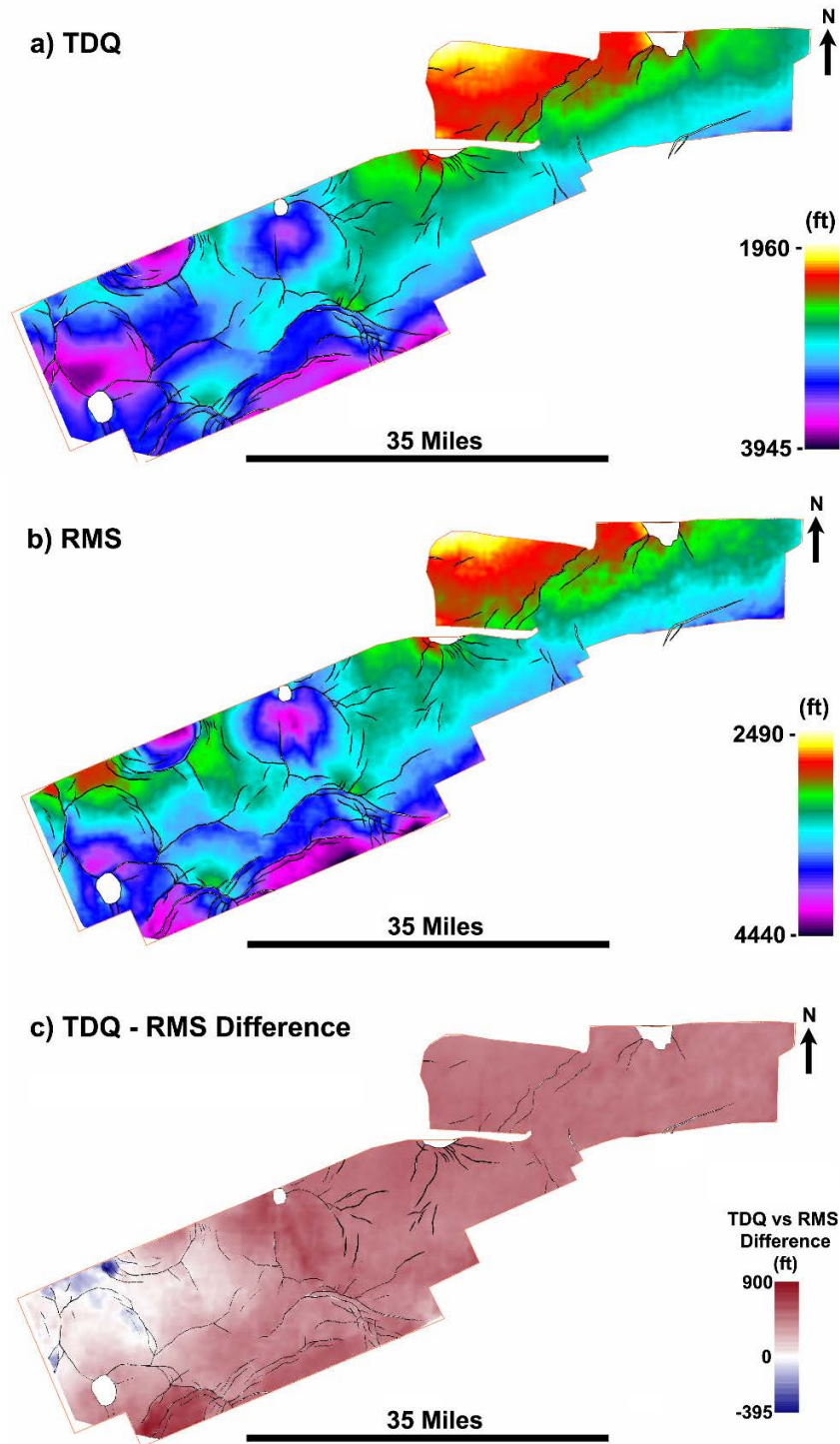


Figure 2.3.6 - MFS05 depth montage depicting a) TDQ method results, b) RMS method results, and c) the difference (TDQ minus RMS) between the two methods.

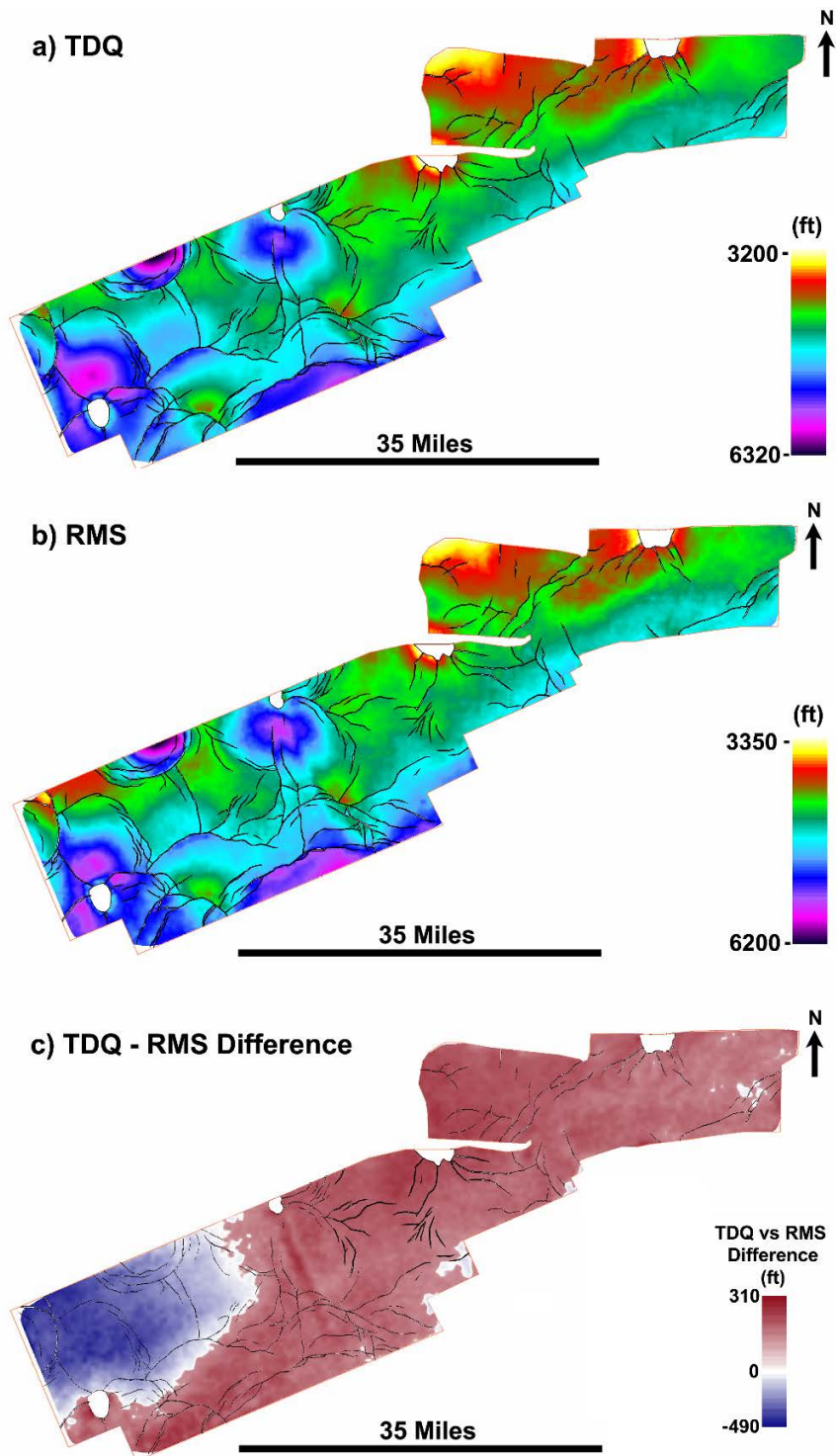


Figure 2.3.7 - MFS07 depth montage depicting a) TDQ method results, b) RMS method results, and c) the difference (TDQ minus RMS) between the two methods.

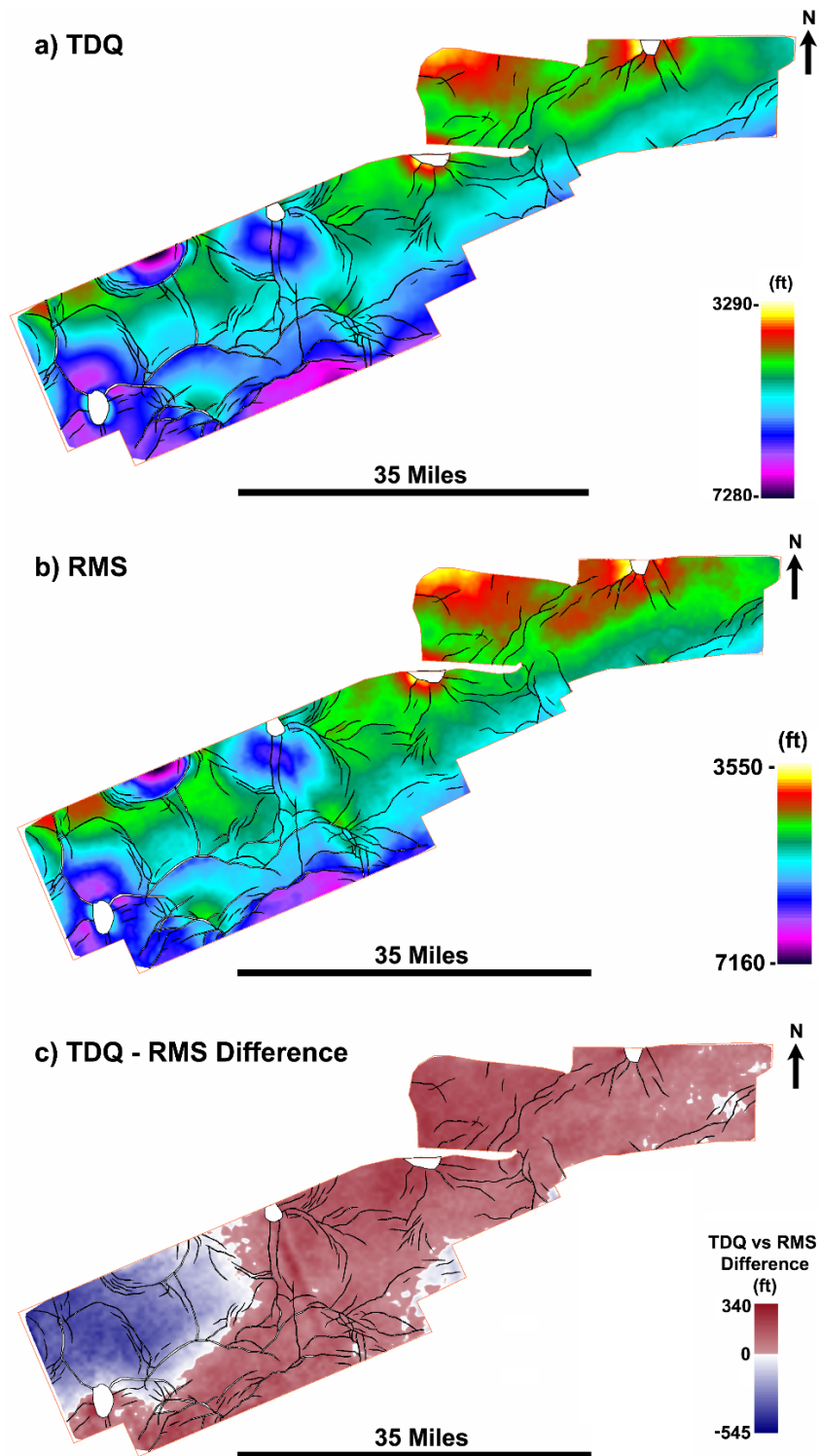


Figure 2.3.8 - SB\_M08 depth montage depicting a) TDQ method results, b) RMS method results, and c) the difference (TDQ minus RMS) between the two methods.

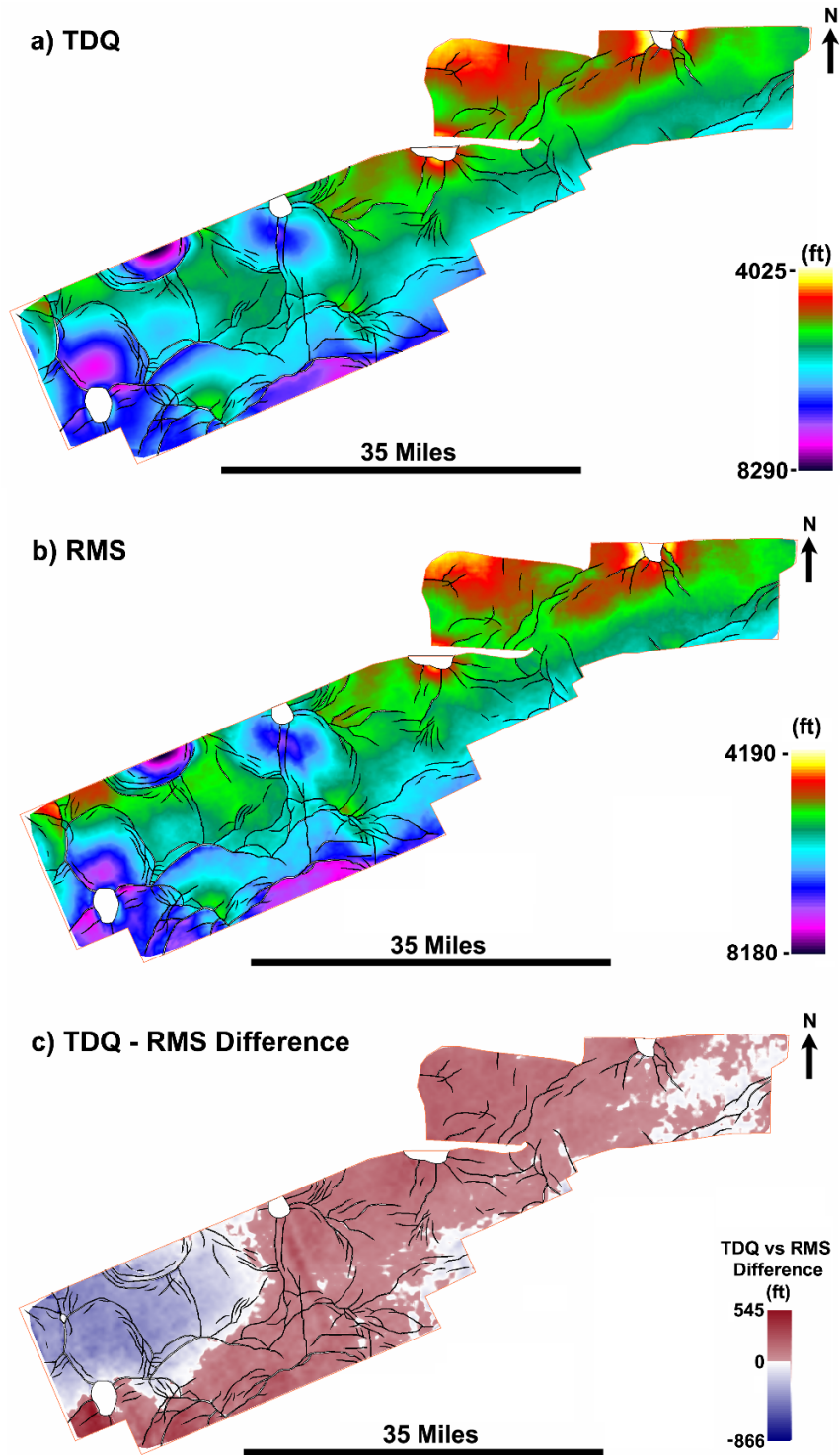


Figure 2.3.9 - MFS09 depth montage depicting a) TDQ method results, b) RMS method results, and c) the difference (TDQ minus RMS) between the two methods.



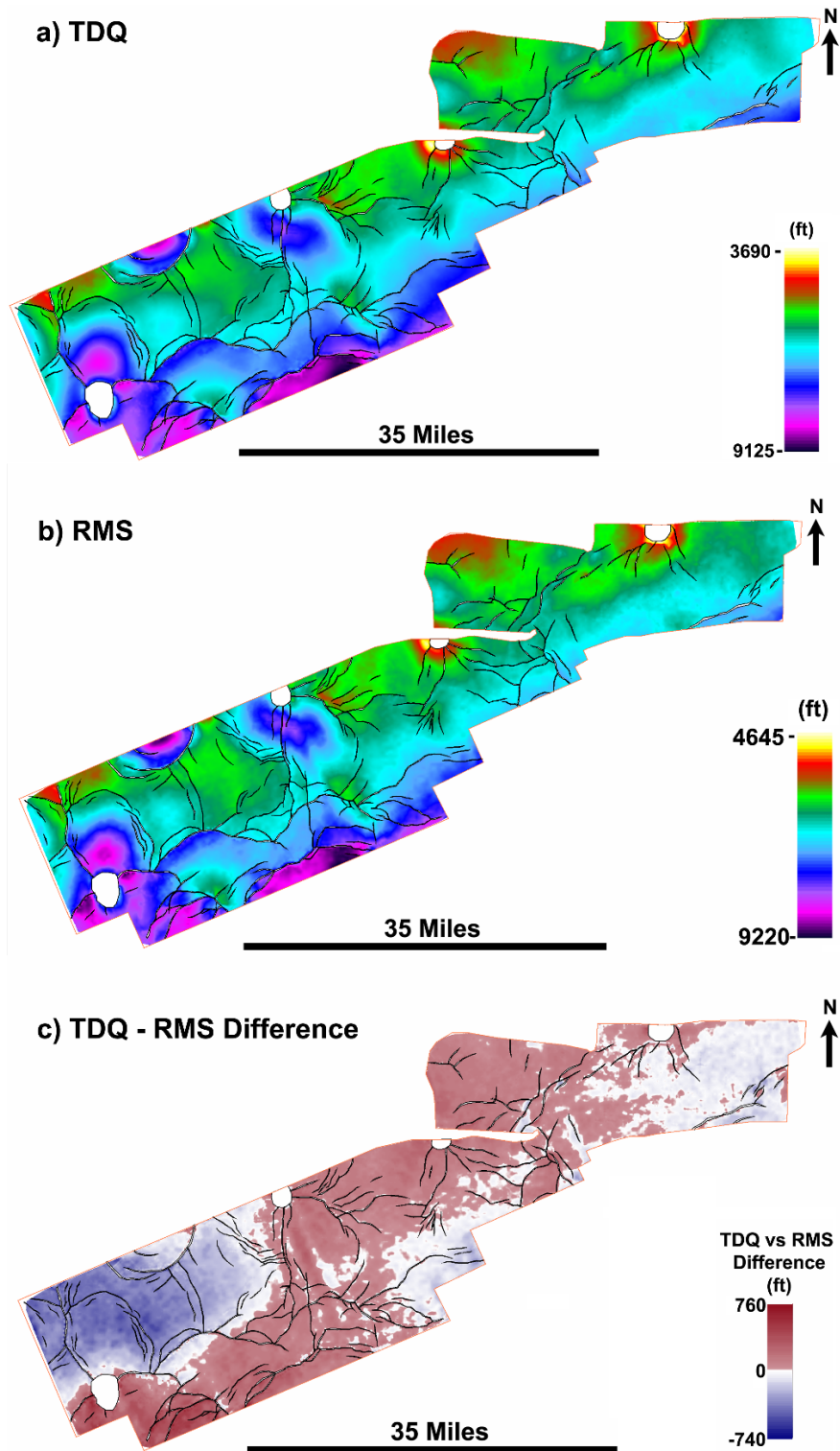


Figure 2.3.10 - SB\_M09 depth montage depicting a) TDQ method results, b) RMS method results, and c) the difference (TDQ minus RMS) between the two methods.

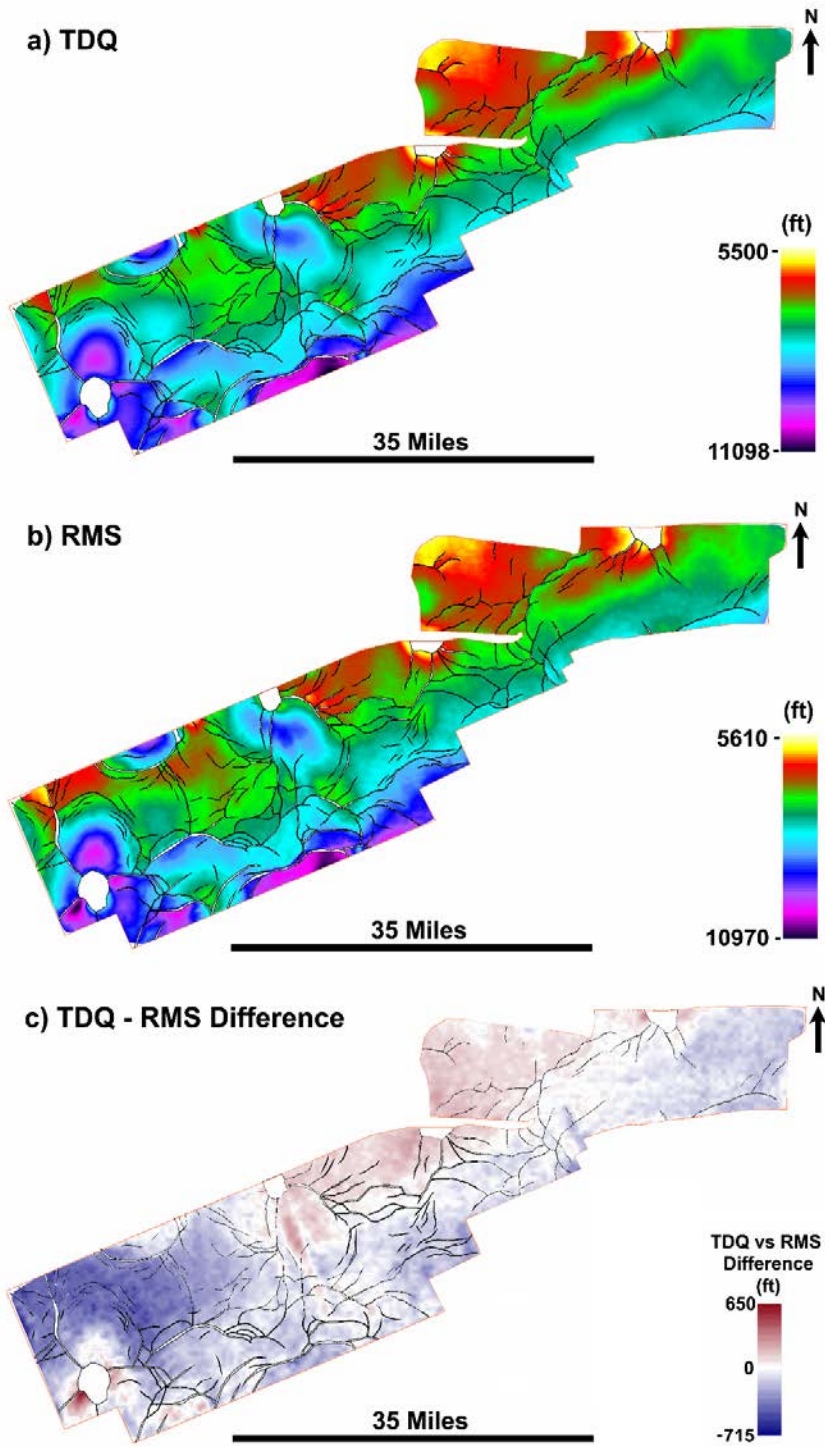


Figure 2.3.11 - MFS10 depth montage depicting a) TDQ method results, b) RMS method results, and c) the difference (TDQ minus RMS) between the two methods.

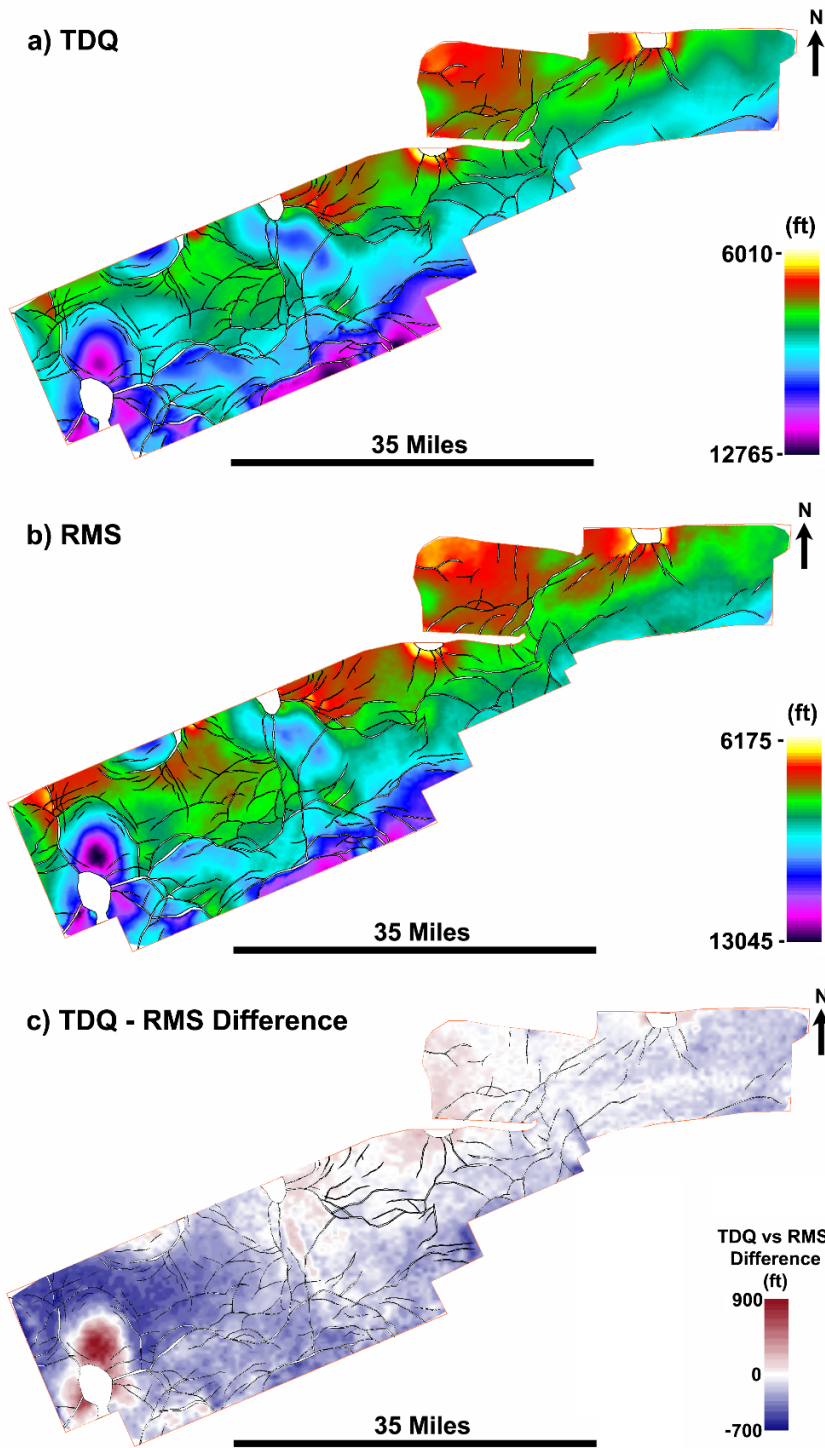


Figure 2.3.12 - MFS12 depth montage depicting a) TDQ method results, b) RMS method results, and c) the difference (TDQ minus RMS) between the two methods.

**Closures, fetch areas, existing fields, and faults vertical displacement**

Integrated analysis was performed on structural closures, fetch areas, existing fields, and fault maximum vertical displacement within the TexLa Merge 3D seismic area. The analysis was based on the MFS09 depth structure map as the structure that represents the bottom of a regional seal and the top of stacked potential reservoir strata (Figure 2.3.13). These reservoirs are within the MFS9 – MFS10 interval and correspond to the Lower Miocene (LM1 – LM4) and the Middle Miocene (MM1 – MM4), MM4 belonging to the *Amphistegina B.* biochronozone, based on the Atlas of Northern Gulf of Mexico Gas and Oil Reservoirs (Seni et al, 1997).

Structural closures are mostly faulted anticlines and 3-way dip fault dependent closures (Figure 2.3.13). These types of closures are also described as oil and gas reservoir plays in the Seni et al atlas (1997). Each closure and its corresponding fetch area was examined for its CO<sub>2</sub> storage resources potential (i.e., its integrity as a CO<sub>2</sub> storage site). The analyses included the number of stacked storage strata below the regional seal, as previously reported for the 10-L site (DeAngelo et al., 2019), and the integrity of the faults, such as the relationship between maximum vertical displacement of the faults versus the sealing capacity and the juxtapositions of the sand-shale strata (Figure 2.3.14). The integrity of the faults, or the closures in general, may be related to the column height of existing gas fields within the TXLA area. The 24-L and 10-L sites provide ideal information for the relationship between fault integrity, juxtaposition, closures, and column height (Figure 2.3.15).

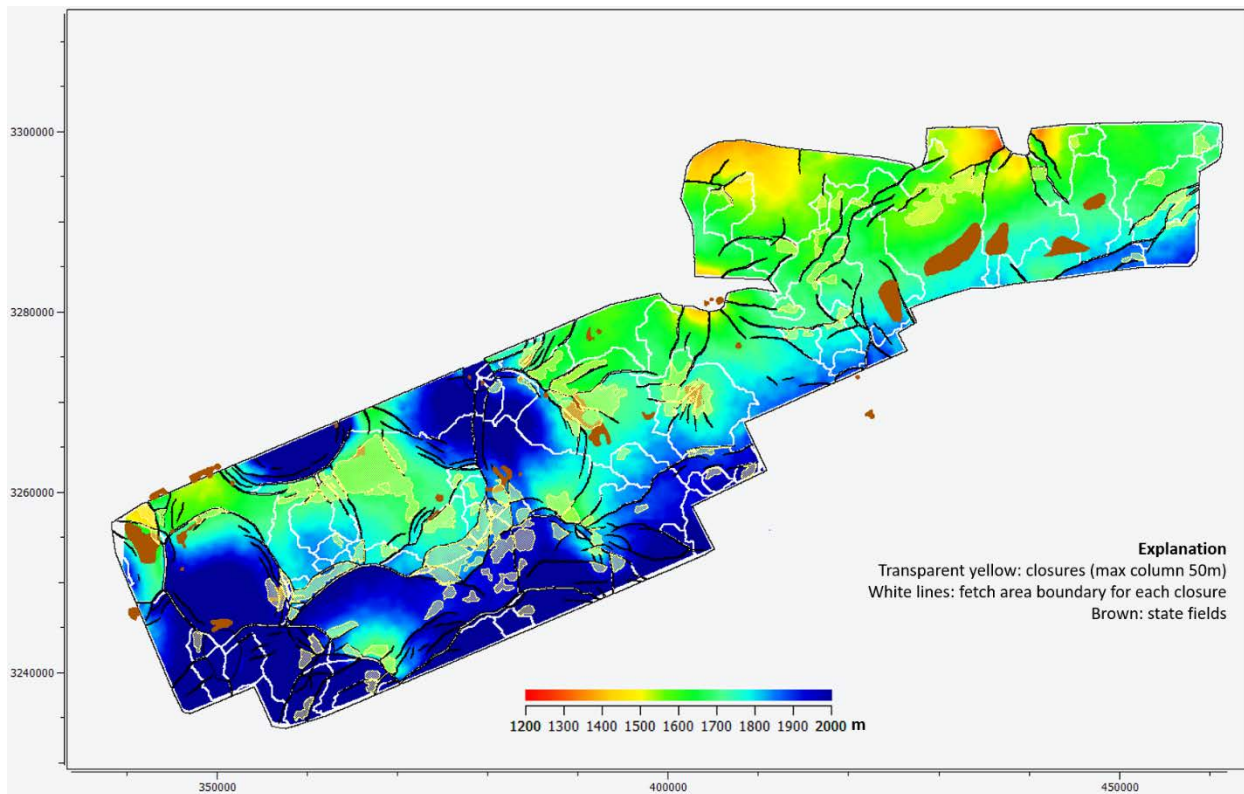


Figure 2.3.13 – Depth structure map of the MFS09 horizon (i.e., the base of regional seal) and the top of stacked reservoir layers within TexLa Merge area. Transparent yellow polygons are structural closures with maximum column height of 50 meters. White lines are the fetch area boundaries for their corresponding closures. Brown polygon are existing oil and gas fields in the state waters as defined by Seni et al. (1997).

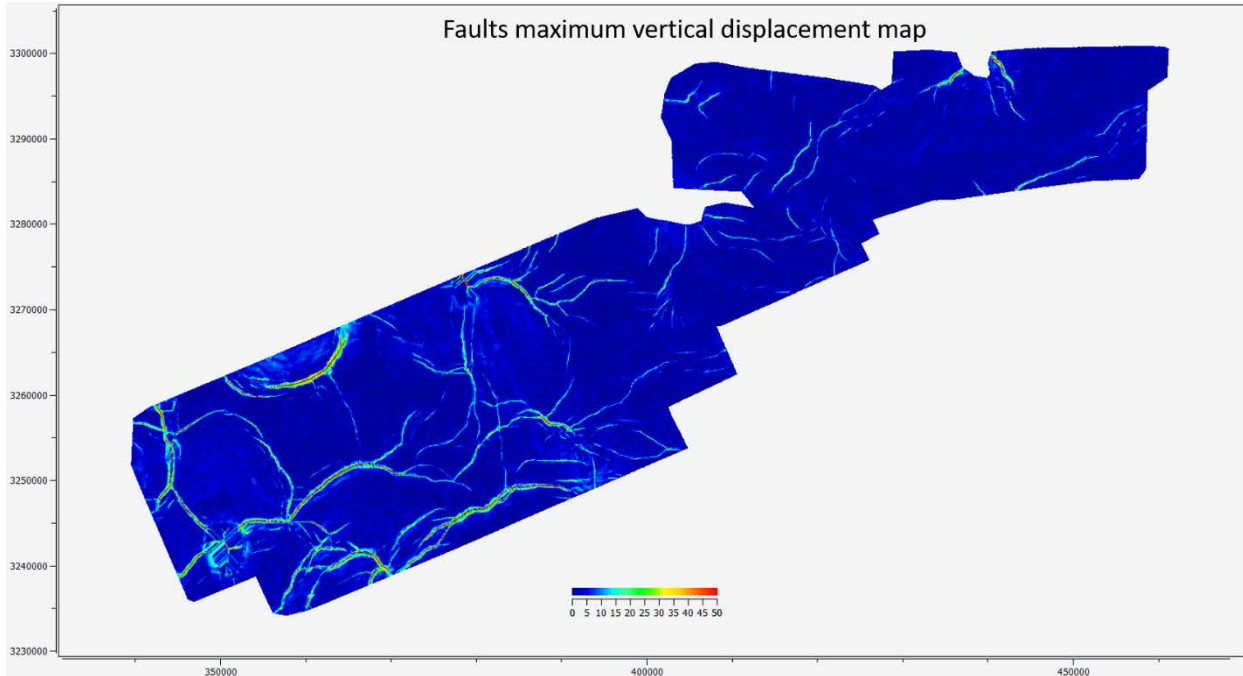


Figure 2.3.14 - Map of faults' maximum vertical displacements. The average displacement is approximately 20 meters; however, some major faults are much more than 50 meters. The scale is set to maximum 50-meter displacement (red) to better show the distribution.

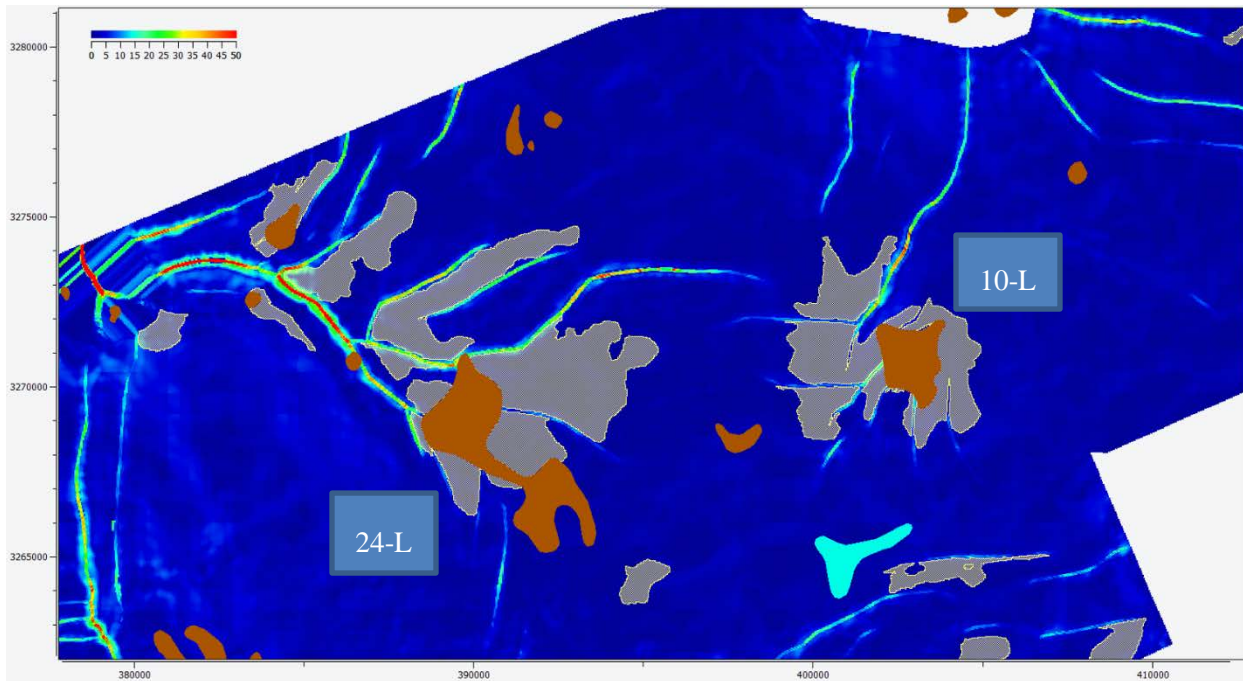


Figure 2.3.15 – Mapped closures (grey) based on 3D seismic; existing field outlines (brown) as defined by Seni et al, (1997) without the benefit of 3D seismic data, and faults' maximum vertical displacements around the 24-L and 10-L sites.

## 2.4 Subtask 2.4 – Assess Seal Interval Characteristics

### A. Micro-Scale Seal Properties: Analysis of Micro- and Nano-Scale Properties

In order to assess small-scale seal (i.e., caprock or confining zone) interval properties, Dr. Jiemin Lu searched the core repository collection of the Bureau of Economic Geology (BEG). A thorough search through the digital and written records of the BEG core archives at two of the BEG’s core repositories (i.e., in Austin and Houston) yielded seven available cores close to the study area, four of which are offshore and three onshore (Table 2.4.1). Two of the cores from West Cameron, Louisiana offshore, were studied in detail (red text in Table 2.4.1). The location of the cores are shown in Figure 2.4.1.

Table 2.4.1 – Two examined cores (red) from West Cameron area among the potentially available cores near the study area.

API Number	Well ID	Location	Lease Name	Top Depth (ft)	Bottom Depth (ft)	Sample Type	Reservoir	Longitude	Latitude
		County: WEST CAMERON State:				SLABBED	WEST		
177004040000	A-3	LOUISIANA	OCS-G-3496	12918	13074	CORE	CAMERON	-93.3312	29.2597
		County: WEST CAMERON State:				SLABBED			
177004063100	C-4	LOUISIANA	OCS-G-4392	13100	13160	CORE	198	-93.3317	29.2287
		County: HIGH IS-L B State:				SLABBED			
427084032600	1	TEXAS	OCS-G-10266	10722	10748	CORE	Unknown	-93.9890	29.4199
		County: WEST CAMERON State:				SLABBED	WEST		
177004061700	C-5	LOUISIANA		11409	11415	CORE	CAMERON 212	-93.3317	29.2287
		County: CAMERON State:				SLABBED			
170230234500	02345	LOUISIANA		17846	17870	CORE	WILDCAT 17	-92.6487	29.6035
		County: CAMERON State:				SLABBED			
170232205700	D-1	LOUISIANA	MIAMI CORP SOUTH	16264	16298	CORE	HIGH ISLAND	-93.0782	29.8700
		County: GALVESTON State:	GILLOCK UNIT			SLABBED			
421673064500	30645	TEXAS	#94	9163	9181	CORE	GILLOCK S	-94.9674	29.3910

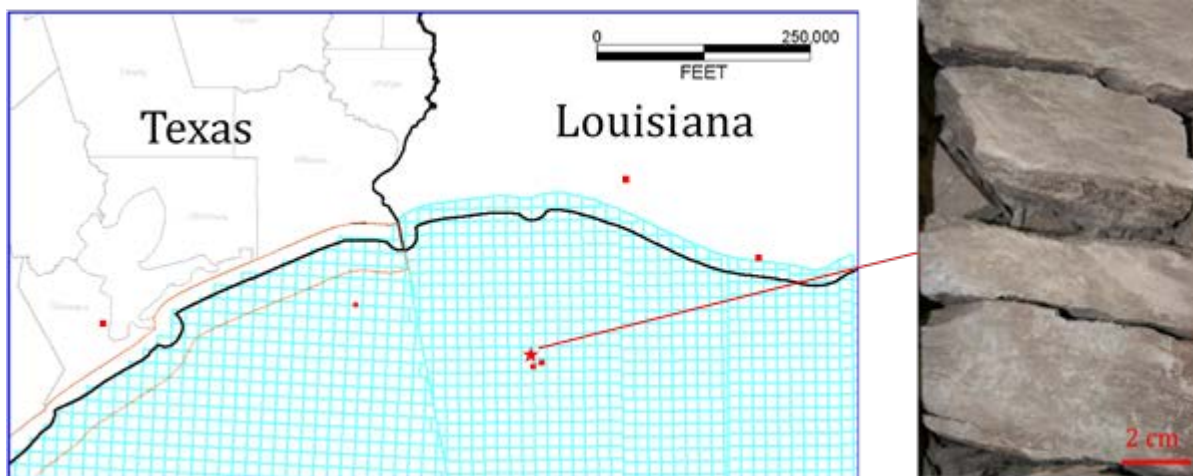


Figure 2.4.1 – Left: Location map of available cores close to project study area. Right: Photograph of the

slabbed core of Miocene mudstone of Well OCS-G-3496 A-3.

One of the cores, OCS-G-3496 A-3 from West Cameron Block 205, offshore Louisiana was shipped from Houston to Austin and was examined. The core's depth ranges from 12918 to 13074 ft and contains 50 ft of continuous marine mudstone succession and 80 ft interbedded mudstone and fine-grained sandstone of middle Miocene age. Four major facies were identified in the core: 1) mudstone with occasional sandstone lenses (Figure 2.4.2a); 2) Burrowed mudstone interbedded with very fine-grained sandstone (Figure 2.4.2b); 3) Weakly laminated sandstone (Figure 2.4.2c); and 4) Burrowed, laminated sandstone with ripple and cross laminations (Figure 2.4.2d). The mudstone facies is the focus of the petrographic analysis for evaluation of seal capacity. Eleven samples (Table 2.4.2) were taken from the core for further analyses, such as scanning electron microscope (SEM), X-ray diffraction (XRD), mercury intrusion capillary pressure (MICP), etc. Two of them have been polished by ion milling and examined using SEM. Four samples (yellow highlights in Table 2.4.2) were examined by Scanning Electron Microscope (SEM) using state of the art ion milling polishing technique. In addition, the whole core was described (Figure 2.4.3).



Figure 2.4.2a. Photograph of shaly mudstone, 12963 ft, OCS-G-3496 A-3



Figure 2.4.2b. Photograph of burrowed mudstone interbedded with sandstone mudstone, 13049 ft, OCS-G-3496 A-3

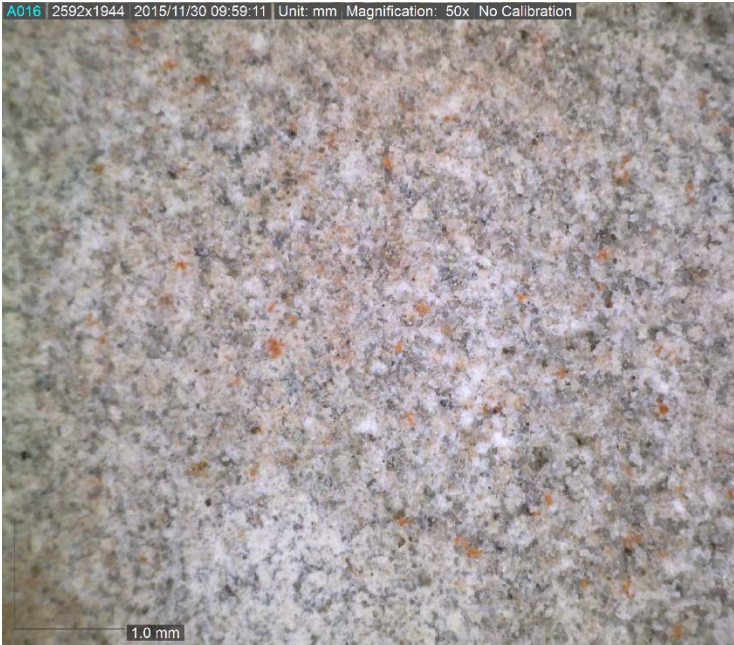


Figure 2.4.2c. Reflected light photomicrograph of weakly laminated fine-grained sandstone, 13056 ft, OCS-G-3496 A-3.



Figure 2.4.2d. Photograph of heavily bioturbated and laminated sandstone, 12923 ft, OCS-G-3496 A-3

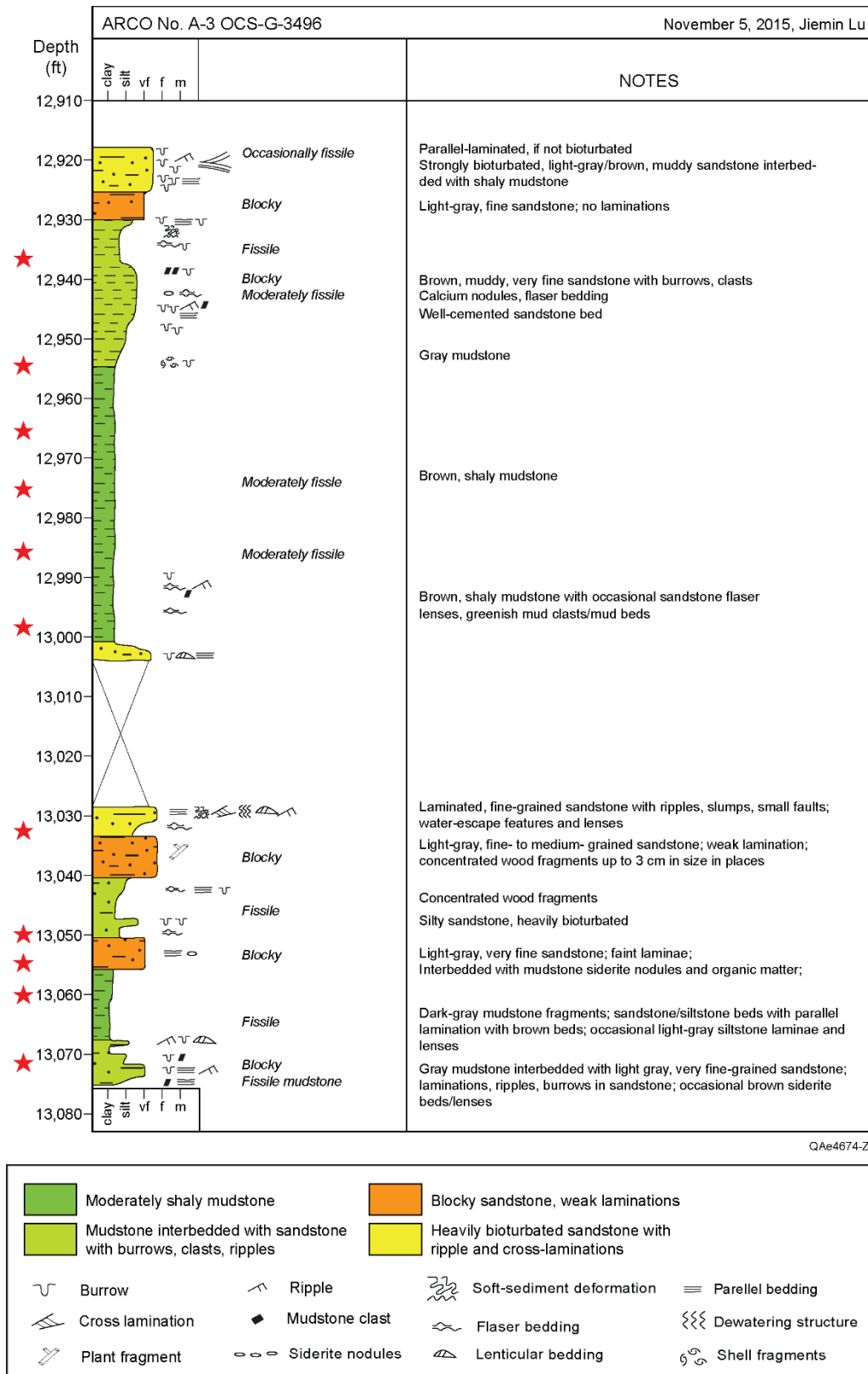
Table 2.4.2 – Core samples taken for petrographic and other analyses. Samples in yellow analyzed with SEM.

Sample ID	Well	Sample depth (ft)	Lithology
1	OCS-G-3496 A-3	12937	Mudstone
2	OCS-G-3496 A-3	12954.2	Argillaceous silty claystone
3	OCS-G-3496 A-3	12966.8	Mudstone
4	OCS-G-3496 A-3	12975.5	Mudstone
5	OCS-G-3496 A-3	12984.9	Mudstone
6	OCS-G-3496 A-3	12999.5	Argillaceous silty



			claystone
7	OCS-G-3496 A-3	13033	Mudstone
8	OCS-G-3496 A-3	13050	Siliceous siltstone
9	OCS-G-3496 A-3	13056	Fine-grained sandstone
10	OCS-G-3496 A-3	13060.5	Argillaceous silty claystone
11	OCS-G-3496 A-3	13071.5	Mudstone

---



QAe4674-Z

Figure 2.4.3 - Core description of OCS-G-3496 A-3, West Cameron Block 205, offshore Louisiana.

Of the examined mudstone samples, (Table 2.4.2: 2, 6, 8, 10) three of, samples 2, 6, 10, are argillaceous silty claystone of facies 1 with varying amounts of silt contents. Sample 8 is a siliceous siltstone of facies 2.

The silty claystone is dominated by extra-basinal siliciclastic detrital grains of quartz, illite, chlorite, mica, and small amounts of plagioclase and K-feldspar (Figure 2.4.4a-d). Silt grains consist mostly of quartz, and small amounts of calcite, K-feldspar, plagioclase, and dolomite (Figure 2.4.4a-d). Silt- and clay-sized calcite grains are predominantly comminuted skeletal debris or grain replacements. The authigenic components include chlorite, kaolinite, pyrite, and rhombic dolomite. For example, Figure 2.4.4e shows foraminifera chambers filled with authigenic kaolinite, chlorite and pyrite framboids. Small amounts of the quartz and calcite are diagenetic.

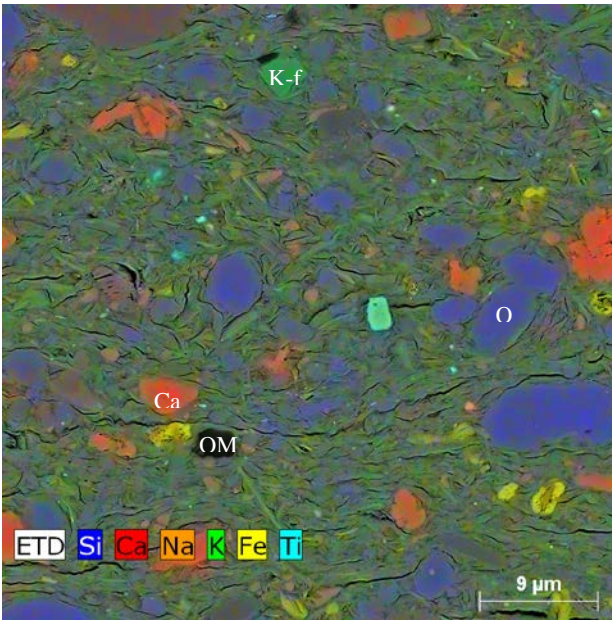


Figure 2.4.4a) EDS map with false color for elements showing silt particles of quartz (Q), K-feldspar (K-f), calcite (Ca), albite (Al) floating in clay matrix. Sample 1

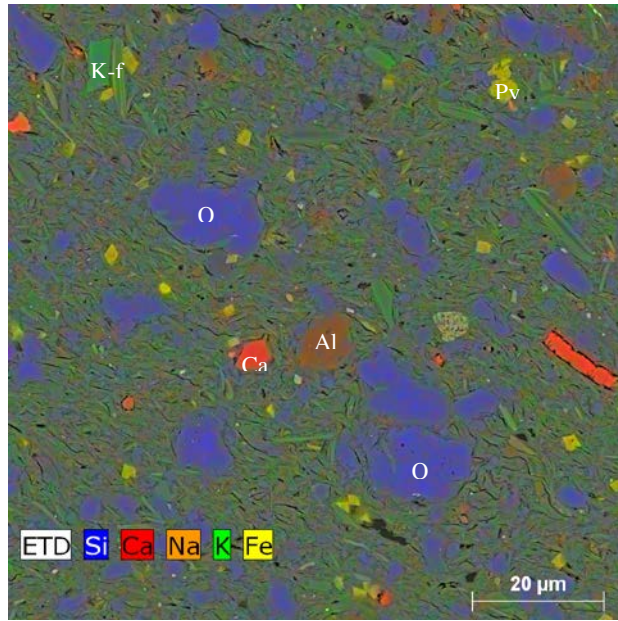


Figure 2.4.4b) EDS map with false color for elements showing the texture of silty claystone with high degree of fabric alignment along the bedding. Sample 6

--	--

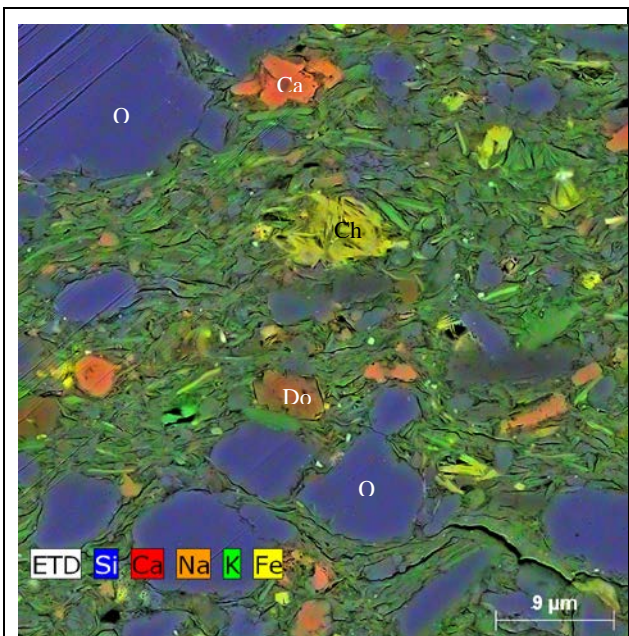


Figure 2.4.4c) EDS map showing quartz (Q) constitute a large portion of the slit-sized grains with small amounts of calcite (Ca) and dolomite (Do). Authigenic chlorite (Chl) often occurs as grain replacement. Sample 1

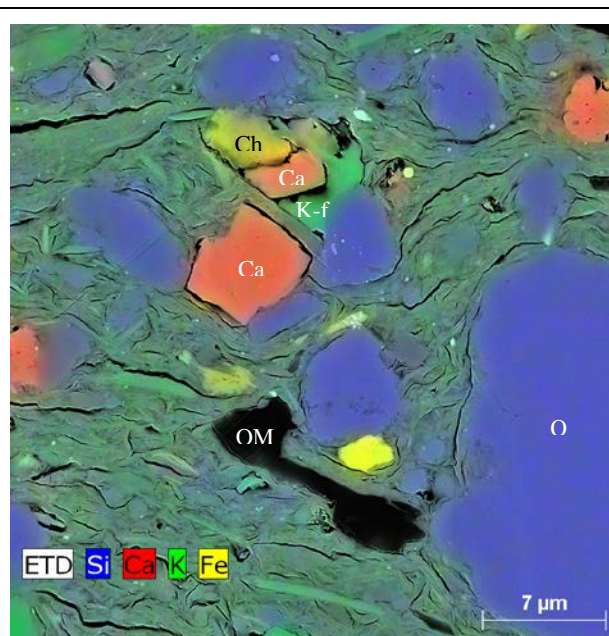


Figure 2.4.4d) EDS map showing a partially dissolved K-feldspar (K-f) grain with authigenic calcite (Ca) and chlorite (Chl) filling up the secondary pores derived from the grain. Organic matter (OM) particle occupies large intergranular space and has a discrete particulate shape. Sample 10

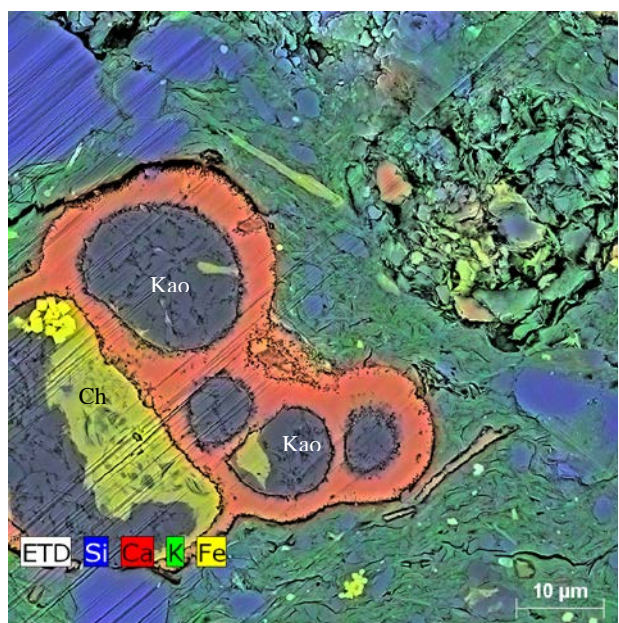


Figure 2.4.4e) EDS map showing a foraminifer

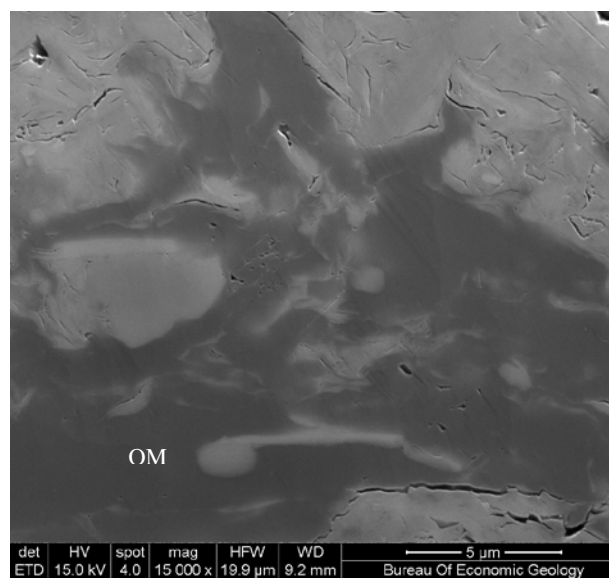


Figure 2.4.4) Secondary electron (SE) image showing dispersed organic matter with convolute

with its chambers totally filled up with kaolinite outlines. Sample 6  
 e (Kao), chlorite (Chl) and pyrite (Py). Sample  
 6

Figure 2.4.4. SEM (grayscale) images and EDS elemental maps (color) of claystone.

Organic matter (OM) content in the samples is less than 1%. The dominant OM exists as isolated particles up to 10 µm in size showing a homogenous texture (Figure 2.4.5a, c). Most of the large OM particles are likely primary kerogen because they occupy large intergranular spaces and have discrete particulate shape; although there is usually a lack of visual evidence to differentiate between marine and terrigenous origin. Another type of OM observed shows dispersed and convolute outlines. It lacks distinct shape and has a homogenous texture. It is often elongated parallel to bedding and engulfs rigid grains. The convolute and fluid shapes of this OM suggest a high degree of compaction.

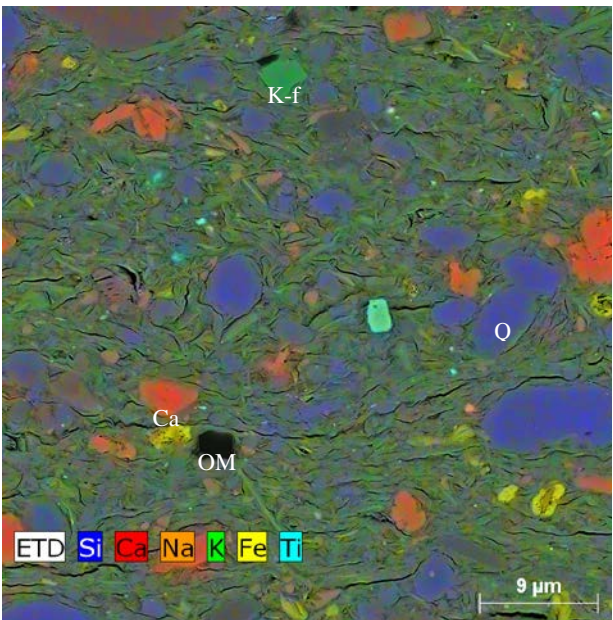


Figure 2.4.5a) EDS map with false color for elements showing silt particles of quartz (Q), K-feldspar (K-f), calcite (Ca), albite (Al) floating in clay matrix. Sample 1

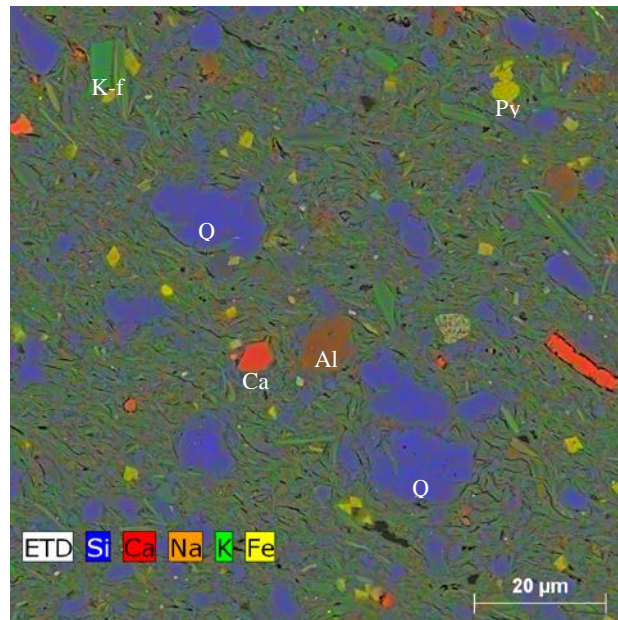


Figure 2.4.5b) EDS map with false color for elements showing the texture of silty claystone with high degree of fabric alignment along the bedding. Sample 6

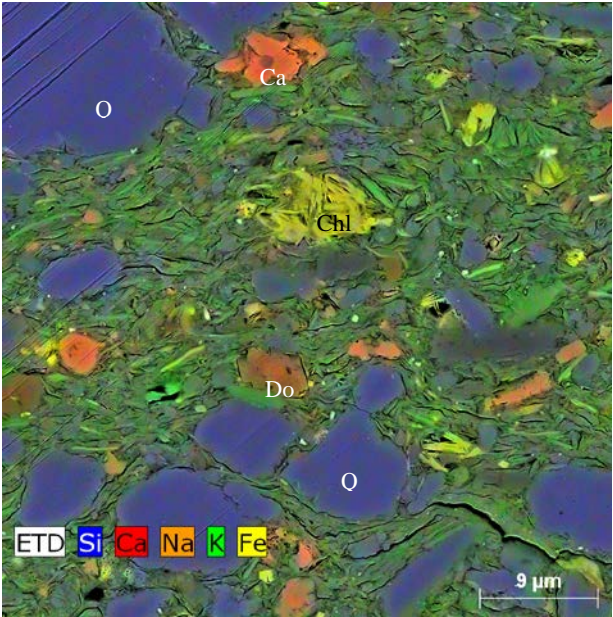


Figure 2.4.5c) EDS map showing quartz (Q) constitute a large portion of the slit-sized grains with small amounts of calcite (Ca) and dolomite (Do). Authigenic chlorite (Chl) often occurs as grain replacement. Sample 1

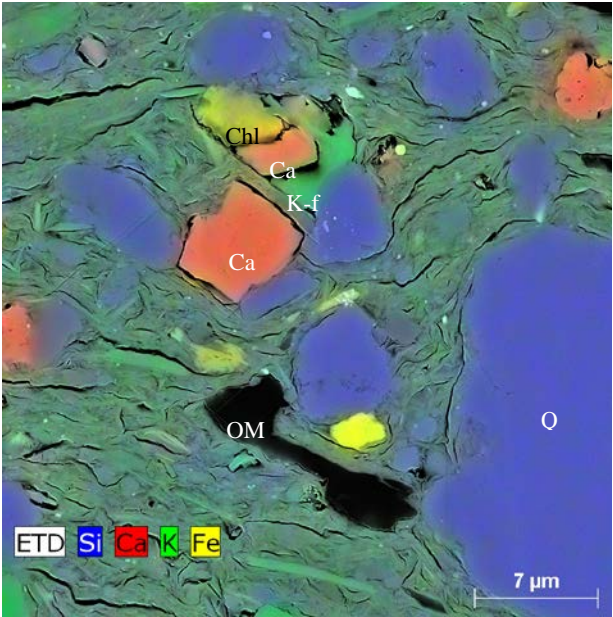


Figure 2.4.5d) EDS map showing a partially dissolved K-feldspar (K-f) grain with authigenic calcite (Ca) and chlorite (Chl) filling up the secondary pores derived from the grain. Organic matter (OM) particle occupies large intergranular space and has a discrete particulate shape. Sample 10

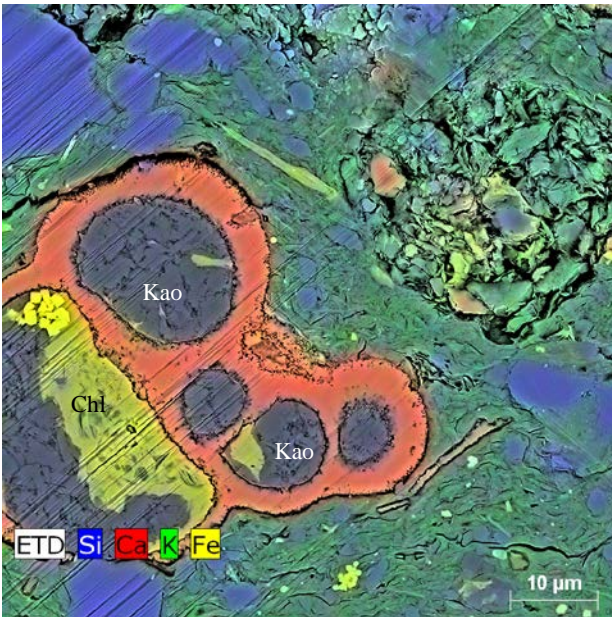


Figure 2.4.5e) EDS map showing a foraminifer with its chambers totally filled up with kaolinite (Kao), chlorite (Chl) and pyrite (Py). Sample 6

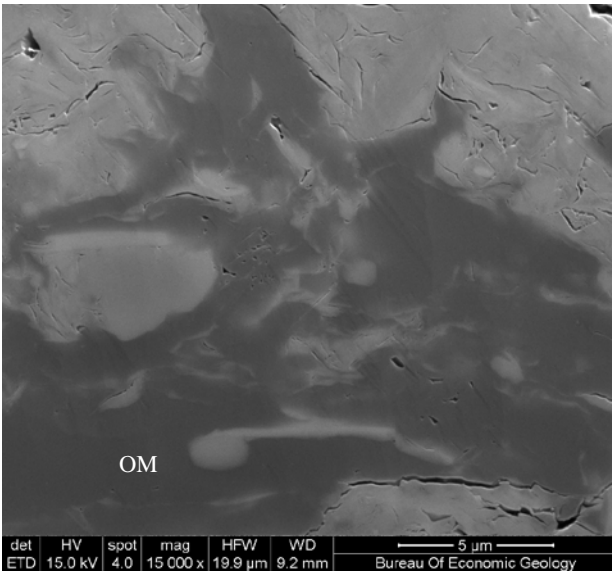


Figure 2.4.5f) Secondary electron (SE) image showing dispersed organic matter with convolute outlines. Sample 6

Porosity is low in the claystone samples. The majority of the observed pores are secondary pores derived from mineral dissolution and later partially filled with diagenetic minerals (Figure 2.4.6a-f). Most precursor minerals were totally dissolved and it is difficult to identify their mineralogy. But in some cases, K-feldspar shows partial dissolution with secondary pores generated beside and within the remaining grains suggesting feldspar dissolution is the main source for the secondary porosity (Figure 2.4.6e, g). Most of remaining secondary pores are partially filled with chlorite, kaolinite, calcite, and pyrite. Figure 2.4.6d shows a partially dissolved K-feldspar grain and that the authigenic calcite and chlorite have totally filled in the secondary pore. Figure 2.4.6a and Figure 2.4.6b shows a number of secondary pores partially filled with chlorite and calcite cements. A small number of intraparticle pores are found mostly in feldspar and calcite grains (Figure 2.4.6h).

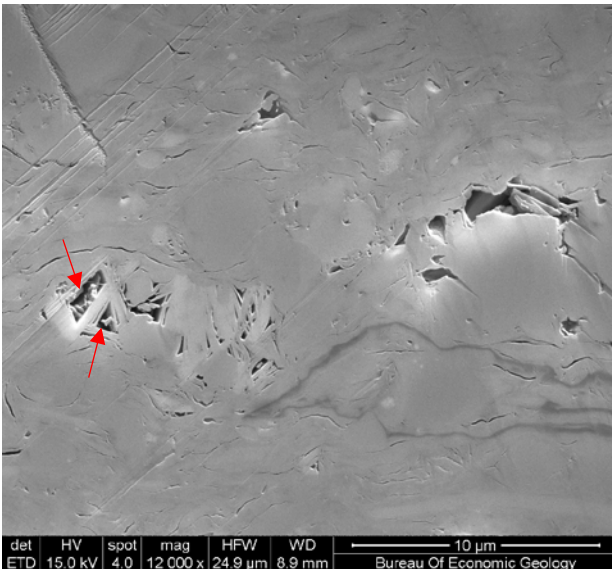


Figure 2.4.6a) SEM image showing secondary pores (arrow) partially filled with chlorite. Sample 1

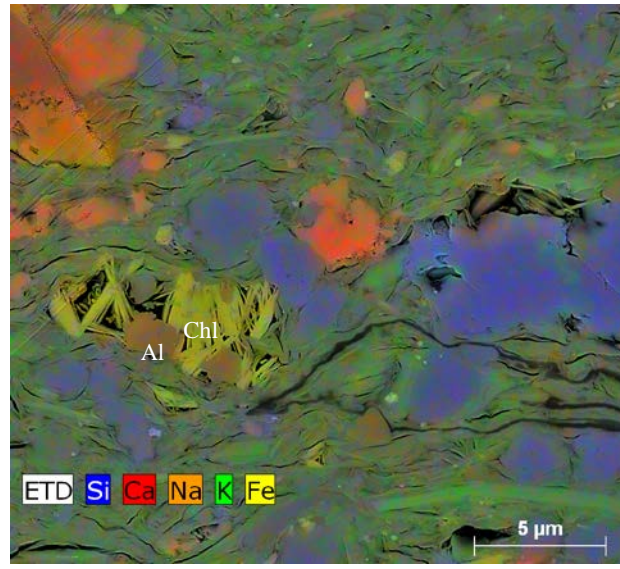
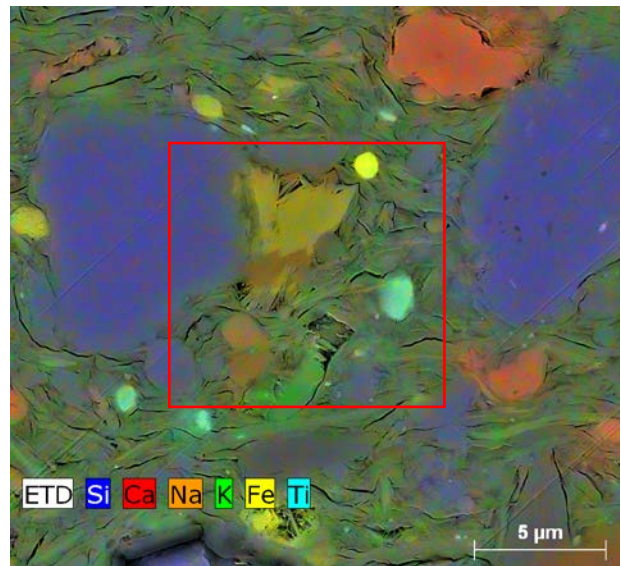
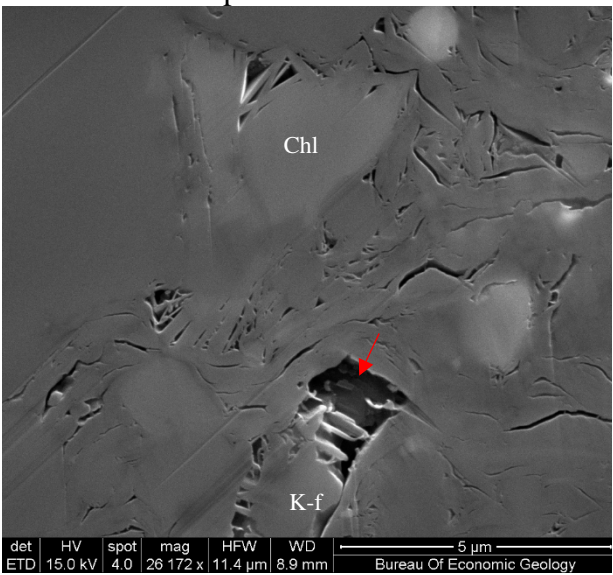
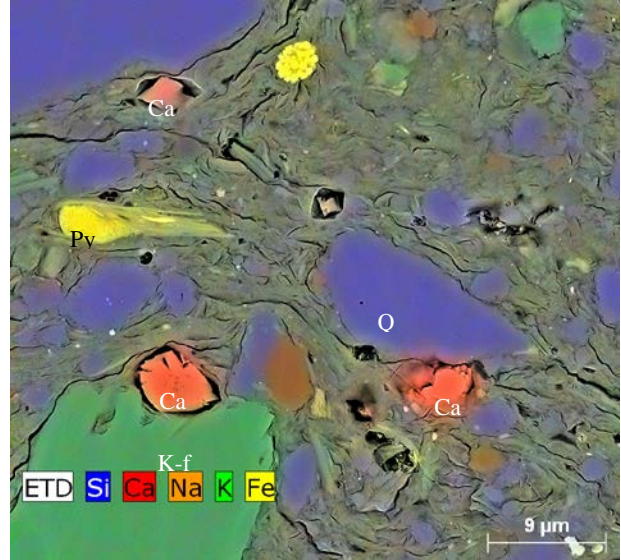
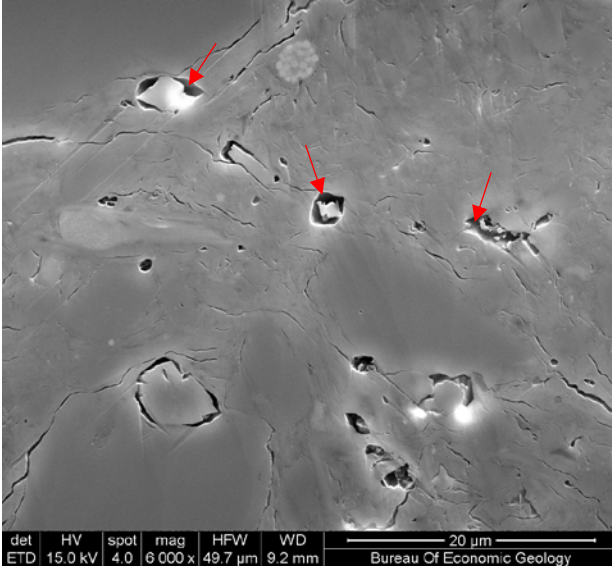


Figure 2.4.6b) EDS elemental map of Figure 2.4.6a.





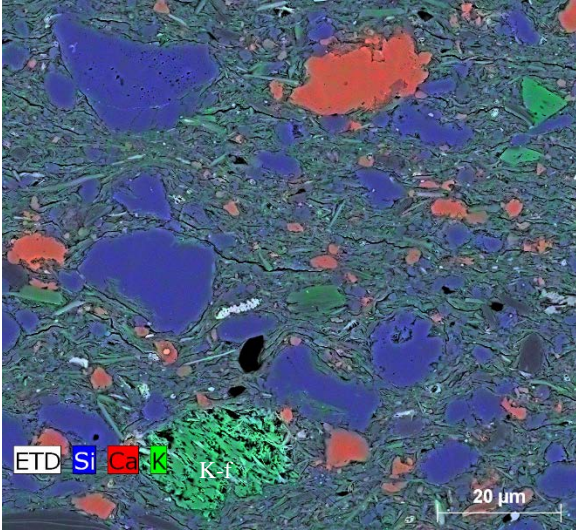


Figure 2.4.6g) EDS elemental map showing a partially dissolved K-feldspar grain (K-f) with dense dissolution streaks. Sample 1

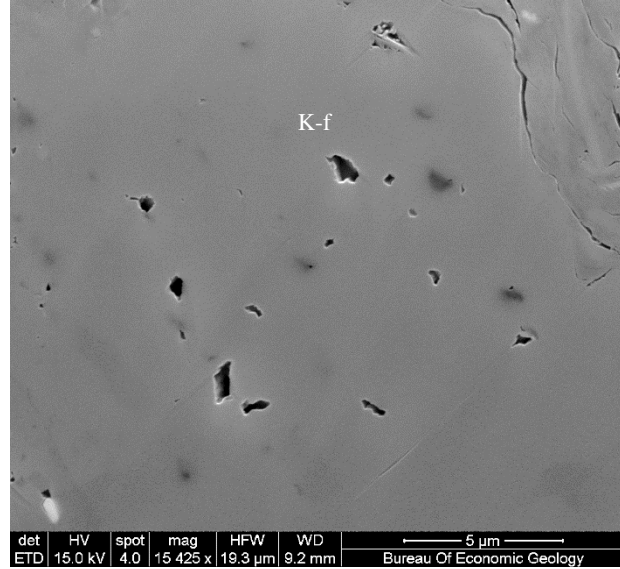


Figure 2.4.6h) SEM image of a K-feldspar grain containing intraparticle pores. Sample 10.

The siltstone sample (Sample 8 of Table 2.4.2) shows a similar mineral composition as the claystone with the dominant silt grains being quartz. In addition to quartz, the silt-sized grains contain small amounts of calcite, K-feldspar, and plagioclase, mostly albite (Figure 2.4.7). Unlike the claystone, the intergranular space in the siltstone is locally dominated by detrital chlorite. Diagenesis is also similar to the claystone samples. Porosity is low and mostly consists of secondary pores. Dissolution of plagioclase and K-feldspar is the most important source of porosity. Authigenic minerals, mostly chlorite, precipitated in the secondary pores.

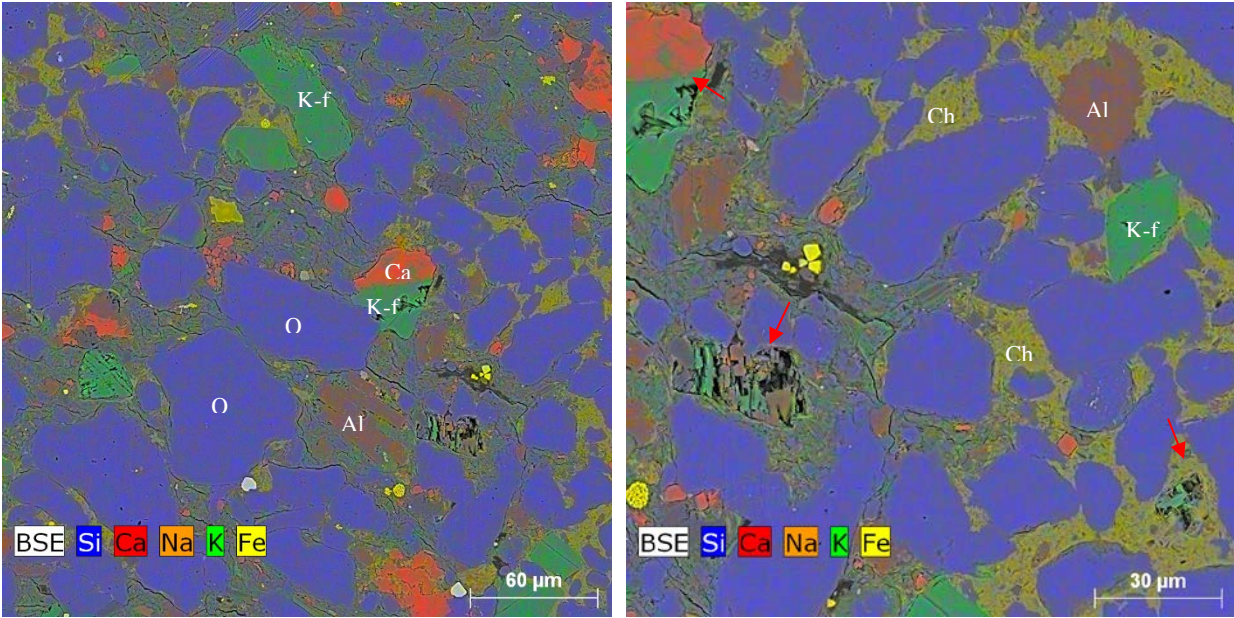


Figure 2.4.7a) EDS elemental map showing the majority of the silt grains are quartz with small amounts of K-feldspar (K-f), albite (Al), and calcite (Ca).

Figure 2.4.7b) EDS elemental map showing locally abundant chlorite (chl). Dissolution of K-feldspar and albite creates secondary pores (arrows).

Figure 2.4.7 - SEM images and EDS elemental maps of siltstone (sample 8)

Mudstone samples from a second core from West Cameron Louisiana offshore (Figure 2.4.8; Table 2.4.3) were also examined. The core from well OCS-G-3492 C-4, described in Figure 2.4.9, ranges from 13,100 to 13,160 ft. It contains ~25 ft of laminated claystone and siltstone interbedded with fine-grained sandstone. The succession contains ripple laminations, cross laminations, planar laminations, burrows, and flaser bedding. The cross lamination and cross bedding in the core are probably hummocky cross-stratification, indicating shallow marine environment. Three samples were examined using Scanning Electron Microscope (SEM) and the ion milling polishing technique. The samples examined are siliceous slit-rich claystone and all comprise similar mineralogy and texture. XRD mineral composition (Table 2.4.4) shows that the samples contain ~50% clay minerals, predominantly illite (~32%) and chlorite (~16%) with small amounts of kaolinite (<3%). Quartz is present at ~30%; plagioclase and K-feldspar combined vary between 13% and 19%. The samples contain zero to ~1% calcite. Small amounts of anatase and pyrite also exist.

Table 2.4.3 – The second examined core (red) from OCS-G-4392 C-4 from West Cameron Block, Louisiana offshore.

API Number	Well ID	Location	Lease Name	Top Depth (ft)	Bottom Depth (ft)	Sample Type	Reservoir	Longitude	Latitude
177004040000	A-3	County: WEST CAMERON State: LOUISIANA	OCS-G-3496	12918	13074	SLABBED CORE	WEST CAMERON	-93.3312	29.2597
177004063100	C-4	County: WEST CAMERON State: LOUISIANA	OCS-G-4392	13100	13160	SLABBED CORE	198	-93.3317	29.2287
427084032600	1	County: HIGH IS-L B State: TEXAS	OCS-G-10266	10722	10748	SLABBED CORE	Unknown WEST	-93.9890	29.4199
177004061700	C-5	County: WEST CAMERON State: LOUISIANA		11409	11415	SLABBED CORE	CAMERON 212	-93.3317	29.2287
170230234500	02345	County: CAMERON State: LOUISIANA		17846	17870	SLABBED CORE	WILDCAT 17	-92.6487	29.6035

170232205700	D-1	County: CAMERON State: LOUISIANA	MIAMI CORP	16264	16298	SLABBED CORE	HIGH ISLAND	-93.0782	29.8700
421673064500	30645	County: GALVESTON State: TEXAS	SOUTH GILLOCK UNIT #94	9163	9181	SLABBED CORE	GILLOCK S	-94.9674	29.3910

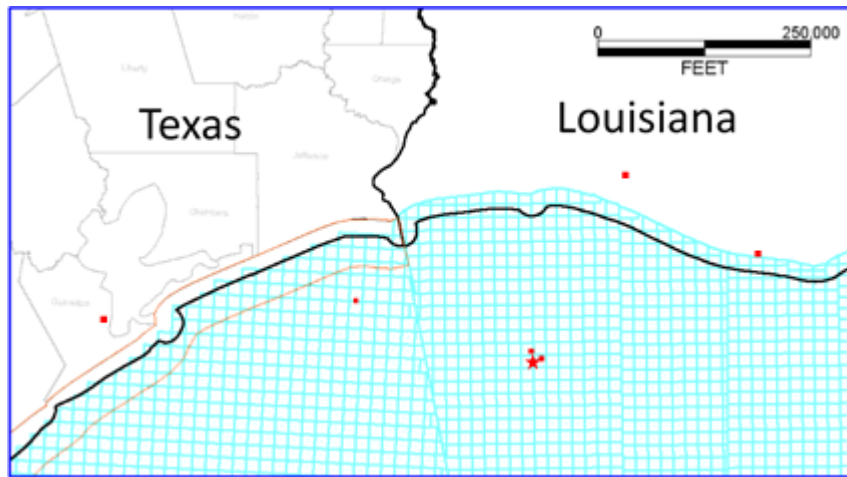


Figure 2.4.8 – Location map of the core from well OCS-G-3492 C-4 (star). The well is slightly south of the other analyzed core OCS-G-3496 A-3 (Figure 2.4.1).

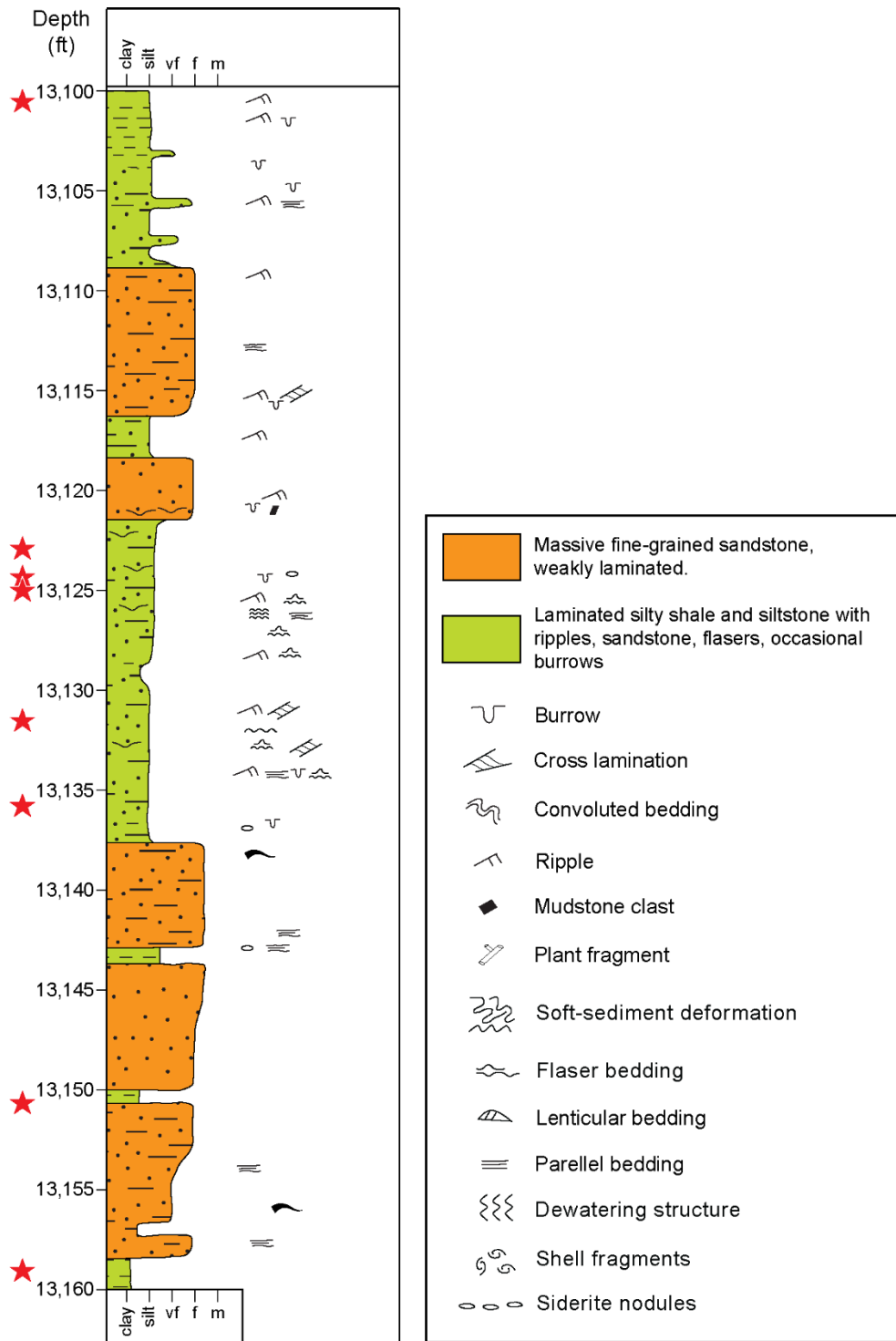


Figure 2.4.9 - Core description of ARCO well OCS-G-3492 C-4, West Cameron Block 205, Louisiana offshore.

Table 2.4.4 – XRD mineral composition of mudstone core samples from well OCS-G-4392 C-4, West

## Cameron Block, offshore Louisiana.

Depth (ft)	Quartz	Calcite	Plagioclase	K-feldspar	Illite	Kaolinite	Chlorite	Anatase	Pyrite
13100.5	31.3	0.2	3.4	9.3	35.2	2.8	14.9	1.4	1.5
13125	29.8		5.2	8.4	33.5	2.5	17.9	1.9	1.0
13136	29.1	1.4	6.1	12.8	29.3	2.1	16.7	1.5	1.0

### SEM Method

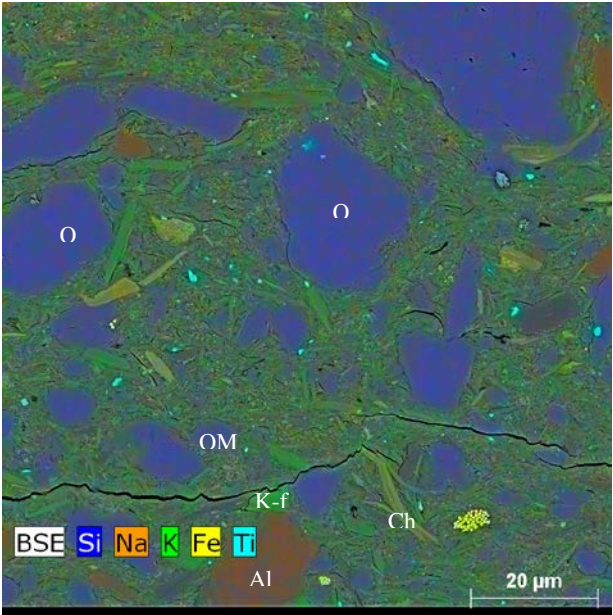
The mudstone samples were ion-milled to create extremely smooth surfaces that were characterized using SEM. For each sample, a piece of core fragment was shaped into a cuboid of approximately  $10 \times 8 \times 5$  mm in size. The samples were polished using a Triple Ion Beam Miller (Leica EM TIC020) with an accelerating voltage of 8 kV, a current of 2.8 mA, and a milling time of 10 hr. The polished view area is perpendicular to the bedding and is triangular (~5 mm wide and ~1 mm high). Iridium was applied to the ion-milled surfaces to create a conductive coating to limit charging during SEM imaging.

The samples with iridium coating were examined on an FEI NovaNano SEM 430 using secondary electron (SE) and backscattered electron (BSE) modes at an accelerating voltage of 10–15 kV and a working distance of 7–9.5 mm. Chemical compositions were analyzed with the aid of two X-ray energy dispersive spectroscopy (EDS) detectors which produce EDS elemental maps for mineralogical analysis. Mineral composition, diagenesis and texture were documented in the SEM images.

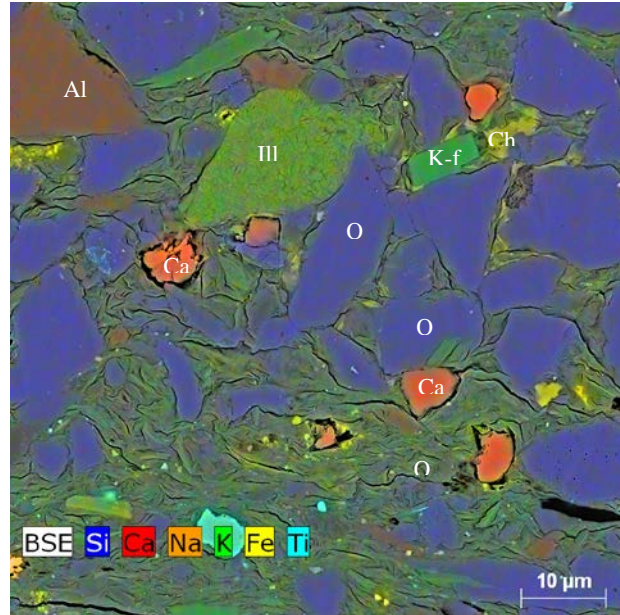
### Results

The analyzed samples are all siliceous, silt-rich claystone with similar mineral compositions. The claystone samples are dominated by extra-basinal siliciclastic detrital grains of quartz, illite, chlorite and alkali feldspar (K-feldspar and albite). Silt grains consist of predominantly quartz, small amounts of K-feldspar and albite, and trace amount of calcite (Figure 2.4.10a, b). Calcite occurs mostly as comminuted skeletal debris or grain replacement. Most silt grains are 10–20  $\mu\text{m}$  in size that are poorly rounded. Because of the presence of abundant silt-sized grains, the degree of fabric alignment of the clay minerals is low (Figure 2.4.10a-c).

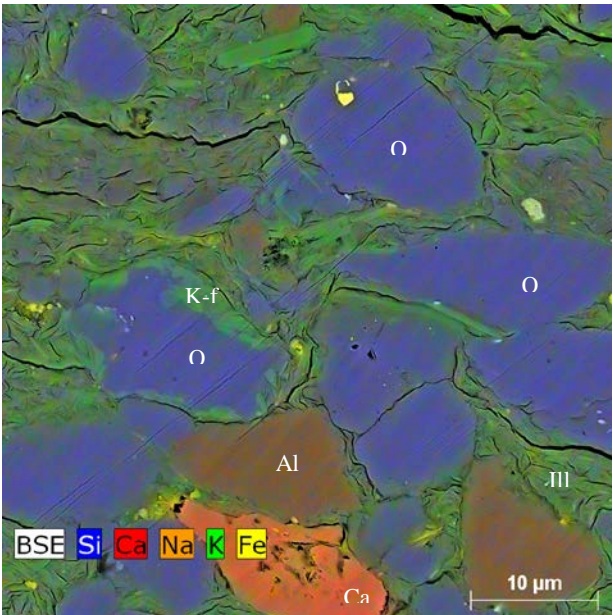
Authigenic minerals include chlorite, kaolinite, pyrite, anatase, and anhydrite (Figure 2.4.10d-f). Occasionally, feldspar partially replacing quartz can be seen (Figure 2.4.10c). Some chlorite forms as a replacement of mica. Pyrite framboids and larger crystals are locally abundant, filling in primary pores (Figure 2.4.10d, f). For example, Figure 2.4.10d shows a layer of authigenic pyrite and organic matter up to 15  $\mu\text{m}$  thick. Clay minerals are compressed around the hard crystals of pyrite, suggesting pyrite was formed before compression, during early stage of diagenesis. Another example shows a pyrite crystal and kaolinite-filled chambers of a cellular structure outlined by OM (organic matter) in Figure 2.4.10e. Calcium sulfate (anhydrite) was observed as filling in late-stage fractures. Pyrite is often seen to coexist with organic matter, indicating that reduction of organic matter is an important factor for its formation.



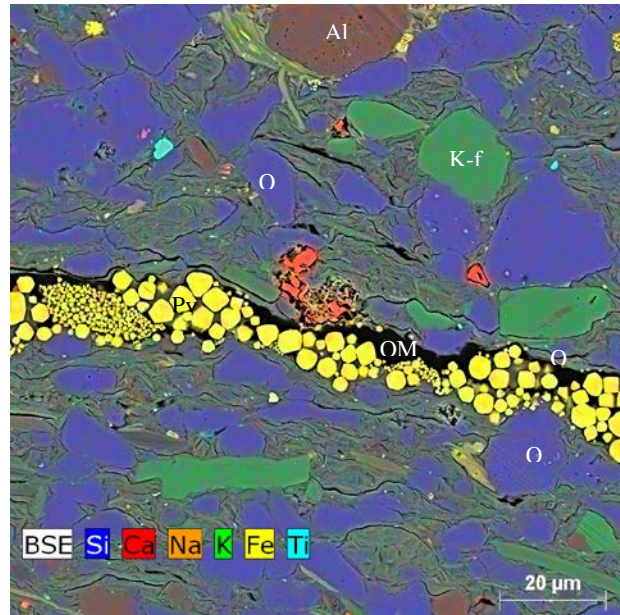
a) EDS map with false colors for elements showing silt particles of quartz (Q), albite (Al), and K-feldspar (K-f) surrounded by clay matrix. Sample from 13,100.5 ft.



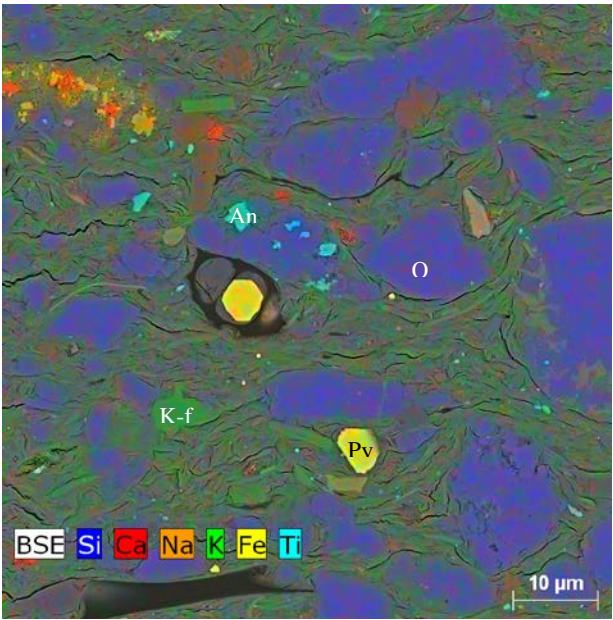
b) EDS map showing slit grains concentrated in upper part and highly aligned clays in the low half. Sample from 13,136 ft.



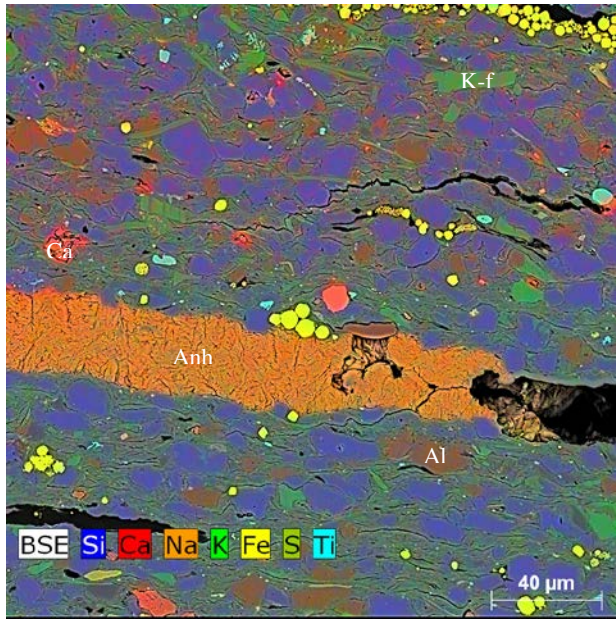
c) EDS map showing that quartz (Q) constitute a large portion of the slit-sized grains with small amounts of albite (Al), K-feldspar (K-f) and calcite (Ca). Sample from 13,136 ft.



d) EDS map showing a layer of concentrated pyrite and organic matter (OM) mixture. Clay minerals bend around large pyrite crystals, suggesting pyrite precipitation during early diagenesis. Sample from 13,136 ft.



e) EDS map showing silty claystone texture. An OM cellular structure with pyrite filled chambers (Py) and kaolinite. Sample from 13,125 ft.

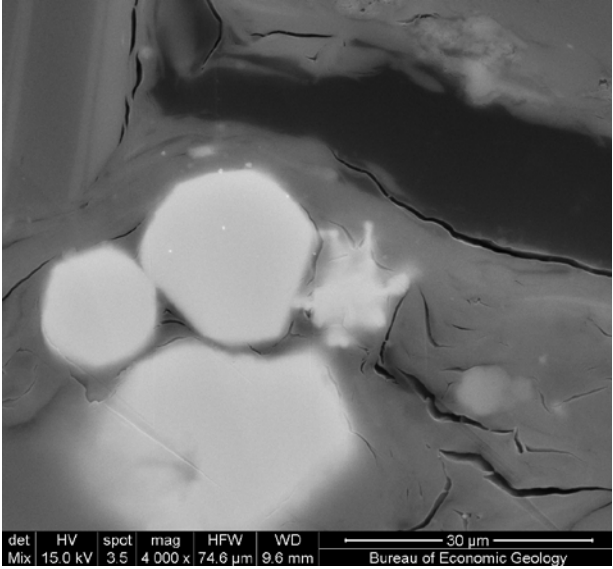


f) EDS showing anhydrite (Anh) precipitated in a fracture. Sample from 13,136 ft.

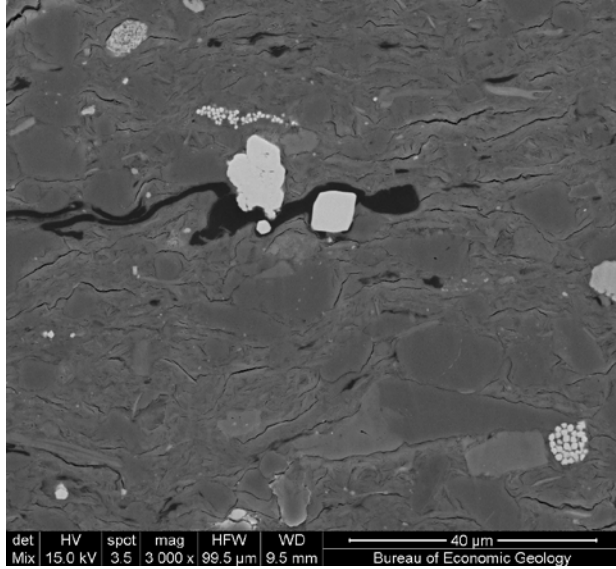
Figure 2.4.10 – SEM images and EDS elemental maps of the samples.

Organic matter (OM) content is generally low (< 2%) and variable between samples (Figure 2.4.11). The sample at 13,100.5 ft contain less OM than the other two. The dominant OM type is elongated particles up to hundreds of micrometers in length that generally follow bedding (Figure 2.4.11), and it lacks distinct shape surrounding rigid grains. It also exhibits a homogenous texture. The convoluted shape of this OM suggests a high degree of compaction. Evidence of bitumen migration is not apparent.

The samples have low porosity due to high clay content and compaction. Rare occurrences of pores are mostly associated with mineral dissolution as shown in secondary electron (SE) and backscattered electron (BSE) SEM modes (Figure 2.4.12). The majority of the observed pores are secondary pores derived from dissolution of calcite and feldspar minerals (Figure 2.4.12a-c). Porosity forming along grain edges is also often observed around calcite grains (Figure 2.4.12b). In some cases, K-feldspar exhibits partial dissolution with secondary pores generated adjacent to and within the remaining grains, suggesting that feldspar dissolution is an important source for secondary porosity (Figure 2.4.12c). Sometimes the precursor minerals were completely dissolved, and the secondary pores are mostly filled with authigenic clays and anatase (Figure 2.4.12d). Most primary pores are filled with illite, chlorite, kaolinite, and pyrite. Small intraparticle pores are present among clay platelets (Figure 2.4.12d, e); though they may not be effectively connected to the pore network.

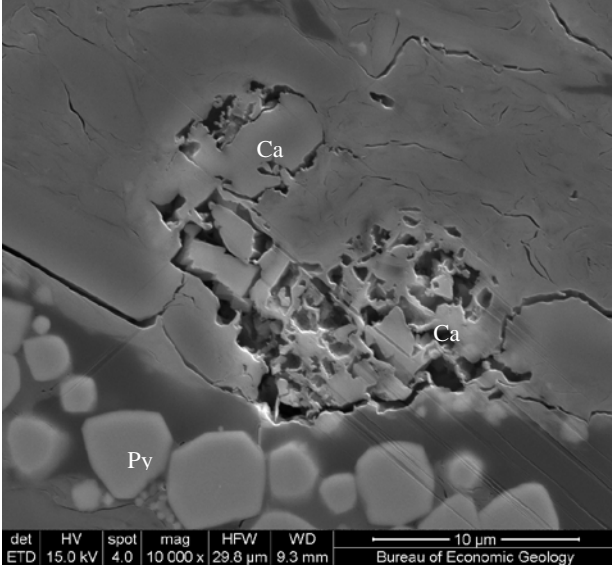


a) Combined SE and BSE image showing pyrite crystals (bright) and homogeneous organic matter (dark). Sample from 13,125 ft.

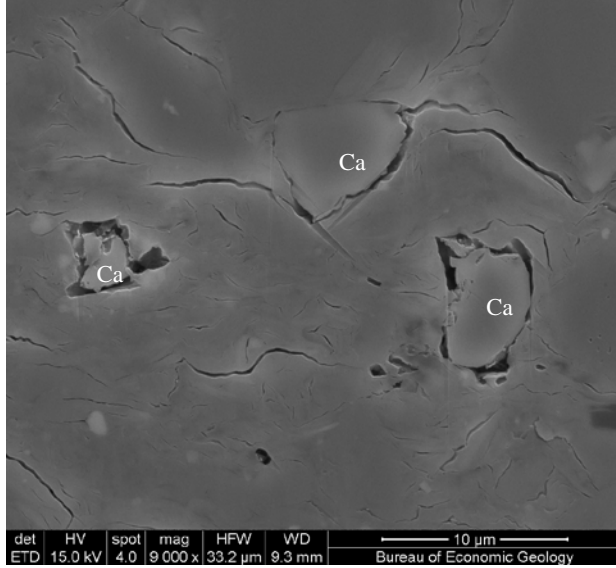


b) Combined SE and BSE image showing an elongated particle ~50 micrometer in length. It follows the bedding, lacks distinct shape and engulfs pyrite crystals (bright). Sample from 13,125 ft.

Figure 2.4.11 – SEM images of organic matter.

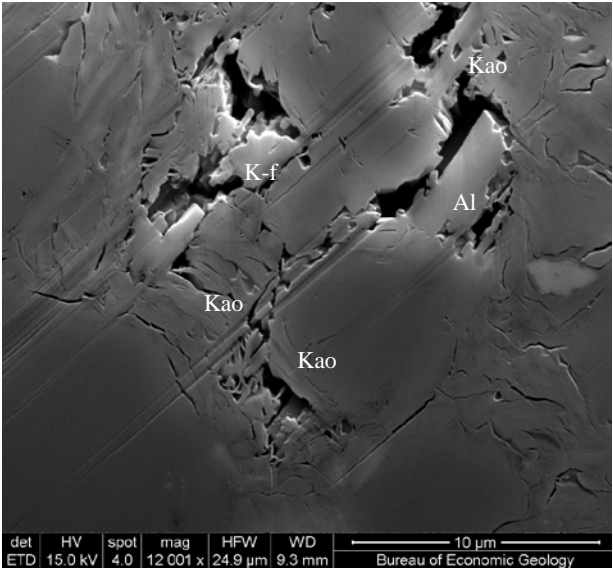


a) SE image showing partial dissolution of calcite. Sample from 13,136 ft.

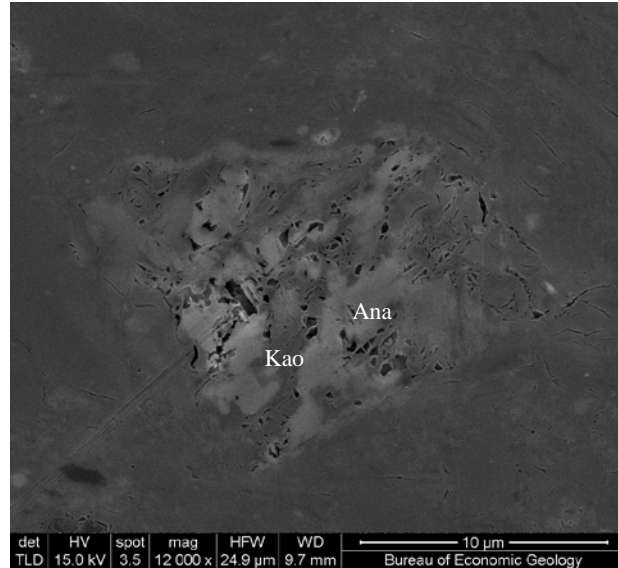


b) Grain edge pores formed when calcite grain edge dissolution occurs. Sample from 13,136 ft.

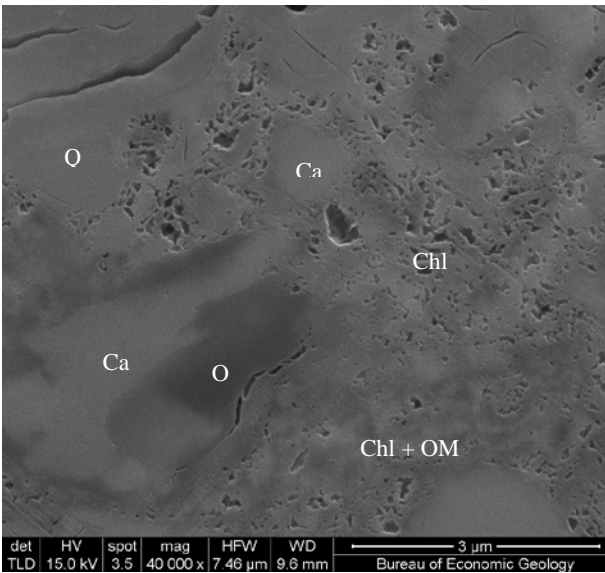




c) SE image showing a secondary pore derived from K-feldspar dissolution is now partially filled with authigenic kaolinite. Sample from 13,136 ft.



d) Pore-filling authigenic anatase and kaolinite. Small pores are still present between clay platelets and around anatase. Sample from 13,100.5 ft.



e) SE image showing chlorite (Chl) contain abundant pores. Sample from 13,125 ft.

Figure 2.4.12 – SEM images showing occurrence of pores.

Because of the scarcity of whole cores with good quality mudstone samples/intervals cuttings from four wells in South Marsh Island block were examined for their suitability for SEM work (Table 2.4.5). The wells were selected because of their proximity to large natural gas fields, Tiger Shoal and Starfak. Ultimately, only one well (OCS-G-2305 #1) provided sufficiently large chips from suitable mudstone intervals for SEM study. Four samples (7990-8020 ft, 9560-9590 ft, 9590-9620 ft, 9980-10010ft) were

examined. The cuttings of the other three wells contain small shale fragments that are not suitable for ion milling (Figure 2.4.13).

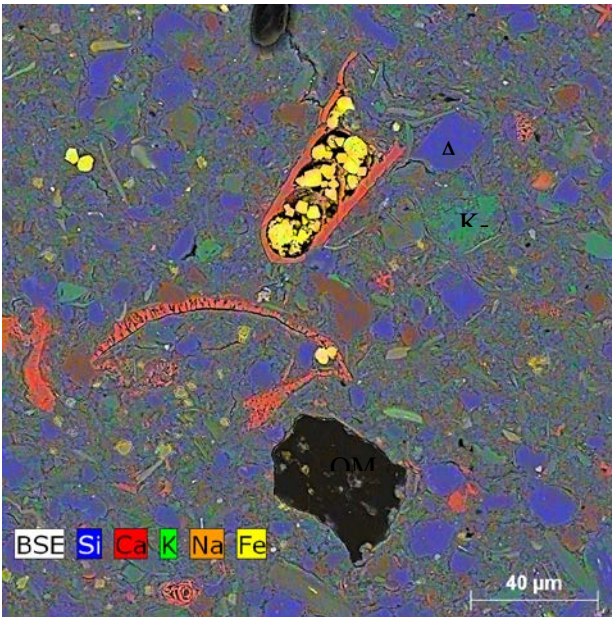
Table 2.4.5 – Four wells examined for suitability of their well cuttings to be used for SEM analyses.

UWI/API	STATE	COUNTY	Well ID	OPERATOR	LEASE	Base depth (ft)	Sample Type
17707400570000	LOUISIANA	S MARSH ISLAND BLK 260	1	OCS-G-2305	OCS-G-2305	10250	CUTTINGS
17707403910000	LOUISIANA	S MARSH ISLAND BLK 232	1	OCS-G-4435	OCS-G-4435	10500	CUTTINGS
17707402610000	LOUISIANA	S MARSH ISLAND BLK 260	A-2	OCS-G-2305	OCS-G-2305	12565	CUTTINGS
17707400430000	LOUISIANA	S MARSH ISLAND	1	OCS-G-2301	OCS-G-2301	15730	CUTTINGS

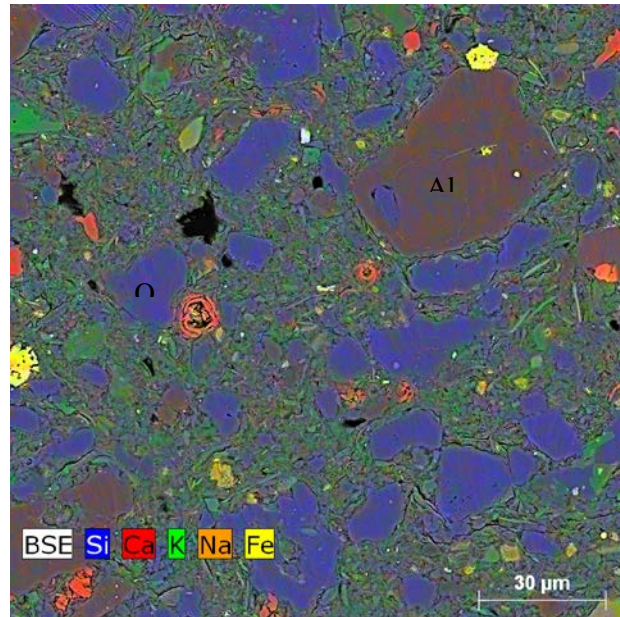


Figure 2.4.13 – Cuttings from OCS-G-4435 #1 contain small, fragile shale flakes not suitable for ion milling and SEM study.

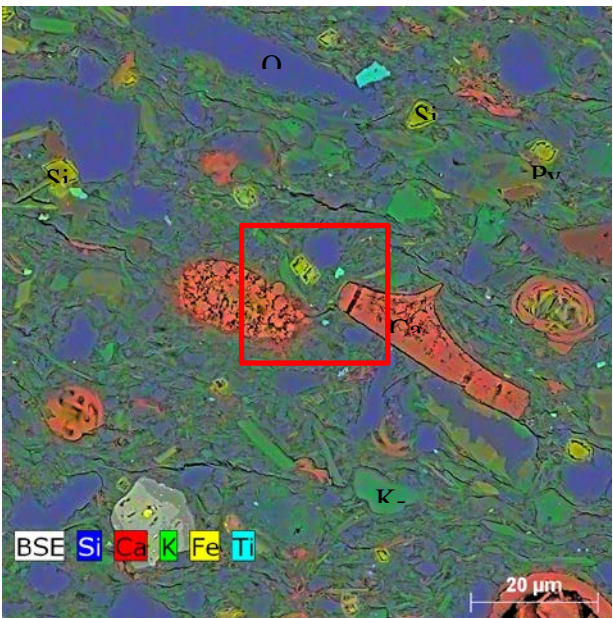
The cutting samples are generally more porous compared to the whole core samples from OCS-G-3496 A-3. Pores are mostly developed within and around carbonate minerals. The largest and predominant pores observed by SEM are primary pores in foraminifera chambers (Figure 2.4.14d) and secondary pores in calcite (shells) and siderite (Figure 2.4.14e, f). Foraminifera chambers are usually partially filled with pyrite, calcite and clays, and are mostly isolated (Figure 2.4.14a, d). Dissolution of calcite and siderite created abundant intraparticle and grain edge pores. Aggregates of shell fragments and clay over 20  $\mu\text{m}$  in size are present and contain high porosity of primary and secondary nature (Figure 2.4.14g). Matrix in these samples are probably more porous too because of the generally low abundance of clay minerals. Unfortunately, the cuttings are generally not suitable for MICP (mercury intrusion capillary pressure) analyses, which provide data regarding capillary entry pressure of  $\text{CO}_2$ .



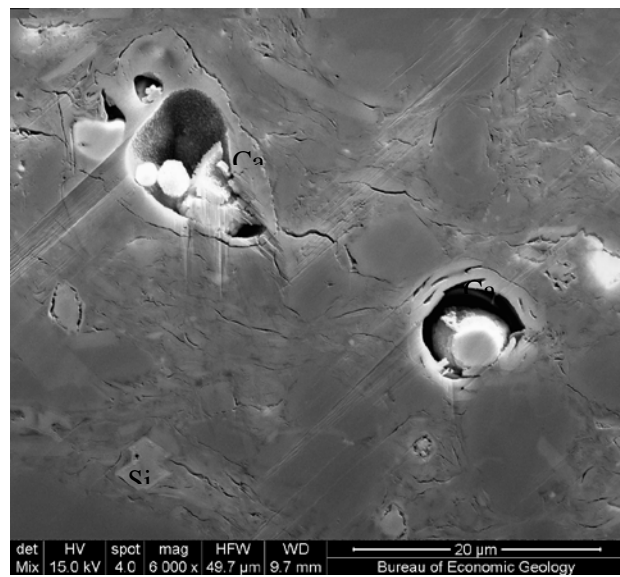
a) EDS elemental map showing the general mineral composition with large shell fragments and foraminifera. 9590-9620 ft.



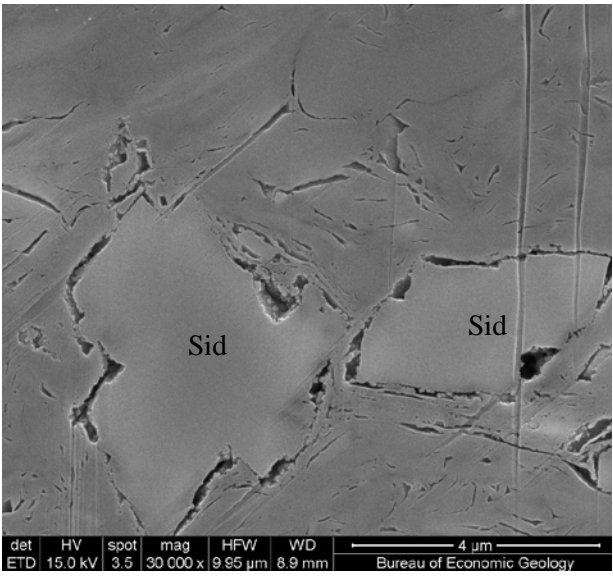
b) EDS elemental map showing silt size quartz (Q) and feldspar grains floating in clay matrix. 9590-9620 ft



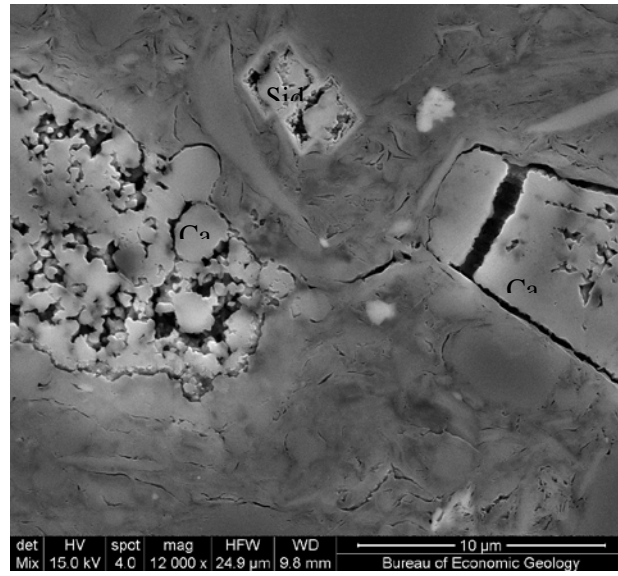
c) EDS elemental map showing shell fragment and rhombic siderite. 9980-10010 ft. See 2.4.13f for red square area.



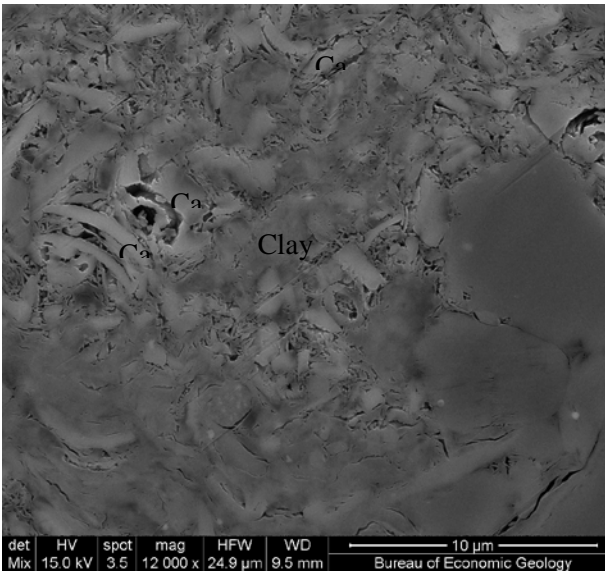
d) Mixed BSE and SE image showing two forams with chambers partially filled with pyrite. 9560-9590 ft.



e) SE image showing grain edge pores around siderite rhombs. 7990-8020 ft



f) Mixed BSE and SE image showing secondary pores in calcite and siderite. 9560-9590 ft.



g) Mixed BSE and SE image showing an aggregate of shell fragments and clays with high primary and secondary porosity. 9590-9620 ft.

Figure 2.4.14 – SEM images and EDS elemental maps of cutting samples from well COS-G-2305 #1.

### *XRD Mineral Composition Analysis of Whole Core Samples*

Nine samples from two wells (OCS-G-3496 #A-3 and OCS-G-4392 #C-4) in the West Cameron OCS (federal offshore continental shelf) were prepared and analyzed on an X-ray diffractometer at The University of Texas at Austin. Quantitative analysis of mineral composition was performed on randomly oriented powder samples prepared from the mudstone core pieces.

#### **Method**

Bulk powders of the original and reacted rock samples for XRD were prepared by means of wet grinding and spray drying. The samples were first disintegrated using a TEMA ball mill before further grinding in a McCrone Micronizing Mill. The samples were ground for 9 minutes in 0.5% (wt./vol) aqueous solution of polyvinyl alcohol to reduce particle size to less than 10  $\mu\text{m}$ . The resultant slurry samples were sprayed from the top of a spray drier and dried. The droplets of randomly oriented powders were collected on a large paper at the bottom of the spray drier. Subsequently, x-ray diffraction analysis was conducted on a Bruker AXS D8 diffractometer. The powder samples were scanned from 4° to 70° 2 $\theta$ , at a scan rate of 1.5 s per 0.015° step with Cu K $\alpha$  radiation. Bruker's Eva software was used to identify mineral phases. Quantitative analysis was conducted using Topas 3, a personal computer software based on the Rietveld method (Bish, 1994). Quantitative phase analysis results from this method are accurate to within 2% absolute error (Hillier, 1999).

#### **Results**

As shown in Table 2.4.6, the samples all have similar mineral compositions. They contain greater than 50% clays with total clay abundance varying from 50 to 60%. Clay minerals are dominated by illite, which is over 30% in all the samples. Chlorite is the second most abundant clay at 14-18% and kaolinite is less than 5%. Quartz abundance in the samples ranges from 20% to 31%; the combination of plagioclase and K-feldspar varies between 9% and 18%. Calcite is the predominant carbonate mineral, up to 7%; although, trace amounts of siderite and dolomite may exist in the OCS-G-3496 well. The OCS-G-4392 well contains 0% to 1% calcite. Small amounts of anatase and pyrite exist in both wells. Additionally, 1-2% Anhydrite was found in the OCS-G-3496 well. The main mineralogical differences between the two wells' samples are the existence of anhydrite in the first well and low calcite content in the second well. Overall, the mudstone samples from the two wells are mineralogically very similar.

Table 2.4.6 – XRD mineral composition of mudstone core samples from two well in West Cameron Block, Louisiana.

Well	Depth (ft)	Quartz	Calcite	Plagioclase	K-feldspar	Illite	Kaolinite	Chlorite	Anatase	Pyrite	Anhydrite	Siderite	Dolomite
OCS-G-3496 #A-3	12954.2	21.4	7.1	4.8	7.9	34.8	4.2	16.0	1.8	0.5	1.2		0.4
	12975.5	22.4	2.9	2.1	7.0	40.2	4.2	16.7	1.6	0.6	1.1	1.3	
	12984.9	19.7	6.1	2.7	9.1	37.2	3.6	17.4	1.5	0.6	1.9	0.3	
	12999.5	20.8	3.4	2.6	8.4	41.3	3.5	16.3	1.5	0.7	1.7		
	13050	26.8	4.2	5.7	10.8	31.7	3.4	14.0	1.3	0.4	1.7		
	13060.5	24.1	3.4	4.9	11.7	35.6	2.6	14.3	1.3	0.4	1.7		
OCS-G-4392 #C-4	13100.5	31.3	0.2	3.4	9.3	35.2	2.8	14.9	1.4	1.5			
	13125	29.8		5.2	8.4	33.5	2.5	17.9	1.9	1.0			
	13136	29.1	1.4	6.1	12.8	29.3	2.1	16.7	1.5	1.0			

## Mercury Intrusion Capillary Pressure

Pore systems and capillary properties of 7 samples from well OCS-G-3496 #A-3 (Table 2.4.7) were characterized using high-pressure MICP measurements conducted by PoroTechnology in Kingwood, TX. All samples were dried at ~100°C prior to MICP tests. Mercury injection pressure was increased in a stepwise manner, and the percentage of rock volume saturated by mercury at each step was recorded, after allowing sufficient time for equilibrium to be established. Mercury intrusion curves were obtained with increasing pressure to ~414 MPa (60,000 psi). MICP permeability was calculated using the following equation (Swanson, 1981):

$$K_{Calc.} = K_{air} = 399(S_b/P_c)_{max}^{1.691} \text{ (md)}$$

where  $S_b$  (mercury saturation) is the maximum value of the ratio of mercury saturation/mercury capillary pressure in pounds per square inch absolute (psia).

### Samples

Table 2.4.7 – Mercury intrusion capillary (MICP) tests' porosity and permeability for mudstone samples from OCS-G-3496 #A-3 well.

Sample Depth (ft)	Porosity (%)	Calculate Permeability (md)	Bulk Density (g/cc)	Grain Density (g/cc)
12954.2	10.82	0.000866	2.40	2.69
12966.8	10.19	0.000754	2.15	2.40
12975.5	10.00	0.000947	2.29	2.55
12984.9	11.93	0.001115	2.29	2.61
12999.5	11.41	0.001049	2.36	2.66
13050	9.77	0.001211	1.93	2.14
13060.5	9.57	0.001502	2.38	2.63

### MICP Results

The MICP porosity and permeability of the mudstone samples do not show significant differences. MICP results show that porosity of the mudstone samples ranges narrowly from 9.6% to 12.0% (Table 2.4.7). The measured porosity is consistent with previously reported SEM observations (see previous quarterly reports). Permeability calculated from mercury intrusion curves also shows small variations between 0.0008 and 0.0015 mD. Figure 2.4.15 shows the relationship between porosity versus permeability of the samples.

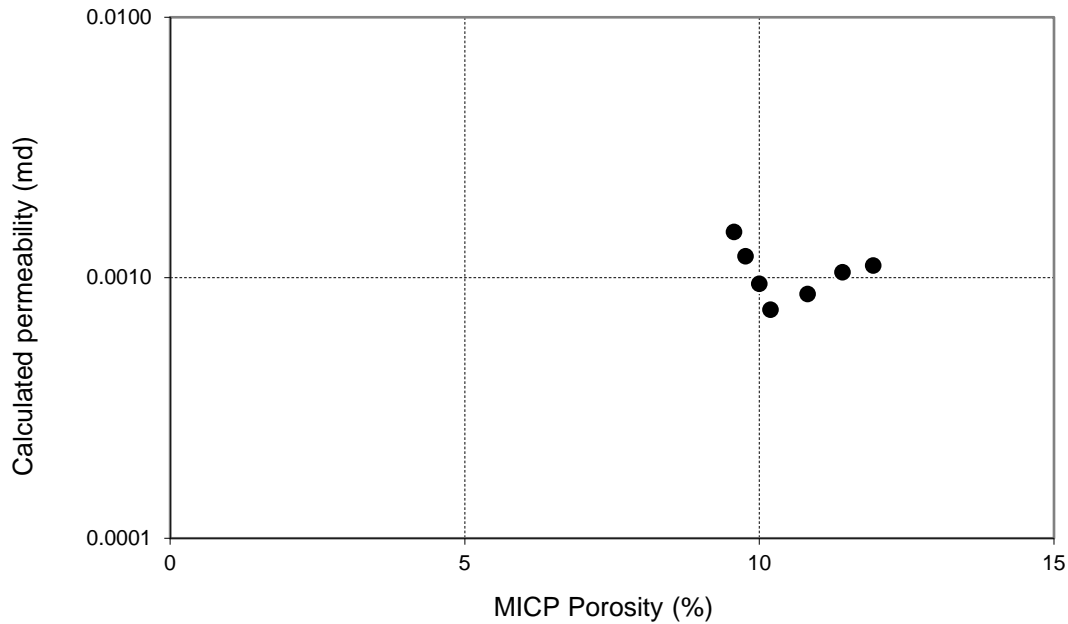


Figure 2.4.15 – Graph of porosity vs. permeability of mudstone samples measured in mercury intrusion capillary pressure tests.

Figure 2.4.16 shows pore throat size distribution of the tested samples. The samples have similar modal pore throat sizes between 0.016 and 0.027  $\mu\text{m}$ . However, the samples show differences in pore throat size distribution. In Figure 2.4.16, the deeper samples appear to contain higher proportions of large pore throats as manifested by their broader pore throat distribution curves. For example, the two deepest samples (13050ft and 13060.5ft) show the widest pore throat distribution curves as they contain larger pore throats up to  $\sim 0.1$  and  $\sim 0.2$   $\mu\text{m}$ . The shallowest sample (12954.2 ft) does not exhibit a significant proportion of pore throats over 0.036  $\mu\text{m}$ . Such a variation in pore size distribution is also reflected in calculated permeability, which shows the deeper samples progressively have higher permeability (Table 2.4.7). Permeability is apparently not controlled with porosity because porosity is lower in the deeper samples; rather, it is controlled by the pore throat size distribution (i.e., higher proportion of larger pore throats results in higher permeability).



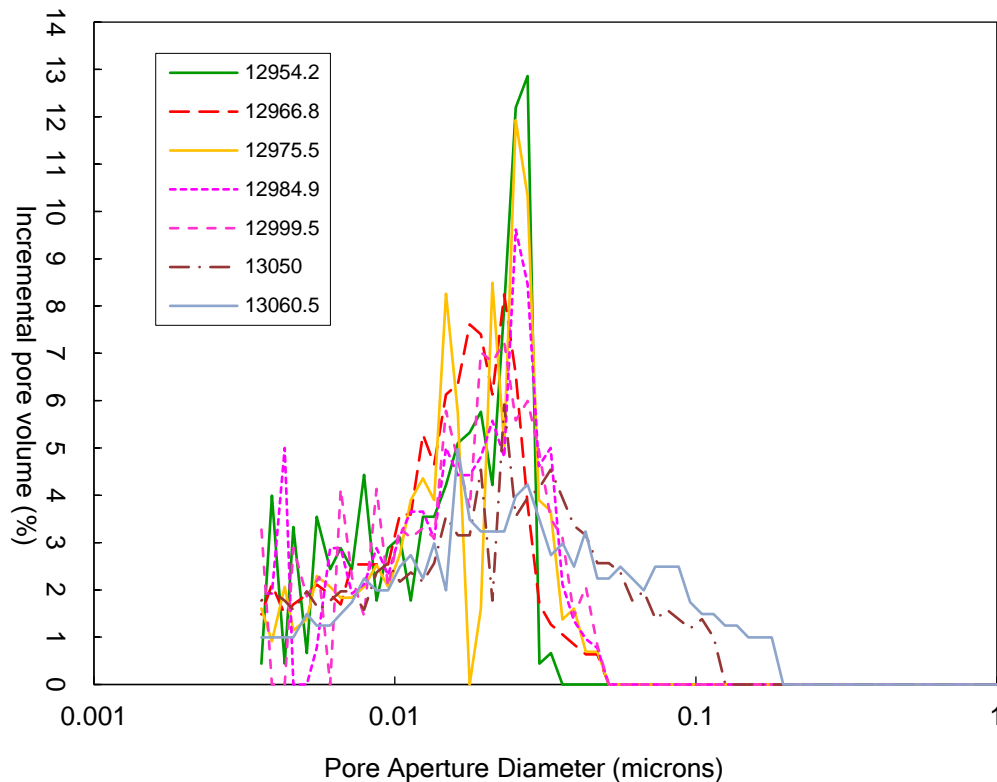


Figure 2.4.16 – Pore-throat-size distribution (incremental pore volume vs. pore aperture diameter) of the mudstone samples from mercury intrusion capillary pressure tests.

### Conclusions

The petrographic and petrophysical results from the core materials suggest consistently good sealing quality of the Miocene mudstone intervals in the West Cameron wells. Porosity is around 10%, more importantly, permeability is low, around 0.001 md. Most mudstone samples are silty claystone with over 50% of clay minerals. Compaction of the abundant clay matrix has largely eliminated the primary pores. The remaining primary pores, generally sub-micron in size, are isolated by the highly-compacted matrix and not connected to the flow path. Secondary pores from mineral dissolution are mostly filled by authigenic minerals, though the partially filled secondary pores are generally larger in size. Pore throat size distribution of MICP tests show modal pore throat size between 0.016 and 0.027  $\mu\text{m}$  for the West Cameron samples, sufficiently small for providing high sealing ability. As a result, the mudstone samples are able to retain a CO<sub>2</sub> column height of 52-309 m.

The cuttings from South Marsh Island area contains relatively higher silt and lower clay contents, but the mineral composition is similar to the West Cameron samples. The cuttings are generally more porous. Pores are mostly developed within and around carbonate minerals which are slightly more abundant in this well. Primary pores in foram chambers and secondary pores in fossil fragments are among the largest pores. Grain edge pores around carbonate grains are also developed. Overall, the mudstone unit of the South Marsh Island well are siltier and more porous than the West Cameron counterparts and will have lower sealing ability. However, the mudstone seals in this area are still sufficiently tight as suggested by the presence of the large gas fields, such as Starfak and Tiger Shoal.

The results show that the mudstone intervals of the Lower Miocene in the West Cameron area are consistent in terms of petrographic and petrophysical properties through the depth of investigation. The sealing

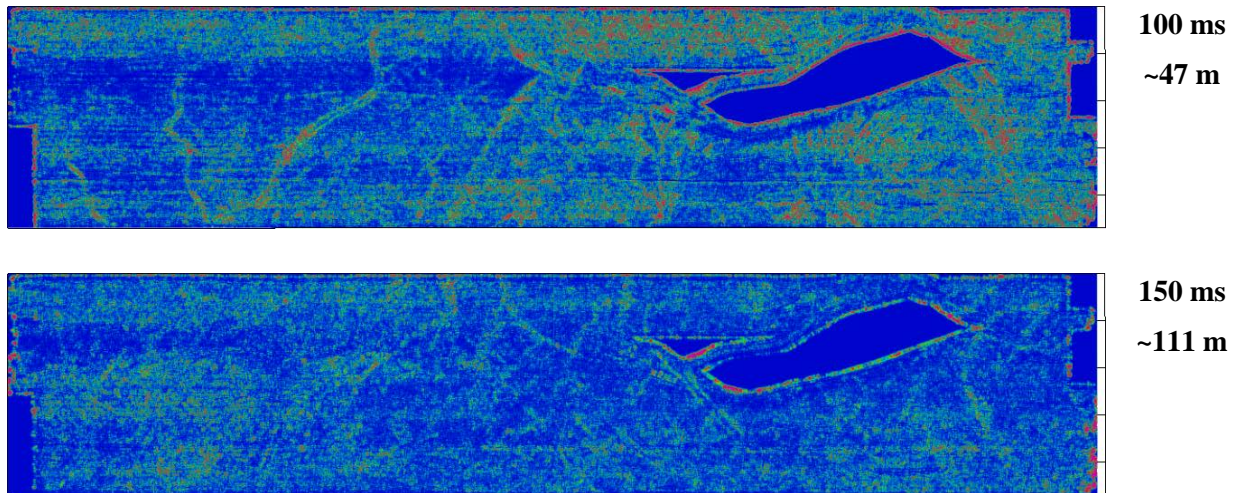
performance should be excellent for the studied intervals.

## **2.4 B. Macro-Scale Seal Properties: Seismic Analysis of Overburden**

In addition to analyzing core samples from seal intervals, the availability of a previously acquired P-Cable high resolution 3D seismic dataset (HR3D) in the project study area provided the opportunity to investigate the macro-scale properties of the geologic overburden including potential seal and non-seal facies, shallow structure and potential natural fluid flow (migration) pathways.

In order to analyze potential fluid pathways in the HR3D dataset, a technique known as diffraction imaging was tested. Diffraction imaging is a seismic imaging technique that operates with waves scattered by geologic heterogeneities such as faults and fractures. This method is often presented as a high-resolution approach. Indeed, diffraction image resolution exceeds resolution of conventional reflection seismic; however it is defined and limited by frequency content of input data. HR3D (a.k.a. “P-Cable”) seismic data have extremely wide frequency bandwidths. In combination with diffractions, these data can provide highly accurate location and characterization of faults and fractures. The end result should be more confident interpretation of vertical dislocations (e.g., along faults) in the area. Such dislocations could function as fluid migration pathways. The technique may also provide more confident fracture evaluation, which could yield more robust porosity and permeability models.

Initial work involved constructing a diffraction imaging time domain volume within the time interval from 75 to 350 ms (milliseconds). The interval corresponds to a depth interval of 35-325 m (Figure 2.4.17). The diffraction image is interpretable at specific time levels (i.e., time slices). In particular, the slice at 100 ms (Figure 2.4.17) displays what are interpreted as channelized features. A number of faults are also apparent on every time slice. The time slice at 200 ms is very interesting in that it displays alternating areas of high diffraction energy and relatively quiet (low diffraction energy) zones. Based on previous interpretations of similar features in other datasets, this high contrast in diffractivity may be associated with relatively higher fluid saturation in the high diffractivity areas. Note that the high-diffractivity area is not evident in conventional time-migrated image (Figure 2.4.18, bottom). In that case, the area is spread over several layers that could be interpreted as a sequence of different rock facies.



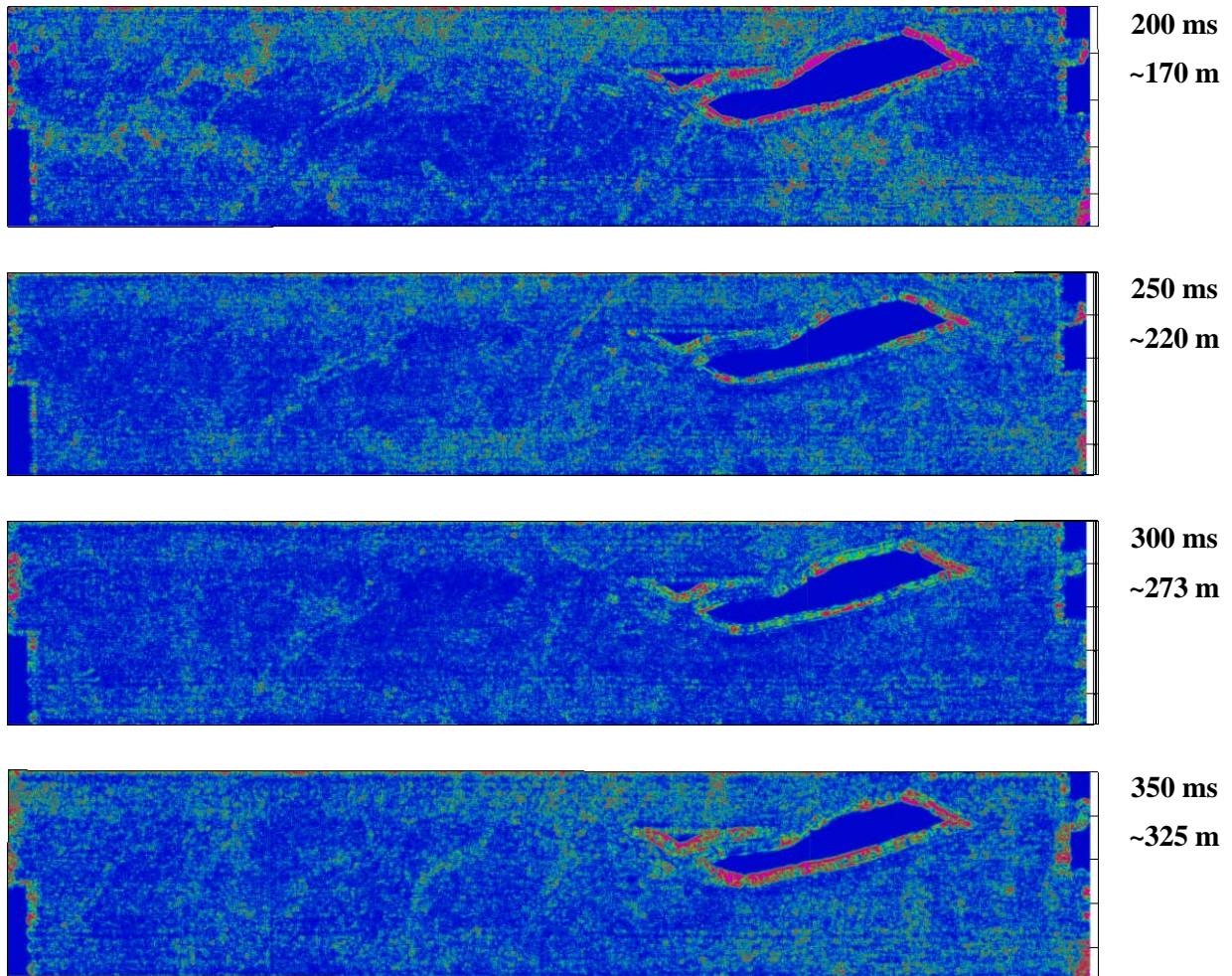


Figure 2.4.17 – Time slices through the diffraction energy attribute volume. Note that the interval corresponding to a time of 200 ms displays areas of high diffraction energy alternating with low diffraction energy zones. This high contrast may indicate fluid saturation in the high-diffraction areas.

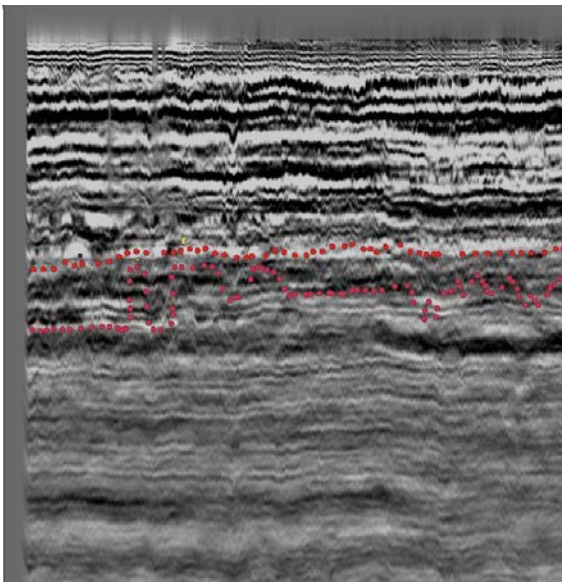
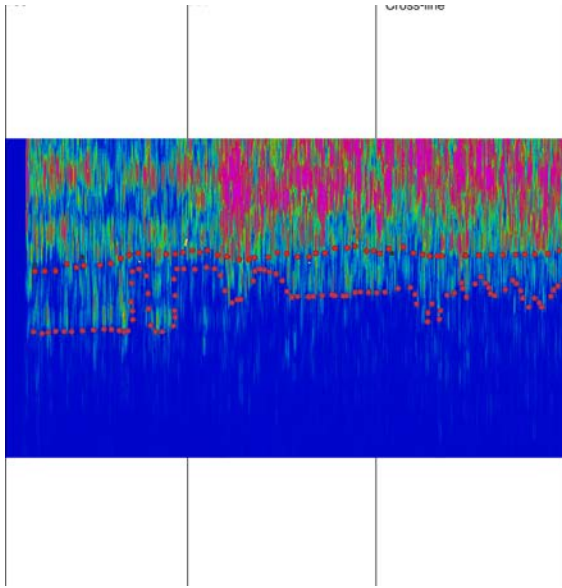


Figure 2.4.18 – Diffraction energy attribute section (top) and time-migrated conventional section (bottom). The red dots outline an area which has high diffractivity. This may be associated with fluid saturation. Note that the strong-diffraction area is not evident in the conventional seismic image (bottom).

Eventually, the diffraction imaging volume was limited to depths above 275 m due to data quality. Seismic interpretation revealed that diffraction energy was not distributed evenly across the section. Several intervals with variable diffraction strength were recognized.

Strongest diffractions were located in the upper part of the analyzed section in which multiple channel features were inferred. These strong diffractors were concentrated along depth intervals characterized by reduced electrical resistivity in nearby wireline well logs (Figure 2.4.19) that allowed associating them with brine.

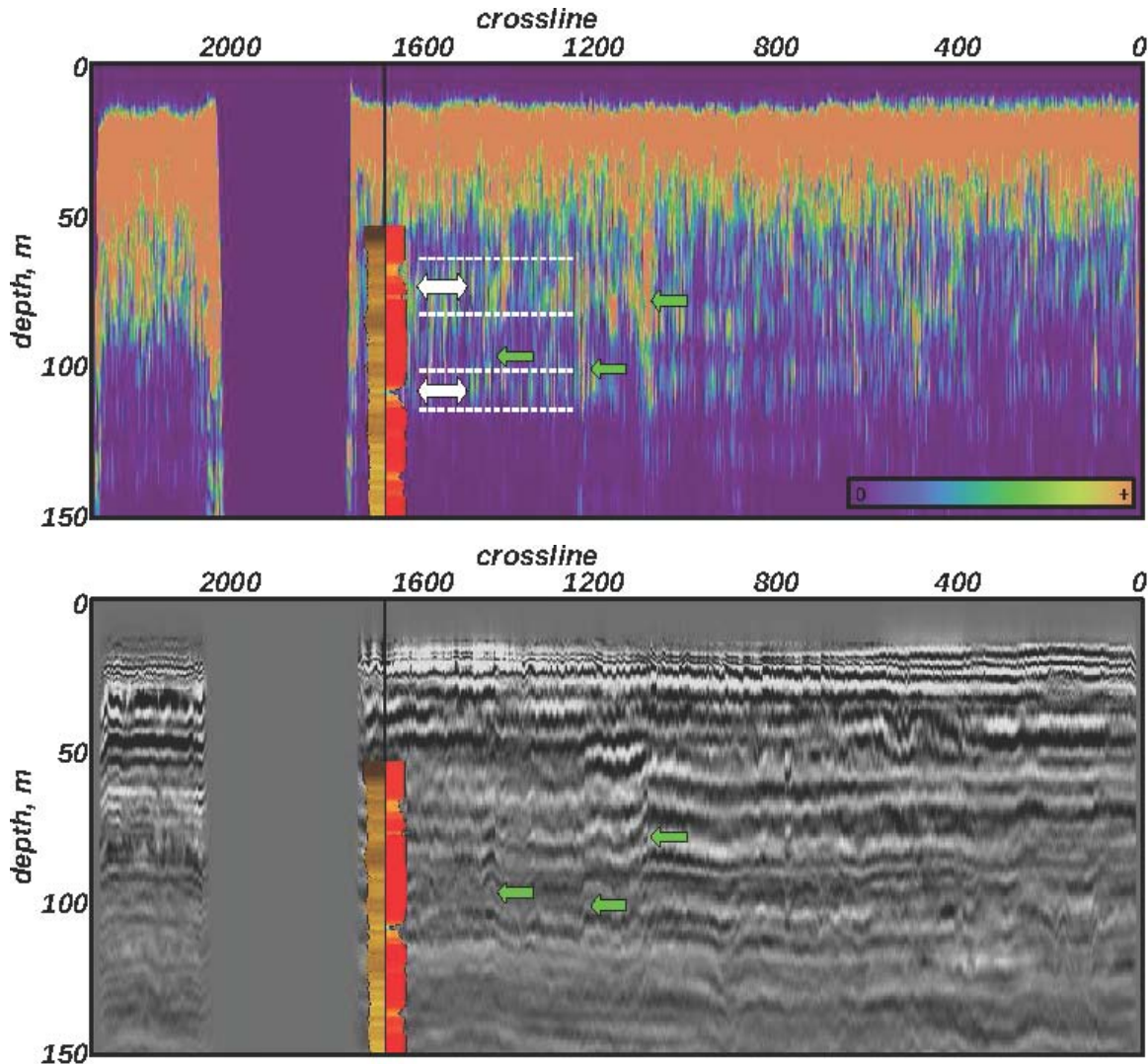


Figure 2.4.19 – Depth domain transect of an inline showing the diffraction energy attribute (top) and the conventional seismic image (bottom). The sections are overlaid by borehole logs (near crossline 1600): spontaneous potential log (left, dark colors indicate more shale content) and electrical resistivity log (right, mostly red color). White arrows in the diffraction energy section indicate two high-diffraction intervals, which correlate with resistivity decrease in the well log. Green arrows show faults connecting those two intervals. The shadow area at crossline 1800 is a data gap that was caused by the need for the HR3D survey acquisition ship to avoid an oil production platform.

With increasing depth, diffraction energy significantly decreased and displayed uneven lateral

distribution. Nonetheless, Figure 2.4.20 exhibits two high-diffractivity anomalies extending vertically and laterally (white dashed lines). We interpret the high-diffractivity anomalies as hydrocarbon migrating from underlying reservoirs because of 1) laterally extensive sub-horizontal strata and inferred lateral continuity of lithologic properties in conjunction with 2) high electrical resistivity of correlative the strata in wireline well logs of nearby wells. In addition, we observe faults in the area as indicated by green arrows in Figure 2.4.20 and accompanying fractures.

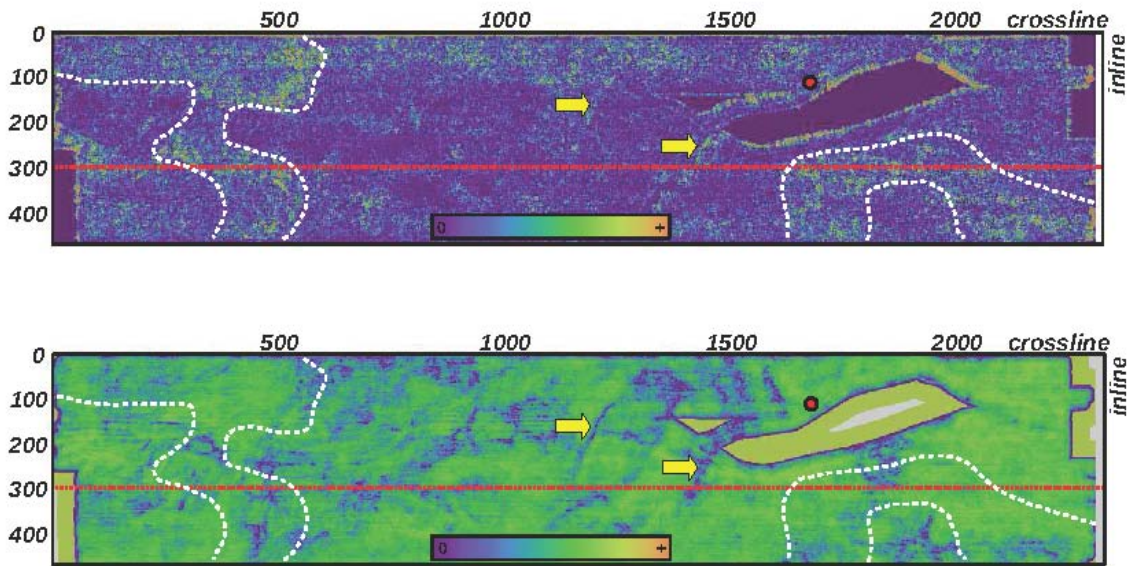


Figure 2.4.20 – Depth slices from 165 m for the diffraction energy attribute (top) and similarity (a.k.a. continuity) attribute (bottom). White dashed lines indicate the boundary between the high-diffractivity and low diffractivity zones. Yellow arrows indicate faults on which two attributes correlate well. Red dot locates a well in which the wireline logs were recorded. Note the data gap area in the upper center-right portion of the survey next to the well.

The hypothesis is that the diffraction volume can better image or validate natural fluid migration in the overburden versus using an amplitude volume alone. The amplitude volume alone displays no obvious active fluid migration (gas chimneys). Analysis of the diffraction volume indicates that the hypothesis has merit.

In order to further test the hypothesis, diffraction imaging was performed on another HR3D dataset located offshore San Luis Pass, Texas (approximately 50 miles southwest of the Bolivar dataset). The San Luis Pass HR3D dataset documents a prominent gas chimney system on an amplitude volume; whereas, a conventional 3D dataset covering the same geographic area and geologic section did not image the gas chimney.

An input HR3D stack volume indicated gaps elongated in the inline direction (Figure 2.4.21). The gaps were corrected using signal processing procedures: slope estimation and data interpolation. Subsequently, the data were migrated using the velocity model developed for the Bolivar data. The two HR3D surveys

were located close enough (50 miles) suggest reasonable migration result. The diffraction volume was constructed in the time domain for time interval 0 - 350 ms. To facilitate interpretation, the diffraction volume was transformed to a diffraction energy attribute volume.

The diffraction volume is consistent with standard seismic attributes (Figure 2.4.22). The gas chimney system exhibits a strong anomaly in the diffraction energy volume. This observation confirms observations of diffractions in the Bolivar dataset, which were interpreted as indicating the presence of gas migration. The gas migration, in turn, suggests poor seal quality in the underlying cap rocks of related portions of the Bolivar HR3D dataset's coverage area.

In summary, analysis of diffraction energy associated with the San Luis Pass gas chimney has improved confidence in the interpretation of active fluid migration in the Bolivar Peninsula HR3D dataset and thus provides higher confidence for using diffraction seismic techniques where fluid migration is not as easily identifiable using standard seismic attributes.

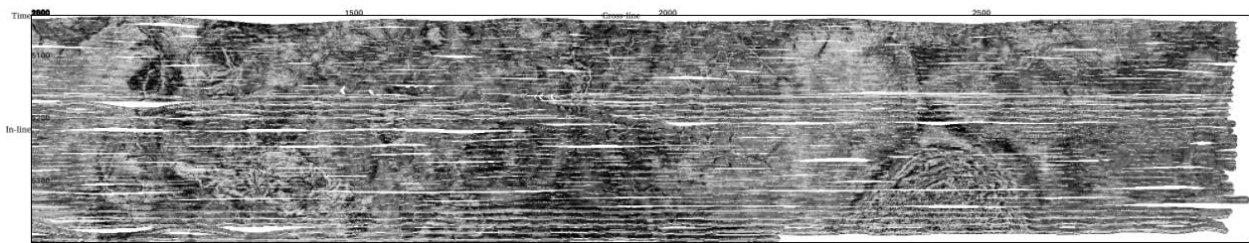


Figure 2.4.21 – Time slice for input stack volume. The data appear with many gaps.

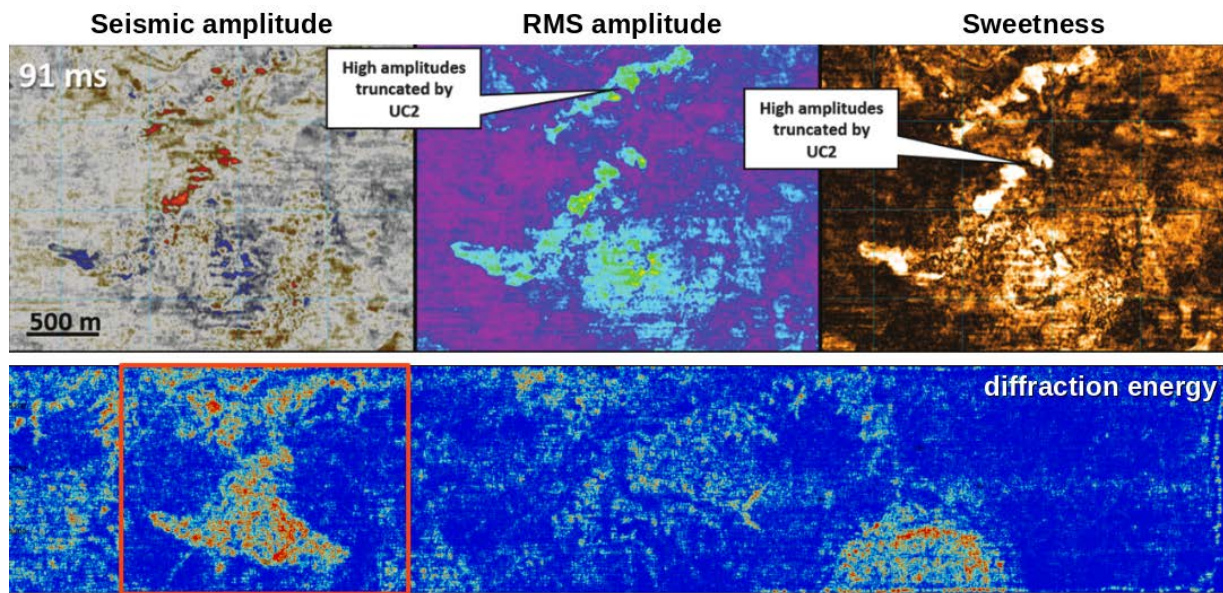


Figure 2.4.22 – Seismic attributes (top) compared with diffraction energy (bottom). The gas chimney system area (red outline rectangle) appears as a strong source of diffraction waves.

## 2.5 Subtask 2.5 – Analyze CO<sub>2</sub> Prospect Categories

In order to better understand reservoir facies and determine depositional systems, whole cores are described and interpreted wherever possible. Whole cores record vertical facies associations (lithology, grain size and physical and biological sedimentary features) that can provide key information, which may be extrapolated to wireline well logs and their stacking patterns. Consequently, core descriptions are integrated with well-log analysis to test the lateral continuity of sedimentary facies and coeval depositional systems.

Four potential wells were identified offshore Texas and onshore Louisiana (Figure 2.5.1). Unfortunately, three of them were either poorly consolidated, only cuttings or no longer available in our whole core collection. Well Vastar Resources SL 59455 (API 42708303160000) in High Island Block 24 had only 4 boxes (8,401-8,431 ft.) of unconsolidated shale fragments (Figure 2.5.2; red dashed line) mostly covered in plastic (Fig. 5). Miami Corp. well (17023226220000) in Cameron, Louisiana (7,410-16,358 ft) comprised only cuttings. The cored interval (10,320-10,413 ft) in E. M. Watkins #59 (171132160800) well in Vermilion, Louisiana was no longer in our storage facility (i.e., returned to a private company). Fortunately, a core (approximately 21 ft) encompassing interval 10,721-10,748, (just below MFS 10 (Figure 2.5.2)) from an Atlantic Richfield well in High Island (Figure 2.5.1) was available and used to interpret its depositional system (Figure 2.5.3). Despite an intensive search, to date, in the study area and specifically for the interval of interest (MFS 9 to MFS 10), only the core from the Atlantic Richfield OCS G10266 has been available and of sufficient quality to be useful for the current project.

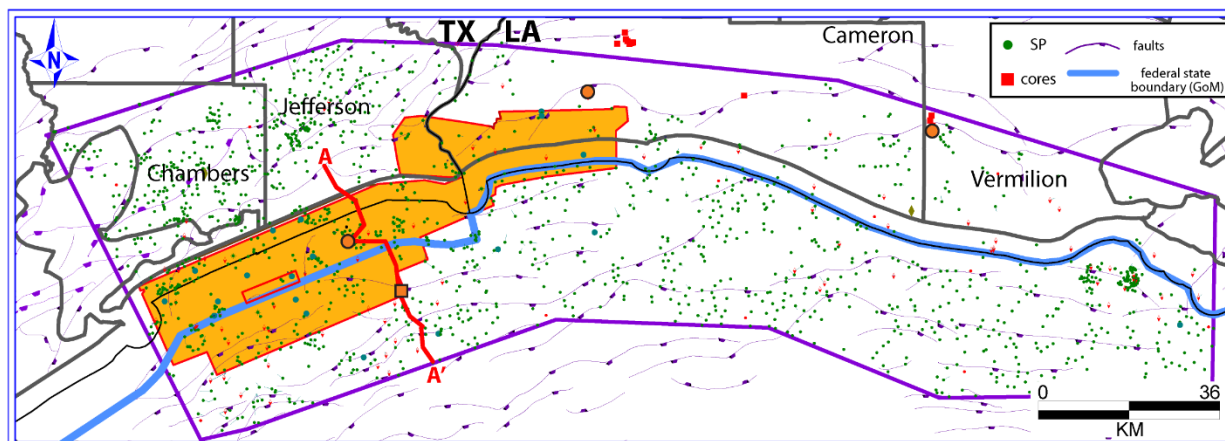


Figure 2.5.1 – Map of the study area showing wells and the primary 3D seismic dataset, “TexLa Merge” (highlighted in orange) The state - federal waters boundary is demarcated by the blue line subparallel to the coast (note that Texas state waters are wider than those of Louisiana).

Approximately, 21 ft of cored interval from an Atlantic Richfield OCS G10266 (API 427084032600) well (orange square), High Island Block, Texas, were described for interpretation of depositional environments. The sandstone is apparently structureless or shows over-steepened laminations and contorted bedding interpreted as being deposited as a result of storm-induced liquefaction on the delta front due to syn-sedimentary deformation in response to rapid deposition and loading. The core comprises very fine-grained, structureless sandstone (Figure 2.5.4A) alternating with parallel laminated sandstone (Figure 2.5.4B) in a slightly fining-upward succession. Soft sediment deformation structures including high angle over-steepened to vertical stratification. Convolute bedding and micro-faults are common (Figure 2.5.4C). Toward the top of the cored interval thinly interbedded sandstone (cm) and mudstone (mm) with micro-faults are present (Figure 2.5.4D). The laminae accentuated by finely comminuted organic detritus and some double mud drapes are present suggesting some tidal influence.

Low angle parallel to undulatory laminations are interpreted as hummocky cross stratification. The



oversteeped stratification is interpreted as the result of very high rates of deposition associated with storm events. Altogether, the facies of the core indicate that the sediments were deposited in a storm-wave dominated deltaic depositional environment.

Locations of three other wells considered, but for various reasons, not examined are shown in orange circles (Figure 2.5.1). A dip well cross-section passing through two of the cored wells is indicated by the red line of section in (Figure 2.5.1).

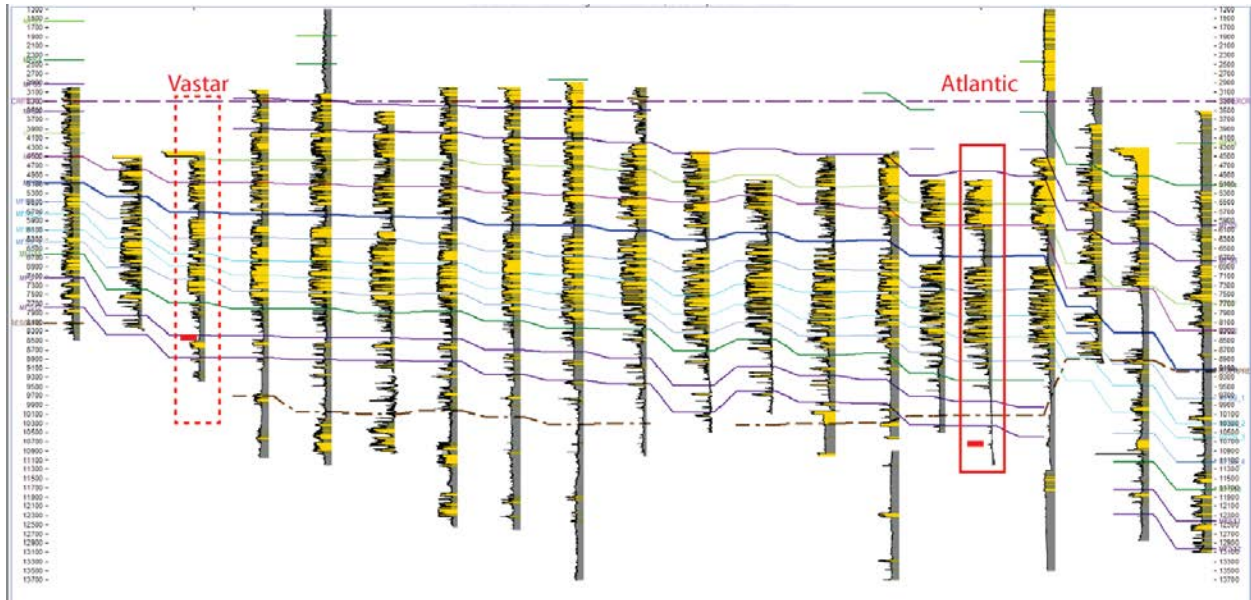


Figure 2.5.2 – Dip-oriented structural well log cross-section (AA' in Figure 5.1) including two wells with cores from the Miocene section. Multiple normal faults offset the stratigraphy (purple lines in Figure 5.1). Cored intervals from the Atlantic Richfield OCS G10266 and Vastar Resources SL 59455 (Figure 2.5.5) wells in High Island are highlighted in red.

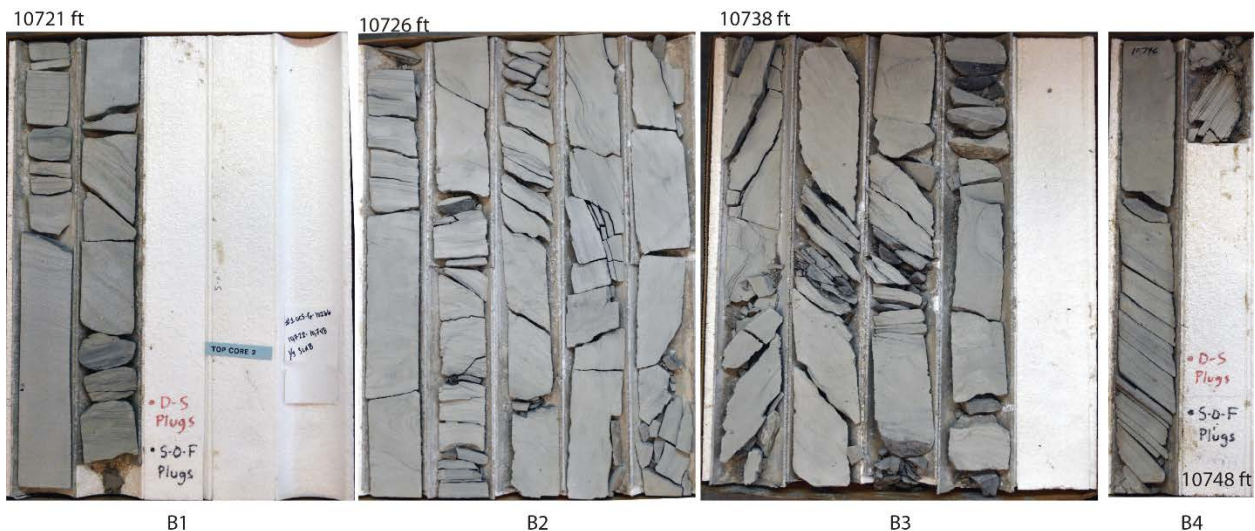


Figure 2.5.3 – Core photographs from the Atlantic Richfield OCS G10266 well — High Island — a sandstone dominated interval (each core sleeve is about 60 cm long and 7 cm wide; the stratigraphic top is the upper left corner).

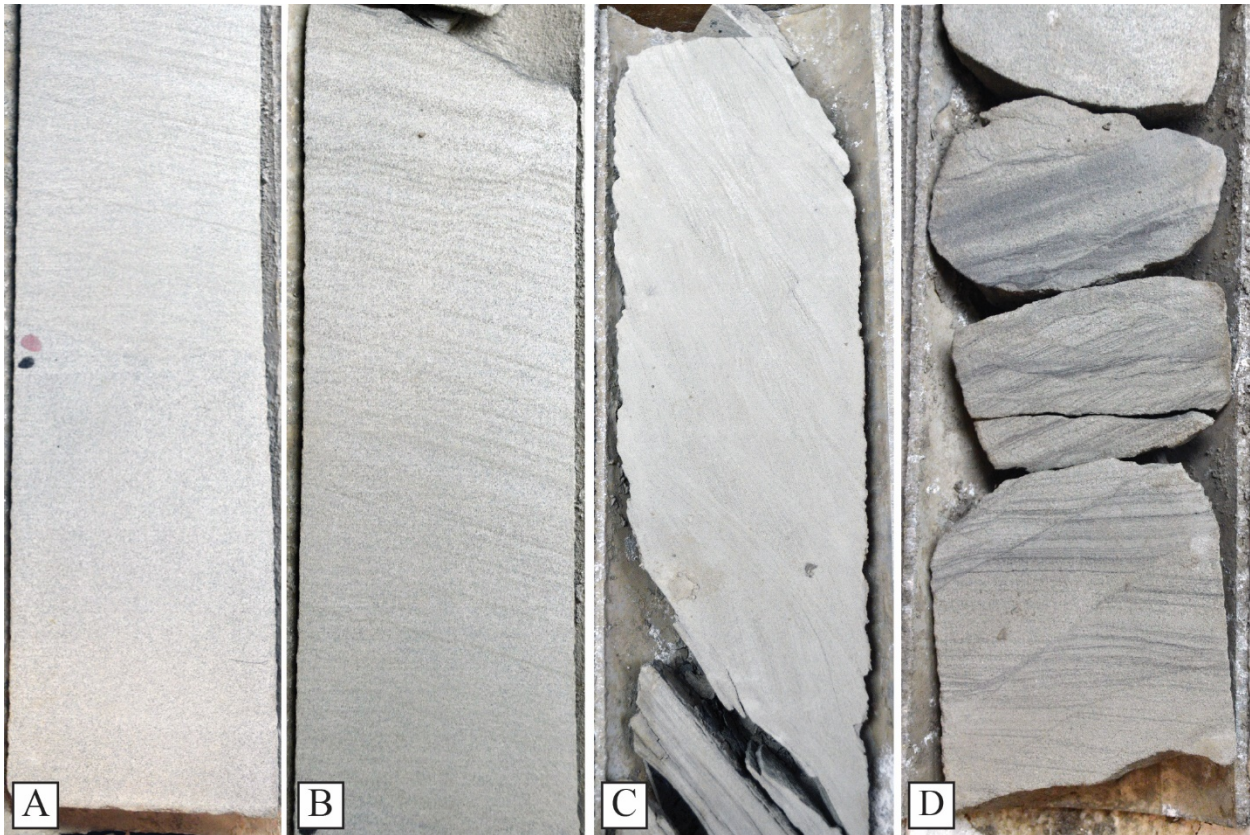


Figure 2.5.4 – Close-up photo of Atlantic Richfield OCS G10266 (API 427084032600) well’s core; each core photograph is 7 cm wide. (A) Very fine-grained structureless sandstone passing upward into slightly parallel laminated sandstone. (B) Low angle parallel to undulatory laminations in very fine-grained sandstone; laminae accentuated by mud drapes (note micro-fault at the top of the photo). (C) Deformed sandstone showing nearly vertical dip to the original laminae. (D) Thinly interbedded sandstone and mudstone with micro-faults; laminae accentuated by finely comminuted organic detritus (some double mud drapes are present).

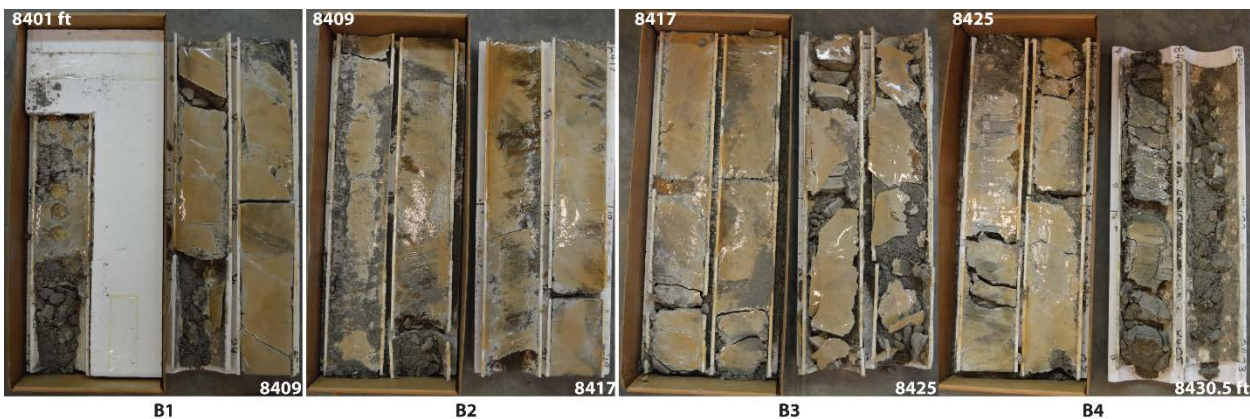


Figure 2.5.5 – Core photographs from Vastar Resources SL 59455 (API 42708303160000) well — High Island — showing a mudstone dominated interval (each core sleeve is about 60 cm long and 9 cm wide; the stratigraphic top is the upper left corner). The poor condition of the core and unconsolidated nature of the sediment made it unsuitable for sedimentologic interpretation.

### 3 Task 3.0 – Static Capacity Estimates

#### 3.1 Subtask 3.1 – Regional Capacity Assessment

Regional static capacity was estimated using the methodology of Wallace et al. (2014), (Equation 3.1.1), which was, in turn, a modification and refinement of the methodology of Goodman et al. (2011). The initial step involved defining the capacity interval (CI). As determined by Wallace et al. (2014) for the study area, the upper limit of the CI (i.e., the minimum depth at which CO<sub>2</sub> is likely to be in a supercritical state) is at approximately at 1006 m (~3,300 ft), and the base of the CI is generally defined by the top of overpressure (Figure 3.1.1), which Pitman (2011) regionally mapped in the depth domain and Burke et al. (2012) published.

Equation 3.1.1

$$G_{CO2net} = A_t h_{net} \phi_{tot} \rho E_{net}$$

Where:  $A_t$  = Total area

$h_{net}$  = Net sand thickness

$\phi_{tot}$  = Total porosity

$\rho$  = CO<sub>2</sub> density

$E_{net}$  = Net storage efficiency factor in a saline aquifer

After defining the top and bottom of the CI, net sand thickness,  $h_{net}$ , was estimated by counting and mapping sand thickness for one of the important potential reservoir intervals, *Amphistegina B* (MFS9) to *Robulus B* (MFS10) (Figure 3.1.1). Figure 3.1.2 presents the resulting, initial net sand map (i.e., first pass). Later in the project, the net sandstone estimation (i.e., grid and map) were refined by adding better quality well data and excluding data of lower quality.

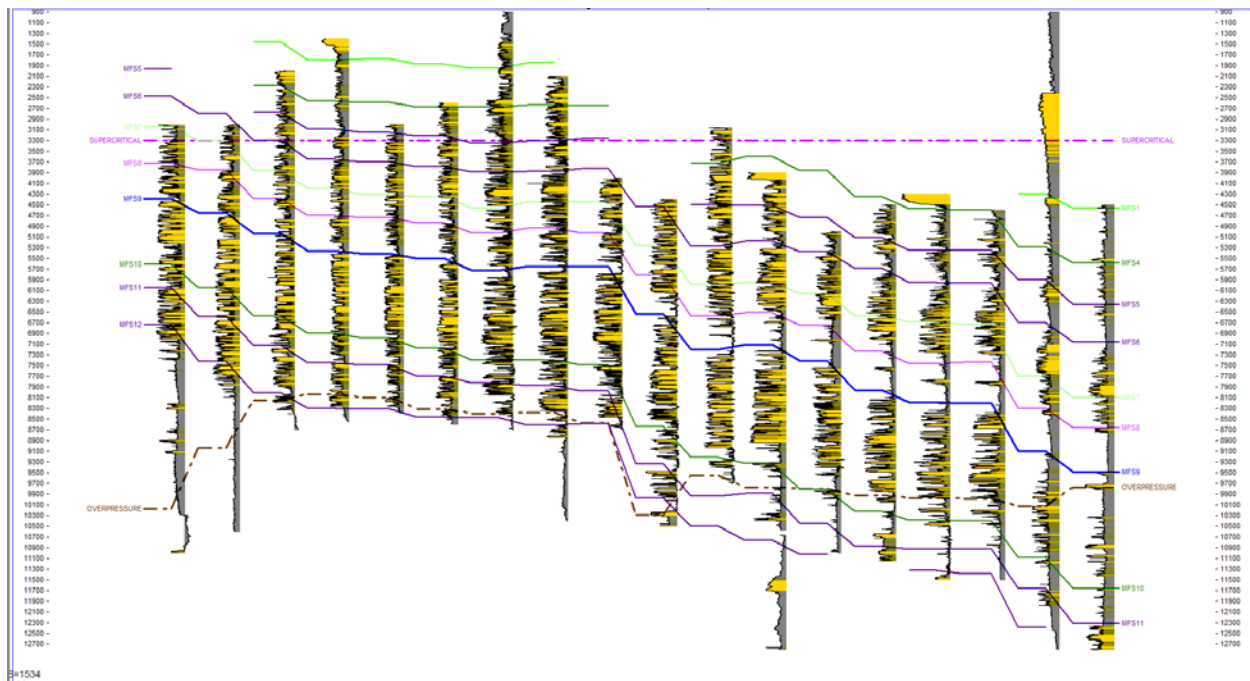


Figure 3.1.1 – Dip-oriented structural cross-section extending along the border between Texas and

Louisiana. The top of the overpressure coincides roughly with MFS12 updip, but due to section displacement and expansion seaward it corresponds to MFS10 and even MFS9 farther downdip. The seal interval associated with MFS9 (*Amphistegina B*) can, in some instances, reach a thickness of about 250m.

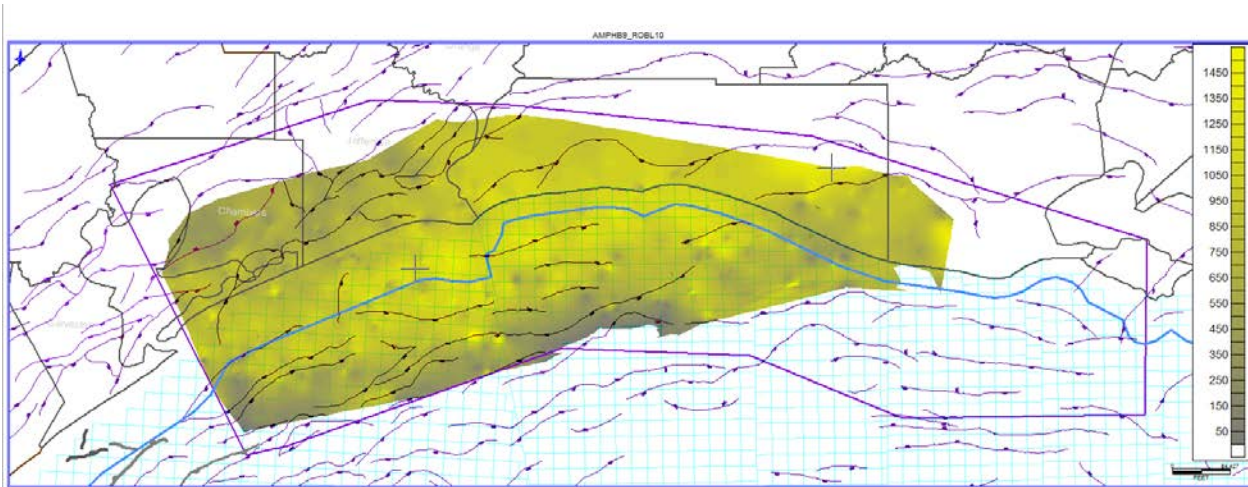


Figure 3.1.2 – Initial net sandstone map of the stratigraphic interval from *Amphistegina B* (MFS9) to *Robulus B* (MFS10). Note that capacity was not estimated for the easternmost portion of the AOI (i.e., within the purple polygon) due to lack of useful well data.

#### Refined Net Sandstone ( $h_{net}$ ) Calculation

A total of 760 wells with SP (Spontaneous Potential) curve (Figure 3.1.3) were used in the calculation of the sandstone thickness for the prospective interval of interest, MFS 9 (*Amphistegina B*) – MFS10 (*Robulus L*) above the top of overpressure (Figure 3.1.4). The net sandstone content at a particular well location is determined by identifying significant deflections in the well’s spontaneous potential (SP) curve. SP curves are the preferred indicator of net sandstone as they highlight intervals of qualitatively higher permeability. SP curves were normalized to make the maximum and minimum deflections equal in all wells by rescaling the curves. The sandstone-shale cutoff was defined as -20 MV. Consequently, SP values between -90 and -20 MV were counted as “sandstone.” If the SP deflection was greater than -20 MV, the interval thickness was counted as non-sandstone (i.e., mudstone or “shale”). The amount of sandstone in the prospective interval was summed at each well; this is the net sandstone for the interval at the, respective, well location. The net sandstone values were then gridded and mapped resulting in the sandstone thickness map in Figure 3.1.4.

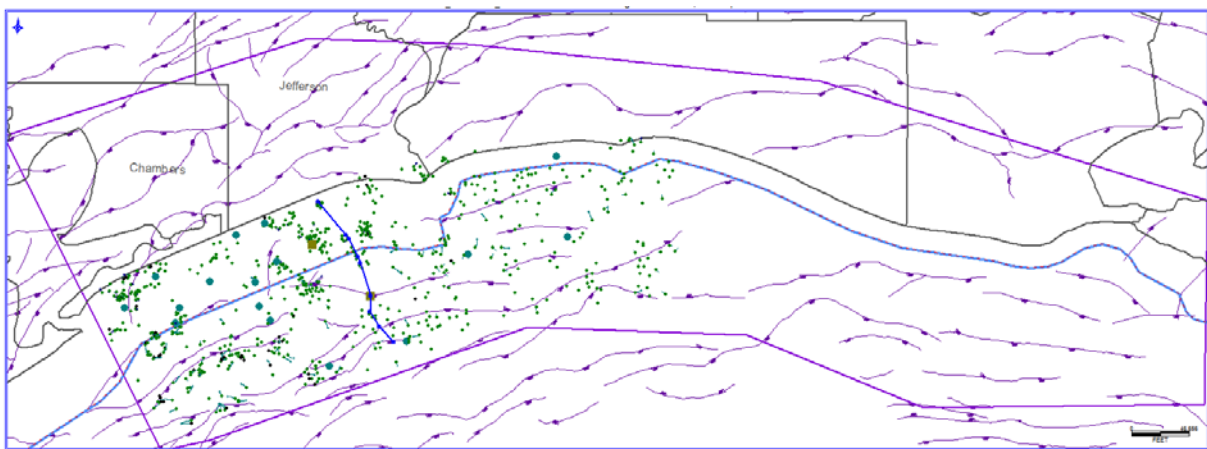


Figure 3.1.3 – Map of the study area showing wells with digital logs in the study area offshore Texas and Louisiana. Out of the 725 digital logs with SP curves, 20 wells also have sonic or density logs (blue circles) and two wells are cored (olive squares). Normal faults (purple lines) and dip cross-section (dark blue line; see Figure 3.1.4) are also indicated.

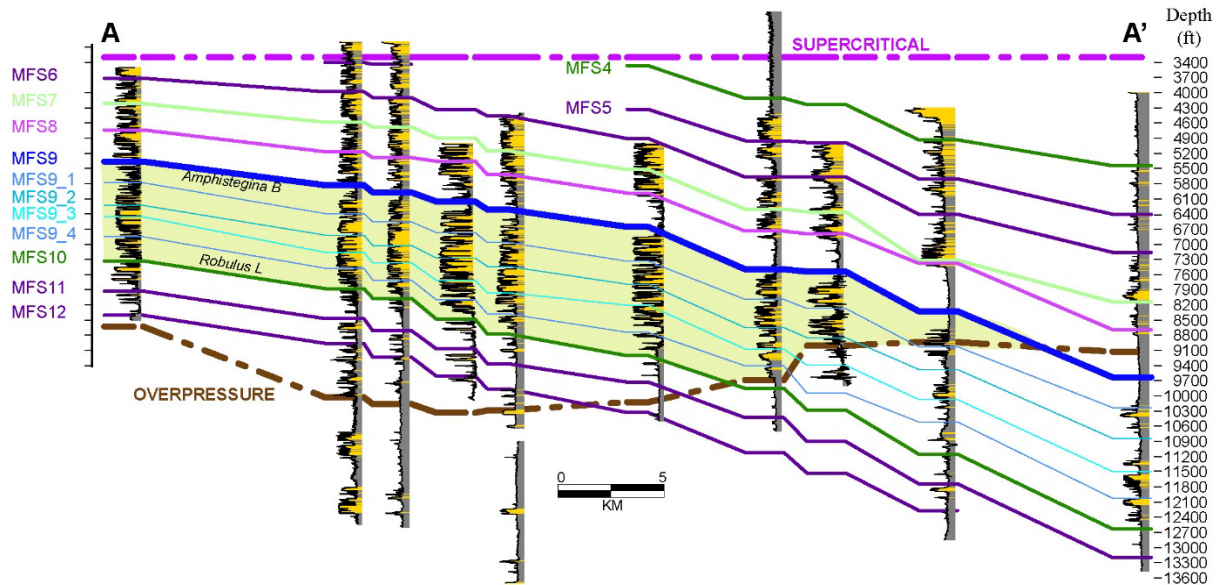


Figure 3.1.4 – Dip-oriented structural cross-section including the most prospective reservoir interval (between *Amphistegina B* - MFS9 and *Robulus L* - MFS10) highlighted in light green. Multiple normal faults offset the stratigraphy. The top of the overpressure (dashed brown line) coincides roughly with MFS12 updip, but due to section displacement and expansion seaward it corresponds to MFS10 and even MFS9 farther downdip (toward the right side of the cross section). The seal interval is associated with MFS9 (*Amphistegina B*), a shale with a maximum thickness of about 250m. Sandstone is shown in yellow in all well logs; non-sandstone facies (mudstone) is denoted by gray.

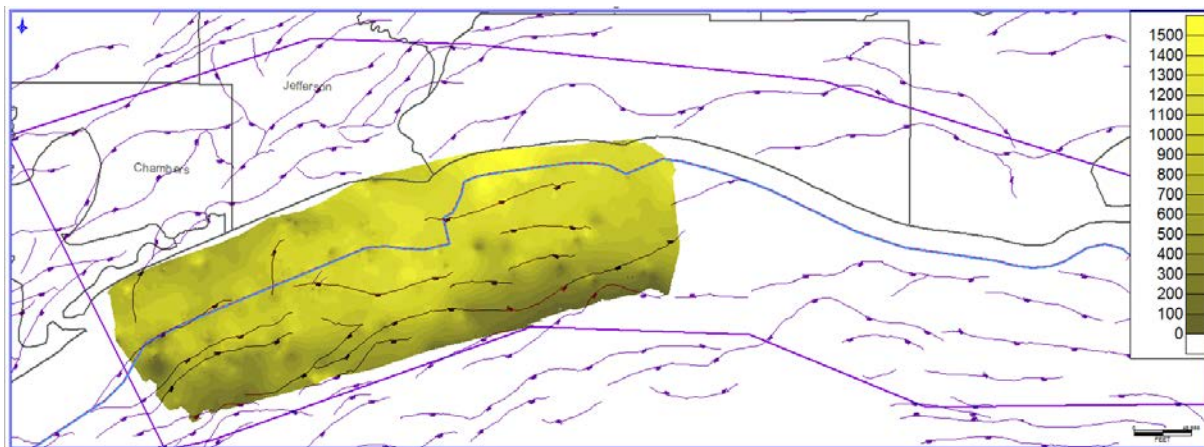


Figure 3.1.5 – Net sandstone thickness ( $h_{net}$ ) map for the prospective interval (total area = 5575 km<sup>2</sup>; total volume = 1476 km<sup>3</sup>). The sandstone has a strike-elongated trend and reaches a maximum thickness of about 1500 ft (minimum 50 ft) and an average of about 900 ft.

### Porosity ( $\phi_{tot}$ ) Calculation

The porosity for the capacity interval is determined using wireline logs with porosity curves (i.e., sonic or density). Porosity calculation is restricted to net sandstone intervals defined by the sandstone cutoff. Porosity values are interpolated and gridded using a least square algorithm. In the regional capacity input grids for the Miocene section of Texas State Waters,  $\phi_{tot}$  varies from 22% to 38% (Wallace et al., 2014); in the study area the porosity is about 30% (Figure 3.1.6).

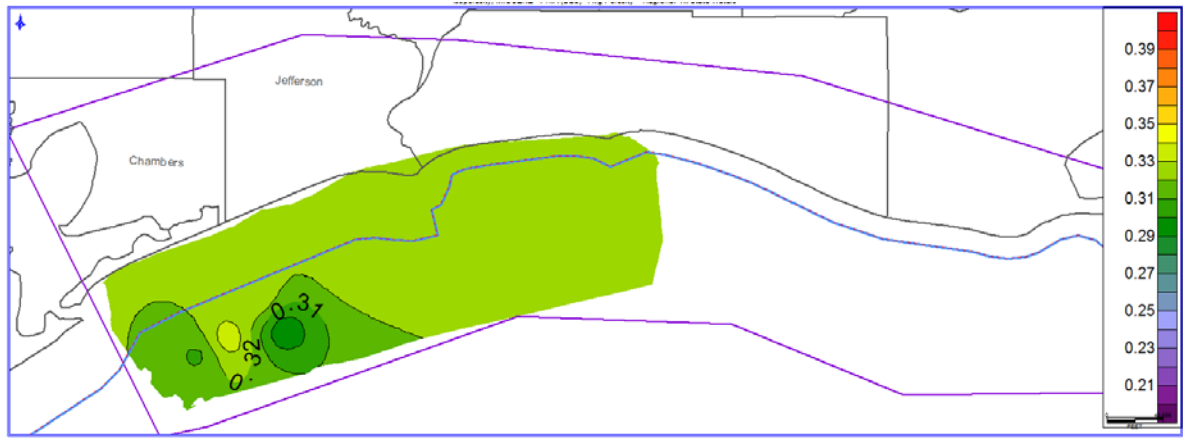


Figure 3.1.6 – Porosity map of the Miocene interval in the study area Higher porosity values (>30%) result in larger pore volumes for CO<sub>2</sub> storage.

### Density ( $\rho$ ) Calculation

In the study area, CO<sub>2</sub> density rapidly increases with depth until it reaches a depth of approximately 1 km, at which point it ranges between 600 and 700 kg/m<sup>3</sup> (Nicholson, 2012). CO<sub>2</sub> density ( $\rho$ ) is determined as a function of depth over the study area by applying a depth-CO<sub>2</sub> density transform (Figure 3.1.7) to the midpoint of the prospective interval. The midpoint of the prospective interval is obtained by dividing the gross thickness grid by 2 and subtracting it from the base of the capacity interval grid. Regional temperature and pressure data have been compiled from wells and produced fields within the Miocene section of Texas State Waters (Meckel et al., 2017). The average temperature trend with depth and hydrostatic pressure gradient were used to determine CO<sub>2</sub> fluid density with depth (Figure 3.1.8).

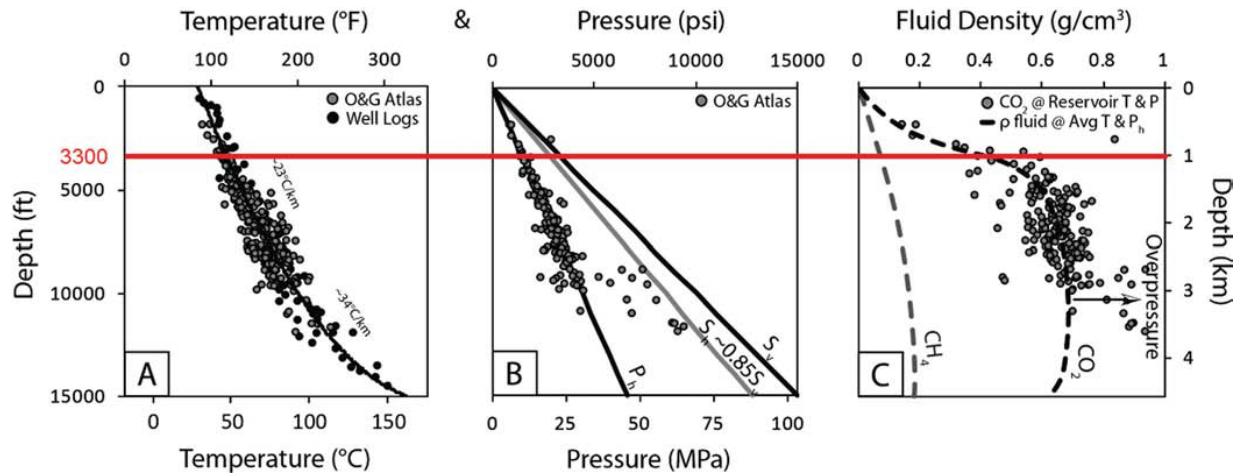


Figure 3.1.7 – Temperature, pressure, and CO<sub>2</sub> fluid density vs. depth. Note that the upper depth limit at which CO<sub>2</sub> remains in a supercritical state is marked by the red line (i.e., ~1 km = ~3,300ft).

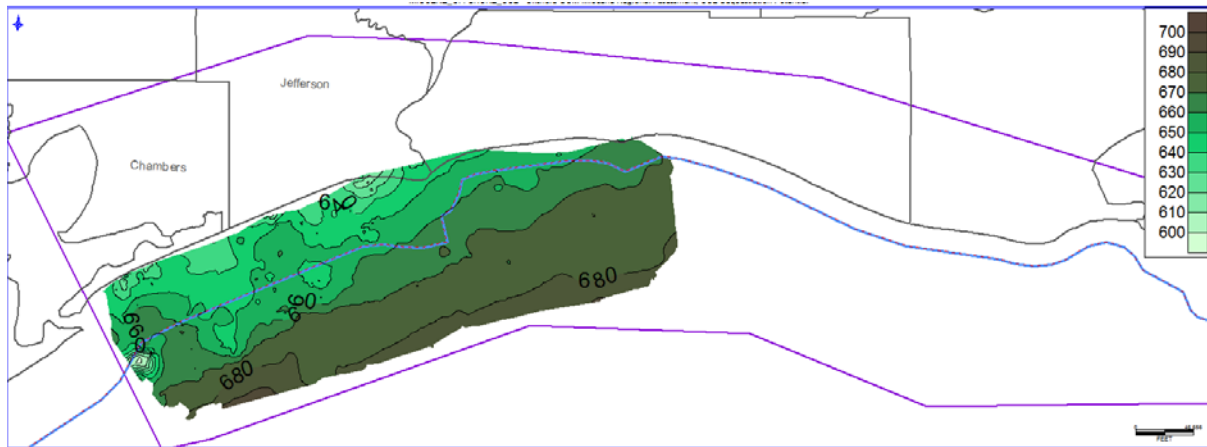


Figure 3.1.8 – Mapped grid of CO<sub>2</sub> density at midpoint depth of the prospective interval. Note that CO<sub>2</sub> density reaches a steady range between 600 and 700 kg/m<sup>3</sup> below supercritical depth with slightly higher values observed downdip.

#### Efficiency Factor Calculation

A range (i.e., from 0.4% to 5.5%) of efficiency factors has been proposed for use in sandstone saline aquifers and for probability values of P10, P50, or P90. A net efficiency factor ( $E_{net}$ ) of 0.045 is selected for the Miocene prospective interval as  $E_{net} = 0.045$  is the P50 value for saline aquifer sandstone reservoirs recommended by the NETL (Wallace et al., 2014).

#### Capacity ( $G_{CO_2net}$ ) Calculation

Utilizing the porosity (Figure 3.1.6), CO<sub>2</sub> density, (Figure 3.1.8) and net sand (Figure 3.1.5) grids and  $E_{net} = 0.045$ , the resulting capacity grid is presented in Figure 7. Specifically, the capacity map in Figure 7 is based on 1) the grid of net sandstone thickness shown in Figure 3; 2) the porosity grid in Figure 4; 3) the density grid in Figure 6, and 4) an efficiency factor of 4.5% (0.045). The capacity distribution shows relatively low static capacity downdip (southward) and increasing storage potential updip along the present-day shoreline.

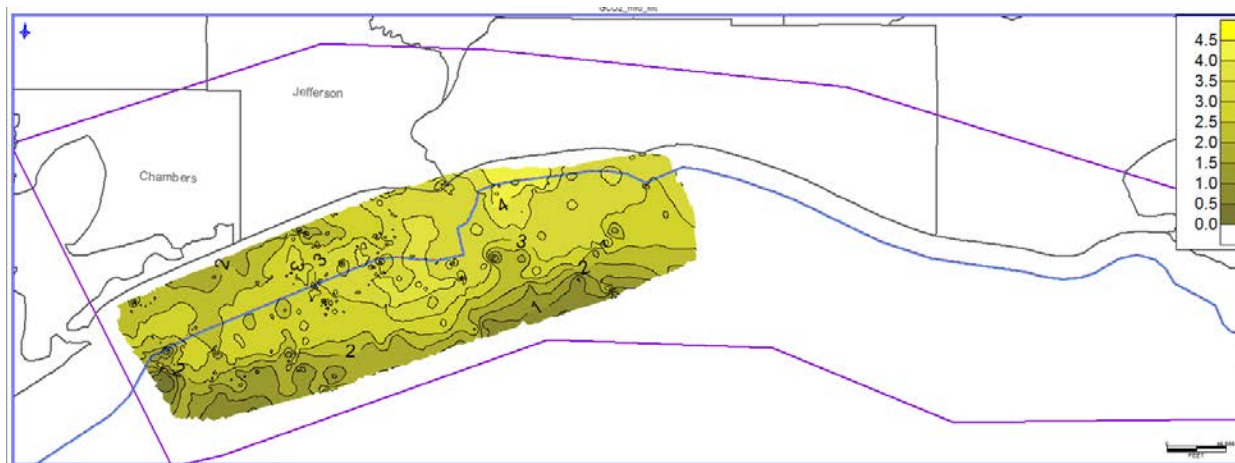


Figure 3.1.9 – Map of static CO<sub>2</sub> storage capacity ( $G_{CO2net}$ ) using the method of Wallace et al. (2014).

### Summary & Conclusions

The static capacity for the calculated area was estimated to be 7.15 gigatonnes (Gt) (Table 3.1.1). Maximum and minimum computed storage values are 4.66 and 0.75 Mt/km<sup>2</sup> (megatonnes per square kilometer), respectively. Average and standard deviation are 2.55 Mt/km<sup>2</sup> and 0.75 Mt/km<sup>2</sup>, respectively. For the Miocene section of the prospective interval  $\phi_{tot}$  varies from 30% to 33% (Figure 3.1.6) and CO<sub>2</sub> density ranges from 640 to 700 kg/m<sup>3</sup> (Figure 3.1.8).

Table 3.1.1 – Summary of static capacity parameters

Total area $A_t$ (km <sup>2</sup> )	Sandstone volume $V_{net}$ (km <sup>3</sup> )	Porosity $\phi_{tot}$ (%)	CO <sub>2</sub> density ( $\rho$ ) (kg/m <sup>3</sup> )	Efficiency factor $E_{net}$	Static capacity $G_{CO2net}$ (Gt)
5575	1476	30-33	640 -700	0.045	7.15

### Porosity Prediction Using 3D Seismic

The calculations presented above fulfilled the requirements of the project scope. However, the availability of the TexLa Merge 3D seismic dataset presented an opportunity to experiment with the possibility of improved porosity prediction from a continuous dataset (i.e., a 3D seismic dataset).

### **Porosity prediction using multi-attribute analysis with limited well log data**

A thorough understanding of porosity distribution in CO<sub>2</sub> reservoirs plays an important role in evaluating CO<sub>2</sub> storage capacity. Conventionally, reservoir properties are estimated from elastic parameters using seismic inversion and rock physics methods. Consequently, a novel workflow to obtain a 3D porosity volume in combination with well log prediction and seismic multi-attribute analysis using neural networks



with limited well log data was explored. Subsequently, the porosity volume can populate a geo-cellular model for estimation of CO<sub>2</sub> storage capacity.

The dataset comprises a post-stack seismic volume with its near-mid-far angle stacks and eight wells. The wells were categorized according to log suite completeness: a) those that have P-wave and density logs, but not porosity logs, and do not cross major faults; b) those that have porosity logs, but no P-wave or density logs and do cross major faults; c) those with P-wave, density and porosity logs that do not cross major faults. A three-step workflow (Figure 3.1.10) was then designed to fully maximize the value of available seismic and well log data.

First, we performed both pre- and post-stack seismic inversion using the type (a) wells which can be tied to the seismic. Unlike post-stack inversion that only derives P-impedance, pre-stack inversion also provides S-impedance, Vp/Vs and density in the subsurface, which are proven to be the major seismic attributes associated with porosity in the later stage. Then, type (b) wells are utilized to predict the missing porosity logs in the type (a) wells, by performing a linear multi-attribute analysis of the common log suites. The final step involved the linear and non-linear (probabilistic neural network, PNN) analysis between the target porosity logs and 29 seismic attributes, which showed good correlation (85% and 93%, respectively) between five seismic attributes and the porosity logs from multiple well locations. Figure 3.1.11 compares PNN-derived porosity volume to the non-linear analysis and indicates that the former has higher resolution and shows finer details of small channels; whereas such fine-scaled features are not captured by the non-linear analysis. The results are also more robust by including extra modeled porosity logs generated from the previous step.

Finally, we populated the porosity volume in a geo-cellular model to estimate CO<sub>2</sub> capacity. Our analysis verifies significant porosity and, therefore, CO<sub>2</sub> storage potential in the Lower Miocene interval of the TexLa Merge 3D dataset's coverage area.

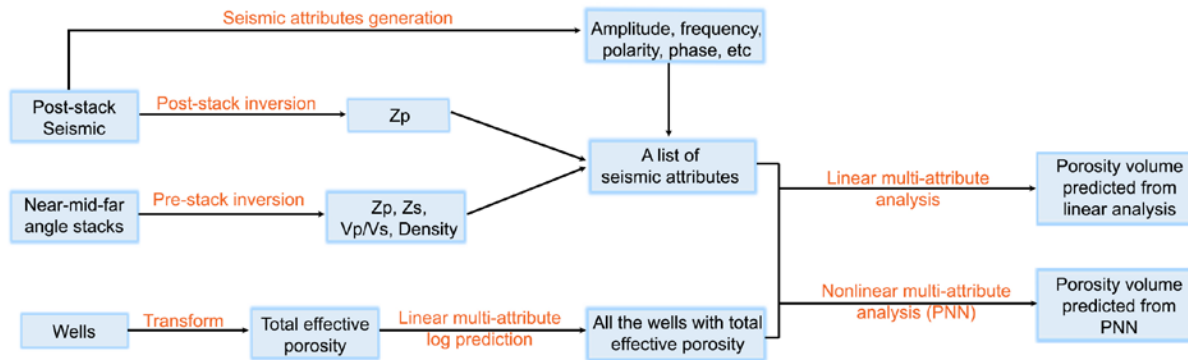


Figure 3.1.10 – Workflow for 3D porosity prediction from well log and seismic data.

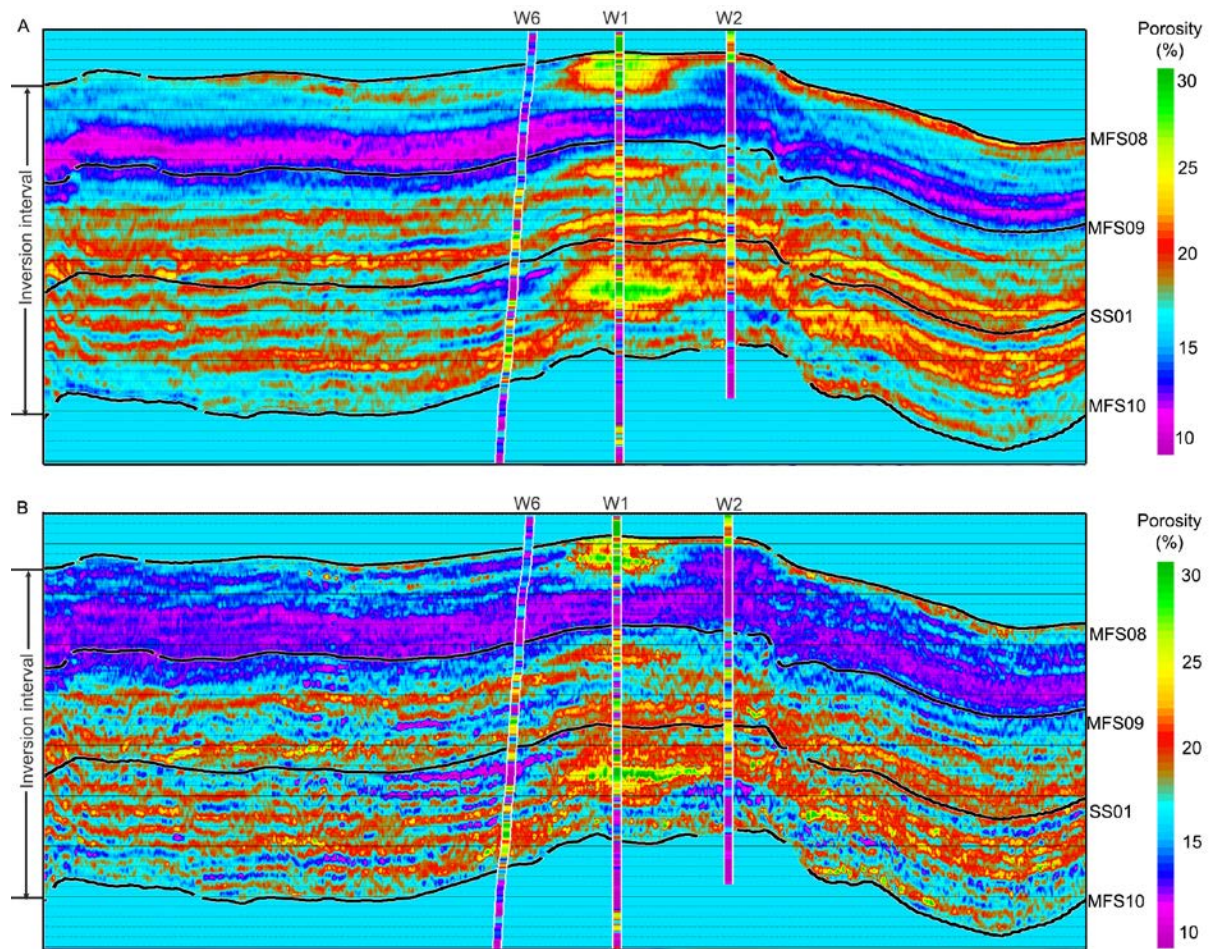


Figure 3.1.11 – Seismic profile showing porosity derived from the (A) linear regression and (B) PNN.

### Validation to porosity prediction using depositional systems and sequence stratigraphic interpretation

In order to validate the 3D seismic-based multi-attribute analysis porosity prediction, it was compared to the depositional systems and sequence stratigraphic interpretation of the studied area. Ultimately, non-linear PNN porosity was selected as the preferred predicted porosity volume due to its high-degree of agreement with the geologic interpretation.

#### *Depositional systems interpretation*

The interval of interest between MFS09-MFS10 is interpreted as a potential CO<sub>2</sub> storage interval because it comprises aggradational sandstones of as much as 750 m overlain by the thick, regionally extensive *Amphistegina B* shale (DeAngelo et al., 2019). Advanced seismic interpretation using stratal slices on seismic attributes was performed in order to improve subsurface imaging of geomorphic features to better understand the depositional systems of this interval (MFS09-MFS10). This was crucial in characterizing reservoirs in term of the distribution, connectivity, and quality.

The RMS amplitude map has been widely used to represent geologic features with regard to their lithofacies

variation (DeAngelo et al., 2019). In this study, we performed interpretation of depositional systems based on RMS amplitude map of the horizon SS01 located in the middle of the interval MFS09-MFS10 (Figure 3.1.12). The predicted porosity volume was compared to the equivalent map of RMS amplitude and evaluated using the interpretation from the RMS amplitude map. The SS01 horizon extracted from both linear and PNN porosity volumes centered at 51 ms window (Figure 3.1.1 A & B), and the RMS amplitude map of SS01 horizon using the same window length of 51 ms (Figure 3.1.1 C).

The RMS amplitude map of this horizon shows prominent channel belts with relatively N-S orientation (darker brown on figure 3.1.1 C and dashed lines on figure 3.1.1 D). The channel belts have widths of 2 – 5 km and comprise smaller, individual, sinuous, meandering, fluvio-deltaic channels. Channels or channel belt features in the RMS amplitude map exhibit low-amplitude, sub-parallel-chaotic seismic facies in the channel versus high-amplitude parallel seismic facies in the adjacent non-channel areas. Normal faults shown by the RMS amplitude map are interpreted as post-depositional. Low RMS amplitude values represent both channels and faults (Figure 3.1.13 C & D) but are easily distinguishable from each other because faults are much narrower than the channel belts.

#### *Sequence stratigraphic interpretation*

Gamma ray log patterns (Figure 3.1.12) of the interval of interest were utilized in order to validate the seismic-based geomorphic features shown in the RMS amplitude map (Figure 3.1.13C). Figure 3.1.12 shows the sequence stratigraphic interpretation of the interval of interest. The interval above MFS10 is interpreted as Highstand Systems Tract (HST), which is characterized by progradational followed by aggradational stacking pattern of parasequence sets. The SS01 horizon, on which the geomorphic interpretation was performed, is interpreted as, a sequence boundary (SB) (or near an SB). The interval above this horizon is interpreted as Lowstand Systems Tract (LST) in the lower part, and mostly Transgressive Systems Tract (TST) in the upper part. The interval is dominated by retrogradational followed by aggradational stacking pattern of parasequence sets. The sequence stratigraphic interpretation suggests that the channels were formed during, or shortly after, a period of relative sea-level fall (LST), in which the channels cut through non-channelized inner shelf deposits. The interpretation supports the interpretation that the horizon with channels is only observed in the middle of the interval between MFS09 and MFS10.

The channel belts in Figure 3.1.13 C were also observed in the porosity maps (Figure 3.1.13 A & B). The agreement between porosity maps and the RMS amplitude map increased our confidence level of the porosity prediction; Channel belts' orientations follow the regional trend of deposition towards the south – southeast. Faults are mostly post-depositional. Circular to sub-circular features (Figure 3.1.13 D) are salt-related post-depositional elements.

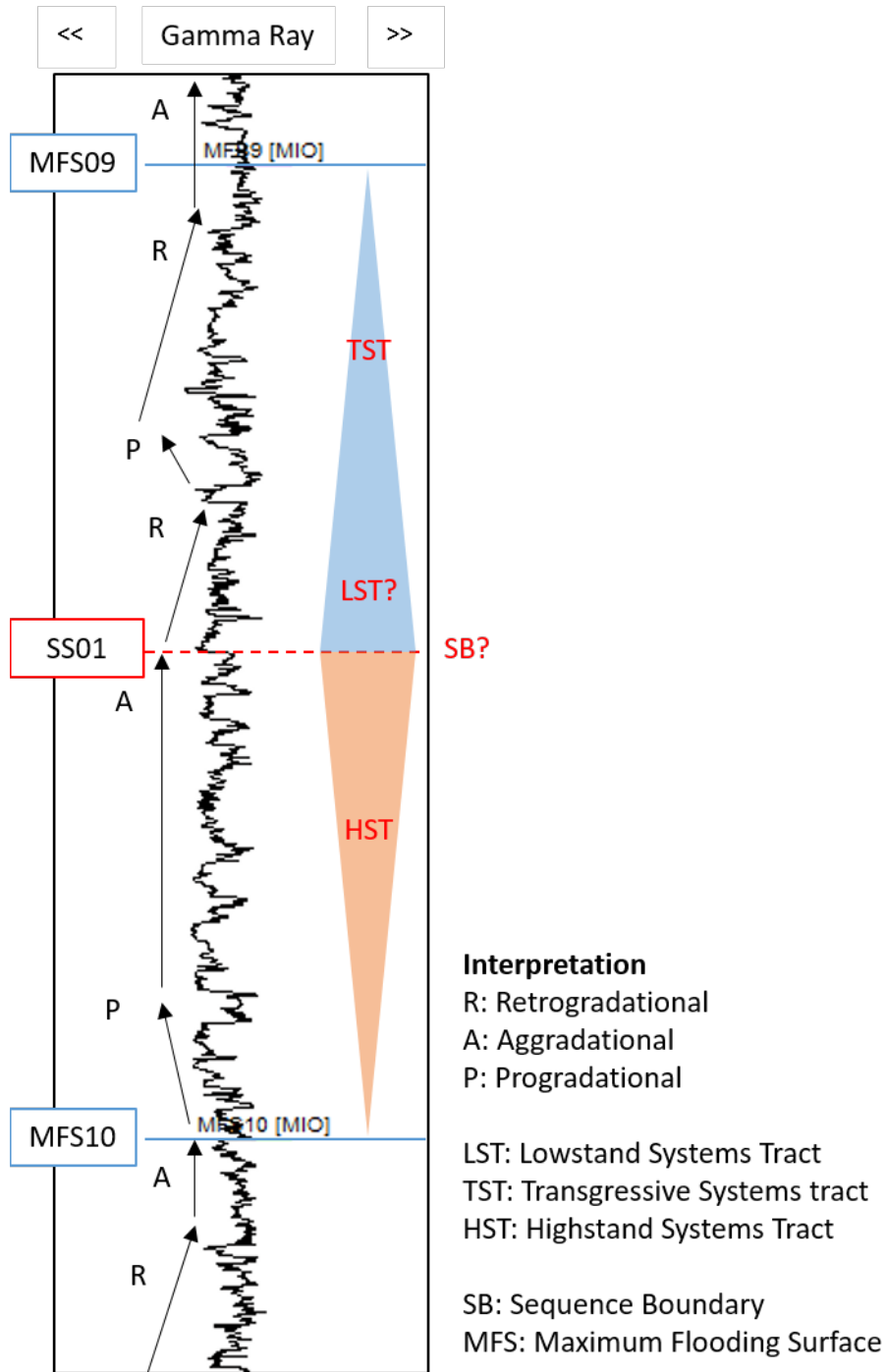


Figure 3.1.12 – Sequence stratigraphic interpretation of Gamma ray log around the MFS09-MFS10 interval. The SS01 is interpreted to coincide with the sequence boundary between MFS09 and MFS10. This supports the development of channelized fluvio-deltaic systems between non-channelized inner shelf deposits below-and-above the SS01 level.

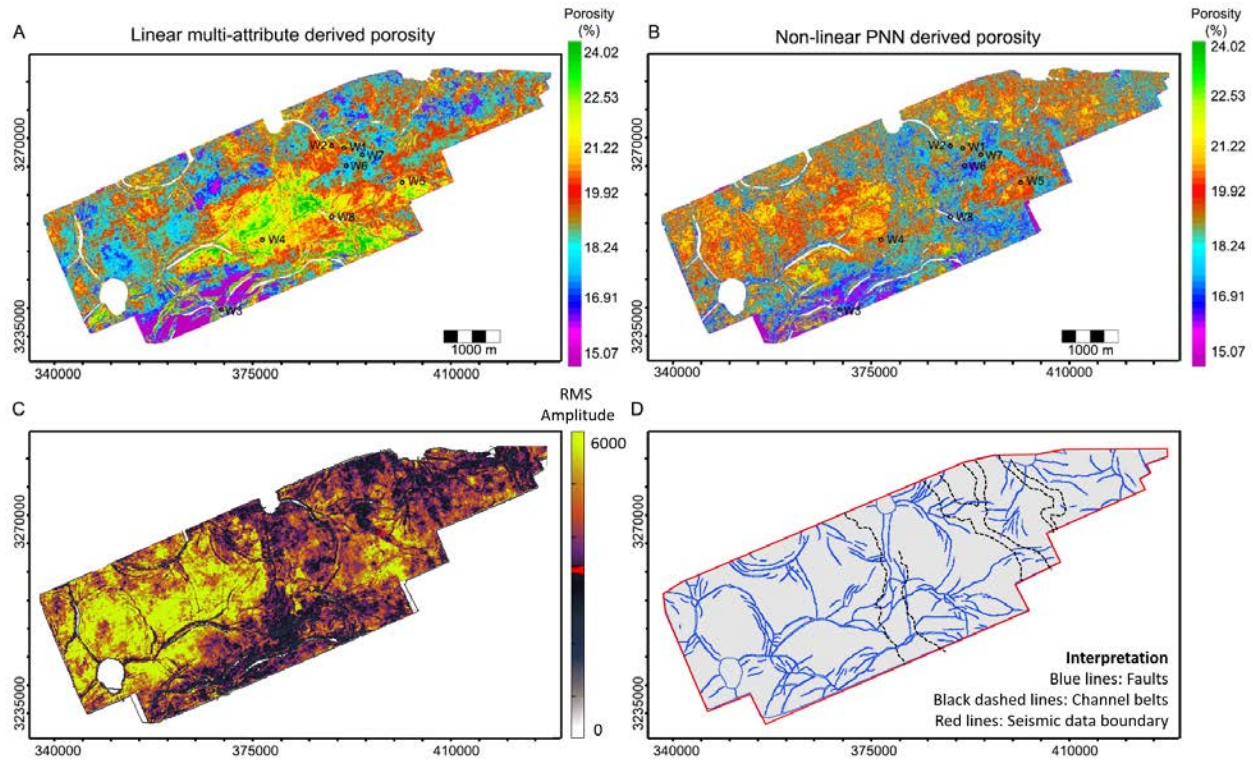


Figure 3.1.13 – A) Linear multi-attribute derived porosity map of horizon SS01; B) Non-linear PNN derived porosity of horizon SS01; C) RMS amplitude map of horizon SS01 showing seismic geomorphic depositional features (channel belts). D) Interpretation of depositional features and faults based on RMS amplitude map of horizon SS01.

## 3.2 Subtask 3.2 – Local Prospect Resource Assessment

### 30 MT CO<sub>2</sub> Storage Site: High Island 24L

The High Island 24-L Field (HI 24L) was discovered in 1967 and is located off the southeast coast of Texas, offshore Jefferson County (Figure 3.2.1). The Offshore Texas State Waters (OTSW) are divided into 3 main districts according to the Railroad Commission (RRC) of Texas). Utilizing RRC reports, HI 24L has produced about 11% of the total amount of natural gas produced from state waters fields and 10% of total state waters oil. This equates to about 470 Bcf of natural gas and 4.5 MMbbl of oil for the field. The most significant single reservoir, the Miocene age “HC sand” reservoir, produced about 40% of the total natural gas from the field (Table 3.2.1). The field currently produces from the “LJ sand” with approximately 2 Bcf of cumulative natural gas as of 2018 and 100 MMcf in the most recently reported month (January, 2019).

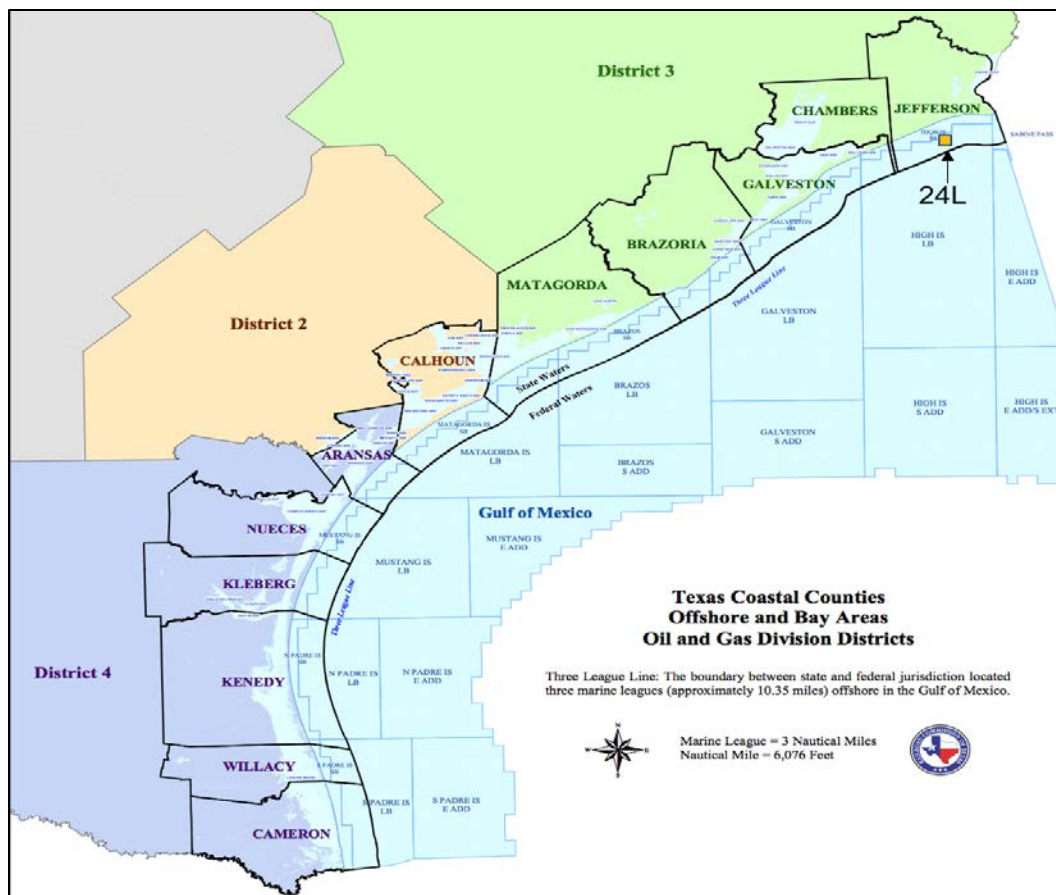


Figure 3.2.1 – Map of coastal Texas districts, Railroad Commission of Texas. HI (High Island) 24L is labeled.

Table 3.2.1 – Cumulative natural gas and oil production from Offshore Texas State Waters, RRC District 3, the HI 24L field, and the field’s HC sand reservoir.

	<b>Cum Gas Production (Bcf)</b>	<b>Cum Oil Production (Mbbl)</b>
<b>Offshore TX State Waters</b>	4207	42538
<b>District 3</b>	3017	25318
<b>HI 24L</b>	469	4360
<b>HC Sand</b>	206	1222

The geology of the HI-24L field has been characterized using (“TexLa Merge” conventional 3D seismic dataset and wireline well log data. The field exemplifies geologic characteristics (e.g., stratigraphy and structure) typical of the Miocene section of southeast Texas and southwestern Louisiana. The presence of trapped hydrocarbons demonstrates significant fluid retention through geologic time, and suggests the potential for high-quality CO<sub>2</sub> storage.

A type log for the field (Figure 3.2.2) illustrates the key bio-stratigraphic surfaces that have been mapped in the area. The storage interval of interest (SIOI) is characterized by thick sands and capped by the Amph

B shale. The storage interval of interest (SIOI) for the field is a thick aggradational package of sands averaging about 1700 ft (~520 m) gross thickness, with an average 350 ft (~105 m) thick overlying shale seal. The SIOI comprises 60-65% net-to-gross (NTG) sand to mudstone (a.k.a “shale”) ratio. The average porosity of the sand strata is approximately 31%.

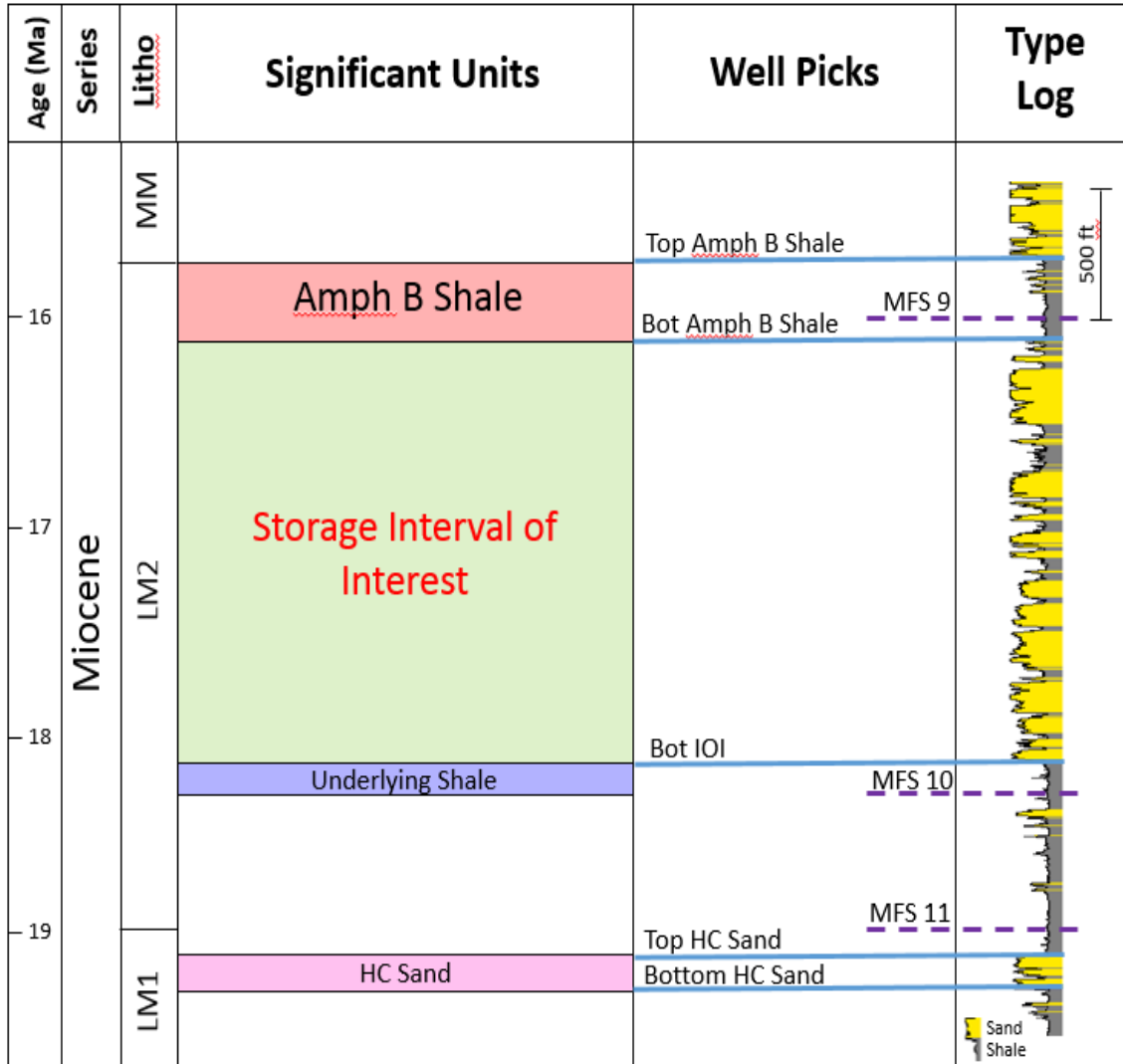


Figure 3.2.2 – Stratigraphic chart and type log for HI 24L.

**Methodology**

Four key horizons, Top Amph B Shale, Bot Amph B, Bot IOI, and MFS 10 (Figure 3.2.2), and well log data (N = 37) have been used to create a 3-D geocellular grid and model reservoir property distribution to estimate CO<sub>2</sub> storage capacity for the SIOI. The structure map of the HC sand generated by seismic interpretation illustrates the important role of faults associated with a typical rollover anticline for trapping hydrocarbon accumulations.

Using the root mean square (RMS) seismic attribute, a field outline for the HC sand was generated; it

represents the historic hydrocarbon footprint (Figure 3.2.3), and it is assumed that the net sand for the SIOI can be utilized for CO<sub>2</sub> injection helps estimate potential CO<sub>2</sub> storage capacity.

Well logs were correlated (Figure 3.2.4) using maximum flooding surfaces MFS09, MFS10 and MFS11, which represent transgressive episodes and relative sea level rise. Most of the sands in the SIOI show a blocky log pattern and with a small fining up towards the top of the package, coinciding with the transgressive event of the *Amphistegina B* unit. The sands are characteristic of shallow marine depositional systems, more specifically a mix of delta fringe and marine shelf sands.



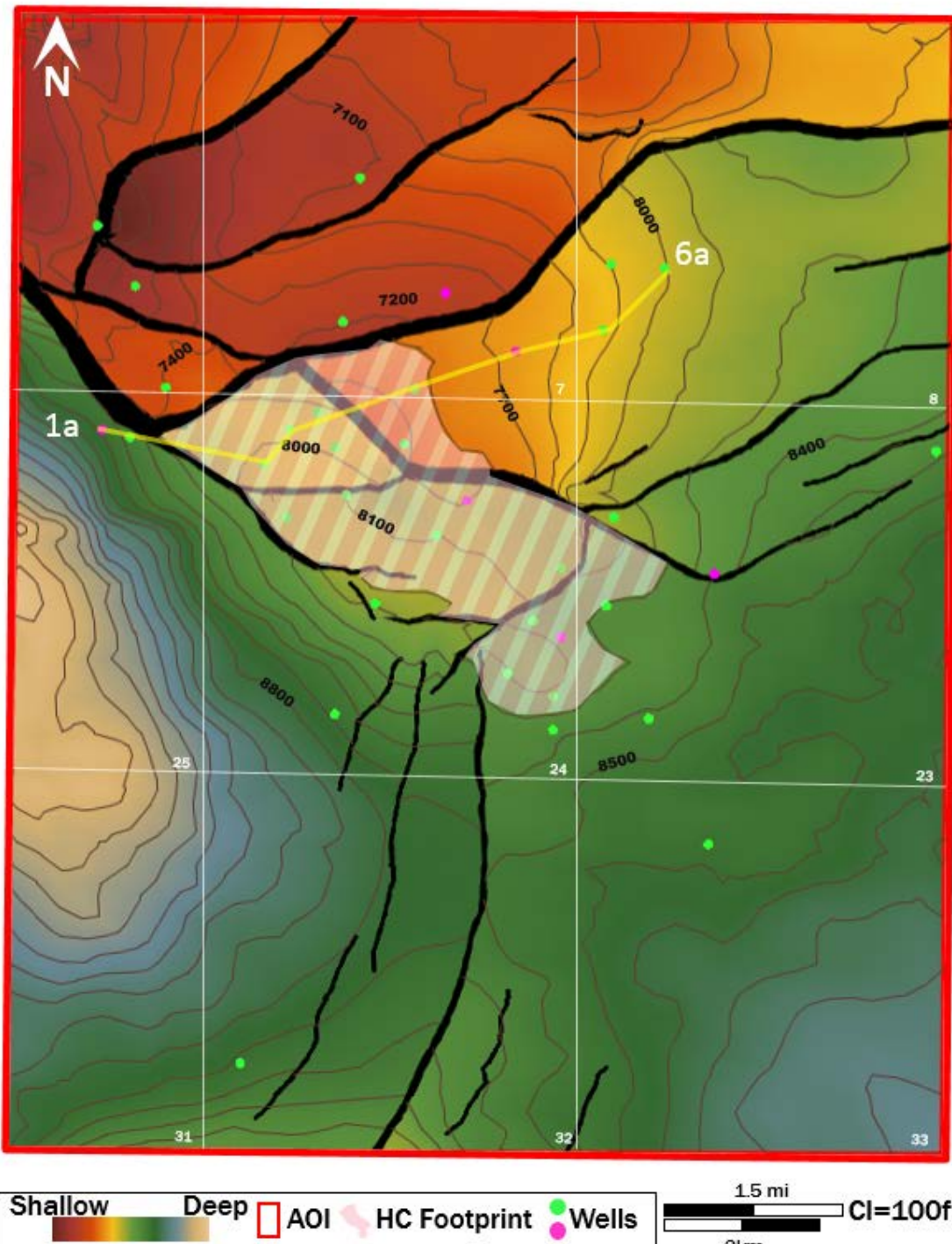


Figure 3.2.3 – Structure map of the HC Sand reservoir. Footprint of historic hydrocarbon footprint is shown in pink striped polygon. Green wells have only a spontaneous potential (SP) curve, magenta wells have both SP and porosity curves. Lease blocks are labeled. Note that most of the hydrocarbon footprint occurs in Block 24.

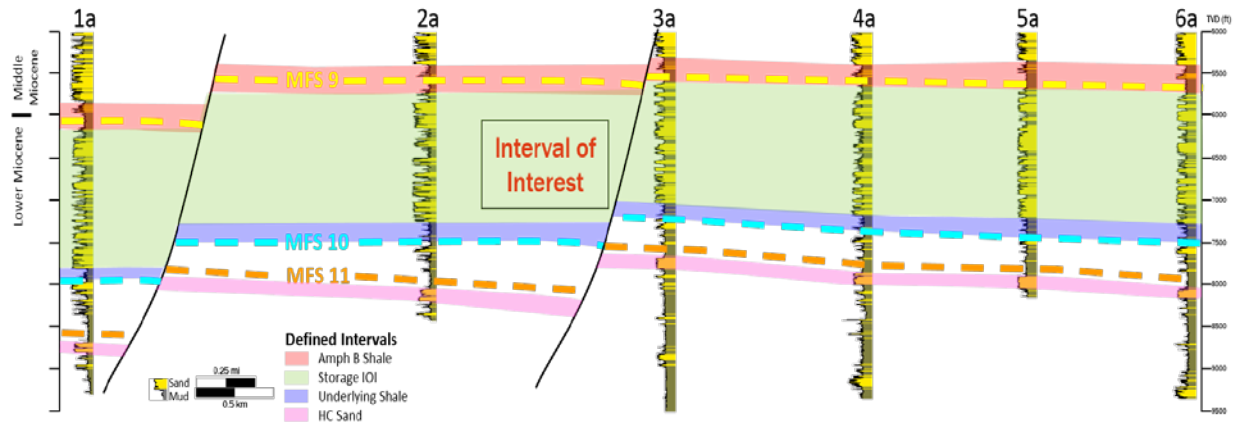


Figure 3.2.4 – Well log cross section oriented along depositional strike and highlighting the informal stratigraphic units mentioned in the text. Note the storage interval of interest (SIOI). Cross section line of section shown on Figure 3.2.3.

### Capacity Estimation

Capacity was estimated using the methodology of Goodman et al. (2011):

$$G_{CO_2} = A_n h_{ntg} \Phi_{eff} \rho E_{saline}$$

$A_n$  = Net area

$h_{ntg}$  = SIOI net to gross thickness (*after* Wallace et al., 2014)

$\Phi_{eff}$  = Effective Porosity

$\rho$  = CO<sub>2</sub> density

$E_{saline}$  = efficiency factor

Where: Net area ( $A_n$ ) equals the historic hydrocarbon footprint area. SIOI ( $h_{ntg}$ ) and effective porosity ( $\Phi_{eff}$ ) was determined by the 3-D geocellular grid and populating it with reservoir properties (facies and porosity). The porosity model was created by calculating effective porosity from well log data and a nonlinear neural network generated porosity volume ( $\Phi_{eff}$ ) (Figure 3.1.11). CO<sub>2</sub> density ( $\rho$ ) was based on Nicholson (2012) with a value of 0.65 g/cm<sup>3</sup>.

The efficiency factor,  $E_{saline}$ , represents the portion of the pore space accessed for storage.

$$E_{saline} = E_{A_n/A_t} E_{h_n/h_g} E_{\Phi_{tot}} E_v E_d$$

$E_{saline}$  includes five variables:  $E_{A_n/A_t}$  = net-to-total area;  $E_{h_n/h_g}$  = net-to-gross thickness;  $E_{\Phi_{tot}}$  = effective-to-total porosity;  $E_v$  = volumetric displacement efficiency; and  $E_d$  = microscopic displacement efficiency. However, since the net-to-total area (hydrocarbon footprint), net-to-gross thickness (3-D facies model), and effective-to-total porosity (3-D effective porosity model) are already known and calculated, the total efficiency factor must increase versus values used for regional static capacity calculation (Table 3.2.2). The justification is that there is no uncertainty in the area, thickness, or porosity. Goodman et al.'s (2011) methodology was developed for regional capacity assessment, but it is, nonetheless, useful for a field scale project with much refined and more confident geological interpretations. The calculated P50 storage volume using the 3-D porosity model is approximately 190 million metric tonnes (Mt). A similar analysis

using NETL's CO<sub>2</sub>-SCREEN tool results in an estimate of 170 Mt. CO<sub>2</sub>-SCREEN (CO<sub>2</sub> Storage Prospective Resource Estimation Excel Analysis) is an Excel-based tool and workflow that was developed by the US-DOE-NETL to screen geological formations for storage. The CO<sub>2</sub>-SCREEN result (Table 3.2.2) is 20 Mt less than the Goodman et al. (2011) calculated capacity because the former works more in a 2-D space as the hydrocarbon footprint area had to be split into 15 equal square grid blocks, and it was not able to capture the entire area. Also, the effective porosities were much lower because a porosity map (convert 3-D to 2-D) was generated for the entire 3-D grid, including all three intervals (*Amphistegina B* unit, SIOI, and subjacent shale). Nonetheless, these values are significant because they equal much more than 30 Mt.

Table 3.2.2 – P10, P50, and P90 values for utilized efficiency factors and storage capacity estimates using two workflows, 1) the NETL CO<sub>2</sub> Screen and 2) the 3D Effective Porosity model.  $E_{\text{saline}} = E_v E_d$  was used for capacity estimations.

	P10	P50	P90
$E_{\text{saline}} = E_{\text{An/At}} E_{\text{hn/hg}} E_{\text{Φtot}} E_v E_d$	0.51%	2%	2.40%
$E_{\text{saline}} = E_v E_d$	7.4%	14%	24%
<b>NETL CO<sub>2</sub> Screen (Mt)</b>	90	170	290
<b>3-D Eff. Porosity Model (Mt)</b>	100	190	325

### 3.3 Subtask 3.3 – Data Management

Throughout the study, an IHS Petra™ project was used as the primary database for well-based data management and interpretation. At the beginning of the project, the availability of a pre-existing Petra™ project, the software's ease of use in interpreting well logs (i.e., correlation and mapping), and the ease of exporting well data from Petra™ to other geologic interpretation packages led to the decision to utilize the software for well-based data management. Initial inspection of the pre-existing IHS Petra™ database resulted in recognition of many dozens of wells with wireline well log (i.e., raster and/or LAS - log ASCII standard) data (Figure 3.3.1). Subsequently, 4337 raster images of well logs were purchased from vendor, MJ Systems. The rasters were from wells in Vermilion and Cameron Parishes, Louisiana and Chambers and Jefferson Counties, Texas. The MJ systems rasters were loaded into the Petra database and are shown in Figure 3.3.2. Where appropriate, paleontological data were added to the Petra™ project for pertinent wells.

It was determined that one or two undergraduate research assistants (URA's) would be of great help in populating and maintaining the geologic database (i.e., wells, well logs, micro-paleontological data, etc.). Consequently, undergraduates were hired to assist, the lead project geologist by digitizing rasters and thus converting the wireline log data to LAS (log ASCII standard). The methodology used by the students was to 1) first look for suitable rasters in the LEXCO™ OWL 7 (Offshore Well & Lease) database (<http://www.lexco.com/about-us/>), which provides "an easy-to-use software/database combination that can find almost any piece of E & P information about the GOM" (Gulf of Mexico). 2) After the correct rasters were identified, the Petra™ database was populated with one or two rasters per offshore block. 3) Then, the rasters are digitized using Neuralog© digitization software, and the resulting LAS curves are loaded into the Petra™ database. Consequently, the study had both raster and digital data for pertinent wells in the offshore Texas and Louisiana areas. Primarily, SP (spontaneous potential) or gamma ray curves were digitized because they are the log curves used to define facies and correlate wells. However, curves useful for determining rock porosity (e.g., sonic (acoustic) and density curves) were also high priority because they provided key information for conversion of seismic data from the time domain to the depth domain.

In addition to the Petra™ database, the project also established and maintained a database for the extensive 2D and 3D seismic datasets that it leased or were available to the public. The seismic database resided in the Haliburton Landmark™ geologic interpretation platform (i.e., “OpenWorks”). Initially, 7542 wells, 1141 LAS files, and 1087 geologic markers (picks) were loaded into OpenWorks database. As well logs were added to the Petra™ database, they were periodically uploaded to OpenWorks. Of the total, 41 wells had sonic and density curves needed for time to depth velocity modeling.

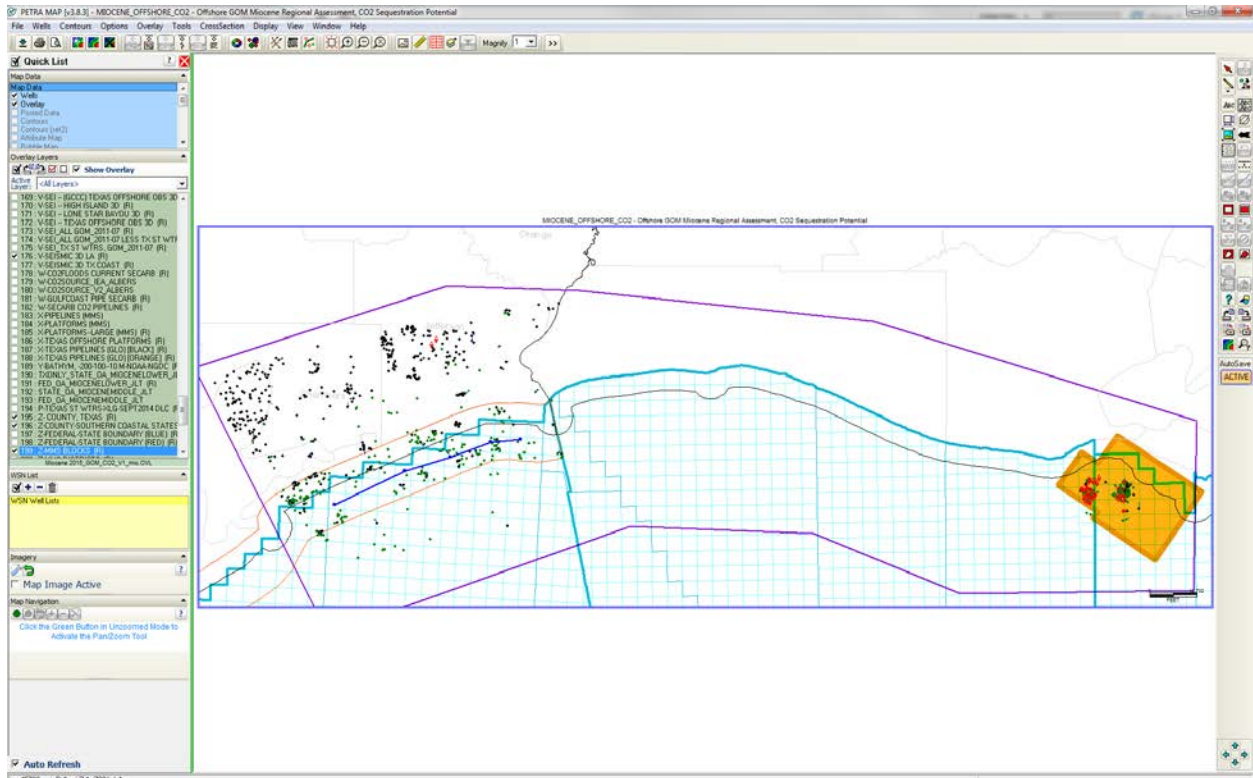


Figure 3.3.1 – Map of the study area (purple polygon) showing the status of the Petra well database as of September 15, 2015. Wells with black dots had raster logs only. Green dots indicate wells with LAS digital SP curves, and red rhombs indicate wells with LAS that include gamma ray.

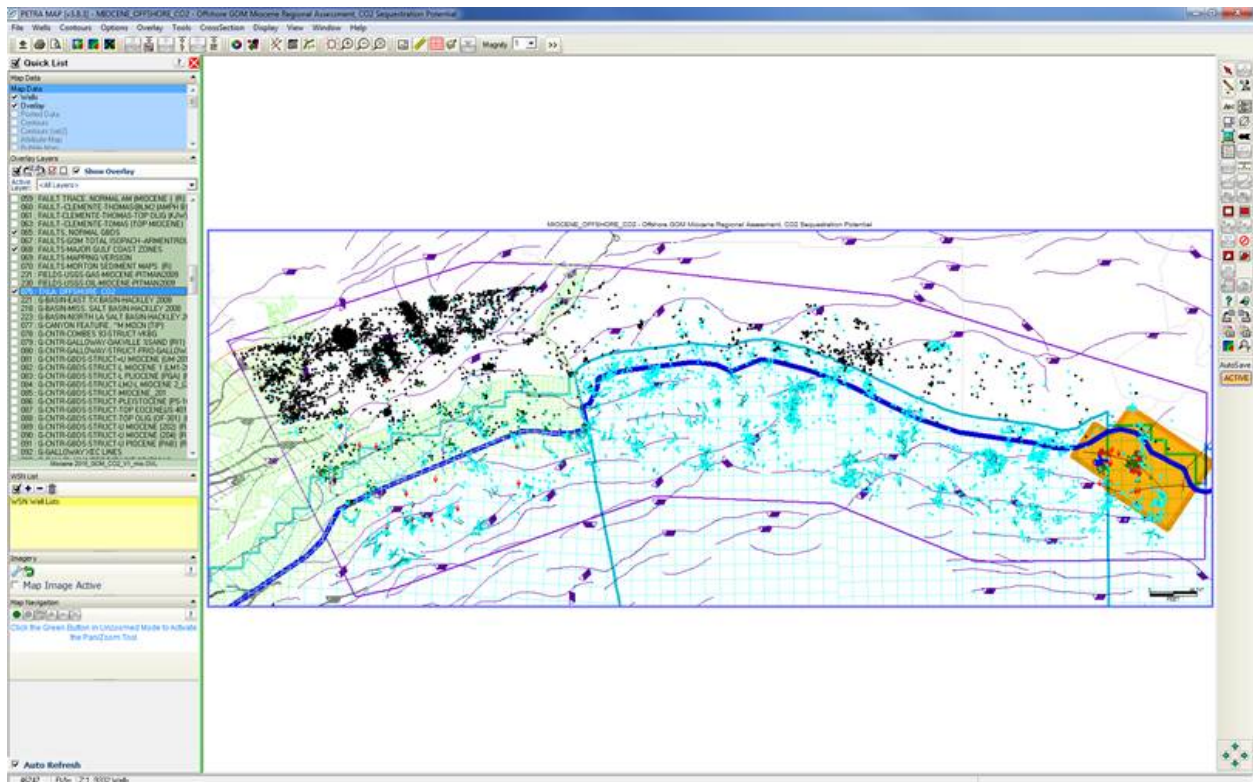


Figure 3.3.2 – Color coded map of the project’s study area showing the status of the well data in the Petra project. Wells with digital (LAS) SP curves are shown as green dots; wells with digital (LAS) gamma ray curves are shown as red rhombs; wells with rasters (no LAS) are showing with black dots, and cyan colored wells indicate wells without any current raster or LAS (digital) data.

Throughout the project, selected items (e.g., in-house digitized well logs (Figure 3.3.3) and post peer-review but pre-publication articles (Figure 3.3.4)) were uploaded to NETL’s EDX site.

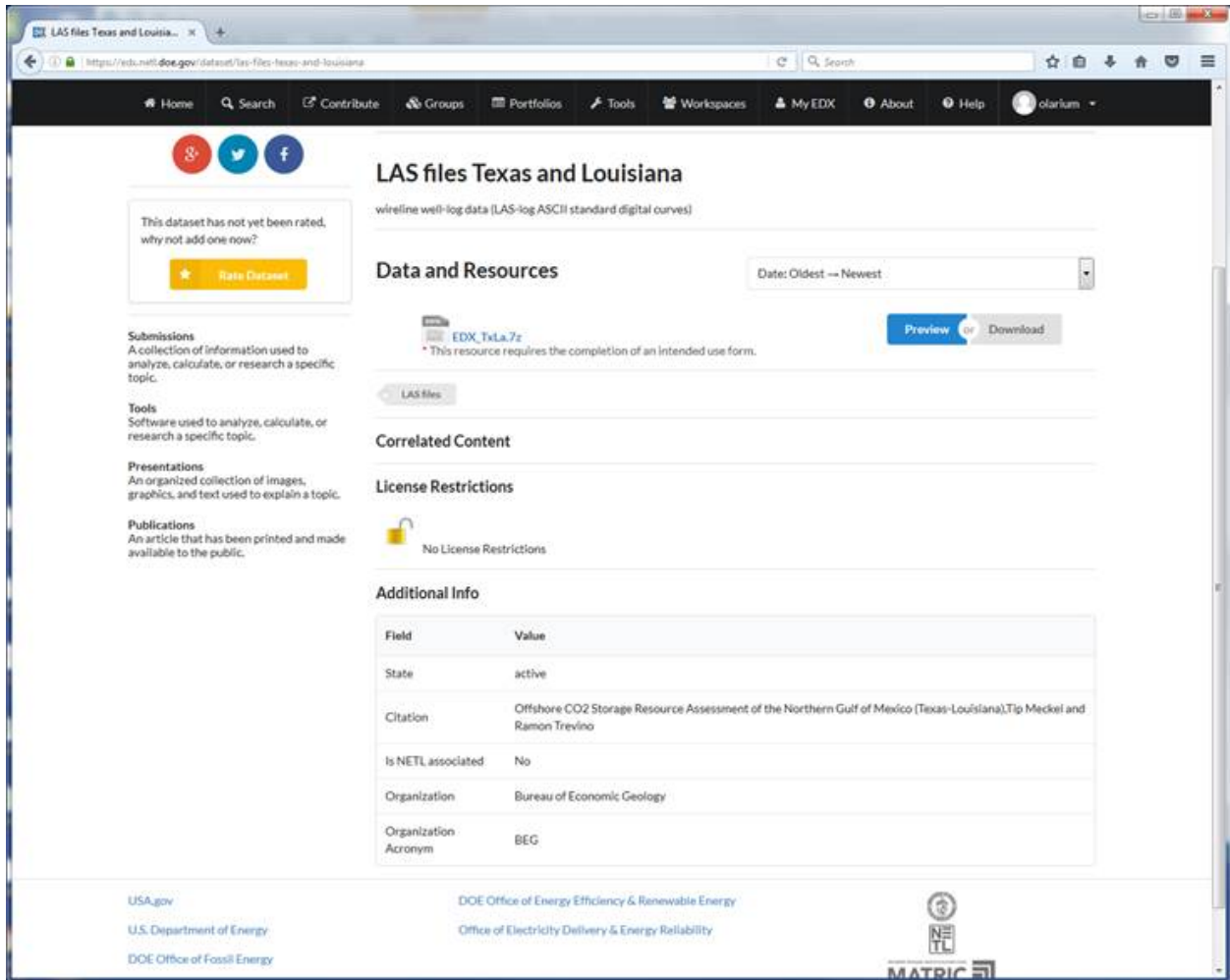


Figure 3.3.3 – Upload of 150 in-house digitized LAS SP well logs from the project database to the NETL EDX site.

**Edit Resources**

- preprint-Klokov-Trevino-M...
- Add new resource

**Submission Summary** View Submission Short Form: Off

**Contribution**

Public

**Type**

Dataset  Tool  Presentation  **Publication**

**Title \*** **URL \***

Diffraction imaging for seal evaluation using ultra high resolution 3D seismic dat: /dataset/ http-dx-doi-org-10-1016-j-mar:

**Description \***

To evaluate the ability for seal intervals to retain fluids in underlying reservoirs, we performed diffraction analysis of the shallow intervals (above 200 m) imaged by high-resolution P-Cable seismic data. We isolated diffractions from the P-Cable data and analyzed diffraction strength across the section, and observed both narrow-linear and broad-sinuuous zones of high diffractivity. We interpreted these broad regions to be a response to variable fluid composition saturation including hydrocarbons, which may have escaped from underlying reservoirs.

**Citation \***

**Generate Citation** Klokov, A., R. H. Treviño, and T. A. Meckel, 2017, Diffraction imaging for seal evaluation using ultra high resolution 3D seismic data: Marine and Petroleum Geology, v. 82, p. 85-96.

**Keywords \***

Fractures x Gulf of Mexico x P-cable x Saturation x shallow seismic x ultra-high resolution 3D x

Figure 3.3.4 – Screen shot of the submission summary screen verifying submission of Klokov et al. (2017) to the NETL EDX site.

## 4 **Task 4.0 - Dynamic Capacity Assessments**

### 4.1 **Subtask 4.1 – Statistical Analysis of Production Data**

The production history and geological data for offshore GOM (Gulf of Mexico) oil and gas fields was obtained from Seni et al. (1997). The data for 100 fields in the GOM includes monthly production history data (oil, gas, and water) as well as reservoir petrophysical properties, drive mechanisms, trap type, and reservoir age. The volumes are reported in surface standard conditions, and we used calculated oil formation volume factor, water formation volume factor, and gas expansion factor to infer, respective, volumes at reservoir conditions.

Decline Curve Analysis (DCA) methodology is usually used for forecasting gas/oil production using historical production data. In the context of geo-sequestration (GS), DCA can be used as a proxy predictor for how historically productive oil and gas reservoirs will function as CO<sub>2</sub> injection reservoirs. We analyzed gas production data from 21 fields containing approximately 500 wells. The wells with good quality production data were studied using decline curve analysis (DCA) theory. The wells' depth vary from 7000-15000 ft. Figure 4.1.1 illustrates the analyzed fields' locations. Table 4.1.1 summarizes the DCA analyzed fields in Texas and Louisiana. Figure 4.1.2 shows the distribution of decline rates for the 21 fields. The plot

shows that most of data fall below 0.002, which is a good indication of the wells' high potential for gas production in the future. Similarly, Figure 4.1.3 shows the distribution of decline coefficients for 21 fields. The plot also illustrates that most of the data fall below 10,000.

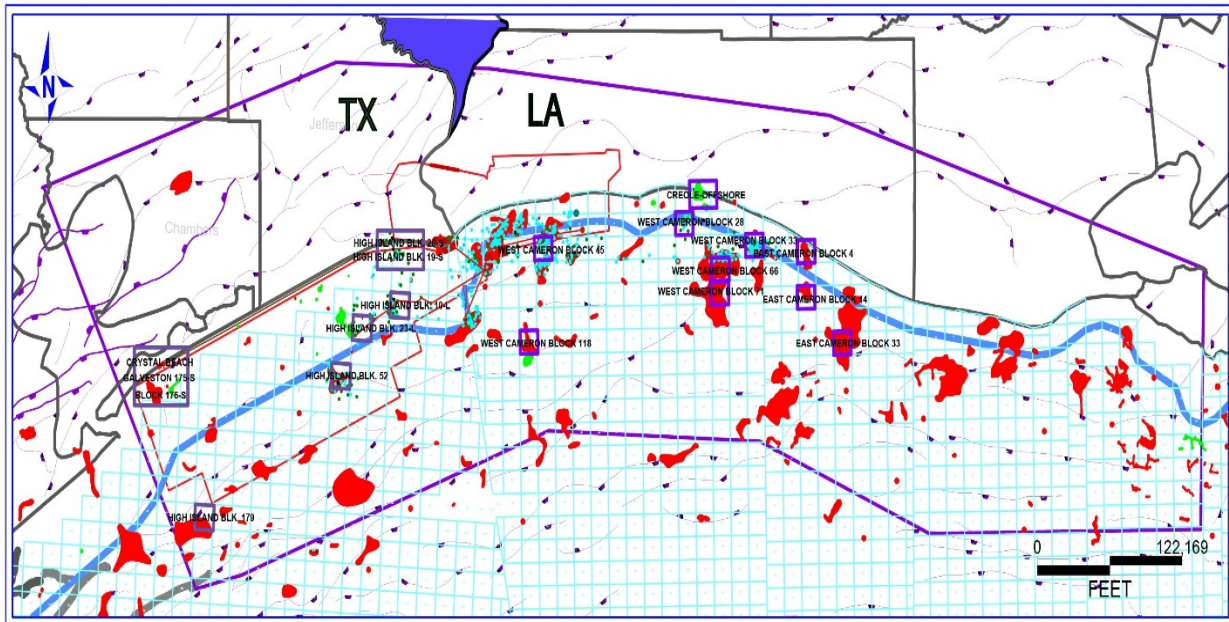


Figure 4.1.1 – The geological location of 21 fields (highlighted) used for decline curve analysis (DCA).

Table 4.1.1 – Texas and Louisiana fields used for DCA analysis states.

Field Name	State	Number of Analyzed Wells for DCA	Depth of the wells
Crystal Beach	Texas	2	8300 ft
Galveston 176-S	Texas	5	6,500-8,500 ft
High Island 10-L	Texas	3	4,800-7,000 ft
High Island 14-L	Texas	15	7,000-10,000 ft
High Island 19-S	Texas	5	5,635 ft
High Island 20-S	Texas	1	5,802 ft
High Island 23-L	Texas	5	10,500-12,000 ft
High Island 52	Texas	19	5,700-9,200 ft
High Island 160	Texas	34	8,350 ft
High Island 179	Texas	40	6,500-11,000 ft
Hog Bayou Offshore	Louisiana	26	8,000-13,000 ft
Creole Offshore	Louisiana	25	6,700 ft
West Cameron 28	Louisiana	8	14,000-15,000 ft
West Cameron 33	Louisiana	24	10,000-11,000 ft
West Cameron 45	Louisiana	99	6,500-10,000 ft
West Cameron 66	Louisiana	72	8,000-12,000 ft
West Cameron 71	Louisiana	81	8,500-14,800 ft



West Cameron 118	Louisiana	17	7,000-9250 ft
East Cameron 4	Louisiana	16	12,200 ft
East Cameron 14	Louisiana	21	11,500-13,500 ft
East Cameron 33	Louisiana	47	11,500-13,500 ft

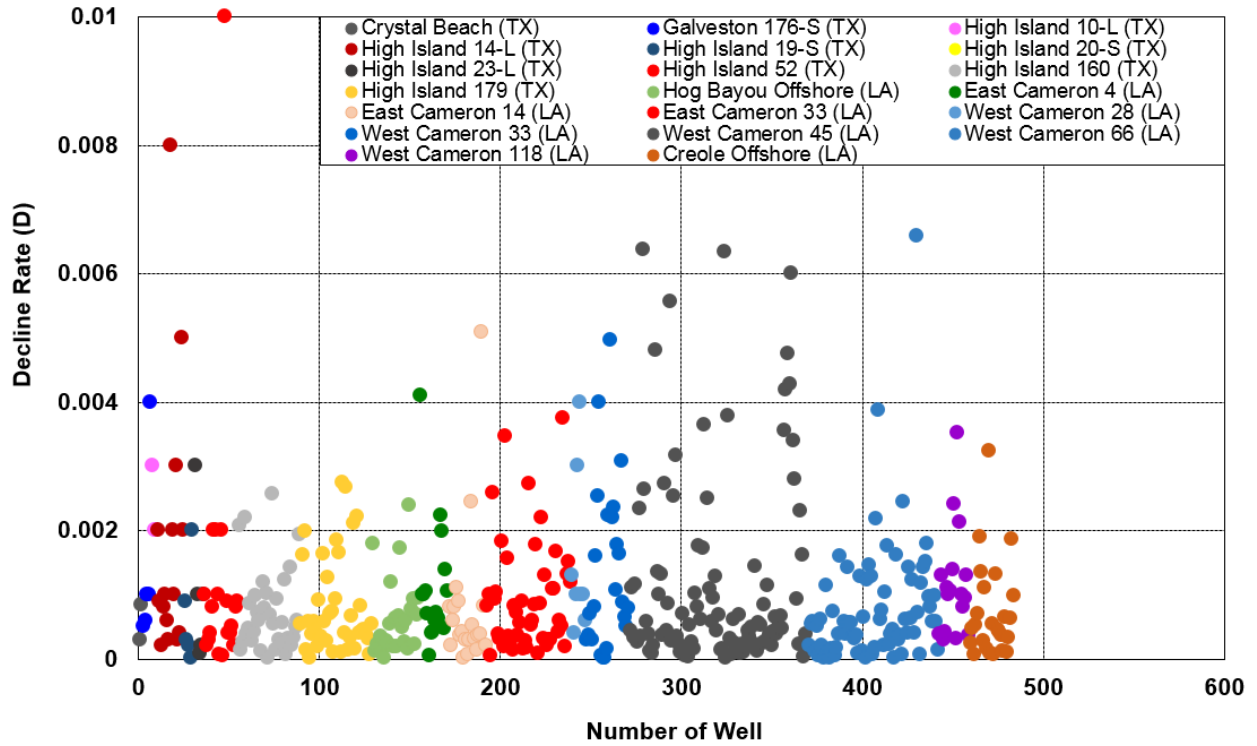


Figure 4.1.2 – Plot of decline rate distribution for wells from the 21 analyzed gas fields.

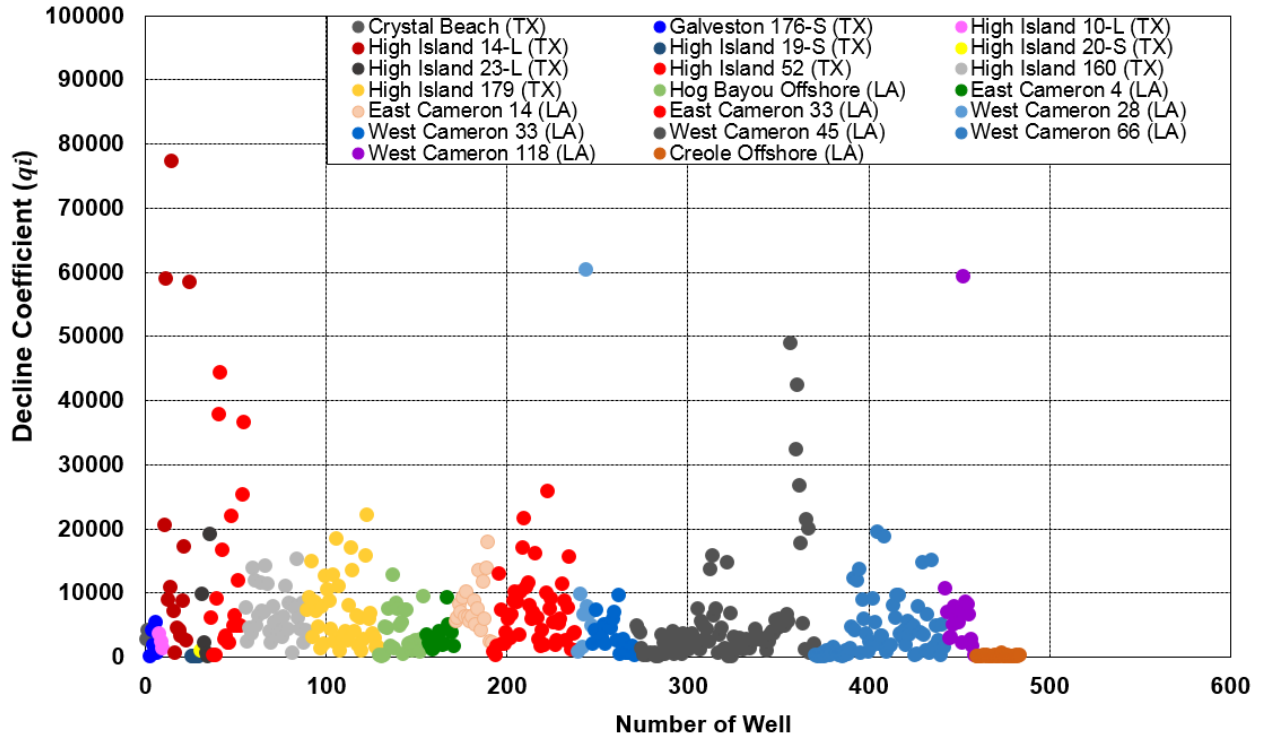


Figure 4.1.3 – Plot of decline coefficient distribution for wells in the 21 analyzed gas fields.

### Statistical Analysis of Production Data (Probability of Non-Exceedance)

Using equation 1 (below) cumulative bulk production (oil and gas) provides insight about the equivalent mass of CO<sub>2</sub> that could be injected.

$$CBP = V_o B_o + \frac{V_g}{5.615 E_g} \quad (1)$$

Where  $CBP$  denotes cumulative bulk production at reservoir conditions,  $V_o$  is total oil production at standard conditions,  $B_o$  is oil formation volume factor,  $V_g$  is total gas production at standard conditions, and  $E_g$  is gas expansion factor. The fields', respective, production zones are Middle and Lower Miocene. The production rate per well,  $q_{well}$ , is obtained by dividing the cumulative bulk production by the number of producing wells in each field,  $N_{well}$ :

$$q_{well} = \frac{CBP}{N_{well}} \quad (2)$$

The probability of non-exceedance (PNE) is calculated using the Weibull plotting position (Makkonen, 2006):

$$PNE(q_{well}) = \frac{m}{N + 1} \quad (3)$$

Where  $m$  is the associated rank number of the value in increasing order and  $N$  is total number of observed values for  $q_{well}$ . The objective of the PNE analysis was to present a statistical investigation concerning production rates in the studied offshore oil and gas reservoirs, with a view to gaining further insight concerning forecasting of likely injection rates for similarly located future CO<sub>2</sub> storage projects.

Figure 4.1.4 shows how reservoir productivity partitions out for two categories based on reservoir age. To better understand the concept of PNE, a probability of 90% was chosen for more clarification. The statistics illustrate that there is a 90% probability that the production rate per well will not exceed 160 MBBL/Year in the Middle Miocene. Similarly, there is a 90% probability that the production rate per well will not exceed 315 MBBL/Year in the Lower Miocene. Figure 4.1.5 shows how reservoir productivity partitions out for two categories based on drive mechanism. The figure illustrates that fields with water drive have higher production rate compared with fields which employ partial water drive. Figure 4.1.6 shows how reservoir productivity partitions out for four categories based on structural trap type. The statistics indicate that rollover anticline structures (into growth faults) yield the best production rates among the four studied reservoir categories.

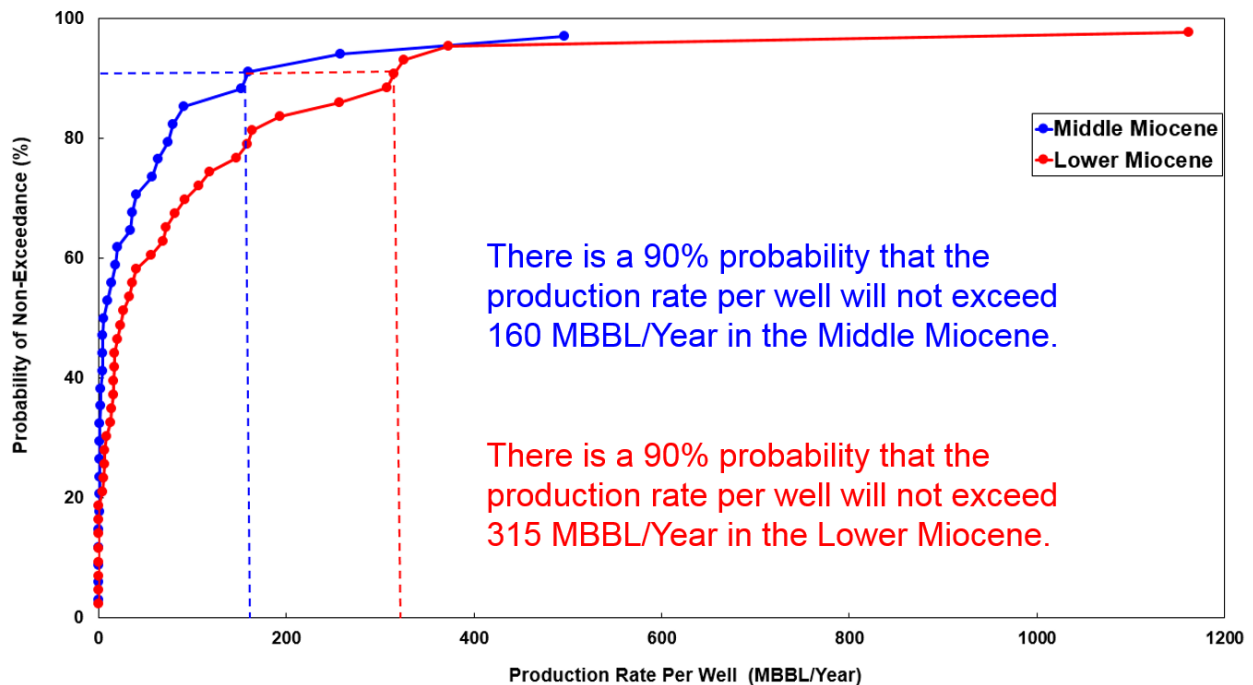


Figure 4.1.4 – Cumulative distribution plot for CBP rate per well in terms of reservoir age.

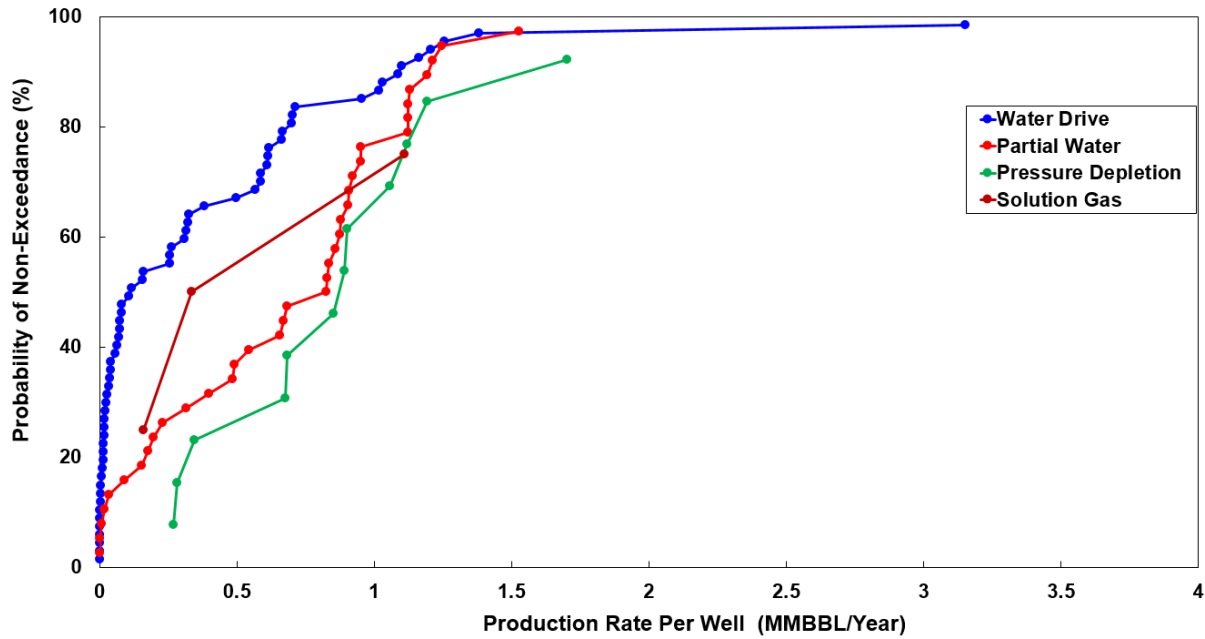


Figure 4.1.5 – Cumulative distribution plot for CBP rate per well in terms of drive mechanism.

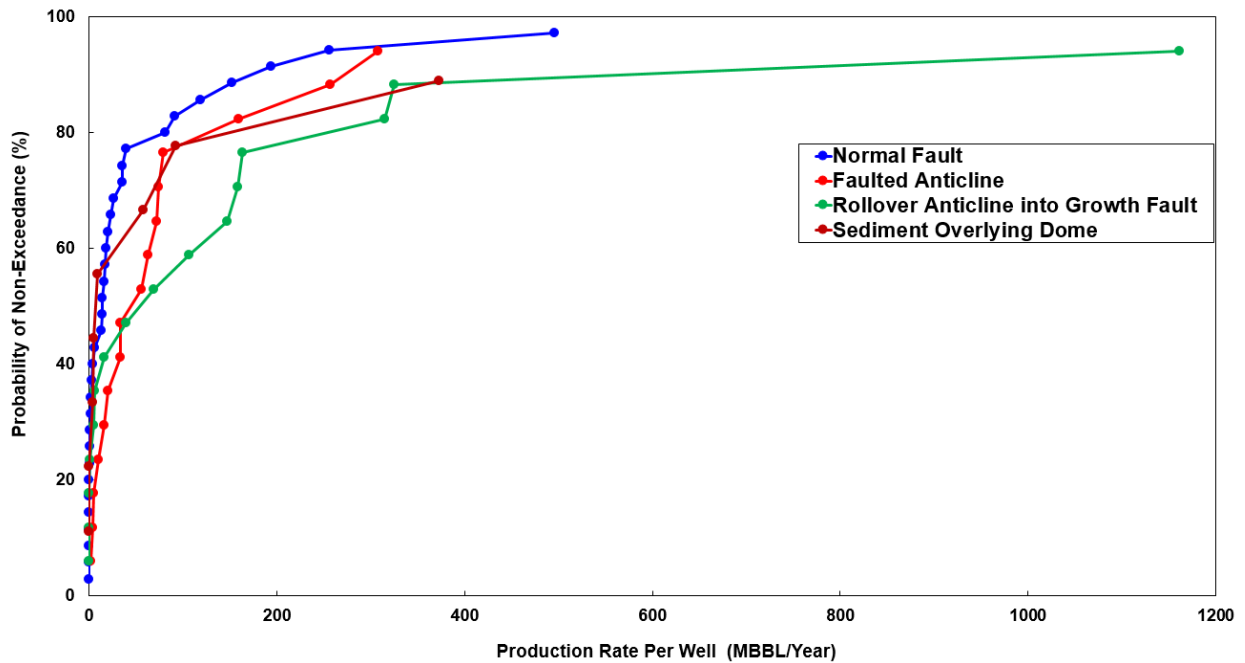


Figure 4.1.6 – Cumulative distribution plot for CBP rate per well in terms of structural trap type.

Figure 4.1.7, Figure 4.1.8, and Figure 4.1.9 show the reservoir productivity partitioning in terms of reservoir porosity, permeability and thickness, respectively. The results illustrate that the porosity range of 0.2-0.3

has the highest production rates and consequently best storage capacity. However, the production does not show higher sensitivity to permeability which might be due to poor prediction of reservoir permeability using literature-derived (i.e., rather than measured) data. Higher reservoir thickness is more favorable for better production rates and reservoir thickness in the range of 5-10 m is optimum for improved productivity and consequently, it is assume that it is also optimum for injectivity.

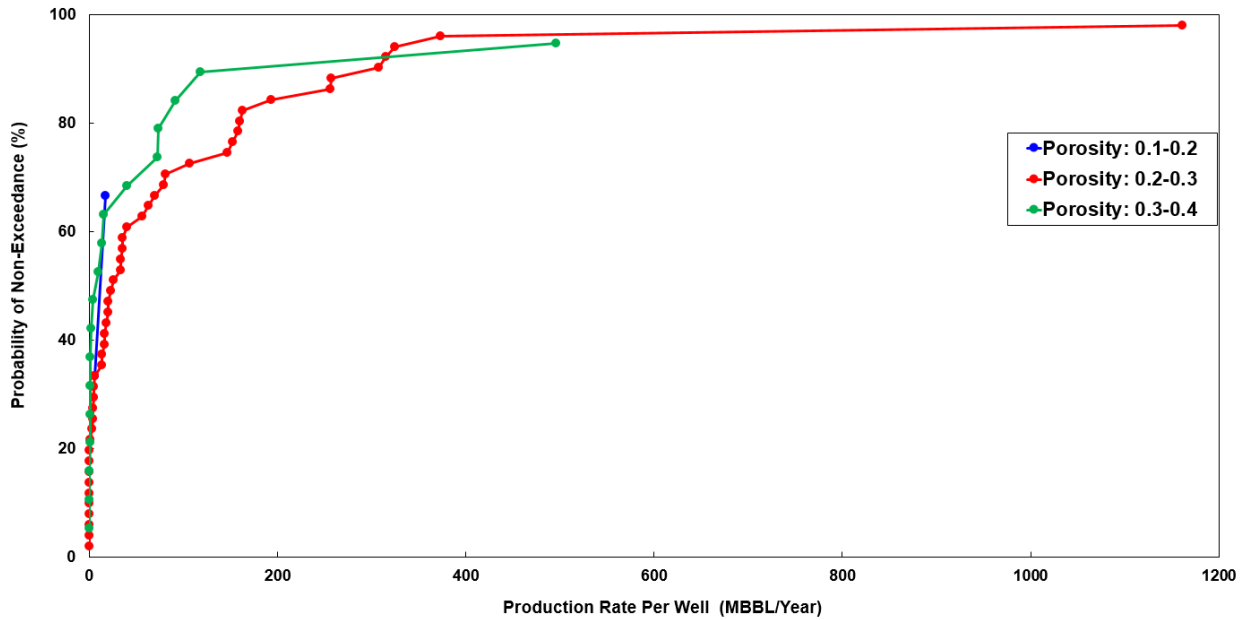


Figure 4.1.7 – Cumulative distribution plot for CBP rate per well in terms of reservoir porosity variation.

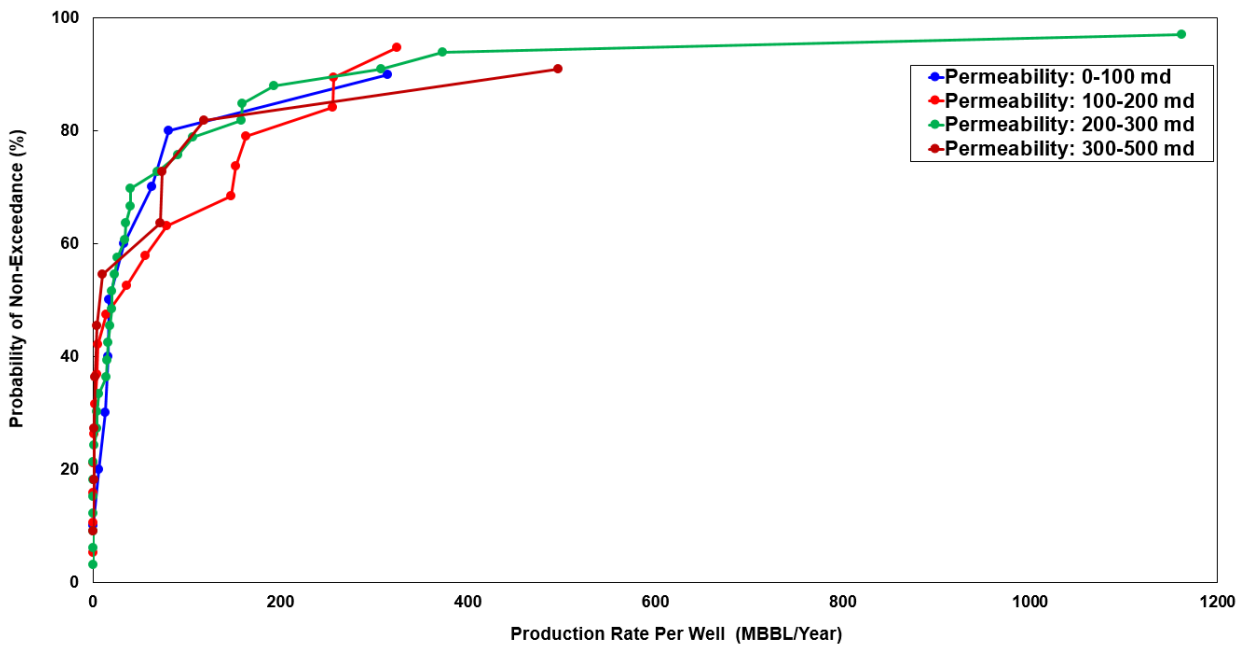


Figure 4.1.8 – Cumulative distribution plot for CBP rate per well in terms of reservoir permeability

variation.

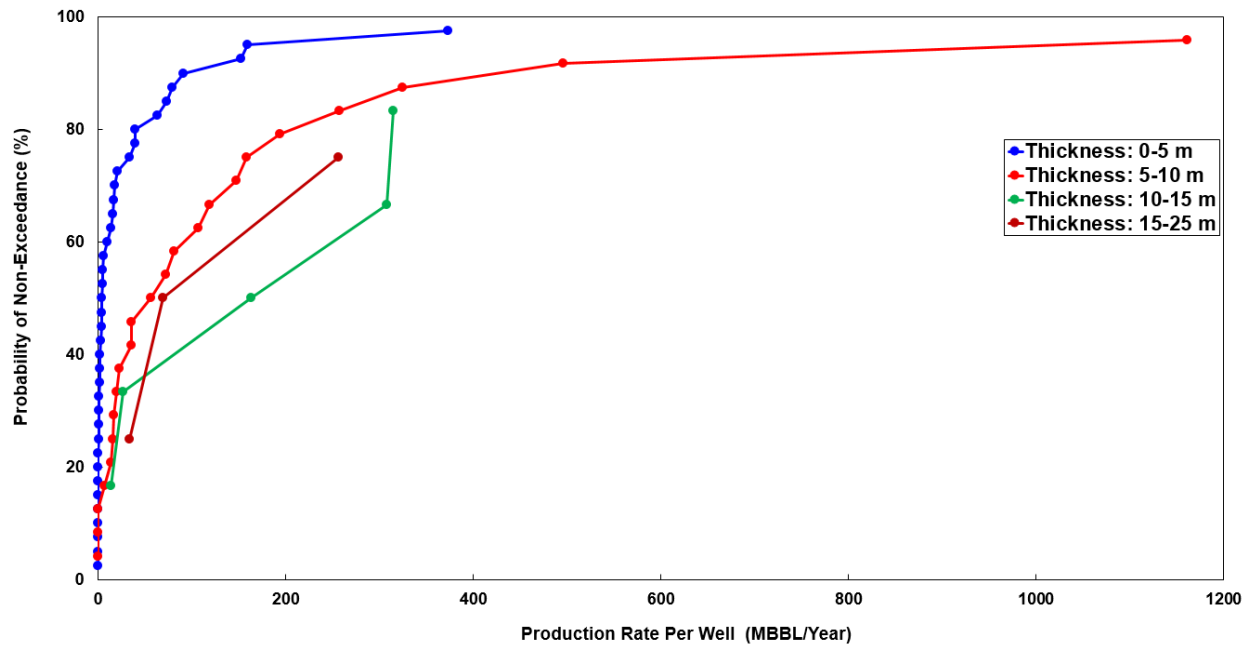


Figure 4.1.9 – Cumulative distribution plot for CBP rate per well in terms of reservoir thickness variation.

According to Goudarzi et al. (2019), “The PNE sensitivity analysis shows that reservoir age, drive mechanism, reservoir trap, and reservoir porosity are the key controlling parameters for productivity and consequently optimum CO<sub>2</sub> storage capacity. Another key finding is the negligible correlation between CBP with reservoir transmissivity and porosity.”

## 4.2 Subtask 4.2 – EASiTool (Enhanced Analytical Simulation Tool) Application

This report presents a review documenting the results from EASiTool analyses including capacity estimates, reservoir performance, summary statistics, and sensitivity analyses. The EASiTool (Enhanced Analytical Simulation Tool) capacity calculator, a GCCC developed Windows application funded under DOE DE-FE0009301, is a closed-form analytical solution that was envisioned to provide fast, yet reliable estimates of CO<sub>2</sub> storage capacities of any geologic formation. It is used as a first screening of study areas containing many storage options, such as the offshore TXLA region.

Results from this first EASiTool screening indicate that the total CO<sub>2</sub> storage capacity of the reservoirs of the analyzed fields is up to ~197 million metric tonnes. We consider this to be a conservative estimate, as the reservoir area required as input for EASiTool was derived from known cumulative production from the studied reservoirs, which constrains the available volume for CO<sub>2</sub> storage.

### EASiTool CO<sub>2</sub> Storage Capacity Estimates

In this subtask we used the EASiTool capacity calculator to assess the dynamic carbon storage capacities of the same 91 oil and gas fields that were selected and analyzed in subtask 4.1. Figure 4.2.1 shows the study area and geographic location of the target reservoirs within the TXLA region delineated by the purple polygon.

The comprehensive data set developed in Subtask 2.2 was used as input for the EASiTool analysis. Because

boundary conditions significantly impact storage capacity, the tool was used assuming both open and closed boundaries to estimate the upper and lower capacity limits, respectively. Given the small reservoir area and thickness of most oil and gas fields in the TXLA region, storage capacity estimates assuming closed boundaries are quite small.

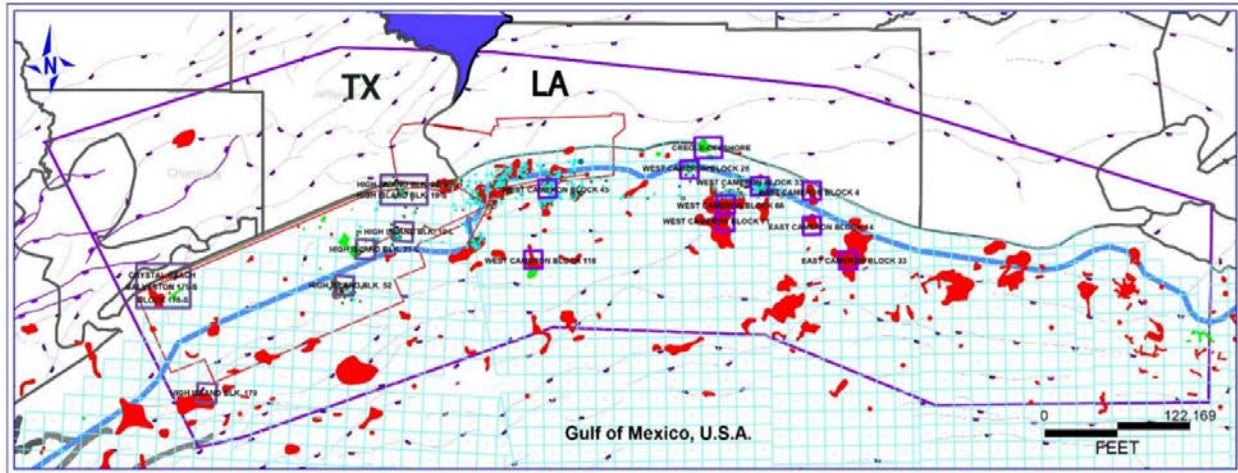


Figure 4.2.1 – Geographical location of the 91 offshore TXLA reservoirs in the study area (purple polygon) where EASiTool CO<sub>2</sub> storage capacity was estimated. Red shapes indicate gas fields, green shapes indicate oil fields.

The total EASiTool-estimated capacity for the studied TXLA region, which is the aggregate of all the individual reservoir storage capacities, ranges from ~1.1 million tonnes (closed boundary scenario) to ~197 million tonnes (open boundary scenario). The wide range exemplifies the strong effect of boundaries on dynamic storage capacity and the importance of adequate reservoir characterization efforts that would capture pressure building, flow confining features that significantly constrain capacity.

Of all the reservoirs studied, West Cameron 71 Field (reservoir 46) provides the largest storage capacity with 16 million tonnes accessible over a period of 30 years through 4 injection wells, in the open boundaries case. Storage capacity estimates grouped according to geologic age of reservoirs are included in Table 4.2.1

For comparison purposes, Table 4.2.1 also includes the storage capacity estimates obtained in subtask 4.1 (Equivalent Mass...) through a production volume replacement approach. Production replacement storage capacity is lower than EASiTool capacity, which was expected as it conservatively assumes that -at least- the volume of produced fluids is available for storage in the reservoir and is consequently constrained by cumulative production to date. Storage capacity results for all reservoirs in the study area are included in Table 4.2.2 EASiTool did not run in cases where the reservoir pressure was too high for CO<sub>2</sub> injection, or where the reservoir area was too small. These cases are identified in table 4.2.2.

Table 4.2.1 – CO<sub>2</sub> storage capacity of oil and gas reservoirs in the TXLA region.

Geologic Age	Capacity EASiTool (Mtonnes) Open Boundary	Capacity EASiTool (Mtonnes) Closed Boundary	*Equivalent Mass CO2 (Mtonnes)
Lower Miocene 1	11.14	0.06361	8.48
Lower Miocene 2	23.69	0.16207	22.85
Lower Miocene 4	77.46	0.40453	56.93
Middle Miocene 4	84.02	0.48424	50.93
Middle Miocene 9	0.58	0.00350	0.01
<b>Total</b>	<b>196.89</b>	<b>1.12</b>	<b>139.20</b>

\*Estimates from Task 4.1 (production volume replacement assessment)

Table 4.2.2 – CO<sub>2</sub> storage capacity of oil and gas reservoirs in the TXLA region.



Geologic Age	Field	Reservoir	Capacity EASiTool (Mtonnes) Open Boundary	Capacity EASiTool (Mtonnes) Closed Boundary	*Equivalent Mass CO2 (Million Metric Tons)
Middle Miocene 4	Crystal Beach (Texas)	7500	0.06	0.00039	0.0124
Lower Miocene 4	Crystal Beach (Texas)	DISCORBIS B, LO.	0.24	0.00174	0.0006
Lower Miocene 2	Crystal Beach (Texas)	S-1	0.57	0.00387	1.0720
Lower Miocene 2	Crystal Beach (Texas)	7700	0.24	0.00149	0.0001
Middle Miocene 4	Galveston 176-S (Texas)	MIOCENE A-12, FB 2	0.13	0.00078	0.0089
Lower Miocene 4	Galveston 176-S (Texas)	MIOCENE D-1	1.17	0.00585	0.0283
Lower Miocene 2	Galveston 176-S (Texas)	MIOCENE S-2*	1.14	0.00789	0.0003
Lower Miocene 2	Galveston 176-S (Texas)	MIOCENE S-1	1.26	0.00749	0.1851
Middle Miocene 4	High Island 10-L (Texas)	6950 SD	0.13	0.00080	0.0002
Middle Miocene 9	High Island 10-L (Texas)	BIG 3	0.16	0.00090	0.0057
Middle Miocene 4	High Island 14-L (Texas)	6700*	0.67	0.00376	0.1186
Lower Miocene 4	High Island 14-L (Texas)	8700	0.98	0.00766	0.9330
Lower Miocene 1	High Island 14-L (Texas)	10000*	5.50	0.03240	7.9197
Middle Miocene 4	High Island 19-S (Texas)	36-B SD.	1.36	0.00104	0.0155
Middle Miocene 4	High Island 20-S (Texas)	5800	Reservoir area too small	Reservoir area too small	0.0007
Lower Miocene 1	High Island 23-L (Texas)	LH-10	0.66	0.00511	0.2070
Lower Miocene 1	High Island 23-L (Texas)	LH-13	4.98	0.02610	0.3502
Middle Miocene 4	High Island 52 (Texas)	M26	Reservoir area too small	Reservoir area too small	0.0467
Middle Miocene 4	High Island 52 (Texas)	M30	Reservoir area too small	Reservoir area too small	0.0244
Lower Miocene 4	High Island 52 (Texas)	M48	0.90	0.00516	0.1938
Lower Miocene 4	High Island 52 (Texas)	M49/M50	2.28	0.01280	0.6572
Lower Miocene 4	High Island 52 (Texas)	M50	4.92	0.02520	4.0975
Middle Miocene 4	High Island 160 (Texas)	B	6.00	0.02290	5.3609
Middle Miocene 4	High Island 160 (Texas)	C	7.20	0.07200	8.6140
Middle Miocene 4	High Island 179 (Texas)	G SD	2.70	0.02320	1.8124
Middle Miocene 4	High Island 179 (Texas)	H8SD	2.10	0.01610	1.6402
Middle Miocene 4	High Island 179 (Texas)	I SD	2.58	0.01170	2.0736
Middle Miocene 4	High Island 179 (Texas)	J3SD	0.72	0.00040	0.2671
Middle Miocene 4	High Island 179 (Texas)	J4SD	1.80	0.00940	0.9085
Lower Miocene 4	High Island 179 (Texas)	N SD	2.26	0.01290	2.0318
Lower Miocene 2	High Island 179 (Texas)	60	2.46	0.01210	0.9795
Middle Miocene 4	Caplen (Texas)	FB-4, 2-B, UP	0.36	0.00225	0.0029
Middle Miocene 9	Caplen (Texas)	MIOCENE 4000	0.42	0.00260	0.0001
Middle Miocene 4	Caplen (Texas)	MIOCENE 4300	0.16	0.00098	0.0065
Middle Miocene 4	Caplen (Texas)	MIOCENE 4430	0.16	0.00098	0.0150
Middle Miocene 4	Caplen (Texas)	MIOCENE 4650	0.16	0.00098	0.0045
Lower Miocene 2	Caplen (Texas)	SIPH D, 7250 SD	0.21	0.00147	0.0039
Lower Miocene 2	Caplen (Texas)	FB-5, 10	0.66	0.00414	0.0752
Lower Miocene 4	East Cameron 14 (Louisiana)	DB-1	4.26	0.02130	4.2010
Lower Miocene 4	East Cameron 14 (Louisiana)	DB-2	5.52	0.02550	4.1895
Lower Miocene 2	East Cameron 14 (Louisiana)	M11-3	0.37	0.00185	0.0856
Middle Miocene 4	East Cameron 33 (Louisiana)	CR54#6	Reservoir pressure too high	Reservoir pressure too high	0.1106
Middle Miocene 4	East Cameron 33 (Louisiana)	NA	2.10	0.01210	1.4990
Lower Miocene 4	East Cameron 33 (Louisiana)	12900	1.62	0.00773	0.8248
Lower Miocene 4	East Cameron 33 (Louisiana)	MA1#10	1.38	0.00628	0.0093
Lower Miocene 4	East Cameron 33 (Louisiana)	NQ	5.70	0.02700	3.4032
Lower Miocene 1	West Cameron 28 (Louisiana)	14000	Reservoir pressure too high	Reservoir pressure too high	0.1311
Lower Miocene 1	West Cameron 28 (Louisiana)	14300	Reservoir pressure too high	Reservoir pressure too high	1.4812
Lower Miocene 1	West Cameron 28 (Louisiana)	15100	Reservoir pressure too high	Reservoir pressure too high	0.0779

**Table 4.2.2 (Cont.)** CO<sub>2</sub> storage capacity of oil and gas reservoirs in the TXLA region.

Geologic Age	Field	Reservoir	Capacity EASiTool (Mtonnes) Open Boundary	Capacity EASiTool (Mtonnes) Closed Boundary	*Equivalent Mass CO <sub>2</sub> (Million Metric Tons)
Middle Miocene 4	West Cameron 33 (Louisiana)	AMPH	Reservoir area too small	Reservoir area too small	0.0057
Lower Miocene 4	West Cameron 33 (Louisiana)	CRIS	Reservoir area too small	Reservoir area too small	0.0038
Lower Miocene 4	West Cameron 33 (Louisiana)	DIS B1	2.82	0.01430	1.7951
Lower Miocene 4	West Cameron 33 (Louisiana)	DIS B2	3.60	0.01480	2.0143
Middle Miocene 4	West Cameron 45 (Louisiana)	AMP5	Reservoir area too small	Reservoir area too small	0.0986
Middle Miocene 4	West Cameron 45 (Louisiana)	AMP6	Reservoir area too small	Reservoir area too small	0.0272
Middle Miocene 4	West Cameron 45 (Louisiana)	AMPH11	Reservoir area too small	Reservoir area too small	0.0820
Middle Miocene 4	West Cameron 45 (Louisiana)	AMPH13	Reservoir area too small	Reservoir area too small	0.1309
Middle Miocene 4	West Cameron 45 (Louisiana)	AMPH14	Reservoir area too small	Reservoir area too small	0.0652
Lower Miocene 4	West Cameron 45 (Louisiana)	DISB1	2.70	0.01410	1.6141
Lower Miocene 4	West Cameron 45 (Louisiana)	DISB2	2.04	0.01040	1.2033
Lower Miocene 4	West Cameron 45 (Louisiana)	DISB5	0.54	0.00294	0.5030
Lower Miocene 4	West Cameron 45 (Louisiana)	E4	0.77	0.00382	0.3336
Lower Miocene 2	West Cameron 45 (Louisiana)	E8/E9/F9	3.60	0.02040	2.1466
Lower Miocene 2	West Cameron 45 (Louisiana)	E9/F4	3.18	0/0193	2.9132
Lower Miocene 2	West Cameron 45 (Louisiana)	F6	9.60	0.09900	15.3838
Middle Miocene 4	West Cameron 66 (Louisiana)	IR	0.53	0.00283	0.0044
Middle Miocene 4	West Cameron 66 (Louisiana)	IT	11.00	0.06510	5.9347
Middle Miocene 4	West Cameron 66 (Louisiana)	JA	7.50	0.03420	2.6521
Lower Miocene 4	West Cameron 66 (Louisiana)	LJ	7.80	0.04160	7.7970
Lower Miocene 4	West Cameron 66 (Louisiana)	MB	Reservoir area too small	Reservoir area too small	0.0080
Lower Miocene 2	West Cameron 66 (Louisiana)	12700	0.04	0.00020	0.0037
Lower Miocene 2	West Cameron 66 (Louisiana)	T	Reservoir pressure too high	Reservoir pressure too high	1.1381
Lower Miocene 2	West Cameron 66 (Louisiana)	TO	0.36	0.00217	0.0000
Middle Miocene 4	West Cameron 71 (Louisiana)	30	4.20	0.02260	2.1510
Middle Miocene 4	West Cameron 71 (Louisiana)	3034	2.64	0.01380	1.7425
Middle Miocene 4	West Cameron 71 (Louisiana)	31	2.40	0.01240	0.7422
Middle Miocene 4	West Cameron 71 (Louisiana)	35	0.53	0.00279	0.2418
Middle Miocene 4	West Cameron 71 (Louisiana)	39	9.00	0.04810	4.0816
Middle Miocene 4	West Cameron 71 (Louisiana)	44	12.50	0.06700	8.8555
Lower Miocene 4	West Cameron 71 (Louisiana)	46	16.00	0.09160	12.9278
Lower Miocene 4	West Cameron 71 (Louisiana)	47	1.56	0.00815	0.6176
Lower Miocene 4	West Cameron 71 (Louisiana)	51	8.40	0.04370	7.5563
Lower Miocene 2	West Cameron 71 (Louisiana)	90	Reservoir pressure too high	Reservoir pressure too high	13.9199
Lower Miocene 2	West Cameron 71 (Louisiana)	94	Reservoir pressure too high	Reservoir pressure too high	2.4796
Lower Miocene 2	West Cameron 71 (Louisiana)	MA10	Reservoir pressure too high	Reservoir pressure too high	10.7366
Lower Miocene 2	West Cameron 71 (Louisiana)	MA2529	Reservoir pressure too high	Reservoir pressure too high	0.7022
Lower Miocene 2	West Cameron 71 (Louisiana)	MA40	Reservoir pressure too high	Reservoir pressure too high	0.7473
Middle Miocene 4	West Cameron 118 (Louisiana)	7150	1.68	0.01700	2.6679
Middle Miocene 4	West Cameron 118 (Louisiana)	9150	2.73	0.01500	0.8794
Middle Miocene 4	West Cameron 118 (Louisiana)	DISCB1	0.66	0.00353	0.0017
Middle Miocene 4	West Cameron 118 (Louisiana)	MO-8	0.26	0.00	0.1156

**Example: West Cameron 71 (Louisiana); Reservoir 46**

An example, the user interface where input parameters are entered is shown in Figure 4.2.2, with parameters corresponding to those of West Cameron 71 (46), the reservoir presenting the largest storage capacity in the area. Figure 4.2.3 shows results for open boundary storage capacity and CO<sub>2</sub> plume extent of four injection wells within the specified reservoir area. Results are shown as they appear on the EASiTool screen. Closed boundary results are displayed in Figure 4.2.4.

1-RESERVOIR PARAMETERS			
Input File Name			
		Min	Max
Pressure [MPa]	34.53	32.53	36.53
Temperature [C]	113.89	108.89	118.89
Thickness [m]	7.71	2.71	12.71
Salinity [mol/Kg]	2	1	3
Porosity [.]	0.27	0.24	0.3
Permeability [mD]	148	50	300
Rock Compressibility [1/Pa]	5e-10	4e-10	6e-10
Max Injection Pressure [MPa]	39.53	38.53	40.53
Reservoir Area [km^2]	15.674		
Basin Area [km^2]	15.674		
Boundary Condition	Open		

2-RELATIVE PERMEABILITY (Brooks-Corey)			
Residual Water Saturation	0.1	0.05	0.2
Residual Gas Saturation	0.7	0.2	0.8
m	3	2	4
n	3	2	4
Kra0	1	0.95	1
Krg0	0.3	0.25	0.35

3-SIMULATION PARAMETERS	
<input checked="" type="checkbox"/> Sensitivity Analysis (Slow)	
Simulation Time [year]	30
Injection Well Radius [m]	0.1
Min Extraction Pressure [MPa]	29
Injection Rate [ton/day/well]	
Extraction Rate [m^3/day/well]	
Max Number of Injectors	4
Number of Extractors	0
Density of Porous Media [Kg/m^3]	
Total Stress Ratio (H/V)	
Biot Coefficient	
Poisson's ratio	
Coefficient of Thermal Expansion [1/K]	
Bottom Hole Temperature Drop [K]	
Young's Modulus [GPa]	
Depth [m]	

Figure 4.2.2 – West Cameron 71 Field (reservoir 46) Input Parameters

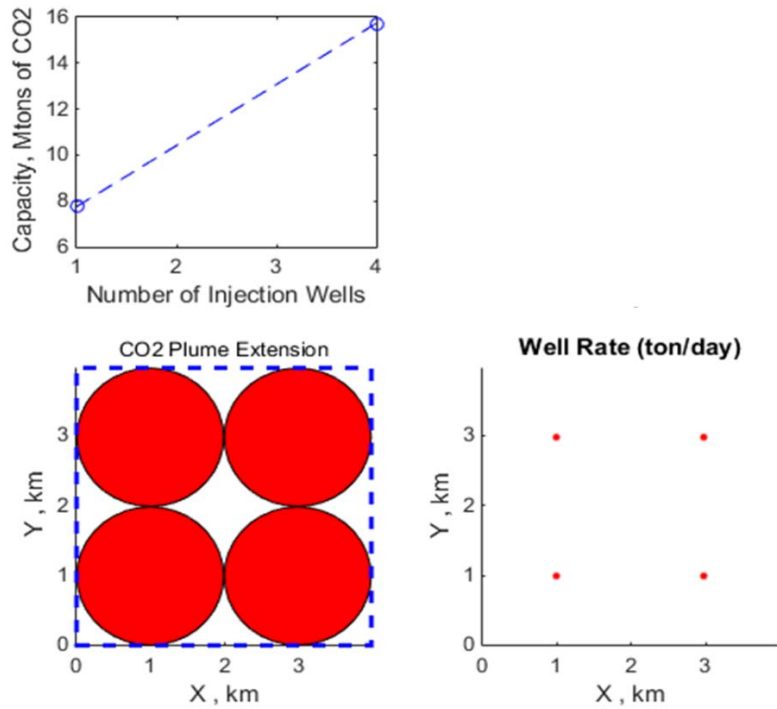


Figure 4.2.3 – Storage capacity results for West Cameron 71 (46). Open boundary scenario.

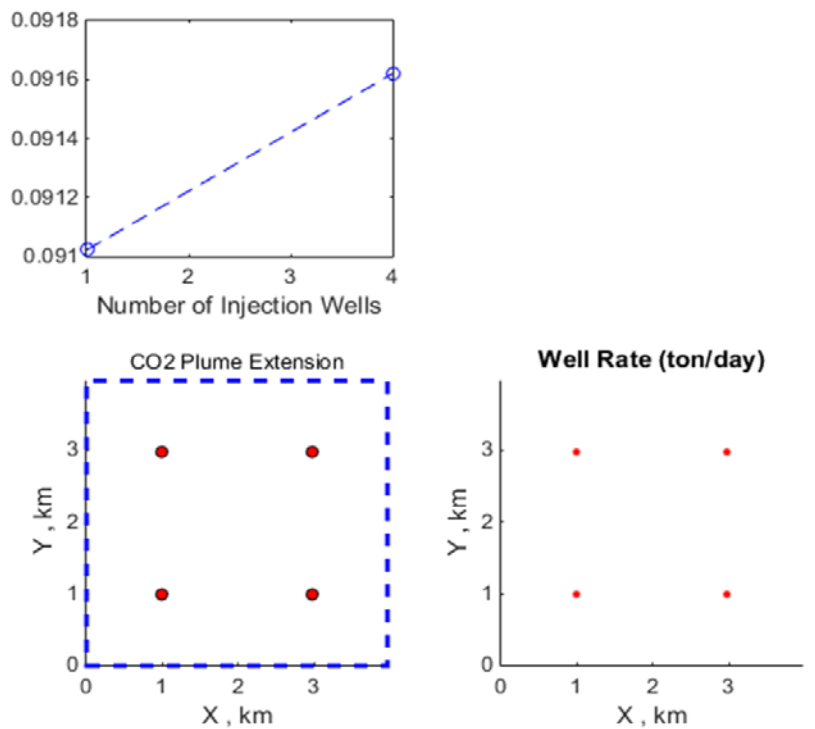


Figure 4.2.4 – Storage capacity results for West Cameron 71 (46), closed boundary scenario.

Another convenient capability of the EASiTool is to easily perform a sensitivity analysis. Figure 4.2.5

shows that in West Cameron 71 (46), reservoir thickness, permeability and pressure are the parameters with the largest impact on storage capacity, with pressure inversely affecting capacity. Another parameter to which storage capacity is sensitive, is fracture pressure, although to a lesser degree. Surprisingly, EASiTool does not identify reservoir porosity as having a strong impact on the dynamic storage capacity of West Cameron 71 (46).

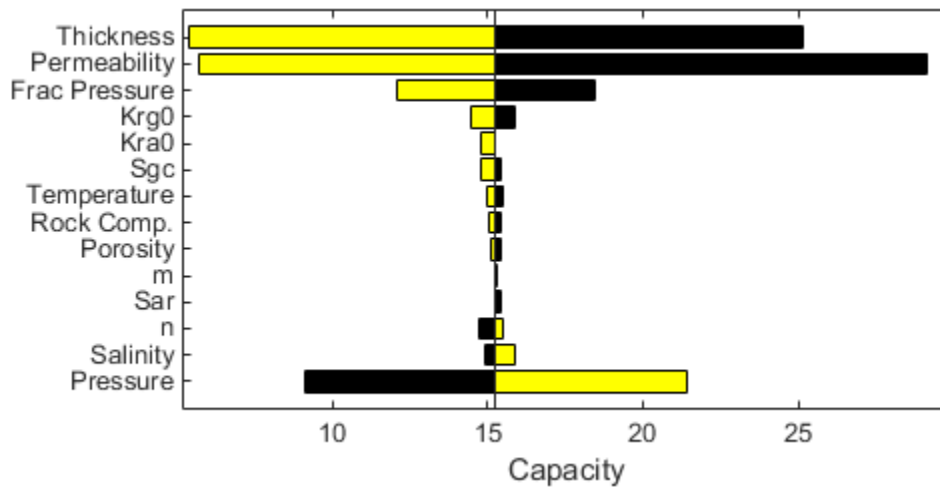


Figure 4.2.5 – Sensitivity Analysis for West Cameron 71 (46).

**Example: High Island 179 (Texas); Reservoir NSD**

Another EASiTool result, High Island 179 Field (NSD reservoir), was selected as an example of a reservoir that is representative of an average capacity in the Lower Miocene 4 production zone. The user interface with input parameters corresponding to High Island 179 (NSD) is shown in Figure 4.2.6. Figure 4.2.7 shows results for open boundary storage capacity (2.26 million metric tonnes), accessible over a period of 8 years, and CO<sub>2</sub> plume extent of one injection well within the specified reservoir area. Results are shown as they appear on the EASiTool screen. Closed boundary results (0.01290 million metric tonnes) are displayed in Figure 4.2.8.

1-RESERVOIR PARAMETERS			
Input File Name			
	Min	Max	
Pressure [MPa]	38.75	36.75	40.74
Temperature [C]	93.33	88.33	98.33
Thickness [m]	5.63	1.63	9.63
Salinity [mol/Kg]	2	1	3
Porosity [-]	0.31	0.28	0.34
Permeability [mD]	203	100	300
Rock Compressibility [1/Pa]	5e-10	4e-10	6e-10
Max Injection Pressure [MPa]	43.75	41.75	45.75
Reservoir Area [km <sup>2</sup> ]	2.236		
Basin Area [km <sup>2</sup> ]	2.236		
Boundary Condition	Open		

2-RELATIVE PERMEABILITY (Brooks-Corey)			
Residual Water Saturation	0.1	0.05	0.2
Residual Gas Saturation	0.7	0.5	0.8
m	3	2	4
n	3	2	4
Kra0	1	0.95	1
Krg0	0.3	0.25	0.35

3-SIMULATION PARAMETERS	
<input checked="" type="checkbox"/> Sensitivity Analysis (Slow)	
Simulation Time [year]	8
Injection Well Radius [m]	0.1
Min Extraction Pressure [MPa]	20
Injection Rate [ton/day/well]	
Extraction Rate [m <sup>3</sup> /day/well]	
Max Number of Injectors	1
Number of Extractors	0
Density of Porous Media [Kg/m <sup>3</sup> ]	
Total Stress Ratio (H/V)	
Biot Coefficient	
Poisson's ratio	
Coefficient of Thermal Expansion [1/K]	
Bottom Hole Temperature Drop [K]	
Young's Modulus [GPa]	
Depth [m]	

Figure 4.2.6 – High Island 179 (NSD) Input Parameters

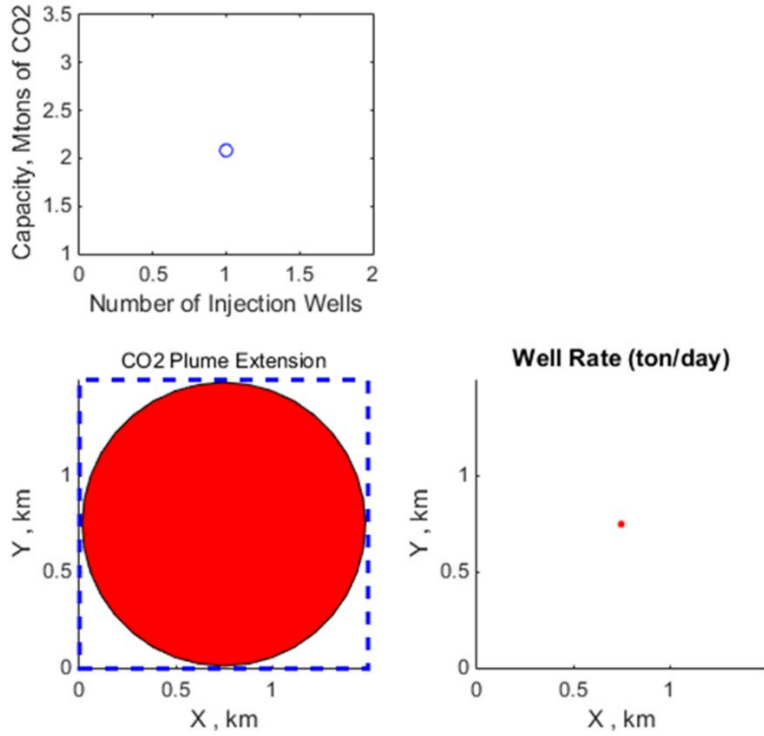


Figure 4.2.7 – Storage capacity results for High Island 179 (NSD). Open boundary scenario.

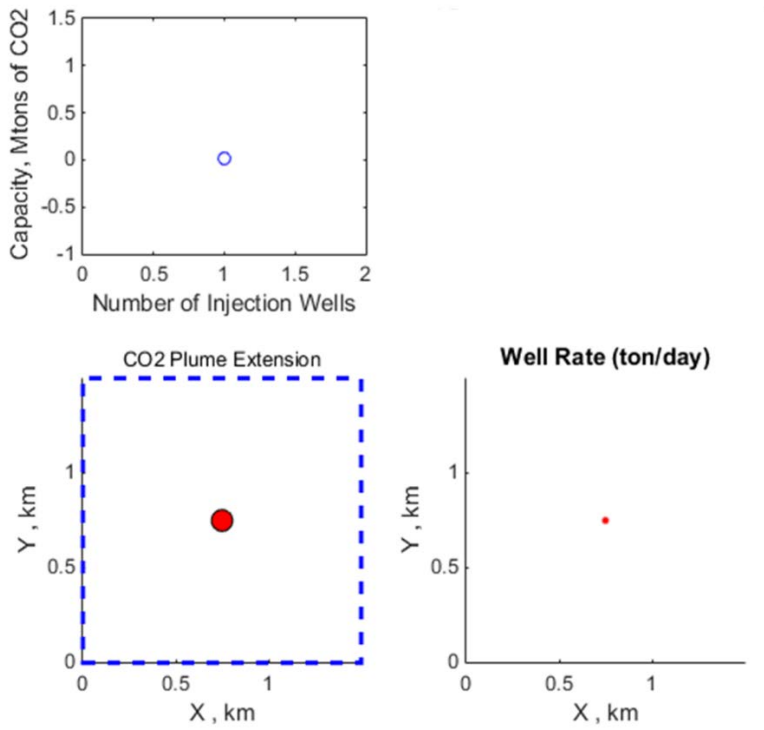


Figure 4.2.8 – Storage capacity results for High Island 179 (NSD), open boundary scenario.

Figure 4.2.9 shows that in High Island 179 (NSD) the largest impact on storage capacity comes from reservoir thickness, permeability, fracture pressure, and reservoir pressure, with pressure inversely affecting capacity. In this case, capacity is less sensitive to permeability than in West Cameron, but more sensitive to fracture pressure.

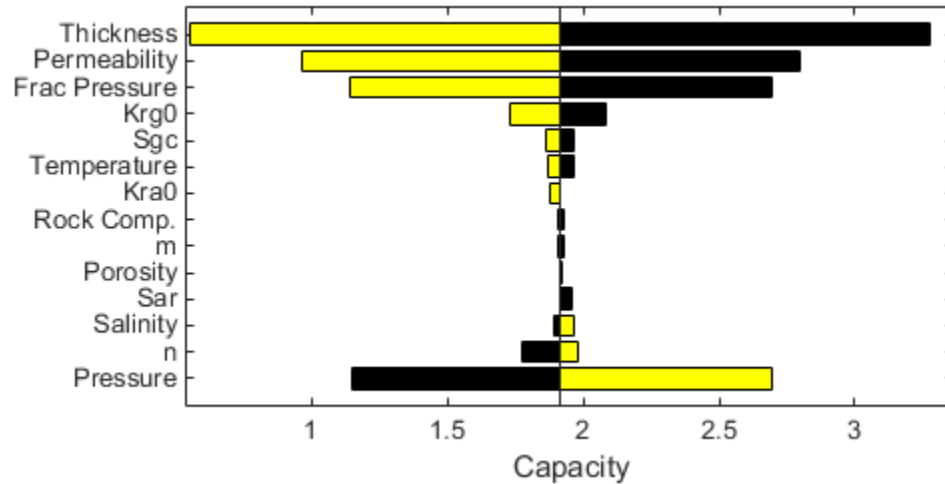


Figure 4.2.9 – Storage capacity results for High Island 179 (NSD). Open boundary scenario.

### **Reservoir Performance**

Reservoir CO<sub>2</sub> injectivity is easy to estimate with EASiTool, given that it not only provides storage capacity but also the time it takes the CO<sub>2</sub> plume to reach the edge of the reservoir volume. For this reason, reservoir injectivity was used as a proxy for reservoir performance. In this task, injectivity refers to the rate at which CO<sub>2</sub> must be injected into the provided reservoir volume so it reaches the open boundary storage capacity by the estimated time to reach that capacity.

The estimate of the time it takes the CO<sub>2</sub> injection operation to reach the maximum capacity in the open boundary case was estimated with EASiTool in an iterative manner. Table 4.2.3 contains estimates of this time with reservoir injectivity as a function of tonnes of CO<sub>2</sub> injected per year, and the number of injector wells required by the injection operation. Dashes in Table 4.2.3 refer to reservoirs for which EASiTool did not run.



Table 4.2.3 – Performance of oil and gas reservoirs in the TXLA region.

Geologic Age	Field	Reservoir	Time to reach capacity (yrs)	Injectivity (Mtonnes/yr)
Middle Miocene 4	Crystal Beach (Texas)	7500	2.5	0.02
Lower Miocene 4	Crystal Beach (Texas)	DISCORBIS B, LO.	2.0	0.12
Lower Miocene 2	Crystal Beach (Texas)	S-1	7.0	0.08
Lower Miocene 2	Crystal Beach (Texas)	7700	3.0	0.08
Middle Miocene 4	Galveston 176-S (Texas)	MIOCENE A-12, FB 2	3.5	0.04
Lower Miocene 4	Galveston 176-S (Texas)	MIOCENE D-1	7.5	0.16
Lower Miocene 2	Galveston 176-S (Texas)	MIOCENE S-2*	7.0	0.16
Lower Miocene 2	Galveston 176-S (Texas)	MIOCENE S-1	7.0	0.18
Middle Miocene 4	High Island 10-L (Texas)	6950 SD	3.5	0.04
Middle Miocene 9	High Island 10-L (Texas)	BIG 3	4.0	0.04
Middle Miocene 4	High Island 14-L (Texas)	6700*	10.0	0.07
Lower Miocene 4	High Island 14-L (Texas)	8700	4.0	0.25
Lower Miocene 1	High Island 14-L (Texas)	10000*	25.0	0.22
Middle Miocene 4	High Island 19-S (Texas)	36-B SD.	4.5	0.30
Middle Miocene 4	High Island 20-S (Texas)	5800	-	-
Lower Miocene 1	High Island 23-L (Texas)	LH-10	6	0.11
Lower Miocene 1	High Island 23-L (Texas)	LH-13	7	0.71
Middle Miocene 4	High Island 52 (Texas)	M26	-	-
Middle Miocene 4	High Island 52 (Texas)	M30	-	-
Lower Miocene 4	High Island 52 (Texas)	M48	12	0.08
Lower Miocene 4	High Island 52 (Texas)	M49/M50	12	0.19
Lower Miocene 4	High Island 52 (Texas)	M50	12.3	0.40
Middle Miocene 4	High Island 160 (Texas)	B	30	0.20
Middle Miocene 4	High Island 160 (Texas)	C	30	0.24
Middle Miocene 4	High Island 179 (Texas)	G SD	30	0.09
Middle Miocene 4	High Island 179 (Texas)	H8SD	30	0.07
Middle Miocene 4	High Island 179 (Texas)	I SD	20	0.13
Middle Miocene 4	High Island 179 (Texas)	J3SD	20	0.04
Middle Miocene 4	High Island 179 (Texas)	J4SD	12	0.15
Lower Miocene 4	High Island 179 (Texas)	N SD	8	0.28
Lower Miocene 2	High Island 179 (Texas)	60	4	0.62
Middle Miocene 4	Caplen (Texas)	FB-4, 2-B, UP	6	0.06
Middle Miocene 9	Caplen (Texas)	MIOCENE 4000	7.5	0.06
Middle Miocene 4	Caplen (Texas)	MIOCENE 4300	3.5	0.04
Middle Miocene 4	Caplen (Texas)	MIOCENE 4430	3.5	0.04
Middle Miocene 4	Caplen (Texas)	MIOCENE 4650	3.5	0.04
Lower Miocene 2	Caplen (Texas)	SIPH D, 7250 SD	5	0.04
Lower Miocene 2	Caplen (Texas)	FB-5, 10	2.8	0.24
Lower Miocene 4	East Cameron 14 (Louisiana)	DB-1	19.5	0.22
Lower Miocene 4	East Cameron 14 (Louisiana)	DB-2	14	0.39
Lower Miocene 2	East Cameron 14 (Louisiana)	M11-3	10.5	0.04
Middle Miocene 4	East Cameron 33 (Louisiana)	CR54#6	-	-
Middle Miocene 4	East Cameron 33 (Louisiana)	NA	10.0	-
Lower Miocene 4	East Cameron 33 (Louisiana)	12900	10	0.16
Lower Miocene 4	East Cameron 33 (Louisiana)	MA1#10	8	0.17
Lower Miocene 4	East Cameron 33 (Louisiana)	NQ	20	0.29
Lower Miocene 1	West Cameron 28 (Louisiana)	14000	-	-
Lower Miocene 1	West Cameron 28 (Louisiana)	14300	-	-
Lower Miocene 1	West Cameron 28 (Louisiana)	15100	-	-

**Table 4.2.3 (Cont.)** Performance of oil and gas reservoirs in the TXLA region.

Geologic Age	Field	Reservoir	Time to reach capacity (yrs)	Injectivity (Mtonnes/yr)
Middle Miocene 4	West Cameron 33 (Louisiana)	AMPH	-	-
Lower Miocene 4	West Cameron 33 (Louisiana)	CRIS	-	-
Lower Miocene 4	West Cameron 33 (Louisiana)	DIS B1	9.0	0.31
Lower Miocene 4	West Cameron 33 (Louisiana)	DIS B2	9.0	0.40
Middle Miocene 4	West Cameron 45 (Louisiana)	AMP5	-	-
Middle Miocene 4	West Cameron 45 (Louisiana)	AMP6	-	-
Middle Miocene 4	West Cameron 45 (Louisiana)	AMPH11	-	-
Middle Miocene 4	West Cameron 45 (Louisiana)	AMPH13	-	-
Middle Miocene 4	West Cameron 45 (Louisiana)	AMPH14	-	-
Lower Miocene 4	West Cameron 45 (Louisiana)	DISB1	10.0	0.27
Lower Miocene 4	West Cameron 45 (Louisiana)	DISB2	10.0	0.20
Lower Miocene 4	West Cameron 45 (Louisiana)	DISB5	2.0	0.27
Lower Miocene 4	West Cameron 45 (Louisiana)	E4	6.0	0.13
Lower Miocene 2	West Cameron 45 (Louisiana)	E8/E9/F9	8.0	0.45
Lower Miocene 2	West Cameron 45 (Louisiana)	E9/F4	12.0	0.3
Lower Miocene 2	West Cameron 45 (Louisiana)	F6	25	0.38
Middle Miocene 4	West Cameron 66 (Louisiana)	IR	15	0.04
Middle Miocene 4	West Cameron 66 (Louisiana)	IT	30	0.4
Middle Miocene 4	West Cameron 66 (Louisiana)	JA	30	0.3
Lower Miocene 4	West Cameron 66 (Louisiana)	LJ	23	0.34
Lower Miocene 4	West Cameron 66 (Louisiana)	MB		
Lower Miocene 2	West Cameron 66 (Louisiana)	12700	0.3	0.12
Lower Miocene 2	West Cameron 66 (Louisiana)	T		
Lower Miocene 2	West Cameron 66 (Louisiana)	TO	2	0.18
Middle Miocene 4	West Cameron 71 (Louisiana)	30	35	0.12
Middle Miocene 4	West Cameron 71 (Louisiana)	3034	25	0.11
Middle Miocene 4	West Cameron 71 (Louisiana)	31	12	0.20
Middle Miocene 4	West Cameron 71 (Louisiana)	35	5.5	0.10
Middle Miocene 4	West Cameron 71 (Louisiana)	39	25	0.36
Middle Miocene 4	West Cameron 71 (Louisiana)	44	25	0.50
Lower Miocene 4	West Cameron 71 (Louisiana)	46	30	0.53
Lower Miocene 4	West Cameron 71 (Louisiana)	47	8.5	0.18
Lower Miocene 4	West Cameron 71 (Louisiana)	51	18	0.47
Lower Miocene 2	West Cameron 71 (Louisiana)	90	-	-
Lower Miocene 2	West Cameron 71 (Louisiana)	94	-	-
Lower Miocene 2	West Cameron 71 (Louisiana)	MA10	-	-
Lower Miocene 2	West Cameron 71 (Louisiana)	MA2529	-	-
Lower Miocene 2	West Cameron 71 (Louisiana)	MA40	-	-
Middle Miocene 4	West Cameron 118 (Louisiana)	7150	7.5	0.22
Middle Miocene 4	West Cameron 118 (Louisiana)	9150	18	0.15
Middle Miocene 4	West Cameron 118 (Louisiana)	DISCB1	2.5	0.26
Middle Miocene 4	West Cameron 118 (Louisiana)	MO-8	2.8	0.1

## Summary Statistics

A cumulative distribution function of estimated CO<sub>2</sub> storage capacities in the offshore TXLA study area (Figure 4.2.10) shows that storage capacities across the region are not normally distributed. Fifty percent of the reservoirs have storage capacities of 1.5 million tonnes or less, meaning that the 50% probability is significantly lower than the average storage capacity (2.8285 million tonnes), with a standard deviation of 3.2881 million tonnes. Ninety percent of the reservoirs have capacities of 7.5 million tonnes or less.

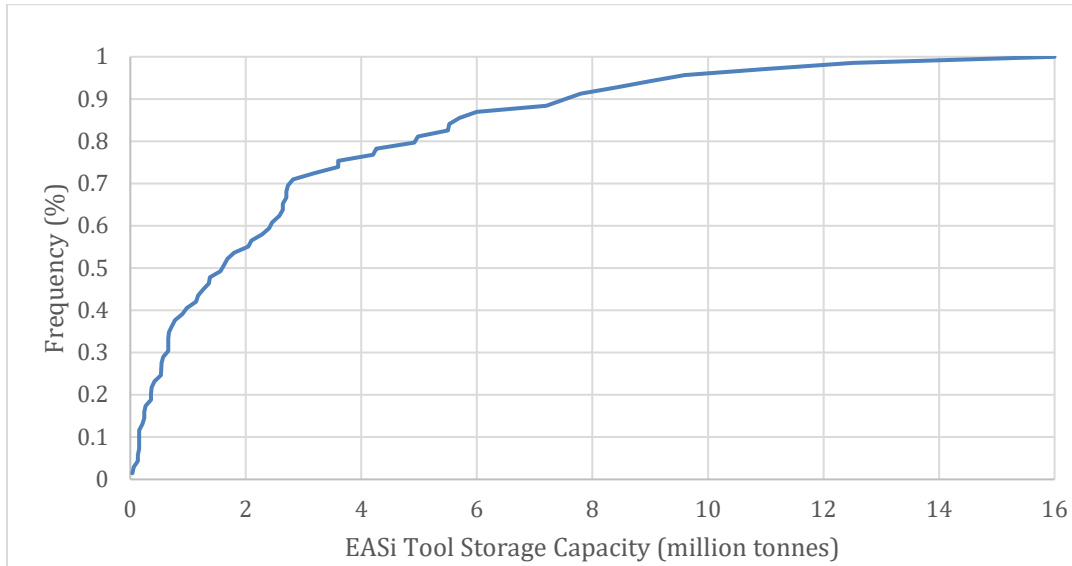


Figure 4.2.10 – Cumulative Distribution Function of storage capacities of oil and gas reservoirs in the TXLA study area.

## 5 Task 5.0 - Outreach and Stakeholder Engagement

The examples of outreach and stakeholder engagement included here are not an exhaustive list. Rather, they represent a small sample of the efforts that were reported on a quarterly basis throughout the project’s four years.

Staff members on the project conducted sustained outreach to the public and stakeholders throughout the duration of the project. The efforts continued until almost the end of the project’s period of performance (Figure 5.1.1, Figure 5.1.2, Figure 5.2.1 and Figure 5.2.2) and commenced in the project’s first quarter as reported by project subrecipient, Southern States Energy Board (SSEB), with the following three entries from 2015:

**9/27/15:** A description of the project was provided in an “SSEB Carbon Management Programs” presentation to the Southern State Energy Board’s Executive Committee. Participants included:

- Rep. Rocky Adkins, KY
- Kathryn Baskin, SSEB
- Heather Breeden, SSEB
- Senate President Bill Cole, WV
- Rep. Myra Crownover, TX
- Turney Foshee, SSEB
- Gary Garrett, SSEB

- Rep. Jim Gooch, KY
- Kimberly Sams Gray, SSEB
- Jeff Herholdt, WV Energy Division
- Larry Malone, WV Office of the Governor
- Ken Nemeth, SSEB
- Sen. Mark Norris, TN
- Jim Powell, SSEB Federal Representative
- Rep. John Ragan, TN
- Kathy Sammons, SSEB
- Sen. Bill Sandifer, SC
- Sen. Brandon Smith, KY
- Ted Thomas, AR Office of the Governor
- Gov. Earl Ray Tomblin, WV, 2014-2015 SSEB Chairman
- Sen. Frank Wagner, VA
- Rep. Weldon Watson, OK
- Christopher Wells, SSEB
- Sen. Eddie Joe Williams, AR

Fact sheets were provided in the registration folders provided to all participants (over 200 individuals) and in the folders provided to board members (governors, state legislators, and governor’s alternates) during their business session on 9/28/15.

**10/14/15:** SSEB launched a webpage for the Southeast Offshore Storage Resource Assessment project, which includes a description of the Texas-Louisiana project. Additional modifications to the site are forthcoming to divide content and provide more detailed descriptions of project locations, goals, and objectives. <http://www.sseb.org/programs/sosra/>

**10/15/15:** A presentation was given by Kimberly Sams Gray (SSEB project Principal Investigator) to SSEB Associate Members in St. Louis, MO. The presentation included mention of the “TXLA” project with UT BEG.

## **5.1 Subtask 5.1 – Local Public and Stakeholder Outreach**

On April 15, 2019 project researcher, Vanessa Nuñez-López, presented at the monthly lunch meeting of the Austin Women in Oil & Gas. Roughly 20 professionals attended and networked with Vanessa to learn more about CCS.



Figure 5.1.1 – Photo of Vanessa Nunez-Lopez (standing) at the Austin Women in Oil & Gas seminar luncheon.

On June 11, 2019 Tip Meckel partnered with the Port Arthur, Texas Chamber of Commerce to hold a meeting (Figure 5.1.2) for local decision-makers and stakeholders to learn about current CO<sub>2</sub> management and the available federal 45Q tax credit opportunities and how organizations can qualify to receive significant tax credits for near-term projects that avoid carbon dioxide emissions.

---

NO TCEQ  
REPORTABLE  
EMISSIONS

# CO<sub>2</sub>

MANAGEMENT & AVAILABLE  
45Q TAX CREDIT OPPORTUNITIES

GREATER  
EQUIPMENT  
EFFICIENCIES

FEDERAL GOVERNMENT INCENTIVES

Management of industrial emissions, carbon dioxide, is a topic of broad conversation currently, and likely to play a significant role in policy discussions 2020. It has never been a more important time to understand the implications CO<sub>2</sub> management has for the strong industrial capacity and ongoing energy infrastructure investment in southeast Texas. Among the various real business opportunities currently are the 45Q Tax Credits related to CO<sub>2</sub> capture, utilization, and subsurface storage, including enhanced oil recovery. The timeline for developing projects that qualify for these credits requires serious consideration now.

---

WE INVITE YOU TO ATTEND A MEETING

that will provide current perspectives on CO<sub>2</sub> management in the Texas energy landscape and the basics of 45Q Credits, including ideas for how near-term projects can be developed to qualify for significant tax credits.


## TUESDAY, JUNE 11


12-3 PM, LIGHT LUNCH INCLUDED.


LAMAR STATE COLLEGE PORT ARTHUR  
CARL PARKER MULTIPURPOSE CENTER  
1800 LAKESHORE DRIVE, PORT ARTHUR


CO<sub>2</sub> MUST BE STORED  
GEOLOGICALLY OR UTILIZED IN  
FEEDSTOCK TO RECEIVE TAX CREDITS

20% MORE ENERGY  
PRODUCED THAN STEAM









Please register to attend: ● 409-963-1107 ● pachamber@portarthurtexas.com ● www.portarthurtexas.com

---

Figure 5.1.2 – Flyer for the outreach meeting held by the Port Arthur, Texas Chamber of Commerce with leadership of project PI, Dr. Tip Meckel.

## 5.2 Subtask 5.2 – Regional Outreach

On April 15 and 16, 2019, Ramón Treviño attended a symposium and field trip (Figure 5.2.1) of the American Beach and Shore Preservation Association (ASBPA), Texas Chapter.



Figure 5.2.1 – Photo of attendees of the ASBPA field trip, April 15, 2019, on the last stop of the field trip, Mustang Island, Texas.

The symposium was held at the Harte Research Institute, Texas A&M University-Corpus Christi. As indicated by ASBPA’s website, the organization’s membership comprises a variety of professionals including engineers, scientists, planners, public officials, and other professionals engaged in the management and operation of the shores and beaches of U.S. bays, harbors, oceans and the Great Lakes and who are also interested in the protection, restoration, and management of these resources.

Treviño presented an introductory CCS symposium talk titled, “Carbon Capture and Sequestration (Storage) – CCS: A Climate Change Mitigation Strategy for the Near-Offshore Northwestern Gulf of Mexico.”

Global climate change, specifically sea-level rise, was either an explicit or implicit focus of most of the symposium talks. Treviño’s talk emphasized the potential of CCS to reduce the amount of CO<sub>2</sub> emitted into the atmosphere from CO<sub>2</sub> point sources and thus mitigate sea level rise and its negative impacts on the coast. After the presentation, several audience members, who were previously unfamiliar with the technology, expressed interest in CCS.

On May 9, 2019 project co-PI, Ramón Treviño presented two talks, “What Offshore CCS Will Look Like in The Gulf of Mexico: Perspectives from Texas” and “Monitoring Stored CO<sub>2</sub> to Document Permanence” at the 50<sup>th</sup> annual Offshore Technology Conference in Houston. The goal of the conference is to provide a venue for energy professionals to transfer knowledge and skills to further scientific and technical advancements in offshore environments.

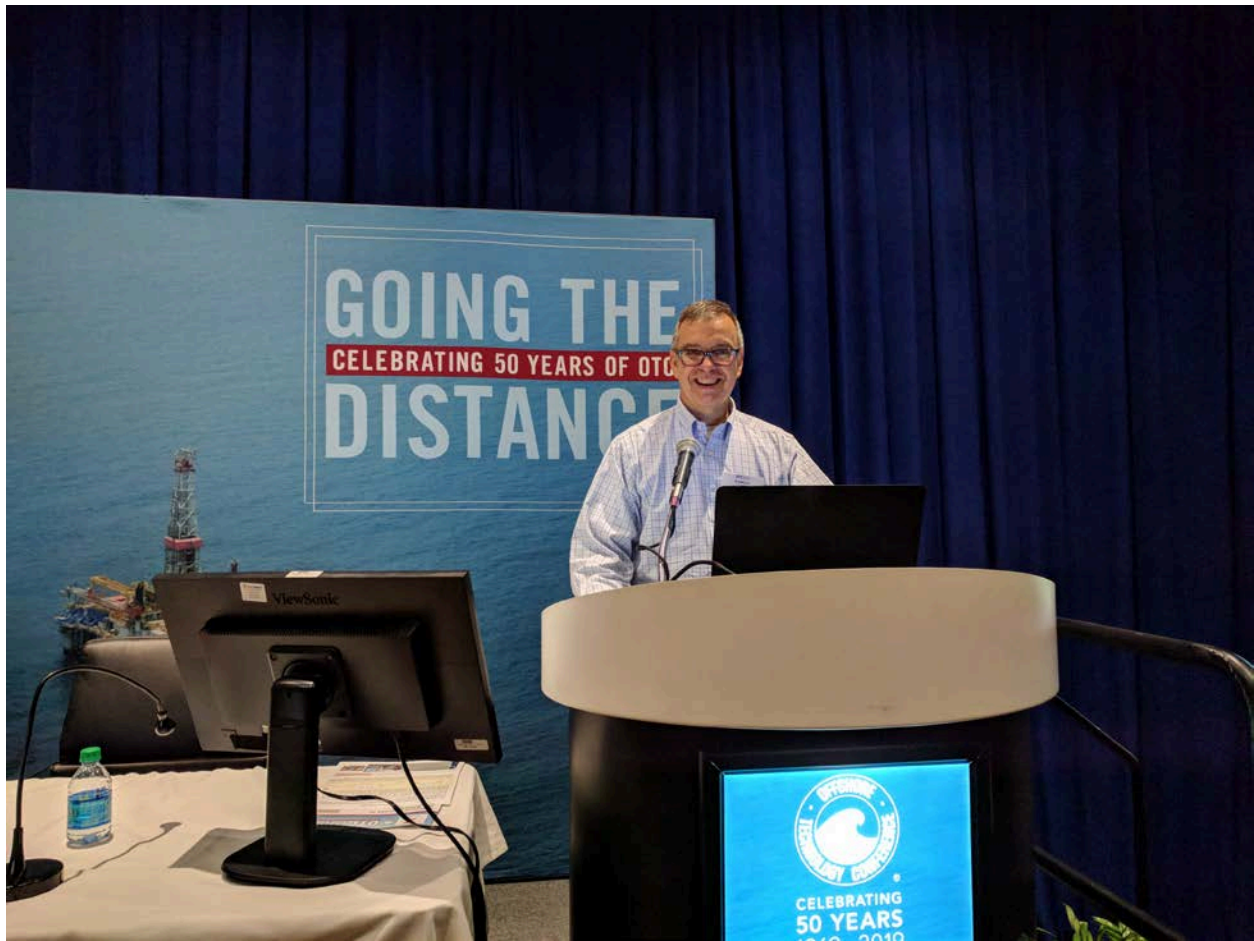


Figure 5.2.2 – Ramón Treviño presenting a CCS talk including results from the project at the 50<sup>th</sup> annual Offshore Technology Conference (OTC) in Houston.

## **6 PRODUCTS**

Complete lists of conference papers, oral and poster presentations may be found in the quarterly RPPRs (research performance progress reports). A small sample, thereof, is provided here.



The following oral presentation was subsequently posted as an extended abstract on the [www.AAPG.org](http://www.AAPG.org) Search and Discovery Datapages© website.

**Offshore CO<sub>2</sub> Storage Resource Assessment of the Northwest Gulf of Mexico Inner Continental Shelf, Upper Texas – Western Louisiana Coast\***

**Ramon H. Trevino<sup>1</sup>, Timothy A. Meckel<sup>1</sup>, Mariana Olariu<sup>1</sup>, Dallas Dunlap<sup>1</sup>, Michael V. Deangelo<sup>1</sup>, Jiemin Lu<sup>1</sup>, Reinaldo Sabbagh<sup>2</sup>, and Alexander Klokov<sup>1</sup>**

Search and Discovery Article #80630 (2018)\*\*  
Posted April 16, 2018

\*Adapted from oral presentation given at 2017 AAPG Annual Convention & Exhibition, Houston, Texas, April 2-5, 2017

\*\*Datapages © 2018 Serial rights given by author. For all other rights contact author directly.

<sup>1</sup>Bureau of Economic Geology, The University of Texas at Austin, Austin, Texas ([ramon.trevino@beg.utexas.edu](mailto:ramon.trevino@beg.utexas.edu))

<sup>2</sup>Jackson School of Geosciences, The University of Texas at Austin, Austin, Texas

**Abstract**

Carbon capture, utilization, and storage (CCUS) continues to be considered one of the most promising technologies for reducing atmospheric emissions from industrial sources of CO<sub>2</sub>. CCUS research programs of the United States and European Union recognize the need to further develop offshore storage resources for successful global deployment of CCUS technologies. Offshore storage of CO<sub>2</sub> has several advantages: (1) Locating sequestration sites away from heavily populated, onshore areas reduces opposition from local populations. (2) Use of offshore sites reduces the difficulty of establishing surface and mineral rights at candidate storage sites; offshore surface and subsurface rights usually belong to a single governmental entity. (3) Offshore storage reduces the risk to underground sources of drinking water. (4) Offshore CCS may provide storage sites near heavily populated coastal areas where onshore sites are unavailable.

The challenge is to assess suitable offshore storage sites that will provide CO<sub>2</sub> emitting industries with a sound environmental alternative to the current practice of venting CO<sub>2</sub> to the atmosphere. The inner continental shelf of the northwestern Gulf of Mexico is an especially prospective CCUS area because it has abundant available geologic data accumulated from decades of hydrocarbon exploration near many large point sources of anthropogenic CO<sub>2</sub>. An ongoing study of the area from Bolivar Peninsula on the upper Texas coast to Vermilion Bay on the Louisiana coast assesses prospective geologic storage resources of depleted oil and gas reservoirs and saline geologic formations for the approximately 8,000 square mile study area. The study, encompassing state and federal waters, utilizes (1) existing rock samples (e.g., whole cores), (2) well logs, and other data from existing or P&A wells, and (3) available 2D, a conventional regional 3D and a high resolution 3D seismic surveys to assess storage resources (e.g., faults, reservoir and seal units, etc.). The study utilizes the available geologic data resources to (1) assess the CO<sub>2</sub> storage capacity of depleted oil and natural gas reservoirs, and (2) assess the ability of saline formations in the region to safely and permanently store nationally-significant amounts of anthropogenic CO<sub>2</sub>. The study also seeks to identify at least one specific site with potential to store at least 30 million metric tons of CO<sub>2</sub> that could be further considered in the future for a commercial or integrated demonstration project.

A poster, resulting from work by project graduate research assistant, Reinaldo Sabbagh, presented at the 2018 AAPG / SEPM annual convention and exhibition, and supported by the current project, was selected as best poster by DEG, Division of Environmental Geoscience. The official notice follows:

Dear Mr. Sabbagh:

I am pleased to inform you, on behalf of the AAPG's Division of Environmental Geosciences (DEG) Executive Committee, that you have been selected to receive the DEG Best Poster Award for your Poster presentation, "Pre-Injection Reservoir Characterization for CO<sub>2</sub> Storage in the Near Offshore Areas of the Texas Gulf of Mexico" at AAPG's ACE 2018. Please accept my sincere congratulations!

Award presentations will occur during the joint DEG/EMD luncheon at the AAPG Annual Convention and Exhibition in San Antonio, Texas. The luncheon will be on Wednesday May 22, 2019. Additionally, your name will be published in the 2019 Honors and Awards program book handed out at the convention.

# 1. INTRODUCTION

**Objective:** Quantitatively evaluate the CO<sub>2</sub> storage capability of the Lower Miocene brine-filled sandstones in the inner continental shelf of the Texas Gulf of Mexico using 3D seismic and well log data. Apply quantitative methods to: (1) estimate reservoir properties to characterize intended CO<sub>2</sub> reservoirs, and (2) understand the effect of injected CO<sub>2</sub> on the elastic properties of the Lower Miocene sandstones.

The injection of CO<sub>2</sub> into the subsurface (carbon capture and storage; CCS) is the most viable approach to significantly reduce industrial emissions of greenhouse gases to the atmosphere. For CCS to be effective, the CO<sub>2</sub> should be monitored during and after injection to guarantee that it is safely retained underground. Among the monitoring methods for CO<sub>2</sub>, the seismic methods provide the volumetric coverage needed to understand the distribution of CO<sub>2</sub> in the subsurface. Seismic methods have been used for monitoring CO<sub>2</sub> sequestration in different geological scenarios through time-lapse applications. As one of the most prolific hydrocarbon provinces and most heavily explored basin in the world, the Gulf of Mexico has incredible potential for CO<sub>2</sub> storage and EOR. The Miocene section of Texas Gulf of Mexico exhibits thick sand intervals with high porosity and permeability, effective trapping mechanism, and regional seals.

This study quantitatively evaluates the CO<sub>2</sub> storage capability of the Lower Miocene brine-filled sandstones in the inner continental shelf of the Texas Gulf of Mexico using 3D seismic and well log data. The first part of this work investigates the relationship between elastic properties and reservoir properties (e.g., porosity, mineralogy, and pore fluid) of the Lower Miocene section using rock physics modeling and simultaneous seismic inversion. The second part of this work studies the effect that CO<sub>2</sub> has on the elastic properties of the Lower Miocene rocks using fluid substitution, amplitude variation with angle (AVA), and statistical classification to determine the ability of the seismic method to successfully monitor CO<sub>2</sub> injected into the subsurface.

### Dataset

The dataset used in this study is comprised of a 3D post-stack seismic volume, three partial angle-stack volumes (near-angle stack, mid-angle stack, and far-angle stack), and three wells (referred as well OCS 511, well OCS 518, and well OCS G6142). The seismic and well data is located in the coastal area of the Texas Gulf of Mexico (Figure 1).



Figure 1: Map of the study area showing the location of the 3D seismic data and the location of the wells used in this study. The red box represents the area covered by the 3D seismic data and the circles the location of the wells.

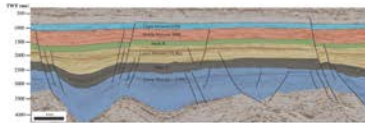


Figure 2: Strike-oriented seismic cross-section interpreted showing the structural style of the study area and the stratigraphic units. The interpreted units include the Upper Miocene (UM), Middle Miocene (MM), Amph. B shale, Lower Miocene 2 (LM2), focus of this study as a intended reservoir for CO<sub>2</sub> storage, Marg. A shale, and Lower Miocene 1 (LM1).

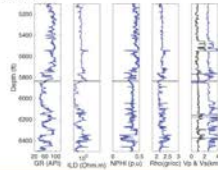
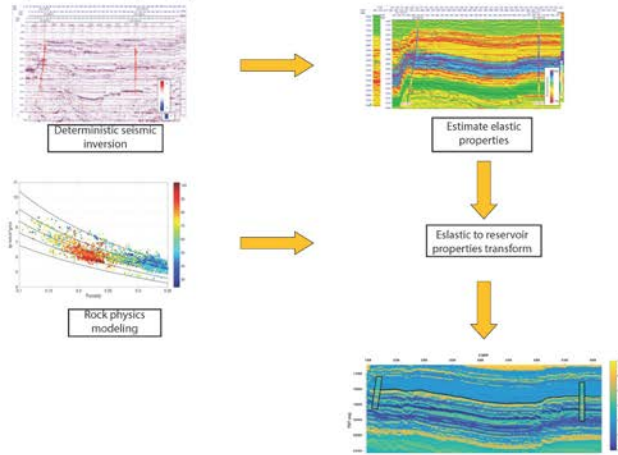


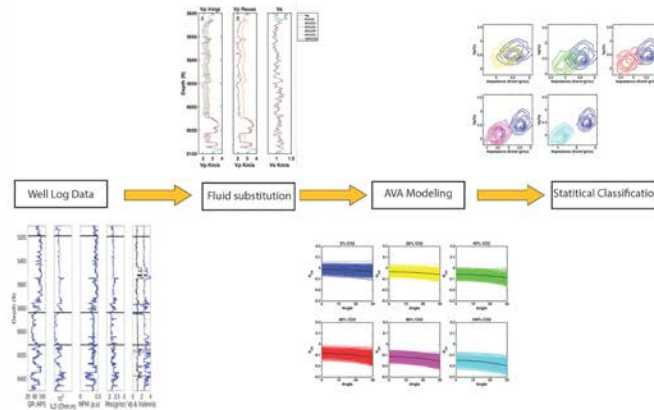
Figure 3: Well logs from well OCS 511. From left to right the well logs are gamma ray (GR), deep resistivity (ILD), neutron porosity (NPHI), bulk density, P-wave velocity, and S-wave velocity. The black line represents the top of the Lower Miocene 2 (LM2) sandstones.

# 2. WORKFLOW

## 2.1 Porosity estimation using rock physics and seismic inversion



## 2.2 Porosity estimation using rock physics and seismic inversion





## Websites

The project website is <http://www.beg.utexas.edu/gccr/research/osra> .

## **7 PARTICIPANTS & OTHER COLLABORATING ORGANIZATIONS**

Name: Tip Meckel, PhD

Project Role: Principal Investigator

Contribution to Project: Dr. Meckel provided leadership to the project team and supervised GRAs Emily Beckham (supported by a fellowship but worked on project research), Izaak Ruiz (partly supported by fellowship), Reinaldo Sabbagh and Omar Ramirez Garcia.

Name: Ramón Treviño

Project Role: co-Principal Investigator

Contribution to Project: Mr. Treviño provided project management (including budget management) & leadership to the project team. Treviño co-chaired team meetings and drafted the quarterly and milestone reports and the final report.

Name: Dallas Dunlap

Project Role: Researcher (geophysicist - seismic interpreter / seismic database manager)

Contribution to Project: Mr. Dunlap maintained the seismic database on the Halliburton Landmark OpenWorks platform.

Name: Michael DeAngelo

Project Role: Researcher (geophysicist seismic interpreter)

Contribution to Project: Mr. DeAngelo conducted structural interpretation of the “TexLa Merge” regional 3D seismic dataset, three recently released (to the public) 3D seismic surveys and regional 2D datasets in the time domain.

Name: Mariana Iulia Olariu, PhD

Project Role: Researcher (geologist – well interpreter / well database manager)

Contribution to Project: Established and maintained well-based database on the IHS Petra geological interpretation software package and correlates regional well logs. She estimated static capacity in the western portion of the study area. She also supervised undergraduate research assistants, Marisa Lindeman, Jordan Alexander, Kindra Nicholaides, Jeremy Martens, John Franey and Izaak Ruiz, who eventually became a project GRA.

Name: Jiemin Lu, PhD

Project Role: Researcher (petrographer)

Contribution to Project: Dr. Lu searched for, identified, examined and analyzed whole cores containing mudrocks facies.

Name: Alexander Klokov, PhD

Project Role: Researcher (geophysicist – seismic interpreter)

Contribution to Project: Dr. Klokov analyzed a high-resolution 3D (HR3D) seismic, shallow-investigation survey (a.k.a. P-Cable) dataset in the southwest portion of the project study area. His analysis focused on generating and interpreting a diffraction volume of the dataset.

Name: Tom Hess  
Project Role: Researcher (geophysicist – HR3D seismic re-processing)  
Contribution to Project: re-processed and improved the 2014 HR3D seismic dataset.

Name: Vanessa Nunez-Lopez  
Project Role: Research Engineer Associate  
Contribution to Project: Conducted EASiTool assessment (subtask 4.2).

Name: Ali Goudarzi, PhD  
Project Role: Researcher (reservoir engineer)  
Contribution to Project: Analyzed fields using decline curve analysis (DCA) (subtask 4.1).

Name: Reynaldy Fifariz, PhD  
Project Role: Graduate Research Assistant and Post-doctoral Fellow  
Contribution to Project: Interpreted the High Island 10-L extension under the direction of Dr. Meckel.

Name: Reinaldo Sabbagh Maciel  
Project Role: Graduate Research Assistant  
Contribution to Project: Investigated the inversion of conventional 3D seismic data from geologic zones of interest with wireline log-derived velocity, density, and porosity data in order to extract lithology properties and spatial distribution.

Name: Omar Ramirez Garcia  
Project Role: Graduate Research Assistant (MS degree graduate)  
Contribution to Project: Interpreted the High Island 10-L extension under the direction of Dr. Meckel.

Name: Izaak Ruiz  
Project Role: Graduate Research Assistant (MS degree graduate)  
Contribution to Project: Interpreted the High Island 24-L under the direction of Dr. Meckel.

In addition, subrecipient, **Southern States Energy Board (SSEB)**, contributed to regional outreach.

## **8 IMPACT**

Eight peer-reviewed articles based on research from the project were published and are listed with their, respective, first pages as follows:



Research paper

## Diffraction imaging for seal evaluation using ultra high resolution 3D seismic data



Alexander Klokov<sup>\*</sup>, Ramón H. Treviño, Timothy A. Meckel

Bureau of Economic Geology, The University of Texas at Austin, USA

### ARTICLE INFO

**Article history:**  
Received 12 May 2016  
Received in revised form 7 October 2016  
Accepted 1 February 2017  
Available online 3 February 2017

**Keywords:**  
Gulf of Mexico  
Shallow  
Cap rock  
Saturation  
Fractures  
P-cable  
Seismic imaging

### ABSTRACT

Cap rock is any impermeable or low permeability formation that may trap oil, gas or water, preventing it from migrating to the surface. Evaluation of sealing properties of the cap rock is a critical task for seismic exploration. It is important for oil and gas prospecting as well as for locating reservoirs appropriate for carbon dioxide storage. The latter has been proposed as one solution to global climate change caused by heat-trapping anthropogenic gases in the atmosphere. A fluid escaped from the reservoir fills voids in the overlying strata thereby causing local changes of acoustic properties. We aim to explore such fluid-saturated areas and thus evaluate sealing properties of underlying cap rocks. We assume that local acoustic impedance changes caused by fluid migration generate seismic diffractions. We isolate diffracted waves from P-Cable seismic data acquired over the area of interest and perform diffraction analysis of the near-surface interval (above 200 m).

In the diffraction image obtained, we interpret an extensive system of broad sinuous channels, narrow linear faults, and diffuse fracture networks. In addition, we detect high-diffractivity anomalies, which extend vertically and laterally. We note no evidence of these anomalies in a conventional seismic image and associated seismic attribute (similarity and fracture density) volumes. We associate this high diffractivity to a variable pore fluid composition and saturation, which we infer to be due to hydrocarbon migration from the underlying strata. Consequently, we conclude poor seal quality for the underlying cap rocks.

During data processing, we test diffraction focusing analysis for velocity model building. This option appears quite valuable for P-Cable data processing because of short offset and limitations of the standard velocity analysis.

© 2017 Elsevier Ltd. All rights reserved.

### 1. Introduction

In addition to determining reservoir properties, a critical task for seismic exploration is evaluation of cap rock sealing properties. A reservoir with high porosity and permeability remains brine-saturated if the overlying top seal is not capable of retaining migrating fluids (e.g., hydrocarbons or carbon dioxide  $\text{CO}_2$ ). In contrast, impermeable rock facies above a reservoir may form part of a trap that allows for accumulation and retention of fluids in the reservoir for a significant time. Consequently, such reservoir-seal scenarios are desirable in oil and gas exploration as well as for locating proper storages sites for anthropogenic  $\text{CO}_2$ .

The sealing capacity of a cap rock is determined by a

combination of various factors. The potential of the fluid to displace into the cap rock is related to capillary properties of the seal (Hubbert, 1953). In general, low permeability facies (e.g., mudstone, shale) comprise high quality seals because their high capillary entry pressure, which inhibits fluid migration into the seal facies. In contrast, sandstone has much lower capillary entry pressure and weaker resistance to fluid pressure (Schowalter, 1979). However, in some cases, a reservoir can be sealed by sandstone (Edlmann et al., 2016). Carbonates can be as highly-penetrable or a reliable seal depending on composition (Ahr, 2008).

Structural factors also affect seal quality. Faulting and fracturing can significantly increase the permeability of the rocks and can decrease sealing capacity. A fault can be sealing or non-sealing depending on the displacement pressure of the fluids and lithologies in contact at the fault (Smith, 1966; Antonellini and Aydin, 1994). The fault is sealing for lateral migration across the plane or vertical migration along the plane if the capillary entry pressure of

<sup>\*</sup> Corresponding author.  
E-mail address: [alexander.klokov@gmail.com](mailto:alexander.klokov@gmail.com) (A. Klokov).

## Diffraction imaging of high-resolution 3D P-cable data from the Gulf of Mexico using azimuthal plane-wave destruction

Dmitrii Merzlikin<sup>1</sup>, Timothy A. Meckel<sup>1</sup>, Sergey Fomel<sup>1</sup> and Yanadet Sripanich<sup>1</sup>

### Abstract

Edge diffractions are responses from such geologic discontinuities as depositional channels, faults, fracture swarms, etc. We apply diffraction imaging to a high-resolution 3D (P-cable) dataset acquired on the inner shelf, Gulf of Mexico. We generate and interpret azimuthal plane-wave destruction diffraction images and focus on two different geological features observed in the diffracted wave-field: (1) faults, and (2) meandering channels with high and low sinuosity. The crucial step in diffraction imaging workflows is the diffraction/reflection separation procedure with the goal of attenuating reflection energy that typically masks weaker diffraction energy. Plane-wave destruction filters successfully serve this purpose. In 3D these filters operate in two directions – along inline or crossline directions. We apply an extended azimuthal plane-wave destruction imaging workflow, which accounts for various orientations of edge diffractions and allows for their orientation determination. We utilize the azimuth information to identify subtle diffractivity zones with orientations similar to the one of corresponding major faults. We show that diffraction images allow for finer discontinuities' delineation as compared to conventional reflection images.

### Introduction

The study area and seismic volume are on the inner shelf of the Gulf of Mexico (GoM) less than ten miles offshore High Island (HI), Texas, east of Galveston Bay. Erosion and deposition from multiple coastal rivers (e.g. Colorado, Brazos, Trinity, etc.) have resulted in the development throughout the Cenozoic of an extensive, low-gradient, clastic dominated shelf along the east Texas coastal plain (Galloway et al., 2011). As a result of relative sea level change, the shallow stratigraphy of the inner shelf contains common fluvial, deltaic, and shoreline depositional systems similar to the modern coastline (Meckel and Mulcahy, 2016). These depositional systems are common reservoir targets in hydrocarbon exploration along many basin margins, although typically at much larger scales and greater depths. Structurally, the overall progradation of the shoreline seaward has resulted in the development of large-scale regional growth faulting that extends for kilometres vertically and laterally (McDonnell et al., 2009). In addition, a complex network of smaller-scale antithetic fault splays is associated with the main growth fault system throughout the inner shelf setting, and these smaller scale structures are associated with the majority of produced gas in the region. The impact that these faults have on active fluid migration is unknown, prompting the recent acquisition of high-resolution 3D data. These stratigraphic and structural features in the relatively shallow stratigraphy are mapped and located on both conventional and azimuthal plane-wave destruc-

tion diffraction images. The high resolution of imaging makes the dataset ideal for evaluating the ability of diffraction imaging to provide additional information for feature identification and interpretation.

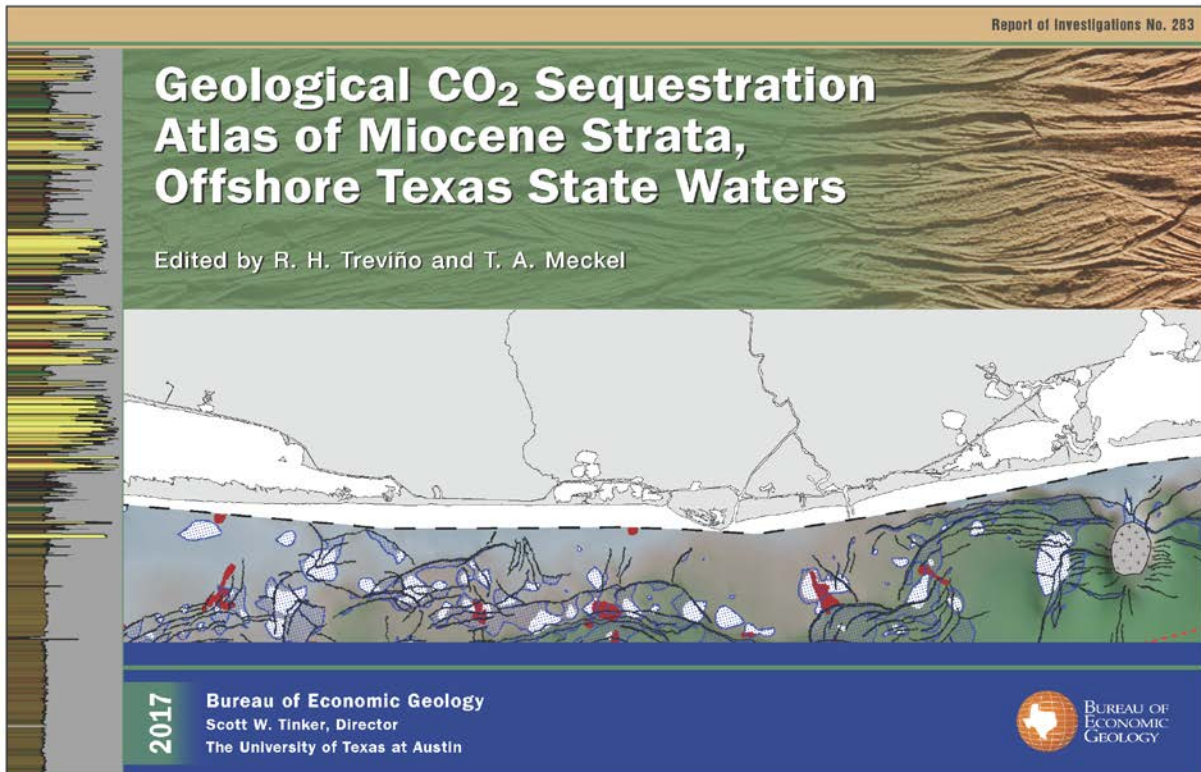
During 2012-2014, a novel shallow-investigation, high-resolution 3D (HR3D) marine seismic acquisition system (P-cable) was deployed in the Gulf of Mexico to characterize structure and stratigraphy. The dataset acquired in 2014 is the focus of this paper. HR3D data can image detailed depositional and structural features in the shallow subsurface that are typically below conventional 3D seismic resolution and/or excluded from commercial surveys which may be optimized for deeper targets. Development of shallow HR3D technology has been primarily driven by an evolving need to understand the shallow interval for geotechnical purposes (Marsset et al., 1998; Brookshire et al., 2015). Brookshire et al., (2016) illustrate the ability of HR3D acquisition system to provide unprecedented resolution of the near surface at low acquisition cost in comparison to conventional acquisition systems.

Information about the subsurface encoded in the diffracted wave-field can benefit the interpreter. Schoepp et al. (2015) discover strong correlation between diffracted energy magnitude and the initial production rates of the wells drilled into the mudstone reservoir. Burnett et al. (2015), Popovici et al. (2015) and Tyiasning et al. (2016) illustrate the ability of diffraction imaging to emphasize smaller scale features in comparison to

<sup>1</sup> University of Texas at Austin, Bureau of Economic Geology, Jackson School of Geosciences, Austin, Texas, USA

\* Corresponding author, E-mail: dmitrii.merzlikin@utexas.edu

Carr, D. L., Meckel, T. A., Lu, J., Rhatigan, J. L. T., Wallace, K. J., Trevino, R. H., Rhatigan, C. H., Nicholson, A. J., Fifariz, R., Yang, C., (2017). *Geological CO<sub>2</sub> Sequestration Atlas for Miocene Strata Offshore Texas State Waters* (R. H. Trevino & T. A. Meckel Eds. Vol. 283). Austin, TX: The University of Texas at Austin, Bureau of Economic Geology.





Klokov, A., Meckel, T. A., & Trevino, R. H. (2018). Confining system integrity assessment by detection of natural gas migration using seismic diffractions. *International Journal of Greenhouse Gas Control*, 75, 32-40.

International Journal of Greenhouse Gas Control 75 (2018) 32–40



Contents lists available at ScienceDirect

International Journal of Greenhouse Gas Control

journal homepage: [www.elsevier.com/locate/ijggc](http://www.elsevier.com/locate/ijggc)



## Confining system integrity assessment by detection of natural gas migration using seismic diffractions



Alexander Klokov<sup>a</sup>, Timothy A. Meckel, Ramón H. Treviño

<sup>a</sup> Bureau of Economic Geology, The University of Texas at Austin, United States

### ARTICLE INFO

**Keywords:**  
Seismic  
Interpretation  
Diffraction  
Faults  
Fractures  
Confining system

### ABSTRACT

Successful carbon capture and storage (CCS) requires secure CO<sub>2</sub> confinement within a geologic reservoir. If associated with a depleted hydrocarbon reservoir, the sealing capability can be determined by examination of the shallow subsurface for hydrocarbon leaks. Numerous seismic signatures have been reported to be hydrocarbon indicators. The interpretation can be advanced by using seismic diffractions, which could indicate subtle hydrocarbon accumulations not detectable by conventional techniques. In this work, we investigate the potential of seismic diffractions for use in shallow gas detection. We extract diffractions from the ultra-high-resolution 3D P-Cable seismic dataset acquired along the Gulf of Mexico inner continental shelf. Interpretation of this dataset revealed numerous seismic signatures associated with hydrocarbon accumulations (e.g., a prominent gas chimney). We analyze scattering features of the detected hydrocarbon accumulations and confirm the correlation between confidently interpreted gas accumulations and seismic diffractions. Based on that, we suggest using diffractions for confining system integrity assessment. Diffraction analysis allows operating with subtle seismic signals that facilitates exploration of reliable CO<sub>2</sub> storage sites.

### 1. Introduction

Effective implementation of a carbon capture and storage (CCS) program requires a superior reservoir as well as a high quality confining system (e.g., top seal or caprock). Therefore, detailed investigation of confining systems, their integrity and sealing properties are an important component of prospecting for potential CO<sub>2</sub> storage sites.

Miocic et al. (2016) evaluated natural CO<sub>2</sub> reservoirs, in which the carbon dioxide has been trapped for million years, and discussed the main factors determining the storage security, which included thickness of the confining system, reservoir depth, and gas density. Faults and fractures were reported as the main conduits for migration of CO<sub>2</sub> within the subsurface. Preliminary assessment of storage security can be done by seismic data analysis. In addition to identifying reservoirs and evaluating of stratal thicknesses, seismic can detect faults in the confining system and overlying strata (Juhlin et al., 2007; Alcalde et al., 2013). In combination with geomechanics, this information is critical for determining the optimal configuration of a potential storage site (Vidal-Gilbert et al., 2010; Teatini et al., 2014; Ward et al., 2016; White et al., 2016).

If associated with a depleted hydrocarbon reservoir, confining properties may be determined by investigating the overlying strata for hydrocarbon accumulations. A minimal indication of hydrocarbons

suggests reasonable sealing properties. Conversely, an increase of detected gas concentrations above the reservoir can indicate poor confining properties.

Løseth et al. (2009) presented an extended overview of seismic features associated with hydrocarbon leakage. Hydrocarbon saturation causes amplitude anomalies (bright spots, polarity reversals, dim spots), which have been exploited as hydrocarbon indicators for decades (Brown and Abriel, 2014). These features are mostly related to reservoir units. However, they also may be observed in rocks with low permeability, which constitute caprocks and seals (Løseth et al., 2009).

One prominent seismic signature associated with hydrocarbon leakage is a gas chimney, which is a vertical zone with discontinuous reflectors (Heggland, 1998; Singh et al., 2016). The migrating gas causes irregular changes in the compressional velocity field that yields scattering and degradation of reflected waves (Arntsen et al., 2007). Zhu et al. (2012) investigated seismic imaging of a target in offshore China and concluded that wave scattering caused by shallow gas was the primary phenomenon causing the reflected waves degradation.

A local hydrocarbon accumulation can create an acoustic impedance contrast sufficient for scattering seismic energy. The linkage between hydrocarbon accumulations and seismic diffractions has been documented in various case studies (Rauch-Davies et al., 2014; Klokov et al., 2014; Ogiesoba and Klokov, 2015; Schoepp et al., 2015; Klokov

<sup>a</sup> Corresponding author.

E-mail address: [alexander.klokov@beg.utexas.edu](mailto:alexander.klokov@beg.utexas.edu) (A. Klokov).

<https://doi.org/10.1016/j.ijggc.2018.05.001>

Received 7 September 2017; Received in revised form 9 March 2018; Accepted 1 May 2018  
1750-5836/ © 2018 Elsevier Ltd. All rights reserved.

Goudarzi, A., Meckel, T. A., Hosseini, S. A., & Trevino, R. H. (2019). Statistical analysis of historic hydrocarbon production data from Gulf of Mexico oil and gas fields and application to dynamic capacity assessment in CO<sub>2</sub> storage. *International Journal of Greenhouse Gas Control*, 80, 96-102. Article ISI://WOS:000454007900009

International Journal of Greenhouse Gas Control 80 (2019) 96–102



Contents lists available at ScienceDirect

International Journal of Greenhouse Gas Control

journal homepage: [www.elsevier.com/locate/ijggc](http://www.elsevier.com/locate/ijggc)



## Statistical analysis of historic hydrocarbon production data from Gulf of Mexico oil and gas fields and application to dynamic capacity assessment in CO<sub>2</sub> storage



Ali Goudarzi<sup>\*</sup>, Timothy A. Meckel, Seyyed A. Hosseini, Ramón H. Treviño

Bureau of Economic Geology, Jackson School of Geosciences, The University of Texas at Austin, USA

### ARTICLE INFO

**Keywords:**  
CO<sub>2</sub> storage in oil and gas reservoirs  
Statistical analysis  
Gulf of Mexico oil and gas data  
Probability of non-exceedance  
Dynamic capacity estimation  
Decline curve analysis

### ABSTRACT

Numerical modeling of CO<sub>2</sub> injection and reservoir flow is typically performed to forecast the number of wells, sustainable injection rates, and total storage volume (or mass). A critical determination for CO<sub>2</sub> storage in depleted oil and gas reservoirs is characterization of reservoir compartmentalization which informs boundary conditions in simulating injection scenarios. Constraining boundary conditions during CO<sub>2</sub> injection into geological formations is a key factor for feasible deployment project. Production history data from 616 wells in 100 oil and gas fields from Gulf of Mexico (GOM) offshore basin can be used to evaluate boundary conditions and total production (oil and gas) and therefore constrain the capacity for potential carbon storage. In general, the combination of decline curve analysis and statistical analysis (to specify constraining boundary conditions) allows the determination of the range of reservoir performance if existing inactive production wells in GOM area of study are used reversibly for CO<sub>2</sub> injection.

To constrain the mass of CO<sub>2</sub> which can be injected, it is useful to consider estimates of cumulative bulk (hydrocarbon + brine) production (CBP), which can be converted to equivalent CO<sub>2</sub> mass considering reservoir conditions. Summary CBP statistics are presented as a probability of non-exceedance (PNE), providing a forecast of likely injection rates and masses for other located CO<sub>2</sub> storage projects with similar geology and boundary conditions in the future. The 50% PNE for Equivalent CO<sub>2</sub> is a novel quantitative approach to investigate the possible injection capacity in CO<sub>2</sub> storage projects. The PNE sensitivity analysis shows that reservoir age, drive mechanism, reservoir trap, and reservoir porosity are the key controlling parameters for productivity and consequently optimum CO<sub>2</sub> storage capacity. Another key finding is the negligible correlation between CBP with reservoir transmissivity and porosity, which implies that other factors than just petrophysical parameters should be studied as constraining factors for CO<sub>2</sub> storage statistical analysis.

### 1. Introduction

Estimating volumetric CO<sub>2</sub> storage capacity in brine aquifers over large regional areas has been addressed in a variety of ways for decades. The overall focus has been on static capacity calculations, with increased recognition that dynamic factors related to injection need to be considered (Ganjdanesh and Hosseini, 2018; Meckel et al., 2017). Furthermore, determining the number of wells required to dispose CO<sub>2</sub> emissions by injecting into geological formations is a key factor for feasible project deployment (Mathias et al., 2013a; Ehlig-Economides and Economides, 2010; Cavanagh et al., 2010; Hosa et al., 2011; Gammer et al., 2011). With dynamic assessments, boundary conditions become very influential on results which will be the main focus of this article.

Injection of mega-tons of CO<sub>2</sub> into deep saline aquifers for geologic carbon sequestration (GCS) will create significant pressure perturbations in the subsurface (Birkholzer et al., 2009; Goudarzi et al., 2018; Hosseini and Nicot, 2012; Nicot, 2008; Eiken et al., 2011). The effect of confinement (boundary conditions) on pressure buildup is vital and constraining boundary conditions is paramount. Safety concerns related to these pressure perturbations include 1) seismicity, 2) storage integrity compromise via wells, faults and fractures, and topseal, and 3) impact on underground sources of drinking water due to seepage (Nicol et al., 2011; Oldenburg and Unger, 2003).

The most crucial parameters influencing injectivity are permeability, porosity, formation thickness, areal extent, pressure, temperature, brine salinity and relative permeability (Mathias et al., 2011, 2013b). The values for these parameters in regions with historic and

<sup>\*</sup> Corresponding author at: Bureau of Economic Geology, Jackson School of Geosciences, The University of Texas at Austin, TX, 78713-8924, USA.  
E-mail address: [agoudarzi@utexas.edu](mailto:agoudarzi@utexas.edu) (A. Goudarzi).

<https://doi.org/10.1016/j.ijggc.2018.11.014>

Received 6 July 2018; Received in revised form 22 November 2018; Accepted 22 November 2018  
1750-5836/ © 2018 Elsevier Ltd. All rights reserved.



Contents lists available at ScienceDirect

International Journal of Greenhouse Gas Control

journal homepage: [www.elsevier.com/locate/ijggc](http://www.elsevier.com/locate/ijggc)

## Statistical analysis of historic hydrocarbon production data from Gulf of Mexico oil and gas fields and application to dynamic capacity assessment in CO<sub>2</sub> storage



Ali Goudarzi\*, Timothy A. Meckel, Seyyed A. Hosseini, Ramón H. Treviño

Bureau of Economic Geology, Jackson School of Geosciences, The University of Texas at Austin, USA

### ARTICLE INFO

**Keywords:**  
CO<sub>2</sub> storage in oil and gas reservoirs  
Statistical analysis  
Gulf of Mexico oil and gas data  
Probability of non-exceedance  
Dynamic capacity estimation  
Decline curve analysis

### ABSTRACT

Numerical modeling of CO<sub>2</sub> injection and reservoir flow is typically performed to forecast the number of wells, sustainable injection rates, and total storage volume (or mass). A critical determination for CO<sub>2</sub> storage in depleted oil and gas reservoirs is characterization of reservoir compartmentalization which informs boundary conditions in simulating injection scenarios. Constraining boundary conditions during CO<sub>2</sub> injection into geological formations is a key factor for feasible deployment project. Production history data from 616 wells in 100 oil and gas fields from Gulf of Mexico (GOM) offshore basin can be used to evaluate boundary conditions and total production (oil and gas) and therefor constrain the capacity for potential carbon storage. In general, the combination of decline curve analysis and statistical analysis (to specify constraining boundary conditions) allows the determination of the range of reservoir performance if existing inactive production wells in GOM area of study are used reversibly for CO<sub>2</sub> injection.

To constrain the mass of CO<sub>2</sub> which can be injected, it is useful to consider estimates of cumulative bulk (hydrocarbon + brine) production (CBP), which can be converted to equivalent CO<sub>2</sub> mass considering reservoir conditions. Summary CBP statistics are presented as a probability of non-exceedance (PNE), providing a forecast of likely injection rates and masses for other located CO<sub>2</sub> storage projects with similar geology and boundary conditions in the future. The 50% PNE for Equivalent CO<sub>2</sub> is a novel quantitative approach to investigate the possible injection capacity in CO<sub>2</sub> storage projects. The PNE sensitivity analysis shows that reservoir age, drive mechanism, reservoir trap, and reservoir porosity are the key controlling parameters for productivity and consequently optimum CO<sub>2</sub> storage capacity. Another key finding is the negligible correlation between CBP with reservoir transmissivity and porosity, which implies that other factors than just petrophysical parameters should be studied as constraining factors for CO<sub>2</sub> storage statistical analysis.

### 1. Introduction

Estimating volumetric CO<sub>2</sub> storage capacity in brine aquifers over large regional areas has been addressed in a variety of ways for decades. The overall focus has been on static capacity calculations, with increased recognition that dynamic factors related to injection need to be considered (Ganjdanesh and Hosseini, 2018; Meckel et al., 2017). Furthermore, determining the number of wells required to dispose CO<sub>2</sub> emissions by injecting into geological formations is a key factor for feasible project deployment (Mathias et al., 2013a; Ehlig-Economides and Economides, 2010; Cavanagh et al., 2010; Hosa et al., 2011; Gammer et al., 2011). With dynamic assessments, boundary conditions become very influential on results which will be the main focus of this article.

Injection of mega-tons of CO<sub>2</sub> into deep saline aquifers for geologic carbon sequestration (GCS) will create significant pressure perturbations in the subsurface (Birkholzer et al., 2009; Goudarzi et al., 2018; Hosseini and Nicot, 2012; Nicot, 2008; Eiken et al., 2011). The effect of confinement (boundary conditions) on pressure buildup is vital and constraining boundary conditions is paramount. Safety concerns related to these pressure perturbations include 1) seismicity, 2) storage integrity compromise via wells, faults and fractures, and to seepage, and 3) impact on underground sources of drinking water due to seepage (Nicot et al., 2011; Oldenburg and Unger, 2003).

The most crucial parameters influencing injectivity are permeability, porosity, formation thickness, areal extent, pressure, temperature, brine salinity and relative permeability (Mathias et al., 2011, 2013b). The values for these parameters in regions with historic and

\* Corresponding author at: Bureau of Economic Geology, Jackson School of Geosciences, The University of Texas at Austin, TX, 78713-8924, USA.  
E-mail address: [agoudarzi@utexas.edu](mailto:agoudarzi@utexas.edu) (A. Goudarzi).

<https://doi.org/10.1016/j.ijggc.2018.11.014>

Received 6 July 2018; Received in revised form 22 November 2018; Accepted 22 November 2018  
1750-5836/ © 2018 Elsevier Ltd. All rights reserved.

DeAngelo, M. V., R. Fifariz, T. Meckel, and R. H. Treviño, 2019, A seismic-based CO<sub>2</sub>-sequestration regional assessment of the Miocene section, northern Gulf of Mexico, Texas and Louisiana: *International Journal of Greenhouse Gas Control*, v. 81, p. 29-37.

*International Journal of Greenhouse Gas Control* 81 (2019) 29–37



Contents lists available at ScienceDirect

International Journal of Greenhouse Gas Control

journal homepage: [www.elsevier.com/locate/ijggc](http://www.elsevier.com/locate/ijggc)



## A seismic-based CO<sub>2</sub>-sequestration regional assessment of the Miocene section, northern Gulf of Mexico, Texas and Louisiana



Michael V. DeAngelo<sup>\*</sup>, Reynaldy Fifariz, Tip Meckel, Ramon H. Treviño

*Gulf Coast Carbon Center, Bureau of Economic Geology, Jackson School of Geosciences, The University of Texas, Austin, Texas, USA*

### ARTICLE INFO

**Keywords:**  
CO<sub>2</sub> sequestration  
Structural closure  
Miocene section  
Northern Gulf of Mexico  
Storage resources  
Site assessment

### ABSTRACT

Relying primarily on 3D-seismic data, an assessment of the major structural elements of the Miocene section, northern Gulf of Mexico (Texas and Louisiana), was initiated to identify prospective subsurface areas for permanent geologic storage of anthropogenic CO<sub>2</sub>. Identifying and mapping fault planes and key stratigraphic surfaces in the seismic data helped identify several areas that may be suitable for Carbon Capture and Storage (CCS) projects of scale. Prospective sites that included proximity to anthropogenic sources of CO<sub>2</sub>, RMS amplitude intervals that indicate confining zones that greatly retard vertical migration of buoyant CO<sub>2</sub>, and structural closures were ranked on a regional scale. Local site (Site 1) assessment used hydrocarbon-based and volumetric-based methods to estimate the amount of CO<sub>2</sub> that can be safely injected into a prospective site's permanent storage reservoirs.

### 1. Introduction

As part of a U.S. Department of Energy project, a seismic-based evaluation of major structural and stratigraphic elements within the Miocene section of the northern Gulf of Mexico (GOM), Texas and Louisiana, was performed to identify suitable areas for Carbon Capture and Storage projects of scale (Fig. 1). The study area encompasses more than 19,680 km<sup>2</sup> (7598 mi<sup>2</sup>) of the onshore and offshore parts of the Gulf of Mexico Basin. The main TexLa Transition Zone Merge (a.k.a. TexLa Merge) 3D survey (Fig. 1) consisted of approximately 3100 km<sup>2</sup> (1197 mi<sup>2</sup>) of high-quality seismic data.

The TexLa Merge 3D area was the focus due to its proximity to significant industrial (anthropogenic) CO<sub>2</sub> sources and an existing pipeline infrastructure that could be utilized to transport CO<sub>2</sub> to dedicated geologic storage locations. In addition, three supplementary 3D (publicly-available from the U.S. Bureau of Ocean Energy Management) surveys (Fig. 1), totaling more than 2279 km<sup>2</sup> (880 mi<sup>2</sup>) were integrated into the regional structural analysis. More than 11,265 km (7000 mi) of 2D-seismic lines (Fig. 1) allowed for integration and correlation among all of the seismic data into a single regional structural framework.

Structural domains affecting the Miocene section of the northern GOM extend as far as 160 km (100 mi) inland, terminating along the Cretaceous shelf edge, which roughly parallels the current Texas-Louisiana coastline. It is bounded on the southwest near the

Texas-Mexico border and on the east near the DeSoto Canyon Salt Basin ("DC S.D.B" in Fig. 2), located offshore of the Florida Panhandle. The southern periphery extends as far as 650 km (404 mi) offshore in the most distal zones. The study focused on the Oligocene-Miocene Detachment (OMD) structural domain, described by Diegel et al. (1995), which dominates the coastal regions of Texas and Louisiana.

#### 1.1. Review of previous work

The focus of this study is the location of dedicated geologic sites (sinks) that can be utilized by large-scale integrated CCS facilities. The U. S. Department of Energy -National Energy Technology Laboratory (DOE - NETL) has determined that to be economically attractive for development, each site should have the capacity to accommodate a minimum of 30 megatons (MT) of CO<sub>2</sub> generated from adjacent onshore industrial sources. Industrial facilities that are involved in chemical production, natural-gas processing, oil refining, and fertilizer production can each produce as much as 1 metric ton per annum (MTPA) of industrially separated CO<sub>2</sub>. Goodman et al. (2011) discussed in great detail the United States Department of Energy (US-DOE) methodology for estimating CO<sub>2</sub> storage potential for oil and gas reservoirs, saline formations, and unmineable coal seams. Those estimates are based on physically accessible pore volume in formations. Those parameters will be determined after initial screenings have determined the highest ranked CO<sub>2</sub> storage reservoirs within the study area.

<sup>\*</sup> Corresponding author.

E-mail address: [mike.deangelo@beg.utexas.edu](mailto:mike.deangelo@beg.utexas.edu) (M.V. DeAngelo).

<https://doi.org/10.1016/j.ijggc.2018.12.009>

Received 13 June 2018; Received in revised form 30 November 2018; Accepted 13 December 2018

Available online 18 December 2018

1750-5836/ © 2018 Elsevier Ltd. All rights reserved.

Olariu, M. I., DeAngelo, M., Dunlap, D., & Trevino, R. H. (2019). High frequency (4th order) sequence stratigraphy of Early Miocene deltaic shorelines, offshore Texas and Louisiana. *Marine and Petroleum Geology*, 110, 575-586

<http://www.sciencedirect.com/science/article/pii/S0264817219303502>

Marine and Petroleum Geology 110 (2019) 575–586



Contents lists available at ScienceDirect

Marine and Petroleum Geology

journal homepage: [www.elsevier.com/locate/marpetgeo](http://www.elsevier.com/locate/marpetgeo)



Research paper

## High frequency (4th order) sequence stratigraphy of Early Miocene deltaic shorelines, offshore Texas and Louisiana



Mariana I. Olariu<sup>\*</sup>, Mike DeAngelo, Dallas Dunlap, Ramon H. Treviño

Bureau of Economic Geology, The University of Texas at Austin, Austin, TX, 78713, USA

### ARTICLE INFO

#### Keywords:

Lower miocene  
Growth fault  
Gulf of Mexico  
Lagarto  
Offshore

### ABSTRACT

Well logs and 3D seismic reflection data are integrated to image Lower Miocene depocenters of the upper Texas and westernmost Louisiana coastal and offshore areas. Although previously interpreted at a large scale (3rd order cycles), the detailed stratigraphy and depositional history of the early Miocene succession has not been fully developed. The upper lower Miocene interval from *Robulus L* (MFS10) to *Amphistegina B* (MFS9) has been further subdivided into five 4th order cycles (each 200–300 m thick) to provide finer scale stratigraphic detail and interpretation of depositional environments. Results of the finer scale correlations are presented in a series of sandstone percent maps. Overall, the maps display a strike-elongate (sub-parallel to the present day coastline) orientation for the sandstone bodies which thin to the southeast (basinward). Net sandstone thickness is relatively low in older cycles and increases in younger cycles suggesting an overall progradation of the deltaic system into the mapped area through time. Continued marine regression and southward movement of the shoreline are also confirmed by seismic amplitude maps. After a major transgression associated with *Robulus L* deltaic progradation occurred under rising sea level conditions. Deltaic sediments prograded southward and sandstone brought to the upper Texas coast was distributed laterally by longshore currents to form strandplain coast lines. Maximum regression occurred during the interval MFS9.2 to MFS9.3 when a deltaic depocenter formed offshore Texas in east High Island area. However, sandstone thickness progressively decreased laterally to the east (offshore Louisiana) where more shale was present and marine processes reworked deltaic derived sandstones into shore parallel bars. There was a clear retreat of the shoreline during the youngest cycle marking the beginning of transgression associated with *Amphistegina B*. Detailed stratigraphic interpretation (at a 4th order scale) shows more variability in the dominant shoreline processes during early Miocene than previously thought. Recognition of sedimentary systems variability at a 4th order scale is critical for improved hydrocarbon exploration and in understanding potential future CO<sub>2</sub> storage in the area.

### 1. Introduction

A thick wedge (about 3000 m) of siliciclastic Miocene age sediments underlies state and federal waters of offshore Texas and Louisiana (Morton et al., 1985; Galloway, 1989a). Miocene sediments were deposited in an unstable basin along the northern margin of the Gulf of Mexico over a time interval of about 18 Ma (Galloway et al., 2000). The lower Miocene depositional episode lasted about 8 My from approximately 24 to 16 My (Fig. 1), encompassing the Aquitanian, Burdigalian, and early Langhian stages (Galloway et al., 1986; Galloway, 1989b). Stratigraphically, the Lower Miocene is bounded at the base by the *Anahuac* shale and at the top by the *Amphistegina B* shale (Galloway et al., 2000) and consists of two major regressive cycles, known as the Oakville (LM1) and Lagarto (LM2) separated by an important, but less

extensive transgressive episode associated with *Marginulina A* (Fig. 1). Two widespread, transgressive deposits associated with *Amphistegina B* and *Textularia W* define the middle Miocene interval (Combellas-Bigott and Galloway, 2006). The upper Miocene depositional episode lasted for about 6.5 Ma (Galloway et al., 2000) and was terminated by a regional flooding event associated with the *Robulus E* biostratigraphic top (Fig. 1).

Many published studies provide analysis on the Miocene stratigraphy, structural style and depositional history at a regional scale (Rainwater, 1964; Kiatta, 1971; Galloway et al., 1986, 2000; Seni et al., 1994), but high resolution stratigraphic interpretations have yet to be performed. Previous subsurface studies used seismic data and well log correlations to identify sediment dispersal patterns and main depocenters at a regional scale and over long time (million years) intervals

<sup>\*</sup> Corresponding author.

E-mail address: [mariana.olariu@beg.utexas.edu](mailto:mariana.olariu@beg.utexas.edu) (M.I. Olariu).

<https://doi.org/10.1016/j.marpetgeo.2019.07.040>

Received 22 April 2019; Received in revised form 24 July 2019; Accepted 25 July 2019

Available online 29 July 2019

0264-8172/ © 2019 Elsevier Ltd. All rights reserved.

PI Meckel led a field trip that included dozens of international experts in offshore CCS. The field trip included a stop at the beach of Sea Rim State Park, Jefferson County, Texas, which is in the west-central portion of the project's study area. The beach is a modern example of ancient sand-rich depositional systems that are potential reservoirs offshore from the field trip stop but at depths of more than 1000 meters.



Figure A – Project PI, Dr. Tip Meckel (right center) during a field trip to Sea Rim State Park on June 20, 2017 discussing the modern beach setting in relation to deeply-buried, ancient shoreface depositional systems in the near offshore state waters.

## **9 REFERENCES CITED**

- Bish, D. L. (1994). *QUANTITATIVE X-RAY-DIFFRACTION ANALYSIS OF SOILS*.
- Burke, L. A., Kinney, S. A., Dubiel, R. F., & Pitman, J. K. (2012). Regional Map of the 0.70 PSI/FT Pressure Gradient and Development of the Regional Geopressure-Grandient Model for the Onshore and Offshore Gulf of Mexico Basin, U.S.A. . *GCAGS Journal*, 1 97-106.

- DeAngelo, M. V., Fifariz, R., Meckel, T., & Treviño, R. H. (2019). A seismic-based CO<sub>2</sub>-sequestration regional assessment of the Miocene section, northern Gulf of Mexico, Texas and Louisiana. *International Journal of Greenhouse Gas Control*, 81, 29-37. <http://www.sciencedirect.com/science/article/pii/S1750583618304146>
- Goodman, A., Hakala, A., Bromhal, G., Deel, D., Rodosta, T., Frailey, S., et al. (2011). US DOE methodology for the development of geologic storage potential for carbon dioxide at the national and regional scale. *International Journal of Greenhouse Gas Control*, 5(4), 952-965. <Go to ISI>://WOS:000294700900035
- Goudarzi, A., Meckel, T. A., Hosseini, S. A., & Trevino, R. H. (2019). Statistical analysis of historic hydrocarbon production data from Gulf of Mexico oil and gas fields and application to dynamic capacity assessment in CO<sub>2</sub> storage. *International Journal of Greenhouse Gas Control*, 80, 96-102. Article. <Go to ISI>://WOS:000454007900009
- Hillier, S. (1999). Use of an air brush to spray dry samples for X-ray powder diffraction. *Clay Miner*, 34(1), 127–135.
- Klokov, A., Treviño, R. H., & Meckel, T. A. (2017). Diffraction imaging for seal evaluation using ultra high resolution 3D seismic data. *Marine and Petroleum Geology*, 82, 85-96. <http://www.sciencedirect.com/science/article/pii/S0264817217300417>
- Makkonen, L. (2006 ). Plotting Positions in Extreme Value Analysis. . *J. Appl. Meteor. Climatol.*, 45 334–340.
- Nicholson, A. J. (2012). *Empirical Analysis of Fault Seal Capacity for CO<sub>2</sub> Sequestration, Lower Miocene, Texas Gulf Coast*. Unpublished Masters Thesis. Unpublished Masters Thesis. Geoscience. The University of Texas at Austin.
- Pitman, J. K. (2011). Reservoirs and petroleum systems of the Gulf Coast: Depth to top overpressure [map]. In <http://www.datapages.com/Services/GISUDRIL/OpenFiles/ReservoirsandPetroleumSystemsoftheGulfCoast.aspx>: U.S. Geological Survey.
- Seni, S. J., Hentz, T. F., Kaiser, W. R., & Wermund Jr., E. G. (1997). *Atlas of Northern Gulf of Mexico Gas and Oil Reservoirs: Miocene and Older Reservoirs* (Vol. 1). Austin, Texas: The University of Texas at Austin, Bureau of Economic Geology.
- Swanson, B. F. (1981). A SIMPLE CORRELATION BETWEEN PERMEABILITIES AND MERCURY CAPILLARY PRESSURES. *Journal of Petroleum Technology*, 33(12), 2498-2504. <Go to ISI>://WOS:A1981MV53400018
- Wallace, K. J., Meckel, T. A., Carr, D. L., Treviño, R. H., & Yang, C. (2014). Regional CO<sub>2</sub> sequestration capacity assessment for the coastal and offshore Texas Miocene interval. *Greenhouse Gases: Science and Technology*, 4(1), 53-65. <http://dx.doi.org/10.1002/ghg.1380>